Ultracold Gas Theory from the Top-Down and Bottom-Up

by

Victor E. Colussi

B.A., Physics and Mathematics, Grinnell College, 2009

M.S., Physics, University of Colorado Boulder, 2013

A thesis submitted to the

Faculty of the Graduate School of the

University of Colorado in partial fulfillment

of the requirements for the degree of

Doctor of Philosophy

Department of Physics

2017

This thesis entitled:
Ultracold Gas Theory from the Top-Down and Bottom-Up
written by Victor E. Colussi
has been approved for the Department of Physics

Prof. Murray J. Holland

Asst. Prof. José D'Incao

Date

The final copy of this thesis has been examined by the signatories, and we find that both the content and the form meet acceptable presentation standards of scholarly work in the above mentioned discipline.

Colussi, Victor E. (Ph.D., Physics)

Ultracold Gas Theory from the Top-Down and Bottom-Up

Thesis directed by Prof. Murray J. Holland

Advances in trapping and cooling of ultracold gases over the last several decades have made it possible to test many formerly outstanding predictions from disparate branches of physics. This thesis touches on three historical problems that have found new life recently in the context of ultracold Bose gases of alkali atoms. The first problem revolves around an outstanding prediction from Boltzmann over a century and half old that the breathing mode of a isotropically trapped classical gas should oscillate indefinitely. I analyze recent experimental results [Nat. Phys. **11**, 1009 (2015)], and attribute observed damping sources to trap imperfections. The second question is about the analogue of first and second sound modes from liquid helium in trapped dilute gases. I present the results of a joint theoretical/experimental investigation of the breathing mode of a finite temperature Bose-Einstein condensate (BEC), attributing a striking collapse revival behavior of the resultant oscillation to in-phase and out-of-phase normal modes of the thermal cloud and condensate. The third problem is that of the formation of Borromean ring-like three-body bound states, referred to as Efimov trimers, in strongly-interacting few-body systems. I extend the predicted spectrum of Efimov states into the realm of many degenerate internal levels, and investigate the difficult three-body elastic scattering problem.

These questions are part of the broader theme of this thesis: How can our understanding of few-body physics in the ultracold limit be translated into statements about the bulk behavior of an ultracold gas? For weakly-interacting Bose gases, this translation is well-known: the many-body properties of the gas are well-described by the tracking just the one and two particle correlations. I analyze a generalization of this procedure to higher order correlations, the general connection between few-body physics and correlations in a dilute gas, and results for the emergence of Efimov physics in the magnetic phase of the strongly-interacting Bose gas.

Dedication

In memory of my undergraduate advisor, Sujeev Wickramasekara.

Time is an ocean but it ends at the shore.

-Bob Dylan-

Acknowledgements

It has undeniably been an interesting journey characterized by a steady progression from instability to stability. First and foremost, I would like to thank my advisor, Prof. Murray Holland, for his support over the last several years. From Murray, I have learned a great deal (partially through osmosis) about conducting research, especially establishing and maintaing collaborations. Throughout my stay in his group, I have always been genuinely impressed by the amount of time each day his door is open to visitors, and the patience he displayed with me while I learned through trials, errors, and false starts.

I would like to thank Asst. Prof. José D'Incao, who has been both a good friend and mentor. Each day at JILA, I have looked forward to our chats and to hearing your perspective. It was a treat to work with Prof. Matthew Davis of University of Queensland on the analysis of the spherical BEC experiment during his sabbatical at JILA in 2015. I have also had the pleasure of working with Prof. Servaas Kokkelmans of Eindhoven University of Technology during the end of Summer 2016 on cumulant theory and resonance superfluity. I have enjoyed many enlightening discussions with Prof. Chris Greene from Purdue University during his Summer 2016 visit and from my time in his group. I want to thank specifically Dan Lobser from the Cornell group and Cam Straatsma from the Anderson group who is very patient even by Canadian standards.

I want to thank my friends who have shared a rope with me, put up with my rants, and grown accustomed to bad puns. My family and two partners in crime, Suzannah and Chief, have always been unconditionally supportive, engaged, and curious even when I haven't eaten recently. Finally, I want to thank Lee Strassel who was the first to show me the beauty of logic.

Contents

Chapter

1 Introduction **1**

1.1 Outline 5

2 Preliminary Concepts **8**

2.1 Single-Atom Physics 9

2.1.1 Harmonic Traps 10

2.1.2 Identical Particle Symmetry 12

2.1.3 Wave-Particle Duality 13

2.2 Two-Atom Physics 14

2.2.1 Classical Regime 15

2.2.2 Quantum Collisional Regime 16

2.2.3 The Ultracold Limit 19

2.2.4 Interatomic Potentials for Alkali Species in the Ultracold Limit 22

2.2.5 Effective Potentials and the Zero-Range Model 25

2.3 Many-Atom Physics: Formalism 30

2.3.1 Second Quantization 31

2.3.2 Many-Body Hamiltonian 33

2.4 The Noninteracting Bose Gas at Finite Temperatures 36

2.5 Summary 38

3 Anomalous Damping of the Breathing Oscillation of a Nondegenerate Bose Gas in an Extremely Isotropic Trap **39**

3.1 Kinetic Theory Above T_c . . . 41

3.1.1 The Boltzmann Equation . . . 44

3.1.2 Consequences of the H-Theorem: The Undamped Breathing Mode . . . 47

3.1.3 Collective Modes Above T_c. . . . 49

3.2 The Breathing Mode Experiment . . . 53

3.3 Theoretical Analysis . . . 55

3.4 Numerical Methods . . . 60

3.4.1 Collisions . . . 61

3.4.2 Drive mechanism . . . 61

3.5 Results . . . 62

3.5.1 Collisionless regime . . . 63

3.5.2 Crossover regime . . . 66

3.6 Conclusion . . . 69

4 Collapse and Revival of the Breathing Mode of a Degenerate Bose gas in an Extremely Isotropic Harmonic Trap **70**

4.1 Zero Temperature: The Mean-Field Theory of the Condensate . . . 74

4.2 Kinetic Theory Below T_c . . . 78

4.3 Collisionless Dynamics . . . 84

4.3.1 Collective modes in an isotropic harmonic trap . . . 85

4.3.2 Coupled-modes analysis . . . 85

4.4 Experiment . . . 89

4.5 Collisional dynamics . . . 93

4.5.1 Simulation of the experiment . . . 94

4.5.2 Extraction of damping rates . . . 95

4.6 Conclusion 100

5 Efimov Physics and the Three-Body Elastic Scattering Phase Shift 102

5.1 Parametrizing the Motion of Three Atoms 104

5.1.1 Jacobi Coordinates 104

5.1.2 Hyperspherical Coordinates 107

5.2 Analytic Solution of the Three-Body Problem in the Zero-Range Model 110

5.3 The Spectrum of Three-Body Bound States 112

5.4 The Three-Body Continuum 116

5.4.1 Signature of Efimov Physics in the Elastic Three-Body Phase Shift 121

5.4.2 Long-Range Contributions to the Elastic Three-Body Phase Shift 124

5.4.3 Removing Disconnected Two-Body Physics from the Elastic Three-Body Phase Shift 128

5.5 Conclusion 135

6 Efimov Physics with Degenerate Internal Levels 137

6.1 Adiabatic hyperspherical representation for spinor systems 139

6.2 Toy Model: Efimov States with Two Internal States 143

6.3 Spin-1 systems 145

6.4 Spin-2 and -3 Systems 152

6.5 Signatures of Spinor Efimov Physics in the Elastic Three-Body Phase Shift 154

6.6 Conclusion 155

7 One, Two, Three, Many: Few Body Physics in Strongly Interacting Bose Gases 157

7.1 Time and Length Scales in Strongly-Interacting Bose Gases 159

7.2 The Cumulant Expansion Method 161

7.2.1 Structure of the Cumulant Equations of Motion 167

7.3 Self-Consistent Solutions of the Cumulant Equations of Motion 172

7.3.1 Truncation of the Cumulant Equations at First Order: The GPE 172
7.3.2 Higher Powers of the Condensate Wave Function: The Three-Body GPE . . 175
7.4 Emergence of Efimov Physics in Strongly-Interacting Bose Gases 176
7.4.1 Quantum Droplets and Magnetic Ordering 177
7.5 Conclusion 184

8 Conclusion **186**
8.1 Outlook 188

Bibliography **191**

Appendix

A Numerical Simulation of Finite Temperature Bose Gases **209**
A.1 Benchmarks 213
A.1.1 Equilibrium 213
A.1.2 Rethermalization after a quench 215

Tables

Table

5.1 Coefficients α_λ for the $1/R^3$ term in Eq. (5.88) and corresponding phase-shifts as given in Eq. (5.89). We denote the coefficients for the three-body system where only one of the pairs interact by $\tilde{\alpha}_\lambda$ while for three-body systems where all pairs interact we denote them by α_λ. The subscript in $\lambda_{(n)}$ indicates the corresponding degeneracy for a given value of λ. 132

6.1 Values of s_ν relevant for f=1 and 2 spinor condensates covering all possible regions of R and for different magnitudes of the relevant scattering lengths. (The $f = 1, 2$ values are from Ref. [36]) We list the lowest few values of s_ν for each $F_{3\mathrm{b}}$ and their multiplicity (superscript) if greater than one. Below, we use $R \ll |a_{\{\mathrm{n}_1,\mathrm{n}_2,\ldots\}}|$ ($|a_{\{\mathrm{n}_1,\mathrm{n}_2,\ldots\}}| \ll R$) as a shorthand for the condition that R must be much less (greater) than all elements in the set $\{|a_{\mathrm{n}_1}|, |a_{\mathrm{n}_2}|, \ldots\}$. 150

6.2 Values of s_ν relevant for $f = 3$ spinor condensates covering all possible regions of R and for different magnitudes of the relevant scattering lengths. (The $f = 3$ values are from Ref. [37].) We list the lowest few values of s_ν for each $F_{3\mathrm{b}}$ and their multiplicity (superscript) if greater than one. Below, we use $R \ll |a_{\{\mathrm{n}_1,\mathrm{n}_2,\ldots\}}|$ ($|a_{\{\mathrm{n}_1,\mathrm{n}_2,\ldots\}}| \ll R$) as a shorthand for the condition that R must be much less (greater) than all elements in the set $\{|a_{\mathrm{n}_1}|, |a_{\mathrm{n}_2}|, \ldots\}$. 151

Figures

Figure

2.1 Left panel: The single-scattering Feynman diagram for the first Born approximation. Right panel: Multiple scattering contributions are represented by diagrams with intermediate states whose momentum must be integrated over. Here, the double-scattering diagram is shown where the **virtual state's** intermediate momentum **q** must be integrated over, violating energy conservation in the system within the bounds of the time-energy Heisenberg uncertain relation. 18

2.2 The direct and exchange scattering pathways in the center of mass frame of the two colliding identical particles. 19

2.3 At medium separations, the total electronic spin is a good quantum number and the interatomic potentials are the singlet $^1\Sigma_g^+$ and triplet $^3\Sigma_u^+$ potentials, which are shown here for ^{85}Rb atoms [77, 78, 79]. At large separations the energies correspond to the hyperfine levels labeled in the inset, shown here for $mf_1 + mf_2 = -4$ at $B = 600$ G, which is the location of a well-known broad Feshbach resonance. 22

2.4 A schematic of a Feshbach resonance. Scattering process in the incoming channel (red) is coupled to the closed channel (blue). When a bound state (dashed lines) is near collision threshold, the colliding atoms form a metastable state which decays over a characteristic lifetime, indicated by the hourglass, exiting out the open channel. 24

2.5 A sketch of the dependence of the cutoff contact interaction on cutoff momentum, p_c. With increasing cutoff, the maximum at the origin diverges as a the cutoff momentum cubed, and the number of oscillations increases. 28

3.1 A two-dimensional projection of μ-space in both it's discrete representation in terms of individual atoms and continuum representation. 43

3.2 In the modified TOP trap, the cloud shifts under the pull of gravity away from the midpoint between the coils. The trap can be made isotropic to harmonic order with the cost of anisotropic anharmonicities. (Adapted from [63].) 53

3.3 Experimental results from Ref. [24] for the monopole and quadrupole damping rates over a range of collision rates. The monopole damping is nonzero and therefore anomalous, but the quadrupole damping agrees with well-known results from Ref. [100]. 55

3.4 Monopole damping rates versus collision rate for a set of frequencies from the JILA experiment with various anisotropy parameters and central frequencies ν_0. The legend gives the level of anisotropy, where λ, ϵ, and $\nu_0 = \omega_0/2\pi$ correspond to rewriting the harmonic confining potential as in Eq. (3.39). 56

3.5 Driving the monopole moment for $A = 0.15$ and initial temperature of 152nK over four periods of oscillation. (a) FWHM of the monopole moment versus holding time. The grey area indicates the time in between the end of the drive and switching on the anharmonic terms in the trapping potential. (b) The % change in the total energy of the cloud between a trapping potential that is purely harmonic and the same potential with anharmonic terms switched on. The vertical line indicates the point at which the anharmonic terms are added to the trapping potential when the % increase of the total energy is on the order of 0.001%. 62

3.6 Resolving the energy dependence of the monopole moment for a drive strength of $A = 0.15$ (9 ± 1.35Hz) and an initial temperature of 152nK. (a) After binning the tracer particles into energy bins, each bin oscillates as an independent monopole. Here, the ratio of the average period of the monopole in each bin and the zero temperature result, $\mathrm{T}_{\mathrm{M}}^{0} = 2\pi/\omega_{\mathrm{M}}^{0}$ along with the standard deviation (grey region), is plotted versus the energy of each bin in units of thermal energy. (b) The statistical weight, $P(\omega)$, of each frequency component in the cloud. The grey region is the theoretical prediction for the shift of the monopole frequency from L (150nK) to R (180nK). 64

3.7 (a) Damping of the monopole over a range of drive strengths $A = \{0.05, 0.1, 0.15, 0.20, 0.25\}$ and temperatures in the collisionless regime. The grey regions are the damping results along with the uncertainty from the JILA experiment [24] for (from bottom to top) 65nK, 125nK, and 152nK. (b) The colored lines are the theoretical predictions for $\Delta\omega_{\mathrm{M}}(T)$ using f_0^{ah} (blue) and using f_0 (red) for the scaling ansatz versus the settled temperature of the cloud. The points are the damping results from (a) for all simulated drive strengths and temperatures in the collisionless regime. The solid black line is a fit to the numerical damping results using Eq. (3.54). 65

3.8 Damping rate versus the equilibrium collision rate. The triangle data points are a result of numerical particle simulations. The blue curves are scaling ansatz predictions using f_0^{ah} for collisional damping of the monopole mode for temperatures 60nK, 80nK, and 100nK from bottom to top, respectively. 67

3.9 Resolving the energy dependence of the monopole moment for A = 0.05 and initial temperature of 60.6nK for a range of total atom numbers. Each data point is the peak component of the Fourier transform of the normalized collective oscillation in the bin. From bottom to top the curves represent frequency spreads in the collisionless, dephasing crossover, and hydrodynamic crossover respectively. 68

4.1 Temperature dependent $m = 0$ quadrupole mode spectrum from Ref. [21] normalized to the radial trapping frequency ω_r. The anomalous upward shift at $T > 0.7T_c$ differs by $10-20\%$ from zero-temperature analytic result indicated by the lower dashed line. 72

4.2 Profiles of the condensate (solid lines) and thermal cloud (dashed lines in inset) densities from noninteracting $\xi \approx 10^{-2}$ (red), $\xi \approx 10^{-1}$ (blue), to the edge of the Thomas Fermi regime $\xi \approx 1$ (green). The densities and radius are rescaled in oscillator units for $N = 10^5$, $T = 0.8T_c$. As χ increases, the difference in mean-field interactions pushes the thermal cloud further out to the wings of the condensate. 80

4.3 A schematic of the collision processes contained in the ZNG equations. 82

4.4 Oscillation frequency of the in-phase ($\phi = 0$) and out-of-phase ($\phi = \pi$) modes as a function of temperature from the coupled-modes analysis (solid lines). The dashed lines represent the TF limit ($\sqrt{5}\omega_0$) and ideal gas limit ($2\omega_0$) for the monopole mode frequency of the condensate and noncondensate, respectively. Assumptions made in the coupled-modes analysis become invalid for $T \lesssim 0.2\ T_c$. 88

4.5 Magnitude of the response of the in-phase ($\phi = 0$) and out-of-phase ($\phi = \pi$) modes to a trap frequency perturbation as a function of temperature. The amplitude of the trap frequency modulation is $\epsilon = 0.01$. 88

4.6 Amplitude of the monopole mode oscillation (squares) for atom numbers of (a) $N = 8.9 \times 10^5$, (b) $N = 9.7 \times 10^5$, (c) $N = 6.7 \times 10^5$, (d) $N = 5.4 \times 10^5$, and (e) $N = 7.9 \times 10^5$. Each frame is labeled with the condensate fraction (N_c/N) and temperature (T/T_c). Error bars represent the statistical uncertainty of multiple realizations of the experiment at each time point. The dashed lines are a fit of the data to Eq. (4.50), which represents the envelope function for the superposition of two sinusoids. From the fit it is found that the beat frequency is $\Delta\omega/\omega_0 \sim 0.13$ on average and the damping rate lies in the range $\Gamma_e \sim 1.5$–$3.5\ s^{-1}$. 92

4.7 Amplitude of the monopole mode oscillation for experimental atom numbers of (a) $N = 8.9 \times 10^5$, (b) $N = 9.7 \times 10^5$, (c) $N = 6.7 \times 10^5$, (d) $N = 5.4 \times 10^5$, and (e) $N = 7.9 \times 10^5$. Each frame is labeled with the condensate fraction (N_c/N) and temperature (T/T_c), and the legend denotes the different modulation amplitudes used in the ZNG simulations. Error bars on the experimental data represent the statistical uncertainty of multiple realizations of the experiment at each time point. (f) Condensed fraction vs temperature for the ideal Bose gas, $N_c/N = 1 - (T/T_c)^3$ (solid line), the equilibrium state of the ZNG simulations (blue points), and the experimental data (red crosses). All simulations are performed with $N = 8 \times 10^5$ atoms. 96

4.8 Simulated mean-square radius of the condensate (1a-1c) and total (2a-2c) densities for a trap frequency modulation amplitude of $\epsilon = 0.03$ at (a) $T = 0.4\ T_c$, (b) $0.6\ T_c$, and (c) $0.8\ T_c$ (black circles) and resulting fit of Eq. (4.51) (blue line). The density of simulated points has been reduced for clarity. 98

4.9 The coupled-mode results (solid line) from Fig. 4.4 overlaid with results of the ZNG simulations (crosses). Crosses are the result of fitting Eq. (4.51) to the condensate density. 99

4.10 Damping rate of the in-phase (squares) and out-of-phase (triangles) mode as a result of fitting Eq. (4.51) to the simulated evolution of $\langle R_c^2 \rangle$ at each temperature for a trap frequency modulation amplitude of $\epsilon = 0.03$. The solid lines are guides to the eye. Representative fits are shown in Fig. 4.8. 99

5.1 Schematic of the mass-scaled Jacobi vectors written in the odd-man-out notation. . . 105

5.2 A plot of the transcendental equations (Eqs. 5.34–5.35) as a function of real (a.) and imaginary (b.) s in the resonant limit $R/|a_0| \to 0$. The s_i are the roots labeled in increasing order, where s_0 is the root associated with the Efimov potential Eq. 5.37. 113

5.3 The canonical plot of the spectrum of three-body bound states (Efimov trimers) near a Feshbach resonance. At resonance, there is a condensation of an infinite number of Efimov states at threshold which is not shown. 115

5.4 The adiabatic three-body potentials for $a_0 < 0$ (a.) and $a > 0$ (b.). The orange shaded region is the scale-invariant region, the yellow shaded region is the transition region, and the green shaded region is the asymptotic region. The black curves are a result of solving the transcendental equations (Eqs. 5.34–5.35) and the red curves are the three-body potentials corresponding to the indicated values. 117

5.5 Diagrammatic representation of the three-body scattering processes which may occur with pairwise interactions. The grey circles represent a pairwise interaction summarized by the two-body T-matrix. I have excluded the permutations of each scattering diagram. 125

5.6 (a) Eigenphase sum for a system with three different negative scattering lengths ($a_1 \approx -10r_{\mathrm{vdW}}$, $a_2 \approx -15r_{\mathrm{vdW}}$ and $a_3 \approx -20r_{\mathrm{vdW}}$). The solid red curve is the eigenphase sum from S_{3B}, and the green-dashed curves are the eigenphase sums for S_1, S_2, S_3. The blue dotted curve is $\Delta_{\mathrm{ep}}^{(C)}$, which scales as K^2 at threshold. (b) Same as (a) but for a system with three different positive scattering lengths ($a_1 \approx +10r_{\mathrm{vdW}}$, $a_2 \approx +15r_{\mathrm{vdW}}$ and $a_3 \approx +20r_{\mathrm{vdW}}$). 134

6.1 The first few roots s_ν obtained for the toy model in the hyperradial region $a_\alpha \ll R \ll a_\beta$. The roots are plotted versus the mixing angle θ. 144

6.2 The roots $s_\nu(R)$ reflect that the internal state $|\chi_{3B}\rangle$ of the Efimov trimer is in a superposition of internal levels. When there is no admixture, the roots are identical to the single-level problem. When there is nonzero admixture ($c_i \neq 0$), the roots are a weighted average ($w_1(\theta) + w_2(\theta) = 1$) of the single-level roots associated with the individual internal states comprising the superposition. Here, this behavior is shown schematically for the lowest root is_0 which tracks between $i1.00624$ and $i0.41370$ depending on the mixing angle (see the lowest curve of Fig. 6.1). 145

6.3 Schematic representation of the relevant regions in R of the three-body potentials $u(R)$. The shaded area, $R < r_{\rm vdW}$, represents the region where the three-body potentials are expected to be non-universal. For all other regions, the potentials are universally given by the form in Eq. (**??**) with $s(R) \equiv s$. 146

6.4 $F_{3\rm b} = 1$ (red solid line), 2 (green dashed line), and 3 (blue dash-dotted line) hyperspherical adiabatic potentials for $f = 1$ atoms with $a_0 = 10^2 r_{\rm vdW}$ and $a_2 = 10^5 r_{\rm vdW}$. (a) For $R \leq \{a_0, a_2\}$ (shaded region) two attractive potentials exist (both with $s_0 \approx 1.0062i$), allowing for two families of Efimov states, and for $R > a_0$, one of these potentials turns into an atom-dimer channel $|F_{2\rm b} = 0, M_{F_{2\rm b}} = 0\rangle|f = 1, m_f = 0\rangle$. (b) For $a_0 \leq R \leq a_2$ (shaded region), only one family of Efimov states exists ($s_0 \approx 1.0062i$), and for $R \gg a_2$ three (asymptotically degenerate) potentials describe atom-dimer channels, $|F_{2\rm b} = 2, M_{F_{2\rm b}} = -1, 0, 1\rangle|f = 1, m_f = 1, 0, -1\rangle$. 149

6.5 $F_{3\rm b} = 0$ (red solid lines), 1 (red dot-dashed lines), 2 (green dashed lines), 3 (blue dashed lines), 4 (purple dashed lines), 5 (cyan dot-dashed lines) and 6 (black dot-dashed lines) hyperspherical adiabatic potentials for $f = 2$ ^{85}Rb atoms with $a_0 \approx -8.97 r_{\rm vdW}$, $a_2 \approx -6.91 r_{\rm vdW}$, and $a_4 \approx -4.73 r_{\rm vdW}$. Note that the potentials for the mixed-symmetry states, $F_{3\rm b} = 1$ and 5, do not display an Efimov potential. 153

6.6 Schematic of the three-body potential for spin-1 with total three-body hyperfine spin $F_{3B} = 1$ and hyperfine scattering lengths $|a_0| \gg |a_2|$. The relevant roots are $s_0 \approx i10062$ and $s_1 \approx 0.4097$ from Table 6.1. 155

7.1 Relevant length scales in the strongly-interacting Bose gas (not drawn to scale.) The blue atoms are part of an Efimov trimer with characteristic length scale l_{3B}. The effective range r_0 is less than the scattering length, which is less than the interparticle spacing, $r_0 \ll a_0 \ll n^{-1/3}$, and the inter particle spacing is indicated between a blue atom and a red atom of the background gas. 161

7.2 The cumulant expansion generates equations of motion for n-atom correlations that depend explicitly on the dynamics of order less than $n + 2$. This forms a hierarchy of explicit and implicit dependence. 162

A.1 The particle is rotated from its initial trajectory along r_i by an angle φ due to the off axis components of $\mathbf{p}_i$. After the particle position is updated to r_f the momentum components are rotated and realigned with the position vector. Due to spherical symmetry the azimuthal angle is not unique and is chosen randomly. This is represented by the area of revolution of $\mathbf{p}_f$ about the final position vector r_f. . . . 211

A.2 Cartoon depiction of the phase space binning process. Particles (black points) are binned in position space using constant volume shells with the radial width of each bin decreasing with r. Within each spatial bin the particles are further binned in momentum space using a 2D grid of equal area bins based on the magnitude of their momentum p and trajectory $\cos\theta = \hat{\mathbf{p}} \cdot \hat{\mathbf{r}}$. 212

A.3 Results from simulation of our spherical ZNG code for the equilibrium thermal and condensate populations with 5×10^4 total atoms in a 9 Hz trap at 12 nK. The total atom number stays within the fluctuation bounds (green region.) 214

A.4 The collision rates per unit length as a function of position in an 187 Hz trap with 5×10^4 total atoms at 200 nK. In both plots, the data points are a result of Monte Carlo sampling of the collision processes, and the solid curves are a result of an analytic calculation using the Bose distribution. Excellent agreement of the analytic and numerical rates is essential to running a stable simulation. 215

A.5 (a.) The results of a quench of the thermal cloud in a 187 Hz trap with 5×10^4 total atoms and an initial temperature of 200 nK. The three sets of data points are from a 3D cylindrical ZNG code reproduced from Ref. [294], a 3D adaptive Cartesian code reproduced from Ref. [293], and our spherical ZNG code. (b.) The drift of the total atom numbers for the three simulations. The green area is the fluctuation bound. . . 217

Chapter 1

Introduction

Understanding how microscopic processes materialize in the phenomenon of macroscopic systems is one of the most challenging questions in all fields. Examples range from personal–How does life emerge from the chemistry of the body?–to practical–How is the behavior of economies related to the psychology of individuals making up the market? In the study of the physics of dilute gases, these questions relate how the behavior of atoms and molecules on nanometer lengthscales emerge in observable characteristics of the bulk gas. These questions are aimed at understanding the quantum mechanical origin of both thermodynamical properties and nonequilbrium phenomenon.

In the ultracold regime, theoretical descriptions begin on the microscopic level with Hamiltonians containing simplified, effective interactions that reproduce the scattering physics in the low-energy limit, using a finite set of parameters. These theories are derived from extremely accurate models for the interatomic potentials that have been continually developed, maintained, and refined over decades. The ultracold dilute gas is therefore the rare system that can be modeled beginning from a nuanced understanding of the microscopic physics.

These systems are also attractive from an experimental standpoint due to advances in trapping and cooling techniques of ultracold gases over the last several decades, allowing for experimental control over atom number and densities. Furthermore, experimenters exercise a high degree of quantum control of the system through application of external fields, forming the basis of techniques that manipulate and select the internal properties of atoms.

These facets have made the field of ultracold gases a testbed for studying both few and many-

body quantum phenomena. One of the basic tools in the study of condensed matter systems for extracting information about the bulk is to investigate the linear response to external perturbation. Often, the linear response of a system can be calculated in the noninteracting limit as the physics is essentially single-particle. The observed shift of the response tells us about the underlying spectrum of the many-body Hamiltonian including interactions. Additionally, damping of the response reveals the rate at which the microscopic physics within the gas conspire to return the system to a state of statistical equilibrium.

These general ideas were first codified by Ludwig Boltzmann in the late 19th century in a famously controversial equation for the dynamics of a dilute gas bearing his moniker. His theory was founded on the idea that a dilute gas is continually in a state of molecular chaos (Stosszahlansatz) arising from the probabilistic decay of correlations between binary collisions and free evolution. Reflecting on these assumptions in a world post-quantum revolution masks how troubling they were to the deterministic worldview of the late 19th century, resulting in community-wide disputes over the reversal and recurrence paradoxes and ultimately in Boltzmann taking his own life. The Boltzmann equation admits our ignorance of the complicated trajectories of each individual atom in the gas. It focuses instead on the dynamics of macroscopic averages, of which the evolution of the single-particle correlations are the most primitive. It is *the* paradigm for including few-atom physics in the dynamics of macroscopic observables, and serves as a both a foundation and launching point for this thesis.

Recently, increasing attention has been paid to the study of how isolated many-body systems reach a state of statistical equilibrium, and old predictions for undamped nonequilibrium motions, including integrable systems like the quantum Newton's cradle [1], have found new life in ultracold gas experiments. Among the set of predictions that came from the Boltzmann equation, is a curious class of undamped collective oscillations that can be probed by external perturbation of a harmonically trapped gas. This includes the dipole or Kohn center of mass mode and the monopole or breathing mode of an isotropic harmonically confinement [2]. Over the last two decades, many experiments with ultracold Bose gases have probed the spectrum of collective excitations both

above and below [3, 4, 5, 6, 7, 8, 9, 10, 11, 12, 13, 14, 15, 16, 17, 18, 19, 20, 21, 22, 23] the critical temperature for Bose-Einstein condensation, confirming the undamped behavior of the dipole mode over a range of geometries, which serves as a sensitive measurement of the trapping frequencies.

That the dipole mode oscillates undamped is a statement about the factorization of the center of mass from the relative motion of the constituent particles. Verifying that the monopole mode oscillates undamped, on the other hand, is a direct, nontrivial test of the assumptions underlying the kinetic theory of gases and is therefore of fundamental importance. Recent experimental results from JILA [24] for the monopole mode of a nondegenerate Bose gas an extremely spherical trap found oscillations persisting over many seconds with small but nonzero damping. It is therefore important to understand whether this damping results from beyond-Boltzmann effects in the gas or is consistent with the effects arising from beyond harmonic order corrections to the trap.

Whereas collective mode experiments with classical dilute gases test the ideas of molecular chaos and irreversibility, experiments with Bose-condensed gases probe the dynamics of quantum many body systems, including the fundamental spectrum of quasiparticle excitations. One of the earliest studies tracing back to mid-20th century was the observation of first and second sound in liquid helium, which inspired two-fluid theories to account for the transport properties of the system and Landau's canonical quasiparticle spectrum of photons and rotons [25, 26, 27, 28]. These studies of liquid helium framed the early language of collective mode BEC experiments in ultracold gases (see for instance Ref. [20]), however the two-fluid picture has limited application to dilute gases.

In liquid helium, the dynamical coupling between superfluid and normal components manifests in in-phase and out-of-phase oscillation of the two components when fluctuations in density and temperature are present, respectively. For finite temperature dilute BECs, the effects of this dynamical coupling can lead to anomalous shifts of the spectrum of collective modes, as was first observed in an experiment probing the $m = 0$ quadrupole mode [21]. The resolution of these effects is based on the collisionless analogue of first and second sound modes as postulated by Stoof and Bijlsma [29]. It turns out however, that signatures of in-phase and out-of-phase oscillations

are generally obfuscated by the coupled spectrum of collective excitations in a trap with broken rotation symmetry. The analysis of the spectrum shift for an isotropic geometry presented in this thesis is therefore important to characterizing the link between liquid helium and dilute BECs.

Advancements in the quantum control of ultracold gases has also provided a means to tuning the effective interatomic interaction strength near a Feshbach resonance [30]. For identical ultracold bosons in the resonance limit, an infinite ladder of three-body bound states, Efimov trimers, appears one by one with binding energies spaced by a fundamental scaling law [31, 32, 33]. These nonperturbative states are characteristic of the sort of unexpected physics that occurs in the regime of strong-interactions, which cannot be understood by extrapolating the behavior of one or two interacting particles. Solutions of the three-body problem in the strongly-interacting regime however do contain the physics of two interacting atoms as a subset, and it is important to understand how, for instance, the two-body continuum and bound state spectrum is embedded in the three. The existence of Efimov states was inferred for the first time in 2006 through giant atom loss rates in an ultracold gas of caesium atoms frozen to a single internal level [34]. The predicted [35, 36, 37] complexity of the trimer spectrum when each atom has access to multiple, degenerate internal levels is however unconfirmed.

In the strongly-interacting regime, nonperturbative few-body physics emerges in the bulk properties of the gas, contributing to the stability and ground state structure of strongly-interacting Bose gases. Although the lifetime of these systems is severely limited by inelastic losses, Efimov physics has been predicted to stabilize the condensate against collapse due to instabilities [38, 39], leading to the formation of novel, self-bound superfluid droplet states of matter. Recently, the observed crystallization of a collapsing dipolar condensate in Ref. [40, 41, 42], has inspired many theoretical works speculating on the source of the collapse stabilization and pattern [43, 44, 45, 46, 47, 48, 49]. How contributions of Efimov physics in strongly-interacting BECs with multiple degenerate internal levels affects the magnetic ordering remains an open question in the community and is partially addressed in this thesis.

To construct a theory of the strongly-interacting BEC and properly account for the role of

Efimov physics in the gas, it is natural to search first for extensions of weakly-interacting models to include three-body correlations. A general procedure was elaborated in Refs. [50, 51, 52] based on the method of the cumulant expansion to generate a complete set of coupled equations for the dynamics of all orders of correlations in the gas. This theory has been used, for example, to sketch the three-body corrections to the energy density [53]. This extension, as well as the general procedure of resonance superfluidity [54, 55, 56] for including bound state physics into the correlation dynamics first applied successful to the strongly-interacting Fermi gas, have not been acknowledged recently as cutting edge experiments have probed into the region of strongly-interacting nondegenerate [57, 58] and degenerate [59] Bose gases, motivating much of the discussion in the later portions of this thesis.

1.1 Outline

This thesis weaves together several of my published works [60, 61, 36, 37, 62], and I have attempted to make this account as self-contained as possible, referring to the relevant references when a discussion has been truncated. To accomplish this, there is a large amount of review material discussed and derived here oftentimes in detail and with proper attribution. Although this is the thesis of a theorist, there is some basic discussion of the experimental apparatus, a modified TOP trap, used to produce the results of Chapters 3–4 along with some details about how the experimental data was extracted and fit. Finally, the latter half of Chapter 5 is composed of so far unpublished work on the three-body elastic scattering problem.

This thesis is divided roughly into two parts: weakly-interacting Bose gases (Chapters 2-4) and strongly-interacting Bose gases (Chapters 5-7). I begin in Chapter 2 with a review of the important preliminary concepts. In keeping with the spirit of this thesis, I start from the relevant microscopic few-body physics before introducing the basic many-body formalism. On the single-particle level, the physics behind the magnetic TOP trap, which is the apparatus analyzed in Chapters 3–4, is discussed first. This is followed by the requirements of identical particle symmetry, and the standard length scale arguments for the semi-classical approximation. On the two-body

level, the basic concepts of scattering theory are introduced including the cross-section and scattering amplitude, followed by the decomposition of the problem into partial waves and arguments for the truncation of this expansion in the ultracold limit. To contextualize these concepts, I discuss the typical length and energy scales of interatomic interactions between two ground state bosonic alkali atoms. In the ultracold limit, effective interactions can be used in lieu of the full interatomic potential, the simplest of which are the so-called zero-range interactions, which are discussed at the end of the two-body section. These one and two particle concepts are the basic foundation of the many-body formalism which is introduced in the language of second quantization. The many-body Hamiltonian is derived including pairwise interactions for zero-range interactions. This formalism provides the foundation of Chapters 4 and 7. Finally, I close the chapter with a discussion of the ideal Bose gas, introducing many of the important concepts that form the basis of later chapters.

Chapters 3–4 focus on the analysis of results for the breathing mode oscillation of an ultracold Bose gas under extremely spherical isotropic confinement. The classical kinetic theory of gases is first developed along with a discussion of Boltzmann's H-theorem and implications for special undamped solutions of the Boltzmann equation–of which the breathing mode is a member. An overview of the standard techniques for analyzing collective modes of a classical dilute gas are then presented and applied to the results of the breathing mode experiment from the Cornell group at JILA [24]. To analyze the breathing mode experiment below the transition temperature, I begin with the standard zero temperature theory of the condensate followed by a semi-classical kinetic theory for the excitation cloud. Results of this formalism applied to the experiment are then presented with emphasis on the in-phase and out-of-phase normal modes of the gas, which provides an explanation for the striking collapse revival of the condensate oscillation observed experimentally. This concludes the portion of this thesis which deals with weakly-interacting Bose gases.

Chapters 5–7 focus on the strongly-interacting Bose gas, beginning with a discussion of the three-body problem in Chapters 5–6. Chapter 5 begins with the basic machinery required to analyze the three-body problem for neutral bosons in the ultracold limit. I outline the problem in the adiabatic hyperspherical representation, the resultant adiabatic three-body potentials, and

the physics of each relevant region of space. Along the way, the spectrum of Efimov states in the resonant limit are introduced. This is followed by a relatively lengthy discussion of the three-body continuum, specifically contributions to the three-body elastic phase shift from Efimov physics, from successive two-body binary interactions, and from disconnected two-body scattering. Chapter 6 translates much of this analysis to the case where each atom has access to multiple degenerate internal levels as is the case for strongly-interacting spinor Bose gases. The rich spectrum of families of Efimov states are enumerated in this case as well as the contribution of spinor Efimov physics to the three-body elastic phase shifts. This discussion feeds into the final chapter, Chapter 7, which begins with a generalization of the many-body formalism presented in Chapter 4 through the method of cumulants to integrate the discussed three-body physics into the equation of motion for the three-particle cumulant. As an illustration of the generality of the cumulant method, I follow Ref. [52] and rederive the zero temperature theory of the condensate and highlight many of the tacit assumptions that were made previously. I then retrace the work of T. Köhler in Ref. [53] to establish a zero temperature theory of the condensate including three-body physics and finish by characterizing the emergence of Efimov physics in the superfluid (summarizing the work of A. Bulgac in Ref. [38]) and magnetic phase of the condensate.

This thesis concludes with a brief sketch of a possible fusion of the cumulant method with the theory of resonance superfluidity to study the unitary Bose gas. This would produce a mean-field like set of equations for the correlation dynamics of one, two, and three body cumulants with additional mean-field equations for the condensed trimer and dimer superfluids that are formally similar to the zero-temperature theory of the weakly-interacting Bose gas. Construction of this theory will rely intimately on the developments presented in Chapters 4–7, and therefore stands as a natural, challenging, and timely extension of the work presented in this thesis.

As a final note: I've set $\hbar = 1$ for notational clarity at the risk of infuriating future readers.

Chapter 2

Preliminary Concepts

This chapter provides the necessary background to understand the theoretical analysis of ultracold dilute Bose gas experiments in the weakly-interacting regime in Chapters 3–4, comprising the first part of this thesis. It also serves as a prelude to the three-body physics and generalized many-body theory discussed in Chapters 5–7 in the context of strongly-interacting Bose gases.

Before jumping into relevant equations and mathematics, it is useful to elaborate very briefly on the descriptors 'ultracold', 'dilute', 'bosonic', and 'weakly' and 'strongly-interacting', reserving more quantitative definitions for the sections and chapters that follow.

These gases are **ultracold** with typically sub-microKelvin temperatures. Semiclassically, this is a statement that the average energy of an atom in the gas is sufficiently low so as to be completely repulsed by the centrifugal barrier of a neighboring atom for nonzero impact parameters. Quantum mechanically, this means that interactions proceed only along the lowest angular momentum partial wave, greatly simplifying the collisional analysis.

These gases are extremely **dilute** with densities of 10^{14} cm^{-3} [63] compared to ordinary gases at around 10^{19} cm^{-3} and liquids at around 10^{22} cm^{-3}. This diluteness is typically further quantified by comparing the typical separation between atoms of order 10^2 nm compared to the spatial extent of the collision, which is on the order of a few nanometers. In the experiments considered in Chapters 3–4, these length scales are separated by at least two to three orders of magnitude. The associated timescales are also comparably separated: the duration of a collision is much shorter than the transit time between collisions. These separations are the basis of a huge

simplification of the many-body problem in terms of correlation decay in the gas.

These gases are composed of **bosonic** atoms. This is a statement about the statistics of identical particles. For instance when two identical atoms collide, it is impossible to track the individual atoms during the collision and to identify which atom is which afterwards. The physics of identical particles manifests in observable effects through a factor of 2 enhancement of the scattering cross section and also globally through Bose enhancement of transition rates responsible for Bose-condensation.

These gases can be either **weakly-interacting** or **strongly-interacting**, which depends on the underlying scattering physics and their relation to the many-body problem. Chapters 3–4 are concerned with the former regime, and Chapters 5–7 with the latter. In this chapter, the two-body scattering problem is however presented quite generally beginning with the basic universal concepts and a discussion of the typical form of the interatomic interaction for ultracold gases composed of alkali atoms.

This chapter begins with a discussion of the physics on the few-atom level present in the gas. The basics of many-body theory are then outlined beginning with the language of second quantization. Finally, the chapter ends with the basic picture of the ideal Bose gas at finite temperatures, which is the reference system for much of the analysis in Chapters 3–4. Each subsequent chapter of this thesis builds upon these concepts, and so this chapter is considered mandatory for what follows.

2.1 Single-Atom Physics

In this section, the few-body physics present in ultracold Bose gas is discussed *in vacuum*, which is an appropriate starting point for gases that are dilute. This begins with single-particle concepts related to the trapping potentials discussed in this thesis, identical particle symmetry, and the quantum mechanical wave particle duality. The basic physics of the scattering of two bosons is then discussed in the following section with emphasis on the ultracold limit. These concepts serve as the building blocks of all analysis presented in this thesis.

2.1.1 Harmonic Traps

The systems considered in this thesis are confined harmonically via a magnetic trap (Chapters 3–4) or an optical trap (Chapter 6.) From a theoretical point of view, often it is convenient to just write down the trapping frequencies, extract the oscillator lengths

$$a_{ho} = \sqrt{\frac{1}{m\omega_0}}, \tag{2.1}$$

where $\omega_0 = (\omega_x\omega_y\omega_z)^{1/3}$ is the geometric mean of the trapping frequencies and to be done with it. However, details of the magnetic trapping potential are crucial to the analysis of Chapter 3–4, where real-world imperfections in the confinement are central to the analysis. I therefore discuss the magnetic TOP trap with this later analysis in mind and omit a discussion of the optical dipole trap (see for instance Ref. [64].)

2.1.1.1 Magnetic TOP Trap

Magnetic traps are based on the coupling of an applied magnetic field with the magnetic moment of an individual atom's intrinsic spin. The spin components are typically broken down into the nuclear **I** and electronic **J** spins, whose interaction in the absence of fields is described by the hyperfine Hamiltonian

$$H_{hf} = C\ \mathbf{I}\cdot\mathbf{J} = C\ \frac{\left[\mathbf{F}^2 - \mathbf{I}^2 - \mathbf{J}^2\right]}{2}, \tag{2.2}$$

written in terms of the total angular momentum of the atom $\mathbf{F} = \mathbf{I} + \mathbf{J}$ where C is a species dependent constant. For instance, the experiment considered in Chapters 3–4 utilized ^{87}Rb with $I = 3/2$ and $J = 1/2$ which has a hyperfine splitting between $F = 2$ and $F = 1$ in the microwave domain at roughly 6835 MHz [65].

When a static magnetic field is applied, the spin Hamiltonian acquires a coupling

$$H_{hf+mag} = H_{hf} + \left[g\mu_B J_z - \frac{\mu_N}{I} I_z\right] B, \tag{2.3}$$

where μ_N is the magnetic momentum of the nucleus, μ_B is the Bohr magneton, and $g \approx 2$ is the g-factor for the electron. The quantity in brackets is the combined magnetic moment of the nucleus

and electron spins projected onto the direction of the applied field, which is arbitrarily chosen to be the z-axis. This coupling splits the hyperfine states as the total angular momentum is no longer a 'good' quantum number. When the Zeeman energy is small compared to the hyperfine splitting, the shift is well approximated by first order perturbation theory [66]

$$\Delta E(F, m_F) \approx g_F \mu_B m_F B \tag{2.4}$$

for a given hyperfine level, where

$$g_F \approx g \, \frac{F(F+1) + J(J+1) - I(I+1)}{2F(F+1)}. \tag{2.5}$$

Maxwell's equations allow a local minima (not maxima!) of the magnetic field to be created, and therefore the hyperfine states which are trapped are the low-field seekers which are not repulsed by the valley of the trap. For ^{87}Rb, one such state is the maximally stretched state which at zero field is in the spin state $|F = 1, m_F = -1\rangle$.

The energy shifts due to the magnetic field can be utilized to spatially trap the atoms by applying a nonuniform gradient. One such scheme is the quadrupole trap, where two parallel circular coils with opposite currents generate a magnetic field that vanishes at the midpoint where the field takes the form

$$\vec{B} = \begin{pmatrix} \frac{B_z}{2} x \\ \frac{B_z}{2} y \\ -B_z z \end{pmatrix}. \tag{2.6}$$

To avoid transfer to an untrapped spin state at the origin, so-called Majorana losses, a fast rotating bias field perpendicular to the quadrupole magnetic field can be used to produce a field of the form [67]

$$\vec{B} = \begin{pmatrix} \frac{B_z}{2} x + B_0 \cos(\Omega t) \\ \frac{B_z}{2} y + B_0 \sin(\Omega t) \\ -B_z z \end{pmatrix}, \tag{2.7}$$

where B_0 is the field strength of the bias field, and B_z is the strength of the quadrupole field. This bias field rotates at angular frequency Ω, which is typically much larger than the Larmor frequency,

precluding the precession of the atomic spin vector about the magnetic field direction. Near the minimum of the trap the cooled atoms experience a time averaged harmonic potential

$$V_{\mathrm{TOP}}(\rho, z) = \mu B_0 + \frac{\mu B_z}{16 B_0}(\rho^2 + 8z^2) \tag{2.8}$$

where μ is the magnetic moment and $\rho = \sqrt{x^2 + y^2}$.

This is the TOP (Time-Averaged Orbiting Potential) trap scheme for magnetically trapping ultracold neutral atoms [68] with a radial trapping depth of ~ 100 μK and was the first potential used to achieve Bose-Einstein condensation in a dilute gas [69]. In the high-field limit ($\mu B_z \gg mg$) the trap is anisotropic with aspect ratio $\omega_z/\omega_\rho = \sqrt{8}$. A modified version of this trap was used to produce the experimental results analyzed in Chapter 3–4. Importantly, this trap, like all real-world setups, is not perfectly harmonic as can be seen by truncating the time-averaged magnetic field to higher order.

2.1.2 Identical Particle Symmetry

In a dilute Bose gas there are many atoms buzzing about each in the same internal state. There is no feasible way in which to tag an atom. From the viewpoint of quantum mechanics, these atoms are identical and therefore indistinguishable. A theoretical description of identical particles should reflect this fact, which requires that a two-particle wave function satisfy

$$\phi(\mathbf{r_1}, \mathbf{r_2}) = A\phi(\mathbf{r_2}, \mathbf{r_1}) = A^2\phi(\mathbf{r_1}, \mathbf{r_2}). \tag{2.9}$$

This equality restricts $A = \pm 1$. When $A = +1$, the identical particles are **bosons**, and when $A = -1$ the identical particles are **fermions**. An alternate viewpoint starts with a wave function for two distinguishable particles $\phi_D(\mathbf{r_1}, \mathbf{r_2})$ and enforces the identical particle symmetry

$$\phi_I(\mathbf{r_1}, \mathbf{r_2}) = \frac{1}{\sqrt{2}}\left[\phi_D(\mathbf{r_1}, \mathbf{r_2}) \pm \phi_D(\mathbf{r_2}, \mathbf{r_1})\right], \tag{2.10}$$

to construct the appropriately symmetrized wave function ϕ_I where the "+" is appropriate for bosons and the "−" for fermions. The remainder of this thesis deals with bosons and so this is the assumed symmetry whenever an ambiguity arises.

Identical particle symmetry plays an important role in the calculation of transition rates and probabilities in a given system. For bosons, the rate of transition into an occupied state is enhanced by the number of bosons already occupying this state. This **Bose enhancement** can be understood by thinking about the time-reversal of this process: there are many possible, *identical* atoms that can make the transition out of the occupied state. In equilibrium, the principle of **detailed balance** ensures that these rates are equal. Identical particle symmetry therefore manifests in correlations of the system even when the individual atoms are noninteracting. This is important for understanding Bose condensation.

2.1.3 Wave-Particle Duality

From the symmetrization requirement arises a natural question: is it appropriate to consider just two bosons in isolation or rather should the wave function be symmetrized with respect to the totality of identical bosons in all of space? This question is addressed by the **Cluster Law**, which states that it does not matter whether different groups of particles are symmetrized or not provided they are isolated to well separated areas and only independent measurements are performed on the groups (see pp. 600 of Ref. [70])

These questions lie at the heart of a larger theme: what aspects of an atom should be treated quantum mechanically and what can be treated classically to good approximation? Answers to such queries are founded on the smallness of plank's constant $\hbar$ to the relevant problem. Clearly, the internal variables of an individual atom should be treated quantum mechanically to retain, for instance, the spectrum of quantized energy, angular momentum,m and spin levels. When studying the internal energy spectrum there are however limits in which internal dynamics can be though of **semi-classically**, which is to say there is a mix of quantum and classical treatments in the problem, for instance in the high lying orbits of Rydberg electrons (see for instance [71]), although such interesting effects are not of relevance to this thesis. Center of mass (COM) variables are, however, often treated as classically. In a trap, this approach is justified if the oscillator length, is much larger than the wave packet and coherence length of the atom, summarized by the de Broglie

wavelength $\lambda_{dB} = k^{-1}$ which is equal inverse the center of mass momentum. When this is the case, the motion of an individual atom can be described classically as a point-particle, like a billiard ball rolling around in a parabolic well.

The above statements must be qualified in a gas: in the presence of other atoms, if the de Broglie wavelength spans the average separation between neighboring particles, all degrees of freedom, including the center of mass motion, must be treated quantum mechanically. Overlapping de Broglie waves signal the regime of **quantum degeneracy**, which requires a many-body treatment.

2.2 Two-Atom Physics

To go beyond the single-atom picture, interactions within the gas must be accounted for. In principle, collisions between two, three, four, etc... atoms takes place inside of the gas, but with increasing atom order, the probability of occurrence for such processes is suppressed by higher powers of the **diluteness parameter**[1] . In Chapter 7, this argument is made explicit by calculating perturbative contributions to the mean-field theory of the condensate in powers of the diluteness parameter. The diluteness parameter reflects the smallness of the spatial extent of the collision, which for ultracold Bose gases is quantified by the s-wave scattering length a_0 discussed in Sec. 2.2.3, compared to the average inter particle spacing $n^{-1/3}$, summarized for a dilute gas as $(na_0^3 \ll 1)$. When the diluteness parameter is much less than unity, two-body scattering physics is the dominant thermalization process within a gas out of statistical equilibrium. Additionally, when a_0 is much less than the distance to neighboring atoms so that the outgoing trajectories of the two atoms are to a good approximation asymptotic, it is sufficient to input into a many-body theory only the results of two-body scattering surrounded by a vacuum. For most experiments with weakly-interacting Bose gases, the spatial extent of the collision is also orders of magnitude less than the oscillator length of the trapping potential, and so results from two-body scattering in free space can be applied[2] . When a two-body bound state or **dimer** lies near the collision threshold, the scattering length can

[1] To see a concrete example of how these processes are suppressed for beam experiments refer to Refs. [72, 73]

[2] For the experiments considered in Chapters 3–4 these length scales are separated by roughly three orders of magnitude

be tuned, and this is addressed in Sec. 2.2.4.

The quantum versus classical argument from Sec. 2.1 demarcates two scattering regimes. When the de Broglie wavelength is less than the spatial extent of the collision, then the collision can be described in terms of classical trajectories. This is the **classical regime** of two-body scattering. In the opposite limit, the collision must be described in the language of quantum mechanics where identical particle symmetry becomes important. This is the **quantum collisional regime**. The classical regime permits a description of collision which aligns closely with our idea of what a scattering trajectory looks like and so serves as a useful launching point into the quantum collisional regime which is the regime of practical interest for ultracold gases.

2.2.1 Classical Regime

Classically, when an object impinges on a fixed target and scatters off, the problem is deterministic. One could in principle track the position of the object throughout the complete trajectory. For instance, this is feasible for planetary dynamics where the scattering orbit occurs over astronomical time and length scales. In the laboratory, however, what can be counted is only the incoming and outgoing trajectories long after a collision has occured over the inaccessible length scale of the width of an individual atom. Therefore, what is experimentally relevant are the asymptotes of free motion before and after the collision. The scattering problem is therefore concerned with calculating the outgoing asymptote given the incoming trajectory.

That the scattering region is inaccessible means that what's relevant is the outgoing asymptote averaged over a range of impact parameters ρ which measure the perpendicular distance that the scatterer is displaced from an axis of the target–a direct hit corresponds to $\rho = 0$. What's observable is the number of atoms that scatter into a particular solid angle $\Delta\Omega$ after many repeated iterations of the same experiment with a consistent beam density n_{inc} of incoming atoms per unit area. The total number of scattered atoms N_{sc} detected over all solid angles should equal the number of incoming atoms that actually struck the target. Therefore,

$$N_{sc} = \sigma n_{inc}, \tag{2.11}$$

where σ has units of area, measuring the collisional size of the target, which is the two-body collisional **cross section**. If a detector is placed over a certain solid angle $\Delta\Omega$ with respect to the target, the cross section $\sigma(\Delta\Omega)$ of that part of target which scatters into $\Delta\Omega$ is measured. When this angle is small the differential cross section can be measured

$$\sigma(d\Omega) = \frac{d\sigma}{d\Omega} d\Omega. \tag{2.12}$$

The differential cross section is the most in-depth information that can be obtained from classical scattering experiment, and, importantly, it is the result of randomization of the impact parameters as a result of the inaccessibility of the atomic length scales on which the collision occurs. This does not prevent, for instance, tracking the deterministic classical trajectories of interacting atoms as was used in the seminal molecular dynamics study by A. Rahman on liquid phase Argon [74] in the 1960s. The Boltzmann equation discussed in Sec. 3.1.1 however takes the opposite stance of studying particle dynamics beginning from the measurable differential cross section and admitting ignorance of the details of the collision event.

2.2.2 Quantum Collisional Regime

For classical scattering, the outgoing trajectory follows along a definite angle with respect to the origin of the collision at the target. In quantum mechanics, the incoming particle is really a wave packet, ϕ with a momentum distribution well-peaked about some incident momentum, $\mathbf{p_0}$. Portions of the wave packet may scatter over a range of solid angles, and the measurement process collapses the outgoing wave packet Ψ onto a specific solid angle with probability

$$w(d\Omega \leftarrow \phi) = d\Omega \int_0^\infty p^2 dp \; |\Psi(\mathbf{p})|^2 \tag{2.13}$$

where the magnitude of the outgoing momentum has been integrated over to yield a probability of scattering into that solid angle regardless of the momentum components. Recall that the classical result is binary: either the outgoing atom is detected or not. The total number of atoms that scatter into $d\Omega$ averaged over many impact parameters

$$N_{sc}(d\Omega) = \int d^2\rho \; n_{inc} w(d\Omega \leftarrow \phi_\rho) \tag{2.14}$$

where $\phi_\rho = \phi e^{-i\rho\cdot\mathbf{P}}$ is the displaced incoming wave packet. The differential cross section follows from Eq. 2.11, 2.12

$$\sigma(d\Omega \leftarrow \mathbf{p_0}) = \int d^2\rho \; w(d\Omega \leftarrow \phi_\rho), \tag{2.15}$$

where ϕ has been replaced by the momentum $\mathbf{p_0}$ parallel to the collision axis.

The scattering problem is concerned with calculating the outgoing asymptote ϕ_{out} and the differential cross section, given the incoming trajectory ϕ. These two states are linked through the unitary evolution of the system, summarized by the scattering operator S

$$S \; |\phi\rangle = |\phi_{out}\rangle. \tag{2.16}$$

When the S operator is factored as $S = 1 + R$, all of the information about the interaction is contained in the remainder operator R. Matrix elements of the remainder operator $\langle\mathbf{p}| \; R \; |\mathbf{p}'\rangle$ are directly related to the differential cross section through the scattering amplitude, $f(\mathbf{p}, \mathbf{p}')$,

$$\langle\mathbf{p}| \; R \; |\mathbf{p}'\rangle = \frac{i}{2\pi\mu_{2B}}\delta(E_p - E_{p'})f(\mathbf{p}, \mathbf{p}'), \tag{2.17}$$

$$\frac{d\sigma}{d\Omega}(\mathbf{p} \leftarrow \mathbf{p_0}) = |f(\mathbf{p}, \mathbf{p}')|^2, \tag{2.18}$$

which has units of length. The quantity μ_{2B} is the two-body reduced mass which for identical bosons is $\mu_{2B} = m/2$ in terms of the single atom mass, m. The energy delta function is a restriction of the problem on the **energy shell** of the collision $E_p = E_{p'}$ as opposed to off shell $E_p \neq E_{p'}$.

A common way of obtaining solutions for the scattering amplitude is through analysis of the Lippman-Schwinger equation for the scattering T-operator in terms of the two-body interacting V and the free Green's operator G_0,

$$T = V + VG_0T, \tag{2.19}$$

$$\text{where} \qquad \langle\mathbf{p}'|T(E_p + i0)|\mathbf{p}\rangle = -\frac{f(\mathbf{p}, \mathbf{p}')}{(2\pi)^2\mu_{2B}}, \tag{2.20}$$

where the notation '$i0$' indicates the limit as zero is approached from above. The Lippman-Schwinger equation can be iterated

$$T = V + VG_0V + VG_0VG_0V + ..., \tag{2.21}$$

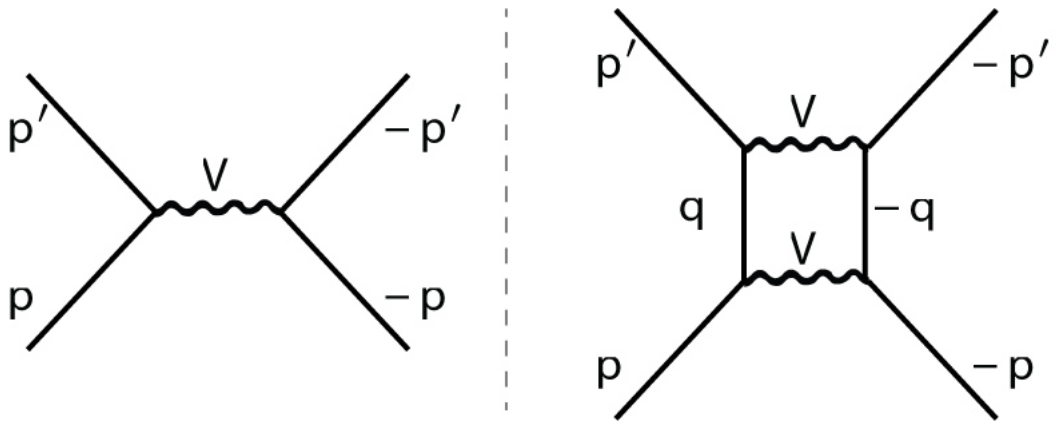

Figure 2.1: Left panel: The single-scattering Feynman diagram for the first Born approximation. Right panel: Multiple scattering contributions are represented by diagrams with intermediate states whose momentum must be integrated over. Here, the double-scattering diagram is shown where the **virtual state's** intermediate momentum **q** must be integrated over, violating energy conservation in the system within the bounds of the time-energy Heisenberg uncertain relation.

to form the **Born series**, whose first order approximation corresponds to $T \approx V$ and is referred to as the **first Born approximation**. The operator G_0 is the Green's operator for the noninteracting Hamiltonian, H_0,

$$G_0(z) = (z - H_0)^{-1}, \tag{2.22}$$

which is an operator function of the complex number z [75]. The Born series is expected to converge at high energies where the denominator of the G_0 is large, and for very weak interactions where higher order terms converge as powers of the interaction strength [75]. Truncating the series in Eq. 2.19 at the first term $T \approx V$ amounts to the first Born approximation, which is commonly used in such scenarios, and the latter scenario is of particular importance to the many-body theories constructed in this chapter. In the interaction picture, the Born series has a diagrammatic interpretation in terms of Feynman diagrams. The Born approximation is commonly referred to as **single scattering**, and the corresponding Feynman diagram is shown in the left panel of Fig. 2.1. The totality of remaining diagrams are referred to as the **multiple scattering** contributions.

Effects due to identical particle symmetry enter at the level of the scattering amplitude. As a general principle of quantum mechanics, all of the amplitudes for indistinguishable pathways

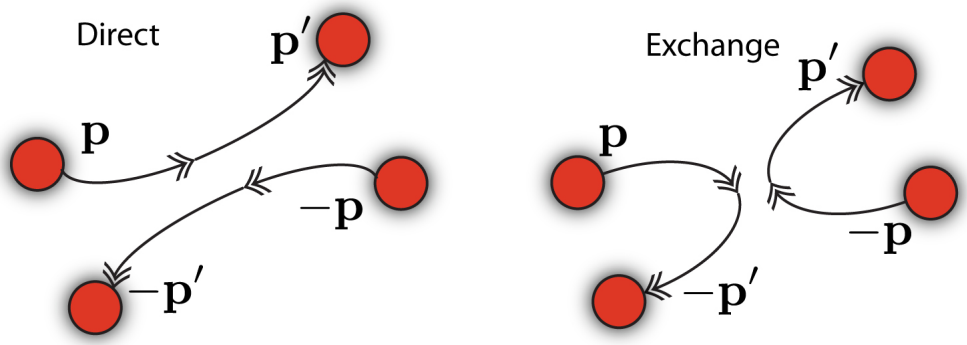

Figure 2.2: The direct and exchange scattering pathways in the center of mass frame of the two colliding identical particles.

must be added before taking the modulus squared and calculating observables and probabilities. For identical particle scattering there are two indistinguishable pathways shown in Fig. 2.2. The first pathway is the one in which the particles are distinguishable, the **direct** pathway. The second pathway is the experimentally indistinguishable from the first, the **exchange** pathway. The correct scattering amplitude for the scattering of two bosons is a coherent sum of the direct and exchange amplitudes

$$\hat{f}(\mathbf{p}, \mathbf{p}') = f(\mathbf{p}, \mathbf{p}') + f(-\mathbf{p}, \mathbf{p}'), \tag{2.23}$$

where the hat indicates the symmetrized amplitude. The symmetrized amplitude for bosons is an even function of the outgoing momentum $\mathbf{p}$ whereas the amplitude for fermions (not shown) is odd. This has direct consequences in the ultracold limit discussed presently.

2.2.3 The Ultracold Limit

In a vague sense, the ultracold limit corresponds to the low-energy limit of scattering, where the problem is considerably simplified. This statement can be made more precise by considering the decomposition of the scattering quantities in terms of angular momentum quantum numbers. When the colliding atoms are spinless, the orbital angular momentum operator $\mathbf{L}$ commutes with the S matrix, which is diagonal in the orbital angular momentum eigenstates $|E, l, m\rangle$

$$\langle E', l', m'| \; S \; |E, l, m\rangle = \delta(E' - E)\delta_{l',l}\delta_{m',m}e^{2i\delta_l(E)}, \tag{2.24}$$

where $\delta_l(E)$ is the phase shift which is a real quantity in this simple, single-channel discussion. The states $\langle \mathbf{r} \mid E, l, m \rangle = y_l(r) Y_{lm}(\hat{\mathbf{x}})/r$ are eigenstates of the noninteracting Hamiltonian, H_0

$$\left[\frac{d^2}{dr^2} - \frac{l(l+1)}{r^2} + p^2 \right] y(\mathbf{r}) = 0. \tag{2.25}$$

The states $\langle \mathbf{r} \mid E, l, m+ \rangle = u_l(r) Y_{lm}(\hat{\mathbf{x}})/r$ are eigenstates of the full Hamiltonian, H

$$\left[\frac{d^2}{dr^2} - \frac{l(l+1)}{r^2} + p^2 - V(r) \right] u(\mathbf{r}) = 0. \tag{2.26}$$

The asymptotic solutions can be written in terms of the phase shift

$$u(r)_l \xrightarrow[r \to \infty]{} e^{i\delta_l(E_p)} \sin[pr - l\pi/2 + \delta_l(E_p)], \tag{2.27}$$

which elucidates the significance of the phase shift.

The scattering amplitude can also be decomposed in terms of contributions from different orbital angular momentum quantum numbers

$$f(\mathbf{p}', \mathbf{p}) = 4\pi \sum_{l,m} Y_{l,m}(\hat{\mathbf{p}}') \; Y_{l,m}(\hat{\mathbf{p}})^* \; f_l(E_p), \tag{2.28}$$

where $f_l(E_p) = \left(\exp(2i\delta_l(E_p)) - 1\right)/2ip$ is the partial-wave amplitude, and Eq. 2.28 is the partial wave expansion of the scattering amplitude. The cross section can be written in terms of a sum over partial waves

$$\sigma(E_p) = \sum_l \sigma_l(E_p) = 4\pi \sum_l (2l+1) |f_l(E_p)|^2. \tag{2.29}$$

The partial wave cross-section, σ_l, is bounded by the unitarity of the phase shift contribution: the **unitarity bound**

$$\sigma_l(E_p) \leq 4\pi \frac{2l+1}{p^2}, \tag{2.30}$$

when the phase shift is an odd multiple of $\pi/2$.

In the low-energy limit $p \to 0$, the leading order threshold behavior of the partial wave amplitude is

$$f_l(E_p) \xrightarrow[p \to 0]{} -a_l p^{2l}. \tag{2.31}$$

When this limiting form inserted into the partial wave expansion for identical particles

$$\hat{f}(\mathbf{p}', \mathbf{p}) = -4\pi \sum_{l,m} Y_{l,m}(\hat{\mathbf{p}}') \left[Y_{l,m}(\hat{\mathbf{p}})^* + (-1)^l Y_{l,m}(\hat{\mathbf{p}})^* \right] a_l p^{2l}, \tag{2.32}$$

it is clear that for identical bosons only even-ordered partial-waves are non vanishing enhanced by a factor of 2. When identical fermions scatter, only odd-ordered particle waves contribute.

Near threshold ($E_p \to 0$) only a finite number of partial waves contribute, and the partial-wave decomposition can be truncated. The classical explanation is that for a given incoming momentum component p_0 along the collision axis and characteristic width w_t of the target, the incoming atom misses for angular momentum $l > p_o w_t$. In the low-energy limit, only incoming atoms with proportionately low angular momentum contribute to the collisional cross section. This criterion carries over to quantum scattering where the characteristic width is replaced instead by the approximate range of the potential, and the higher partial waves are suppressed by the centrifugal barrier of strength $l(l+1)/2mw_t^2$.

When $p_0 < w_t^{-1}$, so that the incoming wave packet is repulsed by all nonzero centrifugal barriers, the scattering process is in the **ultracold limit**, and only the lowest partial wave ($l = 0$) s-wave contributes significantly to the cross section for bosons. To leading order, the s-wave partial amplitude is therefore proportional to a constant a_0 with units of length, which is the two-body s-wave **scattering length**. In the ultracold limit, fermionic scattering is suppressed, occurring to leading order through p-wave contributions which are quadratic in the incoming momentum and therefore vanish in the ultracold limit, which was observed experimentally in Ref. [76]. Truncating Eq. 2.32 to include only s-wave collisions gives the cross section

$$\hat{\sigma} = 8\pi a_0 \qquad \text{(Scattering of identical bosons in the ultracold limit.)} \tag{2.33}$$

The effective range expansion provides corrections to Eq. 2.31 beyond leading order, written here in terms of the s-wave phase shift

$$p \cot \delta_0(E_p) \xrightarrow[p \to 0]{} -\frac{1}{a_0} + \frac{r_0}{2} p^2 + ..., \tag{2.34}$$

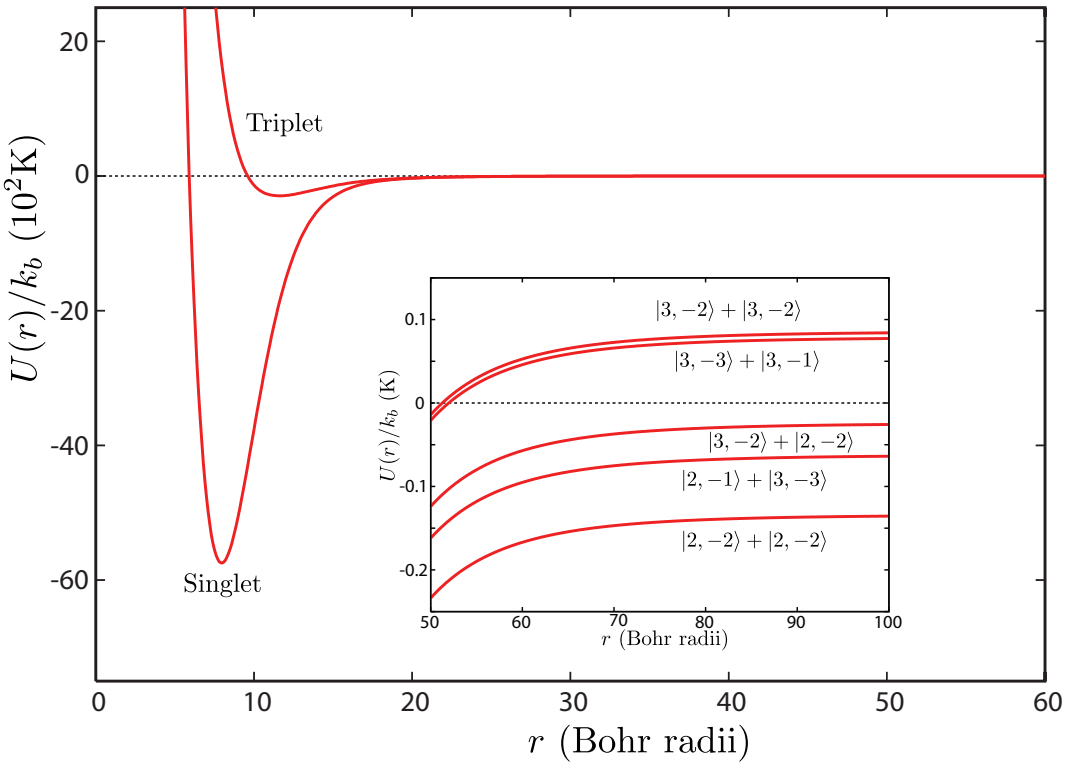

Figure 2.3: At medium separations, the total electronic spin is a good quantum number and the interatomic potentials are the singlet ${}^1\Sigma_g^+$ and triplet ${}^3\Sigma_u^+$ potentials, which are shown here for ^{85}Rb atoms [77, 78, 79]. At large separations the energies correspond to the hyperfine levels labeled in the inset, shown here for $mf_1 + mf_2 = -4$ at $B = 600$ G, which is the location of a well-known broad Feshbach resonance.

where r_0 is the **effective range** often used as a characteristic length scale to describe the range of the potential. If the expansion is truncated to include only the scattering length and effective range, the s-wave scattering amplitude can be extended beyond the zero energy limit

$$f_0(p) = -\frac{a_0}{1 + ipa_0 + r_0 p^2 a_0/2}. \tag{2.35}$$

2.2.4 Interatomic Potentials for Alkali Species in the Ultracold Limit

At this point it is helpful to contextualize these remarks by sketching the typical form of the interactomic potential for alkali atoms in the ultracold limit (see as example the potentials for ^{85}Rb in Fig. 2.3). For neutral alkali species, which are 'Hydrogen-like', there is a single unpaired valence electron which determines much of the collisional physics. At small separations on the order of a

few Bohr radii, a pair of interacting atoms feel the strong repulsion of the ionic core. At medium separations, only the orbits of the valence electrons overlap, and the atoms can covalently bond when the valence electrons are paired in a singlet state, as shown by the deep potential well in Fig. 2.3. They may also pair in a triplet state as shown in Fig. 2.3, however this potential is much shallower than the deep singlet well. However, both potentials can be deep enough to support many bound states. The minimum of these wells for alkali species is roughly at .2–.5 nm separation between nuclei[3] .

At large separations beyond the overlap of the electronic clouds **van der Waals** forces become dominant as each atom feels the electrostatic potential generated by the other, and for neutral atoms, the multipole expansion of this potential begins with the dipole moment. The dominant interaction is therefore that between the dipole moment of one atom with the dipole field established by the other–the dipole-dipole force. The strength of this interaction for ground state atoms can be calculated at fixed nuclear separation beginning at second order in perturbation theory [81]

$$U_{\mathrm{vdW}}(\mathbf{r}) = -\frac{C_6}{r^6} + ..., \tag{2.36}$$

where the power r^{-6} arises through the square of the dipole-dipole interaction energy which goes as r^{-3}, and the positive coefficient C_6 gives an attractive force. In the asymptotic limit, the individual atoms are in the one-body hyperfine states of total angular momentum, whose zero field splitting for alkali species corresponds to temperatures on the order of Kelvins, which is still minuscule compared to the singlet and triplet well depths [65].

For ultracold collisions, the incident energy is insufficient to probe the repulsive short-range details beyond the singlet and triplet electronic potentials. The potential can be written in the following form[4] which highlights the conservation of the total electronic spin [65]

$$U_c = U_0 P_0 + U_1 P_1 = \frac{U_0 + 3U_1}{4} + (U_1 - U_0)\mathbf{S_1} \cdot \mathbf{S_2}, \tag{2.37}$$

in terms of the spin $\mathbf{S_i}$, singlet P_0 projection, and triplet P_1 projection operators. The form

[3] For a summary of important length scales for alkali atoms see pp. 351–389 of Ref. [80].
[4] This is the 'central' portion of the interaction.

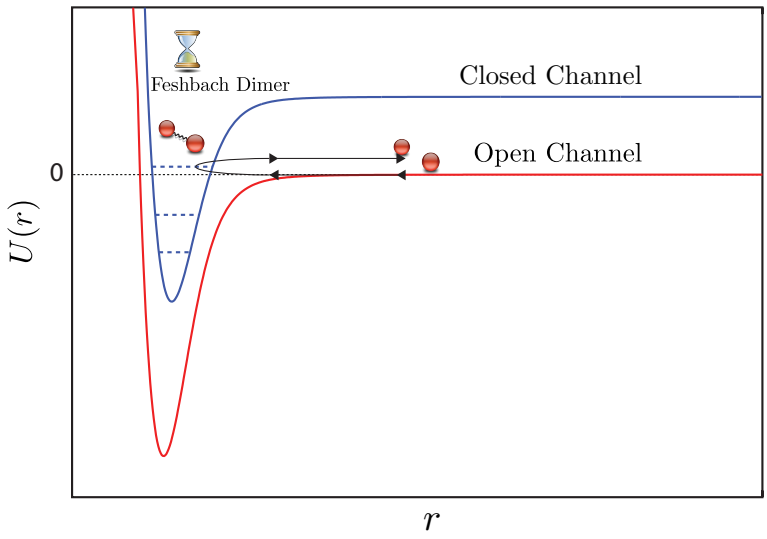

Figure 2.4: A schematic of a Feshbach resonance. Scattering process in the incoming channel (red) is coupled to the closed channel (blue). When a bound state (dashed lines) is near collision threshold, the colliding atoms form a metastable state which decays over a characteristic lifetime, indicated by the hourglass, exiting out the open channel.

of the second equality emphasizes the relevant spin-flip and spin-exchange physics, which mix the hyperfine levels of the incoming atoms. At large distances, these potentials asymptote into attractive van der Waals tails. If the hyperfine splitting is ignored, scattering in the ultracold limit can be summarized by the triplet ($U_1 \propto a_t$) and singlet scattering lengths ($U_0 \propto a_s$). For ^{87}Rb, these are $a_s \approx a_t \approx r_{\mathrm{vdW}}$, which are in the neighborhood of 10^2 Bohr radii. The proximity of these scattering lengths leads to suppression of spin-exchange processes which depend on their difference in Eq. 2.37.

The interatomic potentials are, to a rough approximation, an attractive van der Waals tails with a hard wall cutoff at separations where the details of the ionic core become important. For ultracold energies, the characteristic length of the van der Waals interaction, $r_{\mathrm{vdW}} = (mC_6)^{1/4}/2$, sets the scale of a_s and a_t and is also associated with the 'range' of the potential. For alkali species, r_{vdW} is typically on the order of a few nanometers.

The scattering length can display resonance effects when the collision energy is in the neigh-

borhood of a bound state above threshold[5] as shown schematically in Fig. 2.4. This is known as Fano-Feshbach[6] resonance [82] where the scattering length diverges at a pole, taking on all values between $\pm\infty$. Commonly in ultracold gas experiments, a bound state's energy is tuned to the collision threshold by utilizing a difference in the magnetic moments of the open and closed channels[7] $\Delta\mu$ and the resultant Zeeman energies under an applied magnetic field B. The well-known expression for the magnetic field dependence of the scattering length in this case is

$$a_0(B) = a_{bg}\left(1 - \frac{\Delta B}{B - B_0}\right), \tag{2.38}$$

where a_{bg} is the background scattering length far from the resonance, ΔB is the field width of the resonance, and B_0 is the value of the applied field that brings the bound state degenerate with the collision threshold energy to produce a zero-energy resonance. For ultracold gas experiments, widths on the order of 1 Gauss or less are referred to as *narrow* resonances, and **broad** resonances are associated with widths which greatly exceed 1 Gauss, where the Feshbach dimer has universal characteristics independent of the atomic species over a wider range of detunings (see the review article [30] for a detailed discussion.) The broad or narrowness is correlated with the strength of the coupling between the open and closed channels. The ability to tune the scattering length via a Feshbach resonance underlies much of the discussion of Chapters 5–7.

2.2.5 Effective Potentials and the Zero-Range Model

There are in principle many potentials, perhaps of simpler form, which reproduce, up to a given order, the first few terms of the effective range expansion. Such a potential is referred to as an **effective potential** as opposed to the actual potential. In ultracold gas experiments collisions occur only over a narrow window of energies centered around the thermal energy k_bT. It is therefore inconsequential, from the viewpoint of constructing observables, whether or not the actual or effective potential is used as long as the energy dependence of the observables over

[5] This bound state is referred to as the **Feshbach dimer**.

[6] Or often just 'Feshbach resonance'.

[7] 'Channel' is used to refer to a collisional pathway. 'Open channel' refers to pathways which are energetically accessible asymptotically, and 'closed channels' are inaccessible.

the experimentally relevant window of energies is reproduced. For instance, the actual interatomic potential is typically used to calculate the scattering length, effective range, etc..., and then a simpler effective potential is introduced that simplifies the properly cut-off many-body calculations. The importance of this approach, and the order in which the few-body problem feeds into the many-body problem is of foundational importance to the study of ultracold gases and related condensed-matter systems. In this section, I specifically discuss two effective potentials relevant to this thesis: the Fermi pseudopotential, used in few-body calculations, and the contact interaction, used in many-body calculations.

For single-channel models with a van der Waals tail, the general expression [83] for the s-wave effective range is

$$r_0(a_0) = r_0(\infty)\left[1 - 2\frac{\bar{a}}{a_0} + 2\left(\frac{\bar{a}}{a_0}\right)^2\right] \tag{2.39}$$

where $r_0(\infty) = 2\Gamma(1/4)^2 r_{\mathrm{vdW}}/3\pi$ is the effective range at unitarity and $\bar{a} = 4\pi r_{\mathrm{vdW}}/\Gamma(1/4)^2$. Interestingly, the zero scattering length scenario where $a_0 \to 0$ gives a divergent effective range. At zero magnetic field, for species like ^{133}Cs and ^{85}Rb, the singlet and triplet scattering lengths can exceed both the van der Waals length and the effective range by up to an order of magnitude [80]. For weakly-interacting Bose gases at ultracold energies, even when $a_0 \ll r_0$ as is the case for ^{87}Rb, the effective range contribution is however still a very small correction to the leading order scattering length term in the effective range expansion (Eq. 2.34) for ultracold gases. In this case, an effective potential which captures only the leading order scattering length term of the effective range expansion can be used, which is a potential of **zero-range**. The zero-range potential comes in two common variants: the Fermi pseudopotential and the contact interaction.

In Chapters 5–6, the **Fermi pseudopotential** [84] is used in few-body calculations because it has the distinct advantage that the effect of the potential can be incorporated through enforcement of boundary conditions at the origin alone. The idea is to replace the complicated actual potential with an interaction of the form

$$V_{pseudo}(\mathbf{r}) = g\delta^{(3)}(\mathbf{r})\frac{\partial}{\partial r}(r.) \tag{2.40}$$

with, as of yet, undetermined effective coupling strength g. The coupling strength must be chosen to reproduce the leading order term in the effective range expansion. The delta function must be evaluated at the origin giving a boundary condition of the form

$$u'(0) = -\frac{4\pi}{gm}u(0), \tag{2.41}$$

$$p\cot\delta_0(p) = -\frac{4\pi}{gm}, \tag{2.42}$$

which fixes

$$g = 4\pi a_o/m, \tag{2.43}$$

to reproduce the effective range expansion to leading order for distinguishable particles. Identical particle symmetry is typically enforced, for instance, at the level of the scattering amplitude and cross section construction. The effective range expansion for a pseudopotential interaction therefore only has one term, matching the scattering length dependence exactly. Equation 2.41 reveals how the pseudopotential is implemented in practice through the Bethe-Peierls boundary condition [85].

The other commonly used zero-range potential is the **contact interaction**, used in Chapters 3 and 7 for many-body models, which is similar in form to the Fermi pseudopotential except that it is not regularized at the origin

$$V_\delta(\mathbf{r}) = g_0\delta^{(3)}(\mathbf{r}). \tag{2.44}$$

The mathematical difficulties that arise through an interaction of this form can be seen in its Fourier transform, $V_\delta(\mathbf{p}) \propto g_0$, which is constant in momentum space, coupling momentum components to all orders equally. This poses problems, for instance, when performing calculations that do not converge with higher momentum: An **ultraviolet divergence**. The cure for an ultraviolet divergence is to properly introduce a cutoff p_c in momentum space to the Fourier transform

$$V_\delta(\mathbf{p}) = \begin{cases} g_0/(2\pi)^{-3/2}, & \text{if } p \le p_c \\ \eta(p)\ g_0/(2\pi)^{-3/2}, & p > p_c \end{cases} \tag{2.45}$$

where the function $\eta(p)$ tends to zero past the cutoff, p_c.

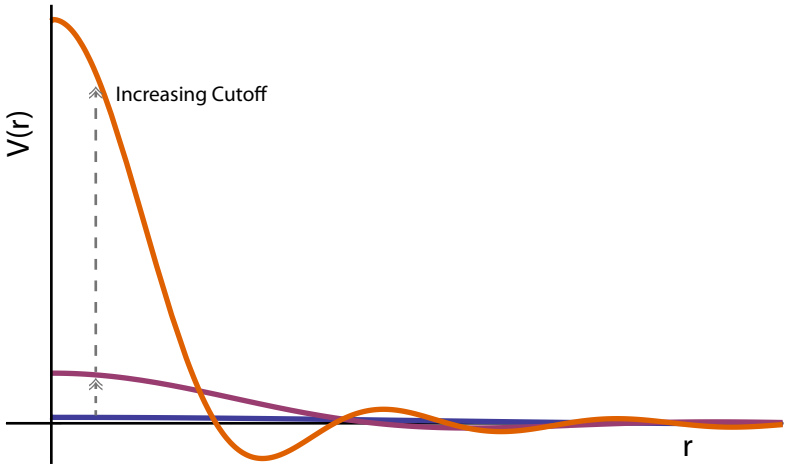

Figure 2.5: A sketch of the dependence of the cutoff contact interaction on cutoff momentum, p_c. With increasing cutoff, the maximum at the origin diverges as a the cutoff momentum cubed, and the number of oscillations increases.

The cutoff contact interaction can be thought of a square well potential in momentum space with depth proportional to g_0, which looks like a sinc function in position space (see Fig. 2.5), and it is in this sharp sense that it will be used presently. The cutoff sets a length scale at short-distances p_c^{-1}, which should be chosen to be at a range shorter than that probed by typical ultracold collisions.

When the cutoff is introduced, it's dependence can be hidden in the coupling constant g_0 through the process of **renormalization**. Specifically, the zero-energy limit of the scattering amplitude obtained using the contact interaction must be matched against Eq. 2.35 to ensure that the low-energy limit of the scattering amplitude is reproduced with zero effective range ($r_0 = 0$), and an expression must be derived for g_0 involving the s-wave scattering length and the cutoff momentum. The contact interaction will be used in the many-body theories constructed later in this chapter, and so it is helpful to outline the process of renormalization in the remainder of this section.

Using the contact interaction the Born series, Eq. 2.21, can be summed via a geometric series, resulting in an analytic expression for the scattering amplitude. This calculation is done in the s-wave limit where the matrix elements of the T-operator are $\langle \mathbf{p}'|T(E_p + i0)|\mathbf{p}\rangle = t(p,p)$ which will

be written simply as $t(p)$ on the energy shell, depending only on the magnitude of the incident momentum. Beginning with the Born series for the matrix elements of the T-operator

$$t(p) = \frac{g_0}{(2\pi)^3} + \langle \mathbf{p}|V_\delta G_0 V_\delta|\mathbf{p}'\rangle + ..., \tag{2.46}$$

$$= \frac{g_0}{(2\pi)^3}\left(1 + \frac{mg_0}{2\pi^2}\left[\int dq \frac{q^2}{p^2 - q^2 + i0}\right] + ...\right), \tag{2.47}$$

where I have made use of the momentum eigenstates $\langle \mathbf{r}|\mathbf{p}\rangle = \exp(i\mathbf{r}\cdot\mathbf{p})/(2\pi)^{-3/2}$ and basic properties of the Dirac delta function [86]. The integral in brackets has a principal-value part and a singular part [87]

$$\frac{q^2}{p^2 - q^2 + i0} = P\left[\frac{q^2}{p^2 - q^2}\right] + i\pi\delta(p^2 - q^2), \tag{2.48}$$

which can be integrated up to the cutoff momentum with result

$$t(p) = g_0 - g_0 t(p)\frac{m}{2\pi^2}\left[p_c + \tanh^{-1}\left(\frac{p}{p_c}\right) + \frac{i\pi}{2}p\right]. \tag{2.49}$$

In the zero-energy limit, the Born series in Eq. 2.47 can be rewritten as a geometric sum

$$t(0) = \frac{g_0}{(2\pi)^3}\left(1 - \frac{mg_0}{2\pi^2}p_c + ...\right) = \frac{1}{(2\pi)^3}\frac{g_0}{1 + g_0 p_c m/2\pi^2} \tag{2.50}$$

and equating with the zero-energy scattering amplitude for distinguishable particles gives the result

$$g_0 = \frac{g}{1 - g\alpha_c}, \tag{2.51}$$

written in terms of the pseudopotential coupling strength g from Eq. 2.43 and a term $\alpha_c = mp_c/2\pi^2$ which hides the cutoff momentum.

Provided $a_0 p_c \ll 1$, the contact interaction adds corrections to the pseudopotential coupling in powers of the small parameter, $a_0 p_c$. The effective range expansion for the contact interaction is also truncated at a single term, but now with added cutoff dependence

$$f_\delta(p) = -\frac{a_0}{1 + ipa_0 - \alpha_c g_0}, \tag{2.52}$$

which complements the idea that adding a cutoff adds a range to the potential. The major advantage of the contact interaction in many-body problems, where it would be difficult to use the boundary

condition formulation of the Fermi pseudopotential, Eq. 2.41, is that it provides finite answers to integrals that would otherwise suffer from ultraviolet divergences and results that are independent of the cutoff chosen provided it is well beyond the typical collision energies in the gas.

Even in the case of resonance scattering where the scattering length diverges at a pole, it is possible to derive effective contact potentials which reproduce the energy dependence of the scattering amplitude. This derivation provides the foundation of the theory of **resonance superfluidity** [55], which was first formulated and studied successfully in the early 2000s when experiments exploited Feshbach resonances to produce the unitary Fermi gas. Recently, experiments have begun probing the unitary Bose gas with the help of Feshbach resonances, and a candidate theory based on the ideas of resonance superfluidity and its generalization to include bound states of higher numbers of atoms has so far not been investigated. This discussion is reserved for the conclusion of this thesis, Chapter 8.

2.3 Many-Atom Physics: Formalism

The one and two atom physics discussed in Secs. 2.1 and 2.2 serve as the basic ingredients for constructing the many-body theory of the ultracold Bose gas. To these ingredients must be added the concept of the **second quantization** which builds upon the eigenstates of the single-particle Hamiltonian to provide a tidy expression for the many-body Hamiltonian in **Fock space**. In the non-interacting limit, I discuss a simple picture for the minimization of the total energy with an additional normalization constraint capturing the basic ideas of the zero-temperature ideal gas BEC. This section finishes with the an effective many-body Hamiltonian written in second quantization in position space including the effect of the contact interaction and therefore valid for long-wavelength phenomenon in the gas. This serves as the basic ingredients for the many-body analysis in this thesis.

2.3.1 Second Quantization

The discussion of second quantization begins with the Hilbert space of a single particle Hamiltonian $\mathcal{H}_1$ spanned by the basis of single-particle orbital wave functions $\phi_\alpha(\mathbf{r}) = \langle \mathbf{r}|\alpha\rangle$, where α represents a set of quantum numbers required to completely specify the state. The many-body Hilbert space describing the quantum mechanical state of N-atoms is the tensor product of N single-particle Hilbert spaces:

$$\mathcal{H} = \mathcal{H}_1^{(1)} \otimes \mathcal{H}_1^{(2)} \otimes ... \otimes \mathcal{H}_1^{(N)}. \tag{2.53}$$

The N-body basis states can be written then as a tensor product of the single-particle basis

$$|\alpha_1\alpha_2...\alpha_N\rangle \equiv |\alpha_1\rangle|\alpha_2\rangle...|\alpha_N\rangle, \tag{2.54}$$

where the product of kets is the tensor product, and the subscript α_i denotes an orbital in the ith single-particle Hilbert space.

When the system is composed of bosons, the basis states of the many-body Hilbert space must by symmetrized through projection by the symmetrizing operator

$$S = \frac{1}{N!}\sum_P P, \tag{2.55}$$

where the sum is taken over the $N!$ distinct permutations P of the single-particle orbitals. The action of the symmetrizing operator on the N-particle basis states is written

$$|\alpha_1\alpha_2...\alpha_N\rangle_S \equiv S|\alpha_1\alpha_2...\alpha_N\rangle. \tag{2.56}$$

Post-symmetrization, the notation of the symmetrized ket, which labels the occupied orbitals in all of the individual single-particle Hilbert spaces, is unnecessary. Rather, it is simpler to report a simpler quantity: The occupation numbers of single-particle orbitals. For instance, if N_α atoms are in the single particle orbital $|\alpha\rangle$, N_β atom are in the single particle orbital $|\beta\rangle$, etc...

$$|\alpha_1\alpha_2...\alpha_N\rangle_S \equiv |N_\alpha N_\beta...\rangle_S, \tag{2.57}$$

for a fixed number of particles $\sum_i n_i = N$, where the sum runs over all possible single-particle orbitals.

This account in terms of occupation numbers is generalized through the concept of a **Fock space**, which is an enlarged Hilbert space $\mathcal{F}$ constructed from the direct sum [88] of the 0,1,2,3,...N-particle Hilbert spaces

$$\mathcal{F} = \mathcal{H}_0 \oplus \mathcal{H}_1 \oplus \mathcal{H}_2 \oplus ... \tag{2.58}$$

The Fock space basis is written in the occupation notation of Eq. 2.57, which includes the vacuum state $|0\rangle$, the single particle state $|1_\alpha\rangle$, the two particle states $|1_\alpha 1_\beta\rangle$ or $|2_\alpha\rangle$ etc... The Fock basis is therefore composed of states of variable particle numbers. Importantly, states without a well-defined number of particles are allowed in Fock space such as the coherent state $|z\rangle$ which is an eigenstate of the raising and lowering operators $a_\alpha|z\rangle = z_\alpha|z\rangle$, where $|z_\alpha|^2$ is the average occupancy of the α orbital with variance $|z_\alpha|^2$.

Basis states of different particle numbers are connected through a linear mapping in Fock space. Specifically, arbitrary symmetric N-particle states can be constructed beginning with the vacuum state through repeated action of the creation $a^\dagger$ and annihilation a operators

$$|1_\alpha\rangle = a_\alpha^\dagger|0\rangle, \tag{2.59}$$

$$|N_\alpha N_\beta ...\rangle = \frac{1}{\sqrt{N_\alpha! N_\beta! ...}} \left(a_\alpha^\dagger\right)^{N_\alpha} \left(a_\beta^\dagger\right)^{N_\beta} ...|0\rangle, \tag{2.60}$$

$$\langle 1_\alpha| = \langle 0|a_\alpha \tag{2.61}$$

$$\langle N_\alpha N_\beta ...| = \frac{1}{\sqrt{N_\alpha! N_\beta! ...}} \langle 0| \left(a_\beta\right)^{N_\beta} \left(a_\alpha\right)^{N_\alpha} ... \tag{2.62}$$

where the particle symmetry is ensured through the canonical commutation relations [89]

$$[a_\alpha, a_\beta] = \left[a_\alpha^\dagger, a_\beta^\dagger\right] = 0, \tag{2.63}$$

$$\left[a_\alpha, a_\beta^\dagger\right] = \langle\alpha|\beta\rangle = \delta_{\alpha\beta}, \tag{2.64}$$

where the subscript a_α indicates the annihilation of an atom in the $|\alpha\rangle$ orbital. The creation and annihilation operators can be transformed from one orbital basis to another, and the transform to

the position space representation is defined by the mappings

$$|\mathbf{r}\rangle = \sum_\alpha |\alpha\rangle\langle\alpha|\mathbf{r}\rangle \equiv \sum_\alpha \phi^*_\alpha(\mathbf{r})|\alpha\rangle, \tag{2.65}$$

$$\psi^\dagger(\mathbf{r}) = \sum_\alpha a^\dagger_\alpha \phi^*_\alpha(\mathbf{r}), \tag{2.66}$$

$$\psi(\mathbf{r}) = \sum_\alpha a_\alpha \phi_\alpha(\mathbf{r}), \tag{2.67}$$

where $\psi^\dagger$, ψ are **field operators** defined on a continuous basis that create or destroy an atom in the position space eigenstate $|\mathbf{r}\rangle$, whose orbital wave function is $\langle\mathbf{r}'|\mathbf{r}\rangle = \delta^{(3)}(\mathbf{r}-\mathbf{r}')$ the Dirac delta function. The position space field operators therefore create or destroy an atom *locally*. This is in contrast to the momentum space field operators $\varphi(\mathbf{p})$, $\varphi(\mathbf{p})^\dagger$ that create or destroy an atom in the orbital wave function $\langle\mathbf{r}|\mathbf{p}\rangle = (2\pi)^{-3/2}\exp(i\mathbf{r}\cdot\mathbf{p})$ which is the nonlocal plane wave state. The position space field operators satisfy the continuous version commutation relations, Eqs. 2.63, 2.64

$$\left[\psi(\mathbf{r}), \psi(\mathbf{r}')\right] = \left[\psi^\dagger(\mathbf{r}), \psi^\dagger(\mathbf{r}')\right] = 0, \tag{2.68}$$

$$\left[\psi(\mathbf{r}), \psi^\dagger(\mathbf{r}')\right] = \langle\mathbf{r}|\mathbf{r}'\rangle = \delta^{(3)}(\mathbf{r}-\mathbf{r}'), \tag{2.69}$$

2.3.2 Many-Body Hamiltonian

Fock space is the natural setting to investigate the thermodynamics of a many-body system for a variable number of particles, and the creation and annihilation operators ensure that totally symmetric systems are mapped onto totally symmetric systems. To translate the many-body problem into Fock space, it is first necessary to rewrite all quantities of interest including the many-body Hamiltonian in terms of creation and annihilation operators. Let us start with the noninteracting N-atom Schrödinger equation in a trap

$$H_0 = \sum_i^N \left[-\frac{\nabla_i^2}{2m} + V_{trap}(\mathbf{r_i})\right] = T + V_{trap}, \tag{2.70}$$

where $\mathbf{r_i}$ is the position vector of the ith atom. The mapping [89] of these one-particle operators onto Fock space is

$$\hat{H}_0 = \sum_{\alpha\beta} a_\alpha^\dagger \langle \alpha | T + V_{trap} | \beta \rangle a_\beta, \tag{2.71}$$

written in terms of a basis of discrete orbitals.

The orbital basis may be transformed into the eigenbasis $|\lambda\rangle$ of the single-particle Hamiltonian with energy E_λ, yielding the many-body Hamiltonian in diagonal form

$$\hat{H} = \sum_\lambda E_\lambda a_\lambda^\dagger a_\lambda, \tag{2.72}$$

where the sum now runs over all orbital eigenstates and the product $a_\lambda^\dagger a_\lambda = \hat{N}_\lambda$ giving the orbital occupancy. Written in the occupancy notation, it is possible to discuss the ground state structure in Fock space. The ground state is the arrangement that minimizes the energy of the system subject to the constraint that the total number of atoms $\hat{N} = \sum_\lambda a_\lambda^\dagger a_\lambda$. These constraints are incorporated by minimizing the grand canonical Hamiltonian, $\hat{K} = \hat{H} - \mu\hat{N}$ with fixed μ, playing the role of the Lagrange multiplier and conjugate variable to $\hat{N}$,

$$\hat{K} = \sum_\lambda (E_\lambda - \mu)\, a_\lambda^\dagger a_\lambda, \tag{2.73}$$

where the identification of μ with the chemical potential is made later in Sec. 4.1 for the interacting zero temperature Bose gas. The expectation value of $\hat{K}$ can be minimized, for instance, through variational methods [89], but for the noninteracting gas, the ground state structure can be uncovered through simple arguments about the structure of Eq. 2.73, depending on the fixed value of μ. For fermionic systems and a given value of μ, all orbitals with energies $E_\lambda \leq \mu$ will be occupied according to the Pauli exclusion principle, and the μ sets the number of atoms in the ground state. For bosonic systems, if E_0 is the lowest orbital energy, then $\hat{K}$ has a ground state only for $\mu \leq E_0$, where condensation occurs for any number of atoms when the equality is satisfied. Minimization of $\hat{K}$ with fixed μ therefore yields the ground state structure of the many-body system in Fock space.

To go beyond the non-interacting many-particle Hamiltonian, pairwise interactions between

the atoms must be written in terms of creation and annihilation operators [89]

$$\hat{V} = \frac{1}{2}\sum_{\alpha\beta\gamma\delta} a_\delta^\dagger a_\gamma^\dagger a_\beta a_\alpha \langle\delta\gamma|V|\alpha\beta\rangle, \tag{2.74}$$

where the factor of 1/2 prevents double counting, and

$$\langle\delta\gamma|V|\alpha\beta\rangle = \int d^3r d^3r' V(\mathbf{r}-\mathbf{r'})\phi_\delta^*(\mathbf{r})\phi_\gamma^*(\mathbf{r'})\phi_\beta(\mathbf{r'})\phi_\alpha(\mathbf{r}). \tag{2.75}$$

In the case of trapped ultracold Bose gases, the many-body Hamiltonian is commonly written in terms of the position space field operators, where the mappings in Eqs. 2.65–2.67 yield the Hamiltonian $\hat{H}$ including pairwise interactions

$$\hat{H} = \int d^3r\ \psi^\dagger(\mathbf{r})\left[-\frac{\nabla^2}{2m} + V_{trap}(\mathbf{r})\right]\psi(\mathbf{r}) + \frac{1}{2}\int d^3r\ d^3r'\ \psi^\dagger(\mathbf{r})\psi^\dagger(\mathbf{r'})V(\mathbf{r}-\mathbf{r'})\psi(\mathbf{r'})\psi(\mathbf{r}), \tag{2.76}$$

and when the contact interaction $V(\mathbf{r}) = V_\delta(\mathbf{r})$ (Eq. 2.44) is used

$$\hat{H} = \int d^3r\ \psi^\dagger(\mathbf{r})\left[-\frac{\nabla^2}{2m} + V_{trap}(\mathbf{r})\right]\psi(\mathbf{r}) + \frac{g_0}{2}\left[\psi^\dagger(\mathbf{r})\right]^2\left[\psi^\dagger(\mathbf{r})\right]^2. \tag{2.77}$$

It is important to reiterate that this is an effective Hamiltonian, valid only for long wavelength, low momentum phenomenon in the gas, where the implicit dependence of g_0 on the cutoff momentum p_c eliminates the influence of short-wavelength degrees of freedom.

Using the Heisenberg equation of motion

$$i\dot{\hat{O}} = \left[\hat{O}, \hat{H}\right], \tag{2.78}$$

equations of motion for arbitrary products $\hat{O} = \psi(\mathbf{r_1})\psi(\mathbf{r_2})...\psi^\dagger(\mathbf{r_j})$ of the field operators can be derived. Rather than deriving these equations presently, they will be developed over the course of the thesis as needed and always in the context of the motivating physics. This chapter finishes with the simplest nontrivial many-body system relevant to this thesis: the ideal Bose gas at finite temperatures, which will serve as the contextual framework that many of the discussions in this thesis will refer to.

2.4 The Noninteracting Bose Gas at Finite Temperatures

At finite temperatures, the many-body problem can be treated through a set of standard approximations depending on the temperature regime of interest relative to the other energy scales in the problem. The experiments analyzed in Chapters 3–4 are well described by the semi-classical approximation, where the center of mass motion of the noncondensed portion of the gas can be treated classically, akin to billiard balls rattling around in a trap bouncing off of one another, rather than fully quantum mechanically. It is therefore instructive to first study the noninteracting, ideal Bose gas at finite temperatures and highlight many important features before moving on to the weakly-interacting Bose gas in Chapters 3–4. Since the experiments analyzed in Chapters 3–4 are in extremely spherically symmetric traps, I will assume an isotropic trapping geometry in this section which also serves to reduce notational clutter.

When interactions have been switched off, the harmonic oscillator states $|\mathbf{n}\rangle$, ($\mathbf{n} = \{n_x, n_y, n_z\}$) are the eigenstates of the grand canonical many-body Hamiltonian with particle number constraint, which has the generalized diagonal form

$$\hat{K} = \omega_0 \sum_{\mathbf{n}=0} (n_x + n_y + n_z + 3/2 - \mu)\, a^\dagger_{\mathbf{n}} a_{\mathbf{n}}, \tag{2.79}$$

where the factor $3\omega_0/2$ is the zero-point energy of the ground state. Combinatorially speaking, there are many distinct sets $\{n_x, n_y, n_z\}$ that yield the same energy $(n + 3/2)\omega_0$, and this degeneracy grows with increasing n. For example, the ground state $n = 0$ is unique, the first excited state is three-fold degenerate, the second excited state six-fold degenerate, the third excited state ten-fold degenerate, and so on. For increasing value of n, the excited spectrum can be treated as approximately continuous. The degeneracy of states between energies E and $E + dE$ in a harmonic trap is

$$g(E) = \frac{E^2}{2\omega_0^3}, \tag{2.80}$$

which is derived from simple arguments for the density of states in many introductory textbooks (see for instance Ref. [90].) The total occupation of the energy neighborhood around E of width

dE is therefore given by the product of the degeneracy with the Bose distribution

$$N(E+dE) = g(E)dE\frac{z}{\exp(\beta E) - z}, \tag{2.81}$$

where $\beta = 1/k_bT$, T is the temperature of the gas, and $z = \exp(\beta\mu)$ is the fugacity. The total population can therefore be calculated at a given temperature, with the reservation that the ground state must be summed discretely

$$N = \frac{z}{\exp(\beta 3\omega_0/2) - z} + \int dE\ g(E)\frac{z}{\exp(\beta E) - z}. \tag{2.82}$$

From the functional form of z restricted on the domain $z \in [0, \infty)$, the Bose distribution approaches its maximum value as $z \to 1$ from below. Values of z exceeding unity give an occupation which is negative and nonsensical. From the discussion of Sec. 2.3.2, we concluded that condensation occurs when μ is approximately equal to the ground state energy of the system. When $z \approx 1$, the number of atoms in excited states, N_{ex} approaches a maximum value, which is the point at which the excited states are saturated by the entire cloud. The temperature T_c at which this occurs can be calculated

$$N_{ex} = N = \int dE g(E)\frac{1}{\exp(E/k_bT_c) - 1} = \zeta(3)\left(\frac{k_bT_c}{\omega_0}\right)^3, \tag{2.83}$$

where

$$T_c = \frac{\omega_0 N^{1/3}}{k_b\zeta(3)^{1/3}}, \tag{2.84}$$

where ζ is the Riemann zeta function [86]. The saturated cloud is referred to as the **thermal cloud**, and is composed of **excitations** out of the condensate. Below the critical temperature, the total number of atoms is split between the thermal cloud and the condensate. The remainder $N - N_{ex}$ is given by the simple relation

$$N_0 = N\left[1 - \left(\frac{T}{T_c}\right)^3\right] \quad \text{(Ground state occupation)}. \tag{2.85}$$

These formulas have been derived by using the approximation $\mu = 0$, and corrections from using the correct relation $\mu = 3\omega_0/2$ go as $N^{-1/3}$ which vanishes in the thermodynamic limit, smoothing the phase transition for finite-sized clouds [65].

This is the theory of the finite temperature ideal Bose gas near the critical temperature for Bose-Einstein condensation, which serves as a basis for the finite temperature analysis of Chapters 3-4 on the weakly interacting Bose gas. Specifically, the ideal Bose gas is the long-time limit of any nonequilibrium dynamics for the interacting Bose gas when inelastic loss mechanisms are ignored. A strange exception to this trend is the breathing mode discussed in Chapter 3, which was predicted by Boltzmann to persist unsettled indefinitely. The study of the dynamics and relaxation of a dilute gas is the subject of **kinetic theory**, which is the starting point for Chapter 3.

2.5 Summary

In this chapter, the background necessary to understand both the theoretical analysis and the relevant experiments discussed in this thesis was outlined. In the following chapters, a many-body theory for weakly and strongly interacting Bose gases is developed along with analysis of nonperturbative three-body physics, and I have chosen to develop the relevant theory along the way on an as-needed basis. For the many-body physics in this thesis, I feel that this approach has the two advantages. *Clarity*: It is easier to appreciate the structure of the many-body theory if it is built up slowly in the context of motivating experimental results. *Convenience*: In a sense, it is natural for the relevant results to be discussed following the relevant theory as would occur in a journal article.

The few-body portion of this chapter was presented in a way that provided the necessary ingredients for the many-body theories of Chapters 3–4. The three-body physics discussed in latter half of this thesis builds upon these ideas, and much of the intuition from the two-body partial wave analysis is retained in the hyperspherical adiabatic representation of the three-body problem outlined in Chapter 5.

Chapter 3

Anomalous Damping of the Breathing Oscillation of a Nondegenerate Bose Gas in an Extremely Isotropic Trap

This chapter contains the results from Ref. [60], which is an analysis of an experiment published in Ref. [24].

The previous background chapter concluded with the thermodynamics of the ideal BEC at finite temperature. There is, however, much to be learned about the gas from its out-of-equilibrium dynamics and subsequent relaxation to thermal equilibrium, and an understanding of these processes requires the incorporation of interatomic interactions. In the regime of linear response, where the gas is only slightly perturbed from equilibrium, the dynamics of the trapped gas can be decomposed into a discrete set of collective modes which have characteristic frequencies and damping rates. In the collisionless limit where collisions within the gas can be neglected, the oscillation frequencies are easily calculated from single-particle considerations. Therefore, the measured frequency shift for an interacting system is a sensitive probe of physics beyond the single-particle level. Additionally, the observation of damping in an isolated system is interesting from a fundamental standpoint. In this chapter, data on a very peculiar collective mode, the breathing mode in 3D under isotropic confinment, from a recent experiment in the group of Eric Cornell here at JILA [24] is analyzed. What makes this mode quite odd is that it was predicted by Boltzmann over a century ago [2] to oscillate undamped indefinitely, awaiting experimental verification (or contradiction!) until very recently. Before jumping into the theory in Sec. 3, I provide some historical context for

this problem.

The Boltzmann equation has had a rich and interesting history in the study of dilute gases. In the late 19th century, Maxwell and Boltzmann uncovered a path to link the Newtonian mechanics of molecular dynamics to the hydrodynamic equations of Euler and Navier-Stokes. The resultant kinetic theory, of which the fluid theories were limiting cases, established many important concepts including the Maxwell distribution and Demon [91, 92], the Boltzmann equation, the H-theorem, and the assumption of molecular chaos or, in Boltzmann's native German, 'Stosszahlansatz' [93]. These fundamental ideas, in particular the H-theorem, famously stirred controversy in the scientific community, which in the 1890s was centered around the "reversal" paradox and the "recurrence" paradox based on Poincaré's theorem [94].

Lesser known, but equally as curious was the discovery by Boltzmann of a class of exact solutions to his kinetic theory of which the Maxwell distribution is a special case [2]. Such solutions included the undamped, nonequilibrium oscillations of a dilute gas with classical statistics under 3D isotropic harmonic confinement: the so-called monopole or **breathing mode**. Whereas some of the most controversial aspects of the Boltzmann equation began to be justified in the early 20th century with the advent of quantum theory[1] , experimental demonstration of the undamped monopole mode oscillation has yet to be fully investigated.

More recent advances in the trapping of ultracold gases have allowed for the study of collective modes under harmonic confinement. Indeed, many experiments have probed the transition between the collisionless and hydrodynamic regimes[3, 4, 5, 6, 7, 8, 9, 10, 11, 12, 13, 14, 15, 16, 17, 18] in anisotropic traps and the resultant collisional shifts of the collective mode spectrum. Such experiments measure the frequencies and damping rates of the various multipole modes and are generally limited by three-body losses approaching the hydrodynamic limit. Engineering an isotropic 3D trap of sufficiently perfect symmetry has remained a technological hurdle to investigating Boltzmann's prediction for the monopole mode.

A recent experiment from the group of Eric Cornell at JILA [24] trapped a nondegenerate

[1] The Boltzmann equation famously predated the experimental verification of the atomistic view of nature.

cloud of ^{87}Rb well above the transition temperature utilized a modified version of the TOP trap described in Sec. 2.1.1 to engineer anisotropies as low as 0.02%. The monopole mode was observed to oscillate over many trap periods; however, the damping was anomalously large given the level of anisotropy present in the system.

This chapter revolves around an investigation of possible sources of damping through a systematic account of imperfections in the trap. Upon first reading, this analysis provides an overview of analytic and numerical[2] methods for studying the Boltzmann equation with increasingly detailed functional form for the experimental trapping potential. There is however a deeper narrative at play: if this analysis does not account for the observed damping, the central tenants of the Boltzmann equation and of kinetic theory in general must come under scrutiny. These tenants also serve as the foundation for the analysis in Chapters 4, 7, and so their verification is of central importance to this thesis. The experiment measuring any violation of nonzero damping is therefore more in the spirit of metrological studies testing the value of fundamental constants, and this narrative is bolstered by the painstaking efforts which were taken to engineer extremely low asphericities. Importantly, the analysis presented in this chapter pinpoints the observed damping to effects consistent with the Boltzmann equation.

This chapter begins with a derivation of the Boltzmann equation and the H-theorem, and then explores the inherent limitations on the observation of an undamped, nonequilibrium monopole mode given a realistic trapping scenario, using the JILA experiment as illustration. The derivation of the Boltzmann equation presented in this chapter is the traditional path beginning from classical phase space considerations. In Chapter 4, the alternate path will be presented, which begins with the many-body Hamiltonian and the field operators.

3.1 Kinetic Theory Above T_c

Before delving into the Boltzmann equation, it is instructive to set the scene. Far above the transition temperature, the center of mass motion of individual atoms can be treated classically

[2] Details of the numerical algorithms used in this and the following chapter are including in Appendix A.

provided λ_{dB} is much smaller than a_{ho}. For finite temperature dilute gases, this comparison is made between the average (thermal) de Broglie wavelength of atoms in the cloud

$$\lambda_{th} = \sqrt{\frac{1}{2\pi m k_b T}}, \tag{3.1}$$

and the oscillator length. The classical treatment is therefore justified provided $\omega_0 \ll k_b T$. When this requirement is met[3] the energy spacing of neighboring oscillator states is difficult to resolve, and the continuum treatment of the excited states which was the basis of Sec. 2.4 is well-justified. This is a semi-classical picture of the gas having both classical and quantum mechanical degrees of freedom.

The gas is entirely composed of atoms with energies

$$E(\mathbf{r}, \mathbf{p}) = p^2/2m + V_{ext}(\mathbf{r}), \tag{3.2}$$

and the local occupation is given by the Bose distribution[4]

$$f(\mathbf{r}, \mathbf{p}) = \frac{z}{\exp\left(\beta E(\mathbf{r}, \mathbf{p})\right) - z}, \tag{3.3}$$

from which the equilibrium density of atoms in the gas can be calculated from the general formula

$$n_{ex}(\mathbf{r}) = \int \frac{d^3p}{(2\pi)^3} f(\mathbf{r}, \mathbf{p}) = \frac{g_{3/2}(\exp(\beta(\mu - V_{ext}(\mathbf{r}))))}{\lambda_{th}^3}. \tag{3.4}$$

Equation 3.3 is valid in thermal equilibrium when it is possible to define global thermodynamical quantities, and it is also valid in local equilibrium when the rate of collisions is sufficiently high that a local thermodynamic quantities can be defined.

There is a convenient framework in which to visualize the dynamics of the gas when the classical trajectories of the atoms can be tracked. In Fig. 3.1 a projection of the μ-space [95] is shown, which is a six-dimensional space tracking the coordinates each atom in the gas. This space can be divided into cells of volume $d^3r d^3p$. The volume must be chosen large enough to hold many particles, while simultaneously not violating the the Heisenberg uncertainty relation, $\Delta x \Delta p \geq 1/2$.

[3] For the experiments considered in Chapters 3–4, $k_b T/\omega_0 \approx 10^1$–$10^2$.

[4] Note the abuse of the notation. I'll use 'f' for both the scattering amplitude and the distribution function. The meaning should be clear from context whenever ambiguity arises.

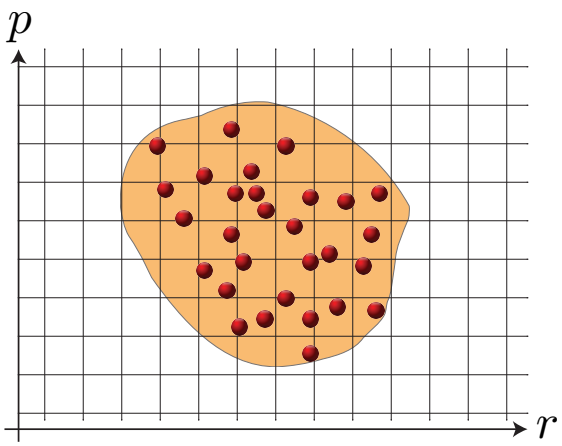

Figure 3.1: A two-dimensional projection of μ-space in both it's discrete representation in terms of individual atoms and continuum representation.

And chosen to be small compared to the characteristic scale of density fluctuations in the system, then the discrete representation (Eq. 3.5) can be thought of as a continuum[5] . In the continuum limit, the number of atoms in a μ-space cell centered about the position $\mathbf{r}$ and momentum $\mathbf{p}$ is $d^3r d^3p f(\mathbf{r}, \mathbf{p})$.

The μ-space and the continuum limit provide a complementary view of the dynamics of the atoms in the cloud, mapping the problem onto a study of the distribution function. Kinetic theory is concerned with how an arbitrary distribution function, which can be written in terms of the discrete coordinates $(\mathbf{r_i}(t), \mathbf{p_i}(t))$ of each atom in the cloud

$$f(\mathbf{r}, \mathbf{p}, t) = (2\pi)^3 \sum_{i}^{N_e x} \delta^{(3)}(\mathbf{r} - \mathbf{r_i}(t))\delta^{(3)}(\mathbf{p} - \mathbf{p_i}(t)), \tag{3.5}$$

evolves in time, relaxing to the equilibrium distribution (Eq 3.3.) In the remainder of this subsection, the kinetic theory for the interacting Bose gas above T_c is detailed. The theory below T_c is the subject of Chapter 4, where it will become necessary to connect the distribution function with the field operators and many-body Hamiltonian.

[5] See Appendix A for cell requirements for numerical computations.

3.1.1 The Boltzmann Equation

In this subsection, I will sketch the traditional derivation of the Boltzmann equation, which is an equation governing the dynamics of $f(\mathbf{r}, \mathbf{p})$, and motivate its generalization to include the effects of Bose enhancement.[6]

Generally, $f(\mathbf{r}, \mathbf{p}, t)$ evolves as atoms pass between cells in μ-space, changing the occupation numbers. This can be as a result of free evolution or as a result of collisions. Importantly, these processes occur on characteristic timescales separated by orders of magnitude for a dilute gas.

To derive the free evolution portion of the Boltzmann equation it is sufficient consider the motion of a individual *points* in μ-space, which manifests as a coordinate transformation. Under the action of an external force $\mathbf{F}$, the point $(\mathbf{r}, \mathbf{p})$ moves to $(\mathbf{r}, \mathbf{p}) \to (\mathbf{r}', \mathbf{p}') = (\mathbf{r} + (\mathbf{p}/m)\, dt, \mathbf{p} + \mathbf{F}dt)$ over the infinitesimal time window dt. If the external force depends only on position, $f(\mathbf{r}, \mathbf{p}, t) = f(\mathbf{r}', \mathbf{p}', t + dt)$ and the single-particle distribution function at that point can expanded in a Taylor series

$$\left[\frac{\partial}{\partial t} + \frac{\mathbf{p}}{m} \cdot \nabla_{\mathbf{r}} + \mathbf{F} \cdot \nabla_{\mathbf{p}}\right] f(\mathbf{r}, \mathbf{p}, t) = 0 \quad \text{(Collisionless Boltzmann equation)}\,, \tag{3.6}$$

where the subscript of the gradient operator indicates differentiation with respect to momentum or position. Free evolution is therefore analogous to the single-particle dynamics of each point in phase-space.

Collisions however intrinsically involve multiple phase space points, and occur over timescales where the free space evolution is negligible. During the evolution $t \to t + dt$, the number of atoms in a cell may decrease as they participate in a scattering process with an atom in a neighboring cell, and these collisions are referred to as **out collisions**. The number of atoms in a cell may also increase as the output of a collision elsewhere in μ-space ends up in the cell, and these collisions are referred to as **in collisions**. Higher order than two-body collisions are increasingly unlikely in the weakly-interacting dilute gas, and it is therefore sufficient to consider only the effect of binary collisions.

[6] For more details, including complete derivations, I typically refer to the seminal texts Refs [95, 96].

The cumulant effect of collisions serves only to locally reorganize μ-space with no net loss of atoms, which can be summarized in the time dependence of the occupation of each cell

$$\left.\frac{\partial f(\mathbf{r},\mathbf{p},t)}{\partial t}\right|_{coll} = R_{in}[f] - R_{out}[f]. \tag{3.7}$$

Let's sketch the form of the in and out coefficients[7] . $R_{in}[f(\mathbf{r},\mathbf{p})]$ represents the sum of all collisions within the gas that wind up contributing an atom to the phase space cell containing the point $(\mathbf{r},\mathbf{p})$. The rate at which these collisions occur is proportional to the quantum-mechanical scattering amplitude $\hat{f}(\mathbf{p}',\mathbf{q}' \to \mathbf{p},\mathbf{q})$, written in such a way as to highlight the incoming atoms with momentum $\mathbf{p}'$ and $\mathbf{q}'$and collisional products $\mathbf{p}$ and $\mathbf{q}$. For cells which are more occupied than others, this process is increasingly likely, and therefore R_{in} should depend on the two-atom distribution function $F(\mathbf{r},\mathbf{p}',\mathbf{q}',t)$ which is the correct measure of the likelihood of finding a particular incoming collisional pair in the cells $(\mathbf{r},\mathbf{p}')$ and $(\mathbf{r},\mathbf{q}')$. R_{in} should also reflect the conservation of total momentum and kinetic energy for each collision. This motivates the expression

$$R_{in}-R_{out} \propto \int d^3q d^3p' d^3q'\ \delta^{(3)}(\mathbf{p}+\mathbf{q}-\mathbf{p}'-\mathbf{q}')\delta(E-E')|\hat{f}(\mathbf{p}',\mathbf{q}' \to \mathbf{p},\mathbf{q})|^2 F(\mathbf{r},\mathbf{p}',\mathbf{q}',t) - \{\mathbf{p},\mathbf{q} \leftrightarrow \mathbf{p}',\mathbf{q}'\} \tag{3.8}$$

where the brackets denotes the exchange of coordinates, reflecting the construction of R_{out} as the time-reversal of R_{in}.

In the ultracold limit, $\hat{f}$ can be replaced by the constant s-wave contribution and can be pulled form the integrals. After collapsing the delta functions, the combined expression is

$$R_{in} - R_{out} = \frac{\hat{\sigma}}{4\pi m}\int d^3q\ d\Omega\ |\mathbf{p}-\mathbf{q}|(F(\mathbf{r},\mathbf{p}',\mathbf{q}',t) - F(\mathbf{r},\mathbf{p},\mathbf{q},t)), \tag{3.9}$$

where $\hat{\sigma} = 8\pi a_0^2$ is the s-wave cross section for identical boson scattering from Sec. 2.2.3.

To reduce Eq. 3.9 further, we follow Boltzmann and assumed that the dilute gas is in a state of **molecular chaos**. The incoming atoms are *not* correlated beyond the single-atom level

$$F(\mathbf{r},\mathbf{p},\mathbf{q},t)) \approx f(\mathbf{r},\mathbf{p},t)f(\mathbf{r},\mathbf{q},t), \tag{3.10}$$

[7] $R[f]d^3rd^3q$ is the associated local collision rate.

which is also required to formulate a closed form expression. If this approximation is not made, the dynamical equation for the two-atom correlation function must be produced which depends on the three-particle correlation function, etc... This chain of equations is known as the BBGKY hierarchy [97], and will be addressed further in Chapter 7.

This truncation gives the canonical form of the Boltzmann equation, including the effect of binary collisions through the **collision integral** I_{coll} that depends on the cross-section for identical particle scattering

$$\left[\frac{\partial}{\partial t} + \frac{\mathbf{p}}{m}\cdot\nabla_{\mathbf{r}} + \mathbf{F}\cdot\nabla_{\mathbf{p}}\right] f(\mathbf{r},\mathbf{p},t) = I_{coll},$$
$$I_{coll} = \frac{\hat{\sigma}}{4\pi m}\int d^3q\; d\Omega\; |\mathbf{p}-\mathbf{q}|(f(\mathbf{r},\mathbf{p}',t)f(\mathbf{r},\mathbf{q}',t) - f(\mathbf{r},\mathbf{p},t)f(\mathbf{r},\mathbf{q},t)), \tag{3.11}$$

which is a nonlinear integro-differential equation for the single-particle distribution. The left-hand side describes the single-particle evolution of the thermal cloud and the right-hand side is the collision integral which drives the system toward a state of statistical equilibrium at a rate proportional to the cross-section. For binary elastic collisions, both the center of mass (COM) momentum and the magnitude of the relative momentum are conserved, and the solid angle integral is over the full range of possible final directions for the relative momentum.

The Boltzmann equation contains the effects of identical particle scattering through the symmetrized scattering amplitude $\hat{f}$. Near T_c, the transition rates R_{in} and R_{out} can be enhanced by scattering into μ-space cells that have a significant occupation. Bose enhancement of the scattering rates occurs also in the more familiar setting of the stimulated output of coherent light in a laser [98]. The relative importance of Bose enhancement can be gauged on a cell by cell basis by the comparison of $f(\mathbf{r},\mathbf{p},t)$ to unity, or in an average sense by evaluating the **phase-space density**

$$\Xi = n_{ex}\lambda_{th}^3, \tag{3.12}$$

where n_{ex} is typically the density of atoms evaluated at the center of the trap or averaged over the entire trap. The phase space density is the ratio of atoms per unit volume to the number of available states that can be occupied at a given temperature per unit volume. This ratio yields the

average number of atoms per state, and $\Xi \approx 1$ provides a ballpark estimate of both the transition temperature T_c and the importance of Bose enhancement [65]. The formal procedure for including Bose-enhancement in the Boltzmann equation is described in [96], however, it is clear that it should appear through the substitution

$$f_{p'} f_{q'} \rightarrow f_{p'} f_{q'} (1 + f_p)(1 + f_q), \tag{3.13}$$

$$f_p f_q \rightarrow f_p f_q (1 + f_{p'})(1 + f_{q'}), \tag{3.14}$$

to reflect enhancement in the output channels. This upgraded form of the Boltzmann equation is known as a **quantum Boltzmann equation** or QBE for short.

3.1.2 Consequences of the H-Theorem: The Undamped Breathing Mode

Basic postulates of thermodynamics can be recovered from conclusions about the long-time behavior of the Boltzmann equation. In particular, the second law of thermodynamics, which states that the entropy of an isolated gas never decreases, was proved by Boltzmann in his famous H-theorem, which I sketch now. The conclusion of the H-theorem leads to a special set of solutions of the Boltzmann equation of which the breathing mode is a member.

In an isolated gas, consider the behavior of the functional

$$h(t) \equiv \int d^3v f(\mathbf{r}, \mathbf{v}, t) \log f(\mathbf{r}, \mathbf{v}, t), \tag{3.15}$$

which seems rather random, but is precisely the quantity which vanishes when the system is in equilibrium, and is decreasing for any initial state. To see this, the time derivative can be written in the following form [95] using properties of the Boltzmann equation

$$\dot{h}(t) = -\frac{\hat{\sigma}}{4} \int d^3v_1 \int d^3v_2 \int d\Omega \; |\mathbf{v_2} - \mathbf{v_1}| \left(f_{v_2'} f_{v_1'} - f_{v_2} f_{v_1} \right) \left[\log(f_{v_1'} f_{v_2'} - \log(f_{v_1} f_{v_2}) \right]. \tag{3.16}$$

Now, the distribution function is generally much less than unity and therefore when $f_{v_2'} f_{v_1'} > f_{v_2} f_{v_1}$, the logarithms satisfy the opposite relation, $\log(f_{v_2'} f_{v_1'}) < \log(f_{v_2} f_{v_1})$. Provided the assumption of molecular chaos is valid so that the factorization in Eq. 3.10 holds, $\dot{h}(t) < 0$ indicates a definitive

direction in time (**the arrow of time**) and vanishes in the long-time limit when the system has reached equilibrium. The entropy, S, is therefore directly proportional

$$h = -\frac{S}{Vk_b}, \tag{3.17}$$

and increases as the system settles towards equilibrium in a volume V. This is the **H-theorem**.

The necessary condition for Eq. 3.11 to vanish is

$$\log(f_{v_2'} f_{v_1'}) = \log(f_{v_2} f_{v_1}), \tag{3.18}$$

$$\log(f_{v_2'}) + \log(f_{v_1'}) = \log(f_{v_2}) + \log(f_{v_1}), \tag{3.19}$$

which has the form of a collisional constraint: the sum before the collision is equal to the post-collision sum. Namely, it restricts $\log(f)$ to a sum of quantities which are collisional invariants $\{\chi_1, \chi_2, ...\}$. This defines a class of possible solutions of the form

$$\log(f(\mathbf{r}, \mathbf{v}, t)) = \chi_1 + \chi_2 + ... \tag{3.20}$$

For a binary elastic collision, this set is spanned by the kinetic energy, momentum, and any velocity independent function, giving

$$\log\left(f(\mathbf{r}, \mathbf{v}, t)\right) = a + \mathbf{b} \cdot \mathbf{v} + c\mathbf{v}^{\mathbf{2}}, \tag{3.21}$$

where $a, \mathbf{b}, \mathbf{c}$ are possibly functions of position and/or time.

The familiar Maxwell-Boltzmann distribution of a stationary dilute gas follows from this expression for the choice $|\mathbf{b}| = 0$, $c = -1/k_{\mathrm{b}}T$ and $a = \log n \left(m/2\pi k_{\mathrm{b}}T\right)^{3/2}$. Generally, these coefficients satisfy a set of coupled differential equations [99]

$$\nabla_{\mathbf{r}} b = 0, \tag{3.22}$$

$$v^2 \dot{b} + \mathbf{v} \cdot \nabla_{\mathbf{r}} (\mathbf{c} \cdot \mathbf{v}) = 0, \tag{3.23}$$

$$\dot{\mathbf{c}} + \nabla_{\mathbf{r}} a + 2b\ \mathbf{F} = 0, \tag{3.24}$$

$$\dot{a} + \mathbf{F} \cdot \mathbf{c} = 0, \tag{3.25}$$

which can be obtained by inserting the general distribution function in Eq. 3.5 into the collisionless Boltzmann equation (Eq. 3.11) where the collision integral vanishes by construction. When the force, **F**, is due to an isotropic harmonic trapping potential, $b(t)$ executes simple harmonic motion at frequency $2\omega_0$, which is the so-called breathing or monopole mode. When $b(t)$ is oscillatory, what is usually identified as the temperature of the cloud oscillates in time in the absence of heat transfer, which is out of phase with the spatial relaxation and contraction of the density profile. It is therefore useful to think of a 'kinetic' temperature associated with $b(t)$ and a 'potential' temperature associated with the density variation. From these definitions, an analogy with a swing-like mechanism can be made as the average of the two temperatures maintains a constant value as the potential and kinetic temperatures oscillate out of phase over a single period [24]. This picture is independent of the amplitude of the oscillation and strength of the binary interactions. It is therefore of fundamental importance to measure the damping rate of this mode as a violation indicate a breakdown of the assumptions underlying the Boltzmann equation.

3.1.3 Collective Modes Above T_c.

The collective modes of a 3D isotropic trap with trapping frequency ω_0 reflect the underlying spherical symmetry and the quadratic form of the trapping potential. Any mode of the trap can be expressed in terms of irreducible spherical tensors, in this case they are multipole modes denoted by the labels (l, m). The $l = 0$ mode is the monopole mode of the system, and is characterized by an undamped oscillation at $2\omega_0$. The $l = 1$ dipole mode is a COM oscillation independent of the character of the interaction and therefore undamped. There are two limiting regimes of oscillation: the collisionless and hydrodynamic regimes. In the **collisionless regime**, the average duration between subsequent binary collisions is much longer than the trap period. This is summarized by the product of the average collision rate $\gamma_{\rm coll} = n(0)v_{\rm th}\hat{\sigma}/2$ with the trap period $\omega_0/\gamma_{\rm coll} \gg 1$. The thermal velocity is given by $v_{\rm th} = \sqrt{8k_{\rm b}T/\pi m}$. In the **hydrodynamic limit**, an average atom undergoes many binary collisions in a trap period $\omega_0/\gamma_{\rm coll} \ll 1$. The $l = 2$ quadrupole mode oscillates at $2\omega_0$ in the collisionless regime and $\sqrt{2}\omega_0$ in the hydrodynamic regime. It is collisionally

damped in the hydrodynamic crossover between the two extremes. In the following, I discuss two common methods for deriving the collective mode spectrum including damping effects in the regime of linear response.

3.1.3.1 Moment method

By taking moments of the Boltzmann equation (Eq. 3.11), a set of coupled equations of motion can be derived that describe the dynamical evolution of various collective modes [95]. For an arbitrary quantity $\chi(\mathbf{r}, \mathbf{v})$, the equation of motion is

$$\frac{\mathrm{d}\langle\chi\rangle}{\mathrm{d}t} - \langle \mathbf{v} \cdot \nabla_{\mathbf{r}} \rangle - \left\langle \frac{\mathbf{F}}{m} \cdot \nabla_{\mathbf{v}} \chi \right\rangle = \langle \chi I_{\mathrm{coll}} \rangle, \tag{3.26}$$

where I_{coll} is shorthand for the collision integral in the Boltzmann equation and the average quantity or moment is defined as

$$\langle \chi \rangle = \frac{1}{N} \int \mathrm{d}^3 r \mathrm{d}^3 v f(\mathbf{r}, \mathbf{v}, t) \chi(\mathbf{r}, \mathbf{v}), . \tag{3.27}$$

The collisional average of this quantity is given by

$$\langle \chi I_{\mathrm{coll}} \rangle = \frac{1}{4N} \int \mathrm{d}^3 r \mathrm{d}^3 \mathbf{v_1} \Delta\chi I_{\mathrm{coll}}[f], \tag{3.28}$$

where $\Delta\chi = \chi_1 + \chi_2 - \chi_{1'} - \chi_{2'}$ with $\chi_i = \chi(\mathbf{r}, \mathbf{v_i})$.

From Eq. (3.26), it is straightforward to form a closed set of coupled equations for the quadratic moments, recalling that moments of the form in Eq. (3.21) have no collisional contribution. For an isotropic trap, taking the moment $\langle \mathbf{r}^2 \rangle$ yields a closed set of equations describing the evolution of the monopole mode:

$$\begin{aligned} \frac{\mathrm{d}\langle \mathbf{r}^2 \rangle}{\mathrm{d}t} - 2\langle \mathbf{v} \cdot \mathbf{r} \rangle &= 0, \\ \frac{\mathrm{d}\langle \mathbf{v} \cdot \mathbf{r} \rangle}{\mathrm{d}t} - \langle \mathbf{v}^2 \rangle + \omega_0^2 \langle \mathbf{r}^2 \rangle &= 0, \\ \frac{\mathrm{d}\langle \mathbf{v}^2 \rangle}{\mathrm{d}t} + 2\omega_0^2 \langle \mathbf{v} \cdot \mathbf{r} \rangle &= 0. \end{aligned} \tag{3.29}$$

Solutions to Eqn. (3.29), where the moments oscillate around their equilibrium values as $e^{i\omega t}$, confirm Boltzmann's general result as previously discussed in 3.1.2 for an undamped monopole mode at oscillation frequency $2\omega_0$.

One can also take $(l = 2, m = 0)$ quadrupole moments of Eq. (3.26) to derive a closed set of six coupled equations for an isotropic trap. However, for the quadrupole mode the moment, $\langle 3v_z^2 - \mathbf{v^2} \rangle$ cannot be expressed in the form of Eq. (3.21), which leads to a nontrivial collisional contribution $\langle (3v_z^2 - \mathbf{v}^2) I_{\rm coll} \rangle$ in its equation of motion. For small amplitude oscillations about equilibrium, collisional contributions of this form can be approximately rewritten in the **relaxation time approximation** [95, 100, 101] which uses the Chapman-Enskog procedure as

$$\langle \chi I_{\rm coll} \rangle = -\frac{\chi}{\tau_{\rm coll}}, \tag{3.30}$$

where the relaxation time $\tau_{\rm coll}$ is given by

$$\tau_{\rm coll} = \frac{5}{4\gamma_{\rm coll}}, . \tag{3.31}$$

As with the monopole mode, the set of coupled equations for the quadrupole mode can also be solved algebraically, giving frequencies of $2\omega_0$ and $\sqrt{2}\omega_0$ in the collisionless and hydrodynamic regimes respectively. However, in the hydrodynamic crossover the quadrupole mode damps due to the nonvanishing collisional contribution.

3.1.3.2 Scaling Ansatz Method

The scaling ansatz method has been used for Bose gases above and below the transition temperature [102, 103, 104, 105, 106, 29, 107, 108, 109]. In the nondegenerate regime, the ansatz method has been used to evaluate the effects of the mean field interaction [107, 108] and to estimate the effects of anharmonic corrections to the trapping potential on the collective mode frequencies and damping rates [109]. Here this method is outlined.

When the thermal cloud is in statistical equilibrium under harmonic confinement, the Boltzmann equation for the equilibrium distribution $f_0(\mathbf{r}, \mathbf{v})$ is just the Poisson bracket:

$$\left(\sum_i^3 v_i \frac{\partial f_0}{\partial r_i} - \omega_i^2 r_i \frac{\partial f_0}{\partial v_i} \right) = 0, \tag{3.32}$$

where the subscript denotes components of a Cartesian vector in 3D and the possibly differing frequency components in each direction. Moments of the equilibrium distribution are the same as

those obtained in the previous Subsection when the temporal derivatives are set to zero.

To describe time-dependent collective oscillations, a **scaling ansatz** on the form of the distribution function $f(\mathbf{r}, \mathbf{v}, t)$ can be made:

$$f(\mathbf{r}, \mathbf{v}, t) = \Gamma f_0(\mathbf{R}(\mathbf{r}, \mathbf{t}), \mathbf{V}(\mathbf{r}, \mathbf{v}, \mathbf{t})). \tag{3.33}$$

This ansatz utilizes the symmetry of the problem and the nature of the collective modes in the forms of the renormalized position, $\mathbf{R}(\mathbf{r}, \mathbf{t})$, and velocity, $\mathbf{V}(\mathbf{r}, \mathbf{v}, \mathbf{t})$, with an additional factor Γ to enforce the normalization.

For the dipole mode, the form of the ansatz is $R_i = r_i - \eta_i(t)$ and $V_i = v_i - \dot{\eta}_i(t)$ with Γ equal to unity. The details of the motion are contained in the time-dependent vector of free parameters, $\vec{\eta}$. Such a scaling clearly describes a translation of the COM of the equilibrium cloud.

For the monopole and quadrupole mode, the ansatz mimics the form of Eq. 3.21:

$$\begin{aligned} R_i &= \frac{r_i}{b_i(t)}, \\ V_i &= \frac{1}{\theta_i^{1/2}} \left(v_i - \frac{\dot{b}_i(t)}{b_i(t)} r_i \right), \\ \Gamma &= \frac{1}{\prod_j^3 (b_j(t)\theta_j(t)^{1/2}),} \end{aligned} \tag{3.34}$$

where there are two time-dependent vectors of free parameters $\vec{\theta}$ and $\vec{b}$. Such a scaling describes the stretching and compression of the equilibrium cloud in μ-space along with a space-dependent and time-dependent translation in the local velocity, while maintaining a stationary COM.

Substituting Eq. (3.33) into Eq. (3.11) and following [107, 108], a Newton-like set of equations of motion for the free parameters can be derived

$$\begin{aligned} \ddot{b}_i + \omega_i^2 b_i - \omega_i^2 \frac{\theta_i}{b_i} &= 0 \\ \dot{\theta}_i + 2\frac{\dot{b}_i}{b_i}\theta_i &= -\frac{1}{\tau_{\text{coll}}} \left[\theta_i - \bar{\theta} \right], \end{aligned} \tag{3.35}$$

where the quantity $\bar{\theta} = \sum_i \theta_i / 3$ is the average temperature. To obtain information about the collective oscillations, the free parameters are linearized about the equilibrium position for small

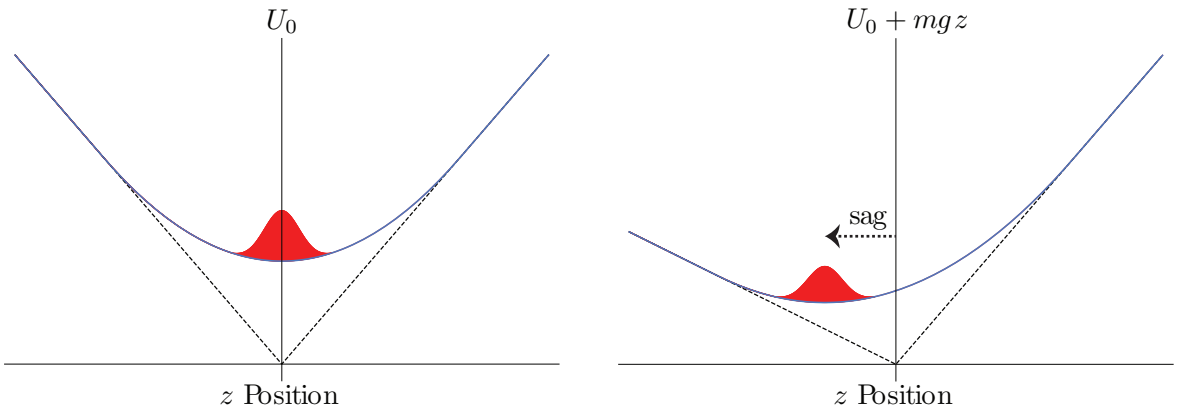

Figure 3.2: In the modified TOP trap, the cloud shifts under the pull of gravity away from the midpoint between the coils. The trap can be made isotropic to harmonic order with the cost of anisotropic anharmonicities. (Adapted from [63].)

amplitude oscillation, $b_i \approx 1$ and $\theta_i \approx 1$, and assumed to have time-dependence of the form $e^{\mathrm{i}\omega t}$. For a harmonic trap, the results obtained agree with the moment method. The advantage of the scaling ansatz method is that it can produce closed form expressions when anharmonic corrections to the trapping potential are included, which will shortly be found necessary.

3.2 The Breathing Mode Experiment

Although this is a theory thesis, it is useful to give a theorists account of the experimental setup used to produce extremely isotropic harmonic confinement because the imperfections of this trap play a dominant role in understanding the observed damping of the breathing mode oscillation. The trapped state of ^{87}Rb is the maximally-stretched spin state discussed in Sec. 2.2.4, and to a decent approximation, we take $a_s \approx a_t \approx a_0 \approx 100$ Bohr radii in the cross section formulas.

To produce isotropic confinement, the quadrupole field strength of the TOP trap (see Sec. 2.1.1.1) is decreased, the effects of gravity become important as the atoms in the trap sag away from the high-field limit trap minimum. The extent of the sag is characterized by the dimensionless quantity $\Lambda = mg/\mu B_z$ and shifted trap minimum $z_0 = -(B_0\Lambda) / \left(B_z\sqrt{1-\Lambda^2}\right)$. The potential expanded

about the sag position z_0 is

$$\begin{aligned} U_{\rm sag}(\rho,z) = \quad & \mu B_0\sqrt{1-\Lambda^2} + \tfrac{\mu B_z^2}{16B_0}(1+\Lambda^2)r^2\sqrt{1-\Lambda^2} \\ & + \tfrac{\mu B_z^2}{2B_0}z^2(1-\Lambda^2)^{3/2}. \end{aligned} \tag{3.36}$$

The ratio of the trap frequencies is

$$\frac{\omega_z}{\omega_\rho} = \sqrt{8\frac{1-\Lambda^2}{1+\Lambda^2}} \tag{3.37}$$

with $\Lambda = 7/9$ giving an isotropic trapping potential. For further details of the modified TOP trap used in the JILA experiment, we refer the reader to Ref. [63].

Utilizing gravity to symmetrize the trap results in trapping frequencies on the order of 10 Hz. In such a loose trap anharmonic corrections become important and must be included in calculations. The potential used in calculations involving the anharmonic corrections has the form

$$\begin{aligned} U_{\rm ah}(\rho,z) = \quad & \tfrac{m}{2}\left(\omega_z^2 z^2 + \omega_\rho^2\rho^2\right) + \tfrac{m\alpha}{3}z^3 + \tfrac{m\beta}{3}\rho^2 z \\ & + \tfrac{m\kappa}{4}z^4 + \tfrac{m\delta}{4}\rho^2 z^2 + \tfrac{m\epsilon}{4}\rho^4, \end{aligned} \tag{3.38}$$

and for general formulation of the cubic and quartic terms see Ref. [63]. The values of the anharmonic coefficients in SI units used in this chapter were quoted from the JILA experiment (Ref. [63]) as $\alpha = 5.58\times10^6$ s^{-2} m^{-1}, $\beta = 4.17\times10^6$ s^{-2}m^{-1}, $\kappa = 5.94\times10^9$ s^{-2}m^{-2}, $\delta = 1.716\times10^9$ s^{-2}m^{-2}, and $\epsilon = 2.469\times10^8$ s^{-2}m^{-2}.

The monopole mode is driven experimentally by applying a sinusoidal variation in the trapping frequency over four periods of monopole oscillation. The strength of the TOP field is changed along with a vertical bias which fixes the minimum of the potential (see Ref. [63]). The net result is a roughly 25% increase in the mean cloud size. The main results of the experiment [24] are shown in Fig 3.3 for the damping rates, where the data was taken over a range of collision rates at temperatures $2T_c < T < 3T_c$ to avoid mean-field effects and to ensure that the gas is close to the regime described by the original formulation of the Boltzmann equation. The monopole damping rate in Fig. 3.3 is small compared to the quadrupole rate and the trapping frequency but nevertheless nonzero, and it should re-emphasized that *any* damping is *anomalous* in light of Boltzmann's

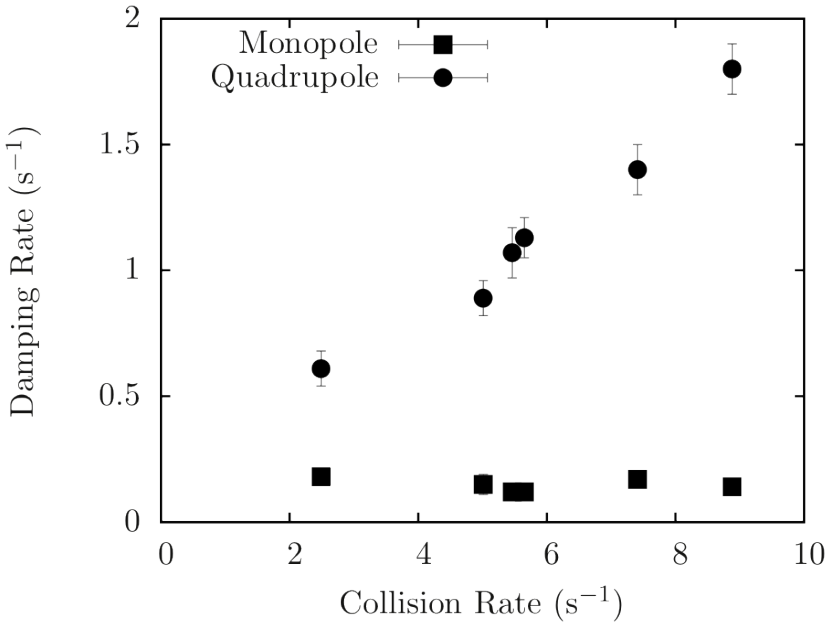

Figure 3.3: Experimental results from Ref. [24] for the monopole and quadrupole damping rates over a range of collision rates. The monopole damping is nonzero and therefore anomalous, but the quadrupole damping agrees with well-known results from Ref. [100].

prediction and therefore potentially relevant to the underpinnings of kinetic theory. The quadruple damping rate is nonzero, agrees with well-known expressions, and is therefore not focused on in this analysis.

3.3 Theoretical Analysis

Slight anisotropies in the harmonic confinement and anharmonic corrections to the trapping potential Eq. (3.38) present possible sources of damping. Modeling these imperfections is discussed in this section using trapping data from the JILA experiment.

3.3.0.3 Damping due to trap anisotropies

Anisotropies in the confining potential lead to coupling between the monopole and quadrupole modes, which are damped in the hydrodynamic crossover regime. The moment method can account

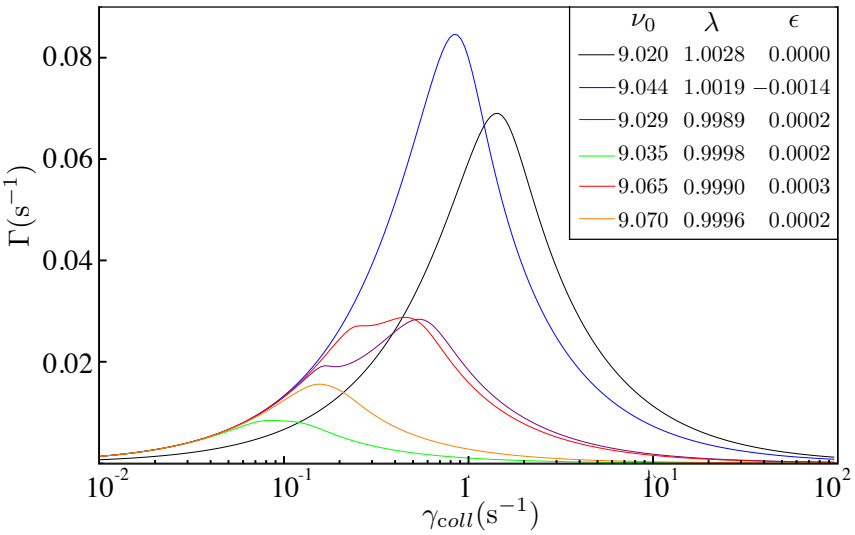

Figure 3.4: Monopole damping rates versus collision rate for a set of frequencies from the JILA experiment with various anisotropy parameters and central frequencies ν_0. The legend gives the level of anisotropy, where λ, ϵ, and $\nu_0 = \omega_0/2\pi$ correspond to rewriting the harmonic confining potential as in Eq. (3.39).

for this coupling in a straightforward way given a potential of the form

$$U(x,y,z) = \frac{m\omega_0^2}{2}\left((1+\epsilon)x^2 + (1-\epsilon)y^2 + \lambda^2 z^2\right), \tag{3.39}$$

where $\lambda = \omega_z/\omega_0$, $\omega_0\sqrt{1+\epsilon} = \omega_x$, and $\omega_0\sqrt{1-\epsilon} = \omega_y$.

Starting with $\langle \mathbf{r}^2 \rangle$, the moment method yields a set of nine coupled equations for the monopole and quadrupole modes (see Ref. [110]). In Fig. 3.4, frequency measurements from the JILA experiment with various anisotropies were used to estimate the damping rate for small oscillations. For nonzero ϵ and λ different from unity, the monopole couples to multiple quadrupole modes and the shape of the curve departs from that expected for the typical transition region shape when $\epsilon = 0$.

The monopole damping measured in the JILA experiment is on the order of 0.1 s^{-1} or larger. Therefore, the trap can roughly be treated as isotropic with $\lambda = 1$ and $\epsilon = 0$ for the lowest four curves in Fig. 3.4. Thus, the observed monopole damping must then be due to some other mechanism that is present even when the harmonic piece of the trapping potential is virtually isotropic.

3.3.0.4 Damping due to anharmonic corrections

Computing the monopole damping using the moment method for nonzero anharmonic coefficients generates an infinite set of coupled equations for successively higher order moments and so is not a viable method. However, the scaling ansatz method, which takes as an input moments of f_0, can provide an estimate for the effects of the anharmonic coefficients which enter through higher order moments of f_0. The usefulness of such an approach hinges on being able to neglect deformations of the equilibrium distribution due to the anharmonic corrections.

Using the scaling ansatz, Eq. (3.35) can be rewritten in a more general form for an arbitrary trapping force, F_i:

$$\begin{aligned} \ddot{b}_i - \frac{\theta_i}{b_i}\langle v_i^2\rangle_0 - \frac{1}{m}\langle F_i(b_j r_j) r_i\rangle_0 = 0, \\ \dot{\theta}_i + 2\frac{\dot{b}_i}{b_i}\theta_i = -\frac{1}{\tau_{\rm coll}}\left[\theta_i - \overline{\theta}\right], \end{aligned} \tag{3.40}$$

where the 0 subscript indicates a moment as in Eq. (3.27) over the equilibrium distribution f_0, and $b_j r_j$ is a short hand notation for the set $\{b_x r_x, b_y r_y, b_z r_z\}$. From Eq. (3.40), the procedure for including even order corrections to the trapping potential is straightforward. However, to include odd order corrections, the equilibrium distribution, f_0, must be deformed. A simple deformation is

$$f_0^{\rm ah}(\mathbf{r},\mathbf{v}) = \left(1 - \frac{m\beta}{3k_{\rm b}T}\left(x^2+y^2\right)z - \frac{m\alpha}{3k_{\rm b}T}z^3\right) f_0(\mathbf{r},\mathbf{v}), \tag{3.41}$$

which is a perturbative expansion to first order in the odd order anharmonic corrections from Eq. 3.38. The deformation does not change the overall normalization nor the value of the even-order moments, and the added terms are collisional invariants of the form Eq. (3.21).

In Sec. 6.5, the validity of this deformation compared to numerical and experimental results for the damping of the monopole mode is addressed. However, in the remainder of this section, the general solution of Eq. 3.40 is discussed for small amplitude oscillations, following the derivation in Ref. [109] and noting that the derivation is the same for $f_0^{\rm ah}$.

Equation (3.40) is solved in both the collisionless and hydrodynamic regimes. Making the

assumption that the monopole damping is much less than the collective mode frequency ($\Gamma_{\rm M} \ll \omega_{\rm M}$) leads to a generally applicable formula for the damping [111]

$$\Gamma \approx \frac{\tilde{\tau}_{\rm coll}}{2} \frac{\omega_{CL}^2 - \omega_{HD}^2}{1 + \omega_{CL}^2 \tilde{\tau}_{\rm coll}^2}. \tag{3.42}$$

In the JILA experiment, $\Gamma_{\rm M}/\omega_{\rm M}$ is on the order of 10^{-3} to 10^{-2}.

In the collisionless regime, $\tau_{\rm coll} \to \infty$, which gives a power law relation between the two scaling parameters: $\theta_i = \frac{1}{b_i^2}$. Using this power law relation, Eq. (3.40) collapses into three differential equations for each component of the parameter b_i. For small amplitude oscillations $b_i \approx 1$, and the substitution $\eta_i = b_i - 1$ linearizes the three differential equations for each component of η_i:

$$\ddot{\eta}_i + \frac{3}{m} \frac{\langle U_i r_i \rangle_0}{\langle r_i^2 \rangle_0} \eta_i + \frac{1}{m} \sum_j \frac{\langle U_{ij} r_i r_j \rangle_0}{\langle r_i^2 \rangle_0} \eta_j = 0, \tag{3.43}$$

where $U_i = \partial U / \partial r_i$ and $U_{ij} = \partial^2 U / \partial r_i \partial r_j$. Equation (3.43) can be treated with matrix methods by defining

$$\begin{aligned} A_{ij}^{CL} &= \frac{3}{m} \frac{\langle r_i U_i \rangle_0}{\langle r_i^2 \rangle_0} \delta_{ij}, \\ B_{ij}^{CL} &= \frac{1}{m} \frac{\langle r_i r_j U_{ij} \rangle_0}{r_i^2}, \end{aligned} \tag{3.44}$$

and solving the secular equation $\left| A^{CL} + B^{CL} - \omega^2 I \right| = 0$ for the collective mode frequencies.

In the hydrodynamic regime, $\tau_{\rm coll} \to 0$, and thus the system is in local equilibrium everywhere. Furthermore, the components of the θ_i's must be equal to their average, $\theta_i = \bar{\theta}$. From the normalization of the ansatz then follows a power law relation between the parameters: $\theta_i = 1/\prod_j b_j^{2/3}$. This implies that Eq. (3.40) collapses to a set of three differential equations for each component of the parameter b_i that couple when the power law relation for θ_i is substituted. Making the small amplitude assumption leads to the following equation:

$$\ddot{\eta}_i + \frac{1}{m} \frac{\langle U_i r_i \rangle_0}{\langle r_i^2 \rangle_0} \left(\frac{5}{3} \eta_i + \frac{2}{3} \sum_{i \neq j} \eta_j \right) + \frac{1}{m} \sum_j \frac{\langle U_{ij} r_i r_j \rangle_0}{\langle r_i^2 \rangle_0} = 0. \tag{3.45}$$

As in the collisionless case, we define matrices

$$A_{ij}^{HD} = \left\{ \begin{array}{ll} \frac{5}{3m} \frac{\langle U_i r_i \rangle_0}{\langle r_i^2 \rangle_0} & i = j \\ \frac{2}{3m} \frac{\langle U_j r_i \rangle_0}{\langle r_i^2 \rangle_0} & i \neq j \end{array} \right\}, \tag{3.46}$$

$$B_{ij}^{HD} = B_{ij}^{CL}, \tag{3.47}$$

and solve the secular equation $\left|A^{HD} + B^{HD} - \omega^2 I\right| = 0$ for the collective mode frequencies.

Solving the secular equation for the hydrodynamic and collisionless regimes yields frequencies for the monopole mode and the (l=2,m=0,2) quadrupole modes. The frequencies have simple expressions in terms of the A and B matrices

$$\begin{aligned} \omega_M^2 &= \delta + \sqrt{\delta^2 - \Delta}, \\ \omega_{Q0}^2 &= \delta - \sqrt{\delta^2 - \Delta}, \\ \omega_{Q2}^2 &= A_{xx} - A_{xy} + B_{xx} - B_{xy}, \end{aligned} \tag{3.48}$$

where

$$\begin{aligned} \delta &= \left(A_{xx} + A_{xy} + A_{zz} + B_{xx} + B_{xy} + B_{zz}\right)/2, \\ \Delta &= \left(A_{xx} + A_{xy} + B_{xx} + B_{xy}\right)\left(A_{zz} + B_{zz}\right) \\ &- 2\left(A_{xz} + B_{xz}\right)\left(A_{zx} + B_{zx}\right). \end{aligned} \tag{3.49}$$

The calculated mode frequencies have temperature dependence through higher-order moments coming from the anharmonic corrections. For a given temperature, the scaling ansatz theory gives the shift in the frequency $\Delta\omega_{\rm M}$ and damping Γ from that anticipated by the harmonic limit $\omega_{\rm M}^0 = 2\omega_0$. The damping Γ is from collisional relaxation in the system.

The shift in the frequency $\Delta\omega_{\rm M} = \omega_{\rm M}^0 - \omega_{\rm M}^{\rm P}$, measures the gap between the result in the harmonic limit $\omega_{\rm M}^0$ and the peak frequency component $\omega_{\rm M}^{\rm P}$ present in the cloud. Centered about the peak component is a spread of frequencies whose width $\delta\omega_{\rm M}$ is not predicted from the scaling ansatz method. To obtain full information about the width, one can perform a numerical simulation as discussed in Sec. 3.4. The width provides a measure of the dephasing-induced damping $\Gamma_{\rm dephase}$, which is responsible for the appearance of actual relaxation in the system and is separate from the collisional damping estimate from the scaling ansatz theory. In Ref. [109] it was argued that for a given width $\delta\omega_{\rm M}$, the dephasing time δt is given approximately by $\delta\omega_{\rm M}\delta t \approx 2\pi$, and therefore $\Gamma_{\rm dephase} \approx 2\pi/\delta t \approx \delta\omega_{\rm M}$. For an anisotropic trap, the frequency shift was used in Ref. [109] in lieu of the actual width to obtain dephasing-induced damping rates which agreed with experimental

results within an order of magnitude. This approximation is reasonable only in the collisionless regime where the spread of frequencies in the cloud begins with the collective oscillation of the lowest energy atoms at $\omega_{\rm M}^0$. As will be made precise in Sec. 6.5, when the collision rate increases, $\delta\omega_{\rm M}$ narrows about the peak value $\omega_{\rm M}^{\rm P}$ and decreases proportionately with $\Gamma_{\rm dephase}$. The shift $\Delta\omega_{\rm M}$ becomes then a poor estimate for the width $\delta\omega_{\rm M}$. As $\Gamma_{\rm dephase}$ decreases a transition regime exists where dephasing effects in the cloud are destroyed through collisions, and collisional damping becomes the dominant effect. Such an effect can account for anomalous damping of the monopole mode in regimes where $\omega_{\rm M}\tau_{\rm coll} \gg 1$, whereas collisional damping dominates when $\omega_{\rm M}\tau_{\rm coll} \approx 1$. We refer to the regime where $\delta\omega_{\rm M}\tau_{\rm coll} \approx 1$ as the *dephasing crossover*, and in Sec. 6.5 this crossover is studied in detail with the aid of numerical simulation.

3.4 Numerical Methods

In this section the numerical algorithm used to simulate the dynamical evolution of the thermal cloud is described, with further details provided in Appendix A. Numerical simulation of the system isolates the roles of various damping mechanisms and permits quantification of the dephasing effects in the cloud. The thermal cloud algorithm from Ref. [112] is adopted, working in the quantum collisional regime [113] where two-body collisions are s-wave. However, the many-particle statistics are still classical and well-described by the Boltzmann equation. The simulation consists of a swarm of tracer particles that act as a coarse-grained distribution function [114]:

$$f(\mathbf{r},\mathbf{p},t) \approx \frac{N_{\rm th}}{N_{tp}} h^3 \sum_i^{N_{tp}} \delta(\mathbf{r}-\mathbf{r_i})\delta(\mathbf{p}-\mathbf{p_i}), \tag{3.50}$$

where $N_{\rm th}/N_{tp}$ is a weighting factor. The sum is over the entire set of tracer particles, where each is uniquely described by their position and momentum $(\mathbf{r_i},\mathbf{p_i})$. The tracer particles first undergo collisionless evolution via a second order sympletic integrator [115, 116]. Following free evolution, the tracer particles are binned in space and tested for collisions.

3.4.1 Collisions

The collision algorithm, which is a procedure for Monte Carlo sampling the collision integral [117], follows that described in Ref. [112]. After binning the particles in space, random pairs in each bin are selected and their collision probability is calculated. If a collision is successful, the particle velocities are updated according to the differential cross-section for an s-wave collision.

For each set of simulation parameters we check that the equilibrium collision rate averaged over the entire cloud matches with the analytic result:

$$\gamma_{eq} = N_{\rm th} \frac{\hat{\sigma}\omega_0^3 m}{2\pi^2 k_{\rm b} T}, \tag{3.51}$$

to $< 2\%$.

3.4.2 Drive mechanism

To mimic the experimental monopole drive scheme, the trap frequency, ω_0, is modulated over four periods of monopole oscillation

$$\omega_0(t) = \left\{ \begin{array}{ll} \omega_0 \left(1 + A \sin(2\omega_0 t)\right) & t \leq 4\pi/\omega_0 \\ \omega_0 & t > 4\pi/\omega_0 \end{array} \right\}, \tag{3.52}$$

where A is a unitless measure of the strength of the drive. During the drive, the anharmonic corrections are neglected, and are switched on when the next oscillation minimum occurs after the drive is turned off. Figure 3.5 illustrates the increase of the monopole amplitude during the drive and the effect of turning on the anharmonic shifts on the total cloud energy. For $A = 0.15$ and a starting temperature of 152nK, the percent increase in the total energy when the anharmonic corrections are switched on is on the order of 0.001%. Neglecting the anharmonic terms during the drive effectively captures the experimental scenario without including the modulation of the bias, quadrupole, and all of the shimming fields. Results are presented then over a range of drive strengths that produce an increase in the mean cloud size at the end of the drive phase on the order with that experimentally measured. Driving the cloud ideally emphasizes the impact of the anharmonic shifts on the monopole mode and eliminates any residual driving of the quadrupole

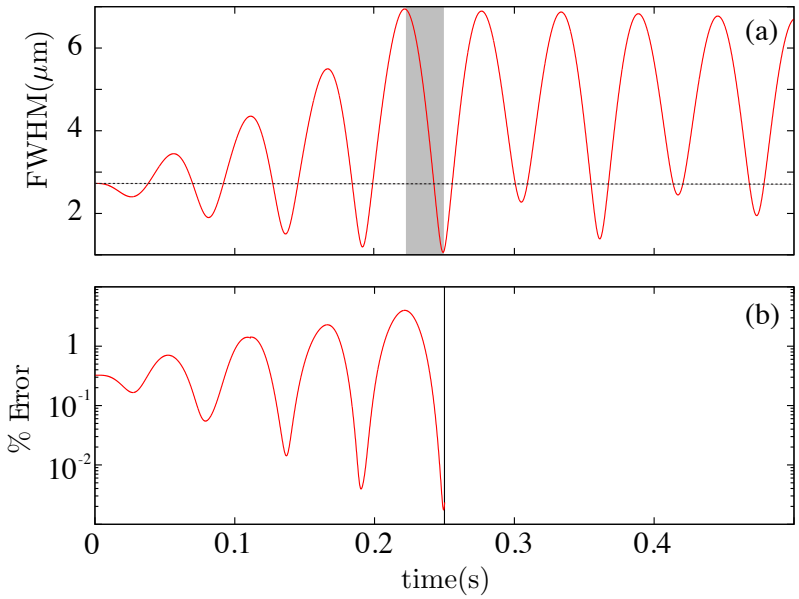

Figure 3.5: Driving the monopole moment for $A = 0.15$ and initial temperature of 152nK over four periods of oscillation. (a) FWHM of the monopole moment versus holding time. The grey area indicates the time in between the end of the drive and switching on the anharmonic terms in the trapping potential. (b) The % change in the total energy of the cloud between a trapping potential that is purely harmonic and the same potential with anharmonic terms switched on. The vertical line indicates the point at which the anharmonic terms are added to the trapping potential when the % increase of the total energy is on the order of 0.001%.

and dipole modes which are not the subject of the current study. For the full details of the drive, refer to Ref. [63].

During the drive there is also a shift in the average temperature and full width at half maximum (FWHM) of the oscillation due to an increase in the energy of the cloud from the work done on it by pumping of the trap.

3.5 Results

We are now in a position to compare and contrast the results of the JILA experiment against the theoretical model and numerical simulation. Here, only data with the monopole drive is considered. Moreover, our analysis is focused on experimental data that is not dominated by effects due to trap anisotropy, as this is well-understood [100, 101]. Characterizing the sensitivity of the

monopole mode to anharmonic corrections around the dephasing crossover is the main result of this chapter. This sensitivity stands as a general issue for undamped, nonequilibrium collective modes, such as the monopole oscillation. The quadrupole modes must also damp around the dephasing crossover; however, these modes are not explored further as they do not fall into the category of undamped, nonequilibrium modes.

In the JILA experiment, the monopole data was taken for a range of atom numbers and temperatures. The small-cloud data ($N \approx 10^4$ atoms) which lies in the collisionless regime is analyzed first. Finally the large-cloud data ($N \approx 10^5 - 10^6$ atoms) which lies between the collisionless and hydrodynamic regimes is analyzed.

3.5.1 Collisionless regime

In the collisionless regime, the many-body dynamics of the thermal cloud are dictated by the single-particle trajectories. Here, the system behaves in analogy with a simple pendulum. For small amplitude oscillations the pendulum executes simple-harmonic motion. However, as the amplitude grows, the small-angle approximation breaks down and anharmonic corrections become important. The pendulum traces out a repeating trajectory but with an energy-dependent period.

The procedure for replacing anharmonic corrections by an energy-dependent harmonic potential in 1D is well-known [111]. The renormalized trapping potential for small amplitude motion along the z-axis is:

$$\begin{aligned} U(0,0,z) &\approx \frac{m\tilde{\omega}_z^2(E)}{2} z^2, \\ \tilde{\omega}_z &= \omega_z(1+\xi_z E), \\ \xi_z &= -\frac{5\alpha^2}{6m^3\omega_0^6} + \frac{3\kappa}{4m^2\omega_0^4}. \end{aligned} \tag{3.53}$$

In Fig. 3.6a, atoms in the anharmonic trap have been binned according to their energy and the collective motion in each bin averaged to obtain the monopole period in each bin. For the first several bins the period of collective oscillation increases linearly with the bin energy. For higher energy bins the scaling is still monotonic; however, the deviation increases as the difference in the

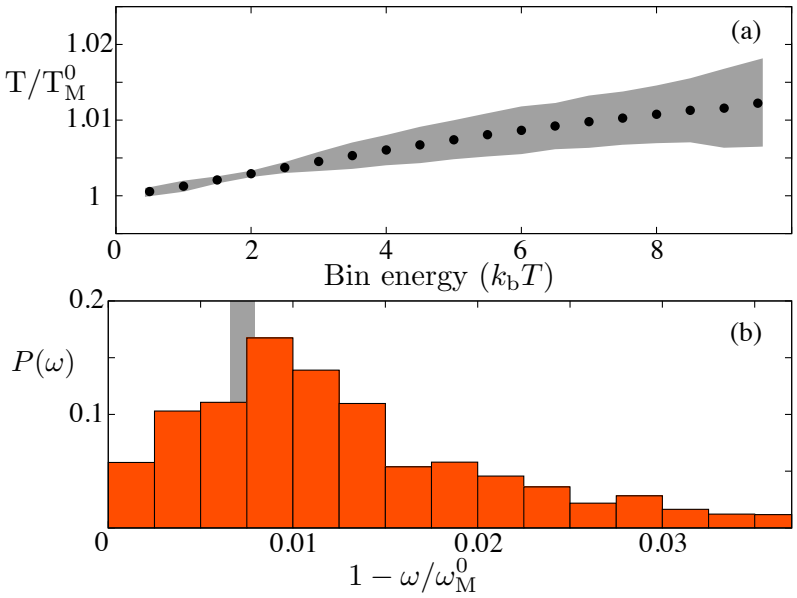

Figure 3.6: Resolving the energy dependence of the monopole moment for a drive strength of $A = 0.15$ (9 ± 1.35Hz) and an initial temperature of 152nK. (a) After binning the tracer particles into energy bins, each bin oscillates as an independent monopole. Here, the ratio of the average period of the monopole in each bin and the zero temperature result, $T_M^0 = 2\pi/\omega_M^0$ along with the standard deviation (grey region), is plotted versus the energy of each bin in units of thermal energy. (b) The statistical weight, $P(\omega)$, of each frequency component in the cloud. The grey region is the theoretical prediction for the shift of the monopole frequency from L (150nK) to R (180nK).

linear correction between the different axes becomes more apparent. At sufficiently high binning energy, the linear correction Eq. (3.53) breaks down as higher-order terms become important, and the atom number in each bin decreases, spoiling the appearance of an undamped collective mode.

In the absence of collisions, the population of atoms in each bin is static over the entire simulation. The statistical weight of each frequency component, as shown in the normalized histogram of Fig. 3.6b, is then also static. The determining characteristics of the frequency distribution are its width and shift of the peak from $\omega_M^0 = 2\omega_0$. The theoretical prediction of $\Delta\omega_M$ from the scaling ansatz using f_0^{ah} is for the shift of the peak (grey region of Fig. 3.6b) and agrees with the numerical result. However, the width, denoted $\delta\omega_M$, of the frequency distribution determines the relative importance of dephasing effects. If the frequency distribution is shifted and sharply peaked, dephasing induced damping is minimal, mimicking the large amplitude oscillation of a single pendulum. Oth-

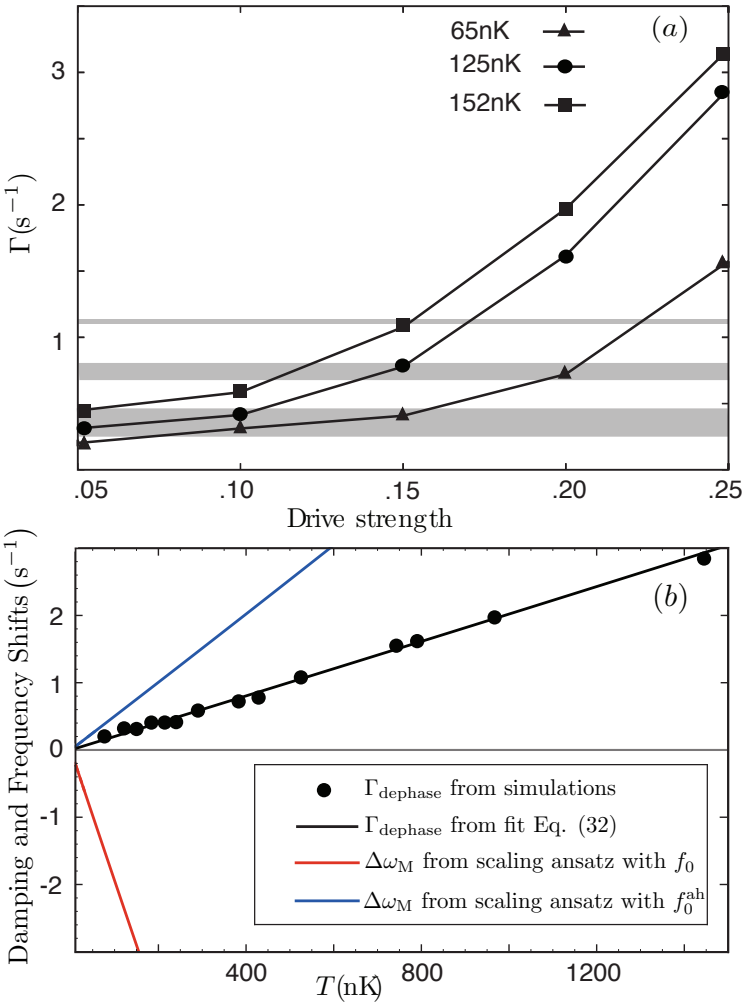

Figure 3.7: (a) Damping of the monopole over a range of drive strengths $A = \{0.05, 0.1, 0.15, 0.20, 0.25\}$ and temperatures in the collisionless regime. The grey regions are the damping results along with the uncertainty from the JILA experiment [24] for (from bottom to top) 65nK, 125nK, and 152nK. (b) The colored lines are the theoretical predictions for $\Delta\omega_{\rm M}(T)$ using $f_0^{\rm ah}$ (blue) and using f_0 (red) for the scaling ansatz versus the settled temperature of the cloud. The points are the damping results from (a) for all simulated drive strengths and temperatures in the collisionless regime. The solid black line is a fit to the numerical damping results using Eq. (3.54).

erwise, if the distribution is broad, as in Fig. 3.6a, the net sum of many 'pendulums' oscillating at shifted frequencies is dephasing induced damping through interference. The scaling ansatz theory also gives a prediction for the damping due to collisional relaxation, and in the collisionless regime, this prediction is vanishingly small as expected (see Fig. 3.8).

We now compare directly to the small-cloud data from the JILA experiment. Starting with

the temperature and atom number quoted in the experiment, the drive strength is varied and the amplitude of the resulting oscillation is fit to a simple exponential decay to compare directly to the fitting function used in the experiment. As shown in Fig. 3.7a, a drive strength of $A = 0.15$ matches the experimental data, suggesting that the anomalous damping seen in the experiment for the small-cloud data is mainly due to dephasing effects. Such effects depend on the settled temperature of the cloud as shown in Fig. 3.7b.

Although the width of the frequency distribution determines the strength of the dephasing induced damping, in the collisionless regime where the distribution is broad, the frequency shift $\Delta\omega_{\mathrm{M}}$ and the width scale proportionately (see discussion at the end of Section 3.3.2) and can be used as a fitting function, looking then for a scaling fit of the form

$$\Gamma_{\mathrm{dephase}}(T) = \Delta\omega_{\mathrm{M}}(\zeta T), \tag{3.54}$$

where ζ is a free parameter independent of the temperature. For the experimental trap parameters, $\zeta = 0.4$ from a fit to the data shown in Fig. 3.7b.

The scaling ansatz result using f_0 instead of f_0^{ah} predicts a decrease of the period with increasing bin energy, which disagrees directly with the numerical result and Eq. (3.53). Additionally, from the red and blue lines in Fig. 3.7b, as the settled temperature increases the deformed gaussian predicts that the peak frequency decreases ($\Delta\omega_{\mathrm{M}}(T) > 0$).

3.5.2 Crossover regime

The collisionless regime picture of a collection of uncoupled monopole modes oscillating at shifted frequencies begins to break down when the dephasing period $\tau_{\mathrm{dph}} = 2\pi/\delta\omega_{\mathrm{M}}$ exceeds τ_{coll}. This is typically in a different collisional regime than the hydrodynamic crossover where $\omega_0\tau_{\mathrm{coll}} \approx 1$, and an average atom suffers a collision on a timescale faster than the oscillation period. Therefore, as the collision rate increases there are two important regimes: the dephasing crossover and the

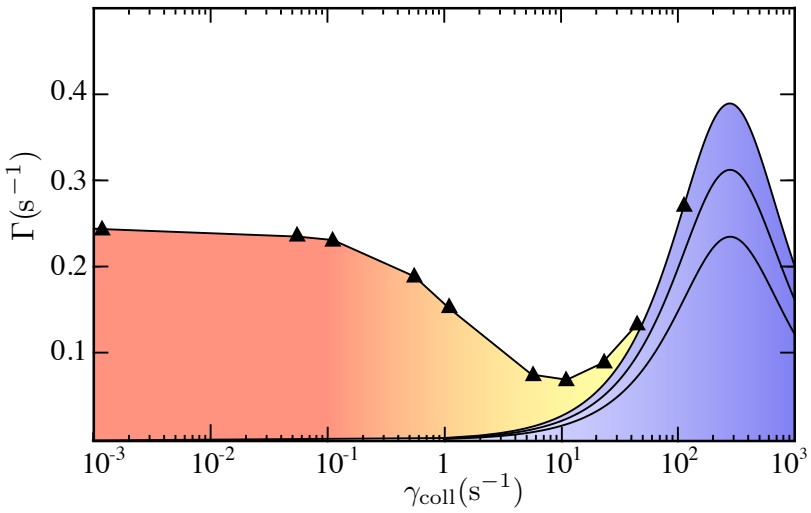

Figure 3.8: Damping rate versus the equilibrium collision rate. The triangle data points are a result of numerical particle simulations. The blue curves are scaling ansatz predictions using $f_0^{\rm ah}$ for collisional damping of the monopole mode for temperatures 60nK, 80nK, and 100nK from bottom to top, respectively.

hydrodynamic crossover.

$$\delta\omega_{\rm M}\tau_{\rm coll} \approx 1 \quad \text{(Dephasing Crossover)}, \tag{3.55}$$

$$\omega_0\tau_{\rm coll} \approx 1 \quad \text{(Hydrodynamic Crossover)}. \tag{3.56}$$

In the remainder of this subsection an individual experimental run from the large-cloud data set at 60.6nK with 3.463×10^5 atoms with measured trap frequencies ($f_x = 9.036$Hz, $f_y = 9.034$Hz, $f_z = 9.034$Hz) is analyzed. From the criteria Eq. (3.56) can be obtained crude estimates for the dephasing crossover $\gamma_{\rm coll} \approx 10^{-1} - 1$ s^{-1} and the hydrodynamic crossover $\gamma_{\rm coll} \approx 10^2$ s^{-1}. This data set corresponds to the green curve in Figure 1 for a quoted collision rate $\gamma_{\rm coll} = 8.88$ s^{-1} which lies between the two regimes. The maximum damping rate due to anisotropies from Figure 1 is on the order of 10^{-3} s^{-1} compared to the experimentally measured rate 0.14 ± 0.02 s^{-1}. Therefore, the harmonic part of the trapping potential is treated as isotropic.

To quantify the effect of the anharmonic corrections in the crossover regime, numerical simulations with $A = 0.05$ over a range of collision rates using the trapping frequency $\nu_0 = 9.035$Hz and initial temperature 60nK were performed. Figure 3.8 contains the results along with the prediction

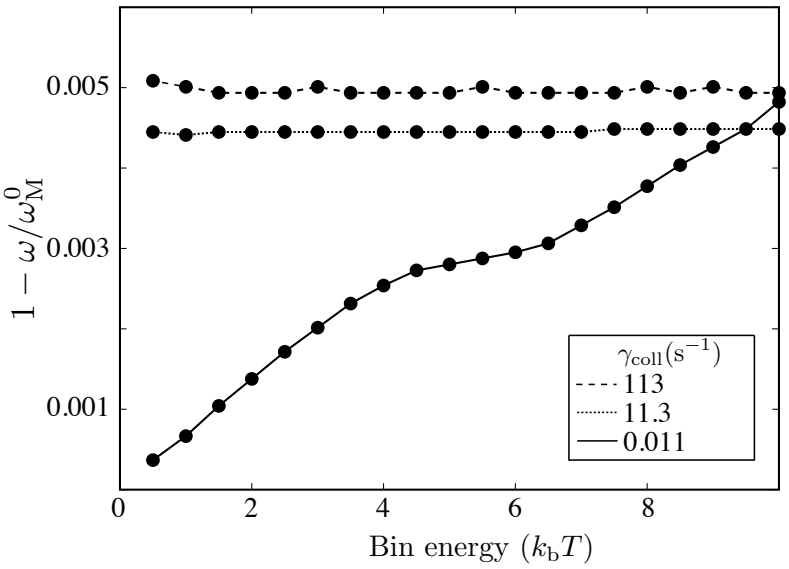

Figure 3.9: Resolving the energy dependence of the monopole moment for A = 0.05 and initial temperature of 60.6nK for a range of total atom numbers. Each data point is the peak component of the Fourier transform of the normalized collective oscillation in the bin. From bottom to top the curves represent frequency spreads in the collisionless, dephasing crossover, and hydrodynamic crossover respectively.

for the collisional damping from the scaling ansatz theory using $f_0^{\rm ah}$. The scaling ansatz prediction is plotted for several temperatures, illustrating the effect of the increase in temperature of the cloud post-drive on the damping.

The estimates for the hydrodynamic and dephasing crossover regimes also agree with the qualitative structure of Fig. 3.8. The dephasing crossover is marked by a decrease in the dephasing induced damping; whereas the hydrodynamic crossover is marked by an increase in the collisional damping. The region in between the two crossovers is characterized by a local minimum in the damping rate. Comparing the 65nK damping rate from Fig. 3.7 with the 60.6nK damping rate from this subsection draws experimental support for this result. That the collisionless regime is characterized by higher damping than the dephasing crossover is a common feature of all of the large-cloud data compared for similar temperatures to the small data [24]. The intermediate regime between dephasing and hydrodynamic crossovers then provides an experimental window where damping from trap anharmonicities can be minimized.

Whereas the physics of dephasing in the collisionless regime is analogous to the uncoupled oscillation of a collection of pendulums with different oscillation energies, in the dephasing crossover the pendulums begin to couple, and, as illustrated in Fig. 3.9, the width of the spread in frequency components narrows. The coupling effectively synchronizes the different pendulums, which leads to a local minima in the damping rate as seen in Fig. 3.8. As the coupling increases, the system nears the hydrodynamic crossover, and the spread in the frequencies is minimal. The damping is then due to the appearance of a temperature dependent anisotropic trap, where the monopole mode damps naturally through coupling with the quadrupole modes whose moments are not collisionally invariant.

3.6 Conclusion

The Boltzmann equation is based on the assumption that the chain of correlations describing the dilute gas can be broken through the assumption of molecular chaos. The resultant theory has a special class of undamped oscillations, which includes the breathing mode in an 3D isotropic trap. In the JILA experiment [24], this prediction was tested for the first time, finding small but nonetheless anomalous damping rates. These rates can be explained by numerical and analytic techniques for solving and simulating the Boltzmann equation when imperfections in the trap beyond harmonic order are included, and therefore the assumptions underlying the Boltzmann equation are not falsified by the experiment.

It is an open question what the damping contributions to the breathing mode are from beyond-Boltzmann effects which include higher order correlation dynamics beyond single-atom level. These effects are evidently swamped by damping due to anharmonicities in the JILA experiment. In the next chapter, the theory of the interacting Bose gas is developed under the semi-classical approximation and compared to the data taken from the same experimental apparatus. The Boltzmann equation will be seen to be a limiting case of the more general theory beginning from the many-body Hamiltonian.

Chapter 4

Collapse and Revival of the Breathing Mode of a Degenerate Bose gas in an Extremely Isotropic Harmonic Trap

This chapter contains the results from a joint theory/experimental collaboration in JILA published in Ref. [61], using the same apparatus as described in Sec. 3.2 and Ref. [24].

As the temperature approaches and is reduced below the critical temperature for Bose-Einstein condensation, Boltzmann's prediction for the breathing mode is stretched beyond the range of validity. This is due to the presence of density dependent mean-field effects, which arise when the de Broglie wavelength becomes comparable to the inter particle spacing, signaling the regime of quantum degeneracy. This is also due to the addition of Bose enhancement in the transition rates of the system as the identical particle symmetry must be accounted for. And, importantly, it is due to the formation of a macroscopically occupied condensate, which introduces a gap to the low-energy spectrum of excitations characteristic of the emergence of superfluidity and establishes a coherent phase within the system. In the semi-classical limit, where the noncondensed portion can be thought of as the thermal cloud of particle-like excitations, the breathing mode can be visualized as the oscillation of a condensate at a frequency $\sqrt{5}\omega_0$ coupled to a thermal component oscillating at the classical result of $2\omega_0$, and this is the subject of this chapter.

It is well-understood that the energy and atom number exchange of these components introduces nonzero damping rates, however there is another intriguing possibility unique to "two-component" systems composed of identical atoms which originates from the study of liquid helium.

In supercooled helium II, a change in the pressure leads to density fluctuations traveling with a sound velocity; however, changes in temperature also lead to fluctuations in entropy propagating with a 'sound' velocity [118]. To distinguish these diffierent propagation modes, the density fluctuations are label **first sound** or ordinary sound and are described by the superfluid and normal component (thermal cloud) compressing and rarefying **in-phase** with each other, mimicking familiar pressure waves. The entropy fluctuations are named **second sound** and are associated however with **out-of-phase** oscillations of the superfluid and normal components at fixed density. Spatially, this appears as a swapping of components superfluid→normal→superfluid→... at a fixed location in space. Importantly, these sound modes result from the bulk coupling of the condensed and noncondensed portions.

It is an intriguing question to what extent these in-phase and out-of-phase oscillations can be observed in degenerate dilute ultracold Bose gases. One obstacle is the difference in the collective modes for a trapped system compared to homogenous systems, and the second difference is orders of magnitude difference in diluteness of the two systems. It might be expected then that ultracold dilute gases display some collisionless analogue of the in-phase and out-of-phase oscillations, and to understand this question requires an account of the recent history of collective mode studies for dilute ultracold Bose gases below the transition temperature.

Experiments probing the collective modes of ultracold gases were carried out shortly after the demonstration of Bose-Einstein condensation in a dilute atomic vapor [69, 119]. In early experiments at JILA [19] and MIT [20], the low-lying quadrupole modes of a nearly pure Bose-Einstein condensate (BEC) were excited, and the observed oscillation frequencies showed good agreement with the Bogoliubov spectrum [120, 121]. Experiments were then conducted over a range of temperatures below the critical point, and temperature-dependent shifts in the oscillation frequencies and damping rates were observed [21, 6].

One mode in particular, the $m = 0$ quadrupole mode reproduced in Fig. 4.1 from Ref. [21], defied early attempts at explanation. At temperatures nearing the transition point where a significant portion of the cloud is in the noncondensed component, the frequency unexpectedly shifted upwards

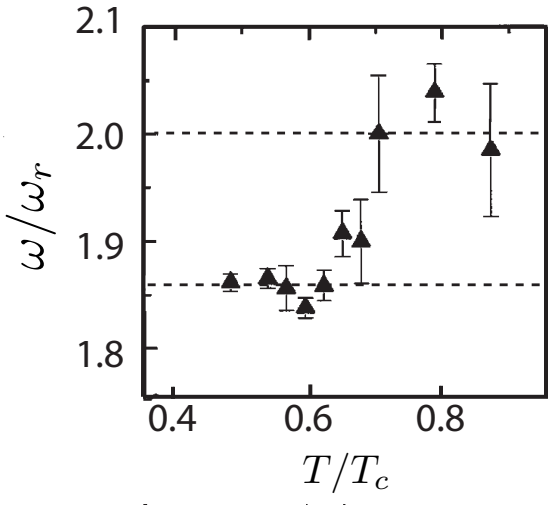

Figure 4.1: Temperature dependent $m = 0$ quadrupole mode spectrum from Ref. [21] normalized to the radial trapping frequency ω_r. The anomalous upward shift at $T > 0.7T_c$ differs by $10 - 20\%$ from zero-temperature analytic result indicated by the lower dashed line.

away from the zero-temperature result. Further exploration of collective-mode behavior at finite temperatures yielded additional puzzling temperature-dependent shifts [22, 23]. The resolution of these difficulties required the inclusion of the dynamics of the noncondensate in analogy with helium II. Using a semi-classical coupled-modes model, Stoof, Bijlsma, and Al Khawaja [29, 122] described the coupled dynamics of the condensate and noncondensate in terms of in-phase and out-of-phase eigenmodes, which were exactly the collisionless analogs of first and second sound hydrodynamic modes [123, 124, 102]. They concluded that the anomalous behavior found in Ref. [21] was the result of simultaneous excitation of both eigenmodes of the system. Numerical simulation of the Zaremba-Nikuni-Griffin (ZNG) equations by Jackson and Zaremba [125, 126, 127] confirmed this picture, and Morgan, Rusch, Hutchinson, and Burnett provided additional analysis in an extension of their previous work [128, 129, 130, 131, 132]. These efforts highlighted the important role of the noncondensate dynamics in the behavior of collective modes at finite temperature.

Experiments to date have operated with anisotropic trapping geometries, which lead to an increased degree of complexity in the collective-mode spectrum and mask effects due to the dynamical coupling of condensed and noncondensed portions of the gas. The signature of this coupling in

Ref. [21] shown in Fig. 4.1 was an upward shift of the $m = 0$ quadrupole mode frequency around $T \sim 0.7T_c$ indicative of a crossover between two distinct branches. Two mode fits of the condensate oscillation revealed the presence of the natural oscillation frequencies of both the condensate and thermal clouds in the condensate oscillation [125]. The upper branch, which was likely the one predominately excited experimentally, corresponds to an in-phase oscillation of the condensate and thermal cloud, as the condensate is being driven by the thermal cloud. In Ref. [133], Geddes, Morgan, and Hutchinson analyzed the breathing mode under isotropic harmonic confinement, predicting strong dynamic coupling between condensate and thermal cloud as a result of mode matching between the condensate and a strong resonance of the thermal cloud near the breathing mode frequency of the classical gas at $2\omega_0$. Importantly, they surmised that the condensate oscillations should be out-of-phase as the cloud warms nearing the transition temperature. In the breathing mode experimental results for an isotropic trap presented in this chapter, the observed striking collapse and revival behavior of the condensate oscillation provides a smoking-gun signature of dynamic coupling between the thermal cloud and condensate.

In this chapter, joint experimental/theoretical results for the breathing mode oscillation below T_c are presented. First, the semi-classical theory of the finite temperature BEC must be developed beginning from the zero-temperature limit and the many-body Hamiltonian. The collisionless coupled-modes model of Stoof and Bijlsma is then presented with results for the temperature dependence of the mode spectrum over the experimental range of interest. The experimental results are then detailed along with a description of the relevant observables. The striking collapse and revival timescales observed in the experiment are then analyzed from the framework of the coupled-modes analysis and from numerical simulations using the ZNG methodology [134] which includes collision processes and can account for the observed damping[1] . The results of this chapter play a dual role. The immediate role is that of extending the many-body theory for ultracold weakly-interacting Bose gases developed thus far and benchmarking it against experiment. There is however also the broader role which is historical context of the results of this chapter with respect

[1] The details of the algorithm are described in Appendix A.

to the study of liquid superfluidity and Bose-Einstein condensation of a dilute atomic cloud.

4.1 Zero Temperature: The Mean-Field Theory of the Condensate

This section picks up from the discussion in Sec. 2.3.2 for the noninteracting Bose gas, where it was concluded that formation of BEC is characterized by a macroscopic population of the ground state orbital of the system. When an orbital becomes macroscopically occupied $N_0 \gg 1 \implies N_0 + 1 \approx N_0$, the added effect of an additional atom become negligible

$$a_0^\dagger |N_0, ...\rangle = \sqrt{N_0 + 1}|N_0 + 1, ...\rangle \approx \sqrt{N_0}|N_0, ...\rangle, \tag{4.1}$$

and therefore $a_0^\dagger \approx \sqrt{N_0}$ appropriate for a coherent state. This approximation can be carried over to the field operators through Eq. 2.66, yielding

$$\psi^\dagger(\mathbf{r}) = \sqrt{N_0}\phi_0^*(\mathbf{r}) + \sum_{\lambda \neq 0} a_\alpha^\dagger \phi_\alpha^*(\mathbf{r}), \tag{4.2}$$

which is commonly written in the form

$$\psi^\dagger(\mathbf{r}) = \Psi^*(\mathbf{r}) + \delta\psi^\dagger(\mathbf{r}), \tag{4.3}$$

with the identifications

$$\sqrt{N_0}\phi_0^*(\mathbf{r}) = \Psi^*(\mathbf{r}) \tag{4.4}$$

$$\sum_{\lambda \neq 0} a_\alpha^\dagger \phi_\alpha^*(\mathbf{r}) = \delta\psi^\dagger(\mathbf{r}) \tag{4.5}$$

of the complex-valued field $\Psi(\mathbf{r})$ describing the **condensate wave function**. The remainder $\delta\psi^\dagger(\mathbf{r})$ is the **fluctuation field**, which is typically small compared to the condensate occupation for zero temperature theories, and near the transition temperature is composed of the thermal cloud discussed in Sec. 2.4.

When an orbital is not macroscopically occupied, the expectation value of its associated creation or annihilation operator is zero:

$$\langle ..., N_\alpha, ...|a_\alpha^\dagger|...., N_\alpha, ...\rangle = \sqrt{N_\alpha + 1}\langle ..., N_\alpha, ...|...., N_\alpha + 1, ...\rangle = 0. \tag{4.6}$$

However, the macroscopic orbital expectation value returns $\sqrt{N_0}$. Therefore, the expectation value of the field operator is nonzero $\langle\psi^\dagger(\mathbf{r})\rangle = \Psi^*(\mathbf{r})$, indicating an underlying **broken symmetry**, which is the U(1)-gauge symmetry, associated with the global alignment of the phase of individual atoms in the ground state orbital [120]. The condensate wave function $\Psi^*(\mathbf{r})$ is the **order parameter** associated with the symmetry broken phase.

When the gas is interacting, the condensate is deformed from the shape of ground state orbital, as we will see shortly. To allow for greater flexibility in the condensate wave function, it is written in the general form

$$\Psi(\mathbf{r},t) = \sqrt{n_c(\mathbf{r},t)}e^{i\theta(\mathbf{r},t)}, \tag{4.7}$$

where $\theta(\mathbf{r})$ is the coherent phase, and n_c is the condensate density. Furthermore, we denote the condensate normalization $\int d^3r\ |\Psi(\mathbf{r})|^2 = N_c$ rather than the orbital occupation, N_0. In the noninteracting limit, $N_c = N_0$.

Let's now derive the equation of motion for the condensate wave function from the Heisenberg equation of motion for the field operator $\psi(\mathbf{r})$ including interactions. The Heisenberg equation of motion $i\dot{\psi} = \left[\psi, \hat{H}\right]$ gives the time evolution for a single field operator

$$i\dot{\psi}(\mathbf{r}) = \left[-\frac{\nabla^2}{2m} + V_{trap}(\mathbf{r}) + g_0\psi^\dagger(\mathbf{r})\psi(\mathbf{r})\right]\psi(\mathbf{r}), \tag{4.8}$$

where the commutation relations, Eqs. 2.68, 2.69 for the field operators have been utilized. The contact strength g_0 therefore plays the role of an effective coupling strength. When $a_0 > 0$, this manifests as a repulsive coupling, and when $a_0 < 0$ it manifests as attractive. To construct an equation of motion for the condensate wave function, the field operator can be replaced by its symmetry broken form (Eq. 4.3) and fluctuation term is ignored in the zero temperature limit

$$i\dot{\Psi}(\mathbf{r}) = \left[-\frac{\nabla^2}{2m} + V_{trap}(\mathbf{r}) + g_0|\Psi(\mathbf{r})|^2\right]\Psi(\mathbf{r}), \tag{4.9}$$

which is the time-dependent **Gross-Pitaevskii equation** (GPE) for the dynamics of the condensate wave function. The rightmost term is a nonlinear term of coupling strength g_0 that takes into account the mean-field produced by the surrounding condensed bosons.

To understand the ground state structure of the condensate at zero temperature, a stationary form of the GPE must be formulated. Generally, the ground state of the many-body system must minimize the expectation value of the many-body Hamiltonian, Eq. 2.77, and when a condensate is present, the substitution $\psi(\mathbf{r}) = \Psi(\mathbf{r})$ yields the energy functional

$$E_{tot}[\Psi] = \int d^3r \ \left[\frac{|\nabla\Psi(\mathbf{r})|^2}{2m} + V_{trap}(\mathbf{r})\Psi(\mathbf{r})|^2 + \frac{g_0}{2}|\Psi(\mathbf{r})|^4\right], \tag{4.10}$$

where it is convenient to denote the respective contributions $E_{tot}[\Psi] = E_{kin}[\Psi] + E_{pot}[\Psi] + E_{int}[\Psi]$. The factor of $1/2$ in the mean-field contribution prevents double counting of interaction energy E_{int} between all distinct pairs of condensate atoms of which there are $N_c(N_c-1)/2 \approx N_c^2/2$. The ground state condensate wave function should therefore minimize this functional along with the normalization constraint $N_c = \int d^3r|\Psi(\mathbf{r})|^2$. The method of Lagrange multipliers recasts this problem as a functional minimization of $E_{tot}[\Psi] - \mu N[\Psi]$ for fixed Lagrange multiplier μ. This minimization is achieved by setting the functional derivative $\delta\left(E_{tot}[\Psi] - \mu N[\Psi]\right) = 0$, which results in a stationary equation for the ground state wave-function [65]

$$\mu\Psi(\mathbf{r}) = \left[-\frac{\nabla^2}{2m} + V_{trap}(\mathbf{r}) + g_0|\Psi(\mathbf{r})|^2\right]\Psi(\mathbf{r}), \tag{4.11}$$

which is the time-independent GPE. Alternatively, the time-independent GPE can be reproduced from the time-dependent GPE by looking for stationary solutions of the form $\Psi(\mathbf{r}) = \sqrt{n_c(\mathbf{r})}e^{-i\mu t}$. The Lagrange multiplier μ is therefore also the eigenvalue of the condensate wave-function. In the remainder of this section, μ is connected with the chemical potential from thermodynamics by analyzing the solutions of the time-independent GPE.

In the absence of interactions, the condensate wave function is simply the harmonic oscillator ground state scaled by the number of atoms

$$n_c(\mathbf{r}) = \frac{N_c^{1/2}}{\pi^{3/4}(a_x a_y a_z)^{1/2}} e^{-\left(x^2/2a_x^2 + y^2/2a_y^2 + z^2/2a_z^2\right)} \quad \text{(Non-Interacting gas.)} \tag{4.12}$$

The quantities a_i are the oscillator lengths along a particular axis of the trap with frequency ω_i, $a_i = \sqrt{1/m\omega_i}$. When this solution is plugged into the time-dependent GPE, assuming an isotropic geometry, the result is $\mu = \sum_i \omega_i/2$, which agrees with the condensation criterion $\mu =$

E_0 from Sec. 2.3.2 for noninteracting Bose gases. Additionally, this is just the average energy per particle, E_{tot}/N_c, which agrees in the non-interacting limit with the general definition of the chemical potential

$$\mu = E_{tot}[N_0] - E_{tot}[N_0 - 1] \quad \text{(General definition)}\,, \tag{4.13}$$

as the variation of the total energy when the total number of atoms is varied.

In the limit where the mean-field interaction term term is large compared to the kinetic energy, captured by the dimensionless parameter $\xi = (N_c a_0/a_{ho}) \gg 1$, the gradient operator in Eqs. 4.11 can be ignored. This is referred to as **Thomas-Fermi** approximation [65], which is a fair approximation in many weakly-interacting Bose gas experiments ($na_0^3 \ll 1$). In the Thomas-Fermi approximation, the time-independent GPE can be solved algebraically for the condensate density

$$n_c(\mathbf{r}) = \left[\mu - V_{trap}(\mathbf{r})\right]/g_0 \quad \text{(Thomas-Fermi approximation.)} \tag{4.14}$$

This is a parabolic profile with a sharp boundary at the position where $V_{trap}(\mathbf{r}) = \mu$. Normalizing the Thomas-Fermi density distribution gives an expression for the chemical potential

$$\mu_{TF} = \frac{15^{2/5}}{2}\xi^{2/5}\omega_0, \tag{4.15}$$

which is no longer equal to the average energy per particle. This can be seen clearly by comparing the result from Eq. 4.10 for E_{tot} with the general expression for μ from Eq. 4.11 which differ by a factor of 2 in the interaction energy

$$\mu = \frac{E_{kin} + E_{pot} + 2E_{int}}{N_c} = \frac{E_{tot} + E_{int}}{N_c}, \tag{4.16}$$

reflecting the fact that the average interaction energy changes with increasing particles, which compliments the scaling of the mean-field interaction with the density of condensate atoms [135]. This also agree with the general definition Eq. 4.13, which completes the identification of μ with the chemical potential even when interactions are included.

The stationary form of the GPE therefore describes the ground state of the condensate including the effects of two-body interactions. Higher order effects can also be incorporated in

a systematic way described in the final chapter of this thesis, Chapter 7. From this viewpoint, the energy functional, Eq. 4.10, is therefore a low-density expansion based on the smallness of the diluteness parameter (see Refs [136, 137] for the lowest order 'LHY' corrections.) In the following section, the finite temperature Bose gas, where the fluctuations $\delta\psi$ are non negligible, is discussed through a kinetic theory for the fluctuation field.

4.2 Kinetic Theory Below T_c

Below the transition temperature, the excitation spectrum is more complex than the particle-like energies of Chapter 3. Namely, there is a transition between particle-like excitations at high energies and long wavelength phonon sound modes, which are number preserving density oscillationsm, at low energies which is captured by the Bogoliubov dispersion relation for the uniform Bose gas with repulsive interactions ($g_0 > 0$)

$$E(\mathbf{p}) = \sqrt{\chi_p^2 - (ng_0)^2}, \tag{4.17}$$

$$\chi_{\mathbf{p}} = \frac{p^2}{2m} + ng_0, \tag{4.18}$$

written in the form emphasizing the gap, ng_0, at zero energies which is an indicator of superfluidity [65]. In a trapped Bose gas, this excitation spectrum is valid over a window which is small compared to the spatial variation of the trap, which generally holds provided the collective oscillation varies sufficiently slowly. Therefore, the short wavelength, particle-like picture holds locally over the entire cloud. The low-momentum modes become collective modes of the trap when viewed over the length scale of the entire gas. In extremely elongated traps, it is possible to produce collective oscillations that are well-approximated by phonon sound modes [138].

The dividing temperature below which particles become phonon-like is $k_b T_* \approx ng_0$. This result applies approximately to a trapped gas using the density at the center of the trap, which for the experiment considered in this chapter gives $T_* < 0.1T_c$. This is well below the temperature range considered in this chapter ($0.7T_c < T < T_c$) and therefore it is appropriate to consider the cloud of excitations as particle-like in constructing a semi-classical kinetic theory.

To formally construct a particle-like expectation spectrum, I make the Hartree-Fock (HF) approximation and consider expectation values of the orbital interaction, Eq. 2.74,

$$\langle N_0, N_1, N_2, ...|\hat{V}|N_0, N_1, N_2, ...\rangle = \frac{1}{2}\sum_{\alpha\beta\gamma\delta}\langle N_0, N_1, ...|a_\delta^\dagger a_\gamma^\dagger a_\beta a_\alpha|N_0, N_1, ...\rangle\langle\delta\gamma|V|\alpha\beta\rangle, \tag{4.19}$$

where $\langle N_0, N_1, N_2, ...|$ is a symmetrized Fock-space ket including the number of atoms, N_i, in the ith orbital. Non-vanishing expectation values correspond to $\delta = \alpha$, $\gamma = \beta$, the direct or **Hartree** contribution, and $\delta = \beta$, $\gamma = \alpha$, the exchange or **Fock** contribution.

For particle-like excitations, it is appropriate to take the expectation value in Eq. 4.19 with respect to plane waves in a cubic volume of side L small compared to a_{ho}. In this case with the zero-range contact interaction (Eq. 2.44), the coupling matrix is a constant g_0/L^3 and the excitation energies are given by

$$\tilde{E}(\mathbf{p}) = \frac{p^2}{2m} + ng_0 + (n - n_\mathbf{p})g_0, \tag{4.20}$$

where $n_\mathbf{p}$ is the density of a plane-waves with momentum $\mathbf{p}$. The tilde has been added to denote energies under the Hartree-Fock approximation. The second and third term in Eq. 4.20 are the mean-field energies associated with the Hartree and Fock contributions, respectively. This gives the generalized expressions including the trapping potential for the local energy of a ($\mathbf{p} = 0$) excitation in the condensate

$$\tilde{E}(\mathbf{r}, 0) = \left[n_c(\mathbf{r}) + 2n_{ex}(\mathbf{r})\right] g_0 + V_{ext}(\mathbf{r}), \tag{4.21}$$

and also gives the energy of the excitations out of the condensate as

$$\tilde{E}(\mathbf{r}, \mathbf{p} \neq 0) = \frac{p^2}{2m} + 2\left[n_c(\mathbf{r}) + n_{ex}(\mathbf{r})\right] g_0 + V_{ext}(\mathbf{r}). \tag{4.22}$$

The factor of two difference reflects the fact that the excited states are not macroscopically occupied and therefore $n - n_{\mathbf{p}\neq 0} \approx n$.

Equation 4.22 is the energy of an atom moving in the combined mean-fields of the condensate and excitations. The factor of two difference in the condensate and thermal cloud energies has ramifications for the the ground state structure. In Fig. 4.2, the thermal cloud and condensate ground state densities are shown over a range of the dimensionless parameter ξ, from noninteracting

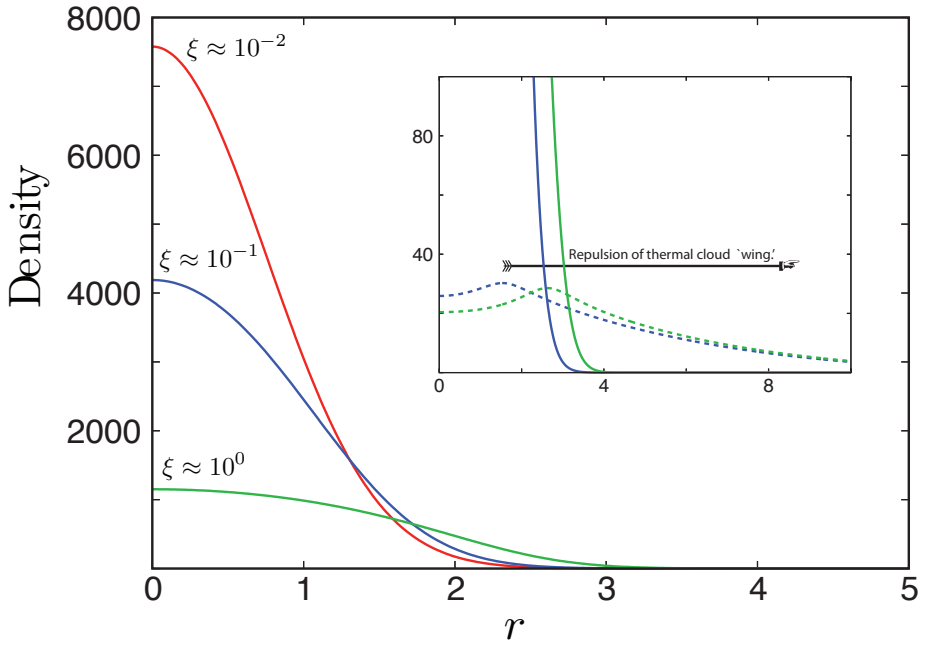

Figure 4.2: Profiles of the condensate (solid lines) and thermal cloud (dashed lines in inset) densities from noninteracting $\xi \approx 10^{-2}$ (red), $\xi \approx 10^{-1}$ (blue), to the edge of the Thomas Fermi regime $\xi \approx 1$ (green). The densities and radius are rescaled in oscillator units for $N = 10^5$, $T = 0.8T_c$. As χ increases, the difference in mean-field interactions pushes the thermal cloud further out to the wings of the condensate.

$\xi \ll 1$ to the Thomas Fermi regime $\xi \gg 1$, where the profile of the thermal cloud on the 'wings' of the condensate becomes pronounced due to the additional repulsion by a factor of $n_c g_0$ in the mean-field energy. These equilibrium profiles are the result of a self-consistent numerical calculation for the ground state of the thermal and condensate clouds using the algorithm described in Appendix A and Ref. [139].

4.2.0.1 The ZNG Equations

At temperatures approaching T_c where the noncondensed portion of the cloud is significantly populated, it becomes increasingly important to include interactions between excitations. Under the Hartree-Fock approximation, the excitations are particle-like and a kinetic theory can be formulated to describe their dynamics in terms of a quasi-probability distribution function, the **Wigner**

distribution, which plays a role analogous to the phase space distribution $f(\mathbf{r}, \mathbf{p}, t)$ from Sec. 3.1, and therefore I use identical notation. Importantly, the Wigner distribution can be derived from an expectation value of the field operators ψ, $\psi^\dagger$

$$f(\mathbf{r}, \mathbf{p}, t) \equiv \left\langle \int d^3r' \; e^{i\mathbf{p}\cdot\mathbf{r}'} \psi^\dagger(\mathbf{r} + \mathbf{r}'/2, t)\psi(\mathbf{r} - \mathbf{r}'/2, t) \right\rangle, \tag{4.23}$$

where $\mathbf{r}$ and $\mathbf{r}'$ are the center of mass and relative coordinates, respectively, and $\mathbf{p}$ is the momentum of a single excitation. Therefore, a kinetic theory for the Wigner distribution function can be derived beginning from the many-body Hamiltonian. Technically, the Wigner distribution function can take on negative values. However, if we are concerned only with it's coarse-grained evaluation on the cells of μ-space, which effectively averages over quantum fluctuations on the order of the uncertainty principle, the resultant distribution function is positive definite and fits within our semi-classical picture [96].

From the Heisenberg equation of motion, it is possible to derive the equation of motion for the Wigner distribution function, which is a **quantum Boltzmann equation** (QBE) given by [96, 112, 139]

$$\left[\frac{\partial}{\partial t} + \frac{\mathbf{p}}{m} \cdot \nabla_{\mathbf{r}} + \mathbf{F} \cdot \nabla_{\mathbf{p}} \right] f(\mathbf{r}, \mathbf{p}, t) = \left. \frac{\partial f}{\partial t} \right|_{coll}, \tag{4.24}$$

where $\mathbf{F} = -\nabla_{\mathbf{r}} \left[2g_0 n(\mathbf{r} + V_{ext}(\mathbf{r}) \right]$ is the local force due to the potential energy of an individual excitation in the Hartree-Fock approximation (Eq. 4.22.) In this chapter, I follow the approach due to Zaremba, Nikuni, and Griffin (**ZNG**) [139] where the collisional contribution on the right hand side of this equation is the sum of two terms

$$\left. \frac{\partial f}{\partial t} \right|_{coll} = C_{12}[f, \Psi] + C_{22}[f], \tag{4.25}$$

where C_{22} is the Bose-enhanced collision integral in the Boltzmann equation, Eq. 3.11, and C_{12} is a new contribution which involves both the condensate wave function and the Wigner distribution function.

The graphical interpretation of these two terms is shown in Fig. 4.3. The C_{22} term represents the effect of binary collisions within the thermal cloud, which serve to bring the excitations into

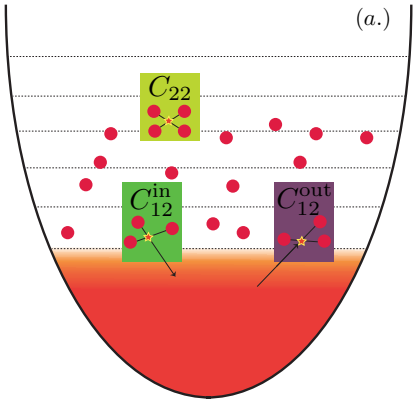

Figure 4.3: A schematic of the collision processes contained in the ZNG equations.

a state of statistical equilibrium. This is precisely the Bose-enhanced version of the collisional integral discussed in Sec. 3.1.1 and has the form

$$\begin{aligned} C_{22}[f] &= \frac{\hat{\sigma}}{\pi h^3 m^2}\int d\mathbf{p}_2 d\mathbf{p}_3 d\mathbf{p}_4 \delta\left(\mathbf{p}+\mathbf{p}_2-\mathbf{p}_3-\mathbf{p}_4\right)\delta\left(\tilde{E}+\tilde{E}_2-\tilde{E}_3-\tilde{E}_4\right) \\ &\times \left[(1+f)(1+f_2)f_3 f_4 - f f_2(1+f_3)(1+f_4)\right]. \end{aligned} \tag{4.26}$$

The C_{12} term represents the scattering of excitations into and out of the condensate, leads to growth or decay of the condensate, and acts to bring both clouds into diffusive[2] and global equilibrium

$$\begin{aligned} C_{12}[f,\Psi] &= \frac{\hat{\sigma}\,|\Psi|^2}{\pi m^2}\int d\mathbf{p}_2 d\mathbf{p}_3 d\mathbf{p}_4 \delta\left(m\mathbf{v}_c+\mathbf{p}_2-\mathbf{p}_3-\mathbf{p}_4\right) \\ &\times \delta\left(\tilde{E}_c+\tilde{E}_2-\tilde{E}_3-\tilde{E}_4\right)\left[\delta\left(\mathbf{p}-\mathbf{p}_2\right)-\delta\left(\mathbf{p}-\mathbf{p}_3\right)-\delta\left(\mathbf{p}-\mathbf{p}_4\right)\right] \\ &\times \left[(1+f_2)f_3 f_4 - f_2(1+f_3)(1+f_4)\right]. \end{aligned} \tag{4.27}$$

Importantly, the condensate must already be seeded for growth and decay to occur. The ZNG approach does not describe spontaneous emission.

In Eqs. (4.27) and (4.26) the delta functions ensure conservation of energy and momentum in a collision, and f_i is shorthand for $f(\mathbf{r_i}, \mathbf{p_i}, t)$. Furthermore, Eq. (4.27) depends on the *local*

[2] Diffusive equilibrium is reached when the chemical potentials of the condensate and thermal cloud are matched. A chemical potential gradient drives a transport of the conjugate thermodynamical variable, which is atom number.

condensate velocity, energy, and chemical potential given by [139]

$$\mathbf{v}_c = \frac{1}{m}\nabla\theta(\mathbf{r},t), \tag{4.28}$$

$$\tilde{E}_c = \frac{1}{2}mv_c^2 + \mu_c, \tag{4.29}$$

$$\mu = -\frac{1}{2m}\frac{\nabla^2\sqrt{n_c}}{\sqrt{n_c}} + V + gn_c + 2g\tilde{n}, \tag{4.30}$$

where the dependence of these quantities on $\mathbf{r}$ and t has been omitted for brevity. The condensate velocity can be extracted from the GPE using the form of the condensate given in Eq. 4.7, and the energy $\tilde{E}_c$ is the Hartree-Fock energy for the zero-momentum mode (Eq. 4.21) in the Thomas-Fermi approximation. The lengthy derivation of the collision integrals C_{22} and C_{12} can be found in Refs. [134, 139] and is not reproduced in this thesis.

The C_{12} term does not conserve the total number of atoms in the thermal cloud, and so in equilibrium there must be a corresponding non-Hermitian contribution to the GPE which maintains detailed balance within the system. The zero-temperatue theory developed in Sec. 4.1 can be generalized to include the effects of the fluctuation field. Namely, from the Heisenberg equation of motion for the field operator ψ, Eq. 4.8, the expectation value for $\delta\psi \neq 0$ gives

$$i\dot{\Psi} = \left[-\frac{\nabla^2}{2m} + V_{trap} + g_0\left(n_c + 2n_{ex}\right)\right]\Psi + g_0\langle\delta\psi\delta\psi\rangle\Psi^* + g_0\langle\delta\psi^\dagger\delta\psi\delta\psi\rangle, \tag{4.31}$$

where the position and time dependence have been suppressed for clarity. Neglect of the pairing term $\langle\delta\psi\delta\psi\rangle$ is consistent with the Hartree-Fock approximation. Retention of the triplet term $\langle\delta\psi^\dagger\delta\psi\delta\psi\rangle$ adds a non-Hermitian contribution which can change the norm of Ψ. In the ZNG approach, the triplet term is expanded in powers of g_0 about it's equilibrium value and truncated at leading non vanishing order which happens to be an imaginary contribution $\langle\delta\psi^\dagger\delta\psi\delta\psi\rangle \approx -iR(\mathbf{r},t)\Psi(\mathbf{r},t)$. This contribution is typically written in a form which makes explicit the link between the C_{12} process

$$R(\mathbf{r},t) = \frac{1}{2\left|\Psi\right|^2}\int\frac{d\mathbf{p}}{(2\pi)^3}C_{12}\left[f,\Psi\right]. \tag{4.32}$$

When Eq. 4.31 is rewritten with $-iR(\mathbf{r},t)$ in place of the triplet term, the resultant equation is a

generalized Gross-Pitaevskii equation (GGPE)

$$i\frac{\partial\Psi(\mathbf{r},t)}{\partial t} = \left\{-\frac{\nabla^2}{2m} + V(\mathbf{r},t) + g[n_c(\mathbf{r},t) + 2\tilde{n}(\mathbf{r},t)] - iR(\mathbf{r},t)\right\}\Psi(\mathbf{r},t), \tag{4.33}$$

The **ZNG equations** are comprised of the two coupled equations, Eqs 4.24, 4.33, for the dynamics of the condensate and thermal cloud. The form of Eq. 4.32 makes the number conservation of the equations explicit. In Appendix A a numerical procedure for simulating these equations is outlined.

From a general standpoint, the ZNG formalism is a prescription for describing a partially condensed Bose gas by breaking the Bose field operator into a condensed part and a noncondensed part. It couples a GGPE for the condensate with a QBE for the noncondensate. It has previously been utilized to study collective oscillations at finite temperature [125, 126, 140, 127], as well as finite temperature effects on solitons [141], vortices [142, 143], and turbulence [144]. In addition, recent work by Lee and Proukakis [145] applies the ZNG method to study collective modes, condensate growth, and thermalization dynamics for both single and multicomponent condensates. It has been particularly successful in describing the temperature range $T_* < T < T_c$ which is within the range of the experiment considered in this chapter.

4.3 Collisionless Dynamics

Here, we provide an overview of the collisionless dynamics of a trapped Bose gas, beginning with a discussion of the limiting cases for collective modes in an isotropic trap. We then discuss the monopole mode of a finite temperature BEC through application of the semi-classical collisionless model from Ref. [29, 122] to a spherically symmetric trapping geometry, and show how the monopole mode response can be cast in terms of two eigenmodes of the system. This analysis provides a framework for understanding the collapse and revival behavior of the condensate oscillation observed in the experimental results.

4.3.1 Collective modes in an isotropic harmonic trap

In an isotropic harmonic trap, the collective modes of a Bose gas are well understood in two limits. In the Thomas-Fermi (TF) limit at zero temperature the ratio of the kinetic to interaction energy is small when the number of atoms in the BEC is large; thus, the kinetic energy can be neglected. The collective-mode frequencies of a BEC in a three-dimensional isotropic harmonic trap in this limit can be estimated using a hydrodynamic approach [121]. The mode frequencies depend on the principle quantum number n and angular quantum number l according to

$$\omega^2 = \omega_0^2 \left(l + 3n + 2nl + 2n^2 \right), \tag{4.34}$$

where ω_0 is the harmonic trap frequency and ω is the frequency of the collective mode. For the spherically symmetric monopole, or breathing mode ($n = 1, l = 0$), the mean-square radius of the condensate oscillates at $\omega = \sqrt{5}\omega_0$, and the motion is undamped. Above the BEC critical temperature, T_c, mean-field effects can be neglected and the gas can be described by a classical Boltzmann equation. In this case, the mode oscillates at $\omega = 2\omega_0$ in both the collisionless and hydrodynamic regimes [100], and the motion is undamped. In the collisionless regime individual atoms may undergo many oscillations before experiencing a collision while the hydrodynamic regime implies the gas is in local statistical equilibrium.

4.3.2 Coupled-modes analysis

To obtain insight into the behavior of the monopole mode at finite temperature in an isotropic trap we apply a model previously developed by Bijlsma and Stoof [29]. This methodology introduces a dynamical scaling ansatz, similar in spirit to the method of Sec. 3.1.3.2, for the condensate and noncondensate that successfully reproduces the limiting cases of the monopole mode behavior described in the previous section. The condensate and noncondensate are described by the QBE (Eq. 4.24) and GGPE (Eq. 4.33) from the the ZNG equations in the collisionless limit, retaining the mean-field couplings. The analysis here assumes a small amplitude perturbation of the system, and a linear response such that the effects of damping are absent.

In the following calculation, a scaling ansatz is made for the time evolution of the condensate density,

$$n_c(\mathbf{r},t) = \frac{1}{\lambda^3} n_c^0\left(\frac{\mathbf{r}}{\lambda}\right), \tag{4.35}$$

and the Wigner distribution function of the noncondensate,

$$f(\mathbf{r},\mathbf{p},t) = \frac{1}{\bar{\alpha}^6} f^0\left(\frac{\mathbf{r}}{\alpha\bar{\alpha}}, \frac{\alpha}{\bar{\alpha}}\left[\mathbf{p} - \frac{m\dot{\alpha}}{\alpha}\right]\right), \tag{4.36}$$

which are written in terms of a Gaussian density profile n_c^0 for the condensate and a saturated Bose-Einstein distribution f^0 for the noncondensate:

$$\begin{aligned} n_c^0(\mathbf{r}) &= N_c\left(\frac{m\omega_0}{\pi}\right)^{1/2} e^{-m\omega_0 r^2}, \\ f^0(\mathbf{r},\mathbf{p}) &= \tilde{N}\left(\frac{\omega_0}{k_B T\zeta(3)}\right) \\ &\times \left[e^{\left(\frac{p^2}{2m}+\frac{1}{2}m\omega_0^2 r^2\right)/k_B T} - 1\right]^{-1}. \end{aligned} \tag{4.37}$$

The number of atoms in the condensate and noncondensate are denoted by N_c and $\tilde{N}$, respectively, and $\zeta(s)$ is the Riemann zeta function. The scaling parameters, $\lambda(t)$ and $\alpha(t)$, capture the oscillation of the widths of the two components, and the bar denotes the equilibrium value. Inserting the scaling ansatz into the GPE and QBE results in a set of coupled equations of motion for the condensate and noncondensate characteristic widths:

$$\ddot{\mathbf{u}} + \omega_0^2 \mathbf{u} = \mathbf{v}(\mathbf{u}), \tag{4.38}$$

where the vector $\mathbf{u}$ contains the scaling parameters

$$\mathbf{u} = \begin{pmatrix} \lambda \\ \\ \alpha \end{pmatrix}, \tag{4.39}$$

and $\mathbf{v}(\mathbf{u})$ is a nonlinear vector function describing the spreading of the cloud due to kinetic energy and the effects of nonlinear interactions (see Ref. [29] for details).

In the limit of a small amplitude oscillation, the total density of the system can be written as

$$n(\mathbf{r},t) = \bar{n}(\mathbf{r}) + \delta n(\mathrm{r}) e^{i\omega t}, \tag{4.40}$$

where the perturbation is generated by modulating the trap frequency with amplitude ϵ:

$$\omega_0(t) = \left(1 + \epsilon e^{i\omega t}\right) \omega_0. \tag{4.41}$$

In this limit Eq. (4.38) can be linearized:

$$-\omega^2 \delta\mathbf{u} + \omega_0^2 \delta\mathbf{u} = \left[\nabla_{\mathbf{u}} \mathbf{v}\right]\big|_{\bar{\mathbf{u}}} \cdot \delta\mathbf{u} - 2\epsilon\omega_0^2 \bar{\mathbf{u}}, \tag{4.42}$$

and the eigenfrequencies ω_n and eigenmodes $\mathbf{u}^{(n)}$ of the homogeneous part of Eq. (4.42) can be extracted with a solution of the form

$$\delta\mathbf{u} = 2\epsilon\omega_0^2 \sum_n \frac{\mathbf{u}^{(n)} \cdot \bar{\mathbf{u}}}{\omega^2 - \omega_n^2} \mathbf{u}^{(n)}. \tag{4.43}$$

From this solution, we find two eigenmodes that we refer to as the in-phase and out-of-phase modes of the system. The in-phase mode corresponds to the condensate and noncondensate monopole modes oscillating together (no phase difference $\phi = 0$), and the out-of-phase mode corresponds to the condensate and noncondensate monopole modes oscillating opposed (phase difference $\phi = \pi$). In Fig. 4.4 the frequencies of the in-phase and out-of-phase modes as a function of temperature are shown.

Given the eigenmodes of the system, the time-averaged work done by a perturbation of the trap frequency can be used to characterize the response of the system:

$$W = \sum_n \frac{b_n}{\omega^2 - \omega_n^2}, \tag{4.44}$$

where the b_n are a measure of the magnitude that each eigenmode responds with when the system is perturbed. Figure 4.5 shows the b_n as a function of temperature for the two modes discussed above. For temperatures $T > 0.2\ T_c$ both modes of the system will be excited by a perturbation of the trap frequency.

The coupled-modes analysis suggests that the oscillation of a single component of the gas (e.g., condensate) is described by a superposition of two eigenmodes oscillating at slightly different frequencies. Therefore, we expect measurements of the condensate width as a function of time for temperatures $T > 0.2\ T_c$ to beat at a frequency corresponding to the frequency difference between

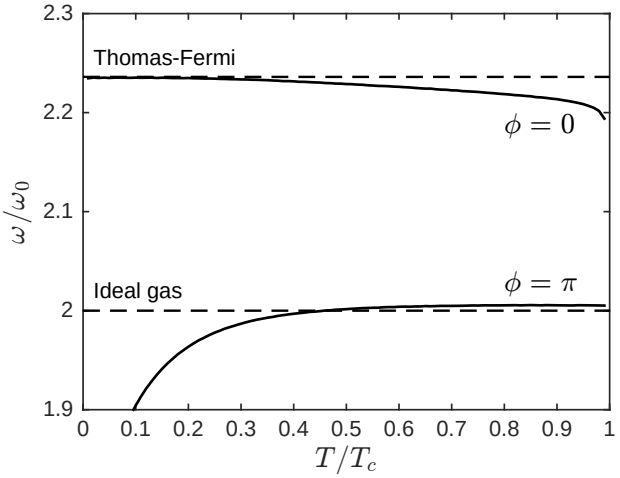

Figure 4.4: Oscillation frequency of the in-phase ($\phi = 0$) and out-of-phase ($\phi = \pi$) modes as a function of temperature from the coupled-modes analysis (solid lines). The dashed lines represent the TF limit ($\sqrt{5}\omega_0$) and ideal gas limit ($2\omega_0$) for the monopole mode frequency of the condensate and noncondensate, respectively. Assumptions made in the coupled-modes analysis become invalid for $T \lesssim 0.2\ T_c$.

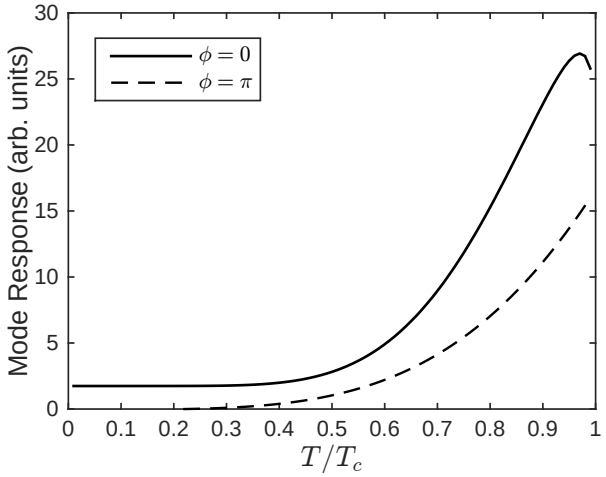

Figure 4.5: Magnitude of the response of the in-phase ($\phi = 0$) and out-of-phase ($\phi = \pi$) modes to a trap frequency perturbation as a function of temperature. The amplitude of the trap frequency modulation is $\epsilon = 0.01$.

the two eigenmodes, $\Delta\omega/\omega_0 \sim 0.2$–$0.25$ (see Fig. 4.4). Given this result, we present experimental observations of the monopole mode in an isotropic trap in the next section.

4.4 Experiment

The experimental system is a Bose gas of ^{87}Rb atoms cooled to quantum degeneracy via forced radio-frequency evaporation in a time-averaged, orbiting potential (TOP) trap [68]. A standard TOP trap configuration results in an oblate harmonic trap with an aspect ratio of $\omega_z/\omega_r = \sqrt{8}$, where ω_z (ω_r) is the axial (radial) trapping frequency. Here, the overall harmonic confinement of the trap is reduced and the trap minimum is allowed to sag under the force of gravity. This causes the curvature of the magnetic field along the z axis to decrease, which effectively decreases the ratio ω_z/ω_r. The end result is an isotropic harmonic trap with $\omega_0 \equiv \omega_r = \omega_z = 2\pi \times (9.03(2)$ Hz) with a residual asphericity of less than 0.2%. This system was used in previous work to study the monopole mode of a Bose gas above the BEC critical temperature [24], and a detailed description of the apparatus can be found in Ref. [63].

The monopole mode was excited below the BEC critical temperature in the range of approximately 0.75–0.9 T_c. The experimental procedure parallels that of Ref. [24]—beginning from a system at equilibrium, the trap frequency is sinusoidally modulated at a driving frequency $\omega_D \approx 2\pi \times 18$–19 Hz for four periods with an amplitude $\epsilon \approx 0.1$:

$$\omega(t) = [1 + \epsilon \sin(\omega_D t)]\, \omega_0. \tag{4.45}$$

After driving, we find that the peak TF radius of the condensate is 10–15% larger than the equilibrium value for all of the experimental data sets. The system is then allowed to freely evolve in the static isotropic trap for a time t before six nondestructive phase-contrast images record the integrated column density of the cloud at intervals of 10 ms or 17 ms, sampling between 1 and 1.5 oscillation periods of the monopole mode. This experimental procedure is repeated between 2–4 times for each t, and for times up to $t \approx 1.5$ s.

Each phase-contrast image is analyzed using a 2D bimodal fit to the atomic column density.

The fitting function is the sum of a Gaussian and integrated TF function [146]:

$$\begin{aligned} n_{\rm col}(x,z) &= A_G \exp\left[-\left(\frac{x-x_c}{\sigma_{G,x}}\right)^2 - \left(\frac{z-z_c}{\sigma_{G,z}}\right)^2\right] \\ &+ A_{TF}\left[1-\left(\frac{x-x_c}{\sigma_{TF,x}}\right)^2 - \left(\frac{z-z_c}{\sigma_{TF,z}}\right)^2\right]^{3/2} \\ &+ C_{\rm col}, \end{aligned} \tag{4.46}$$

where A_G and A_{TF} are the amplitudes of the Gaussian and TF functions, respectively, x_c and z_c are the center points of the cloud, $\sigma_{G,i}$ are the Gaussian widths, $\sigma_{TF,i}$ are the TF widths, and $C_{\rm col}$ is a constant offset. Note that the TF function is defined to be zero if the argument in brackets is negative.

The dynamics of the condensate monopole mode are captured by the spherically symmetric quantity

$$\sigma_M^2 = \left(\sigma_{TF,x}^2 + \sigma_{TF,y}^2 + \sigma_{TF,z}^2\right)/3. \tag{4.47}$$

During the data runs for this experiment, images were consistently taken in the xz plane. In earlier measurements described in Ref. [24], data were also taken along the xy plane, but technical difficulties were encountered with the imaging system along this axis during the course of the experiments discussed here. However, the limited data available from the xy plane suggests that the cloud was highly symmetric [63]. Therefore, we set $\sigma_{TF,y} = \sigma_{TF,z}$ in Eq. (4.47) when calculating the amplitude of the condensate monopole mode. Although we observe excitation of other collective modes (dipole and quadrupole), we find that the key features of the experimental results for the monopole mode are independent of whether this assumption is made or $\sigma_{TF,y}$ is simply excluded from Eq. (4.47).

We determine the instantaneous amplitude of the condensate monopole mode by fitting a fixed frequency sine wave to each set of six consecutive time points. The fitting function is of the form

$$g_\sigma(t) = A_\sigma \cos(2\pi\nu t) + B_\sigma \sin(2\pi\nu t) + C_\sigma, \tag{4.48}$$

where $\nu = 19$ Hz, and A_σ, B_σ, and C_σ are fit parameters. This functional form is chosen because we

are concerned with the amplitude of the mode, not the frequency, which enables a straightforward linear regression analysis for computing A_σ, B_σ, and C_σ. Finally, we present the data in the form of a fractional amplitude given by

$$A_M = \frac{A_\sigma^2 + B_\sigma^2}{C_\sigma^2}, \tag{4.49}$$

where A_σ, B_σ, and C_σ correspond to the fit parameters of Eq. (4.48). The results of this analysis are shown in Fig. 4.6, where time $t = 0$ is defined as the point at which the modulation of the trap frequency ceases.

A central feature of the data is that the amplitude of the condensate monopole mode does not decay exponentially. Across the five data sets, there is a consistent collapse in the amplitude of the monopole mode between $t = 0.3$–0.5 s, and a partial revival around $t = 0.7$–0.9 s. Motivated by the results of the coupled-modes analysis, we fit the data to an envelope function that represents the superposition of two sinusoidal modes, and we include an overall exponential damping factor to represent the loss of amplitude with time:

$$g_{\rm e}(t) = A_{\rm e} \cos\left(\frac{\Delta\omega}{2}t\right)^2 e^{-\Gamma_{\rm e}t}, \tag{4.50}$$

where $A_{\rm e}$ is the initial amplitude, $\Delta\omega$ is the beat frequency, and $\Gamma_{\rm e}$ is the damping rate of the envelope. The results of this fit are overlaid with the data in Fig. 4.6. From the fit, we find $\Delta\omega/\omega_0 \sim 0.13$ on average, and damping rates in the range $\Gamma_{\rm e} \sim 1.5$–3.5 s^{-1}. The observed beat frequency is less than $\Delta\omega/\omega_0 \sim 0.2$ as expected from the coupled-modes analysis. We attribute this disagreement to the naive form of the fitting function, which assumes that the two sinusoidal modes damp at the same rate, respond equally to the trap frequency perturbation, and have no phase difference between them. These assumptions are investigated further in the next section where the two sinusoidal modes are identified with the in-phase and out-of-phase modes predicted by the coupled-modes analysis.

Before moving on, it is important to note that in Ref. [60] it was shown that anharmonic corrections to the trap geometry were likely responsible for the anomalous exponential damping of the monopole mode observed above the critical temperature [24]. As shown in Ref. [24], this

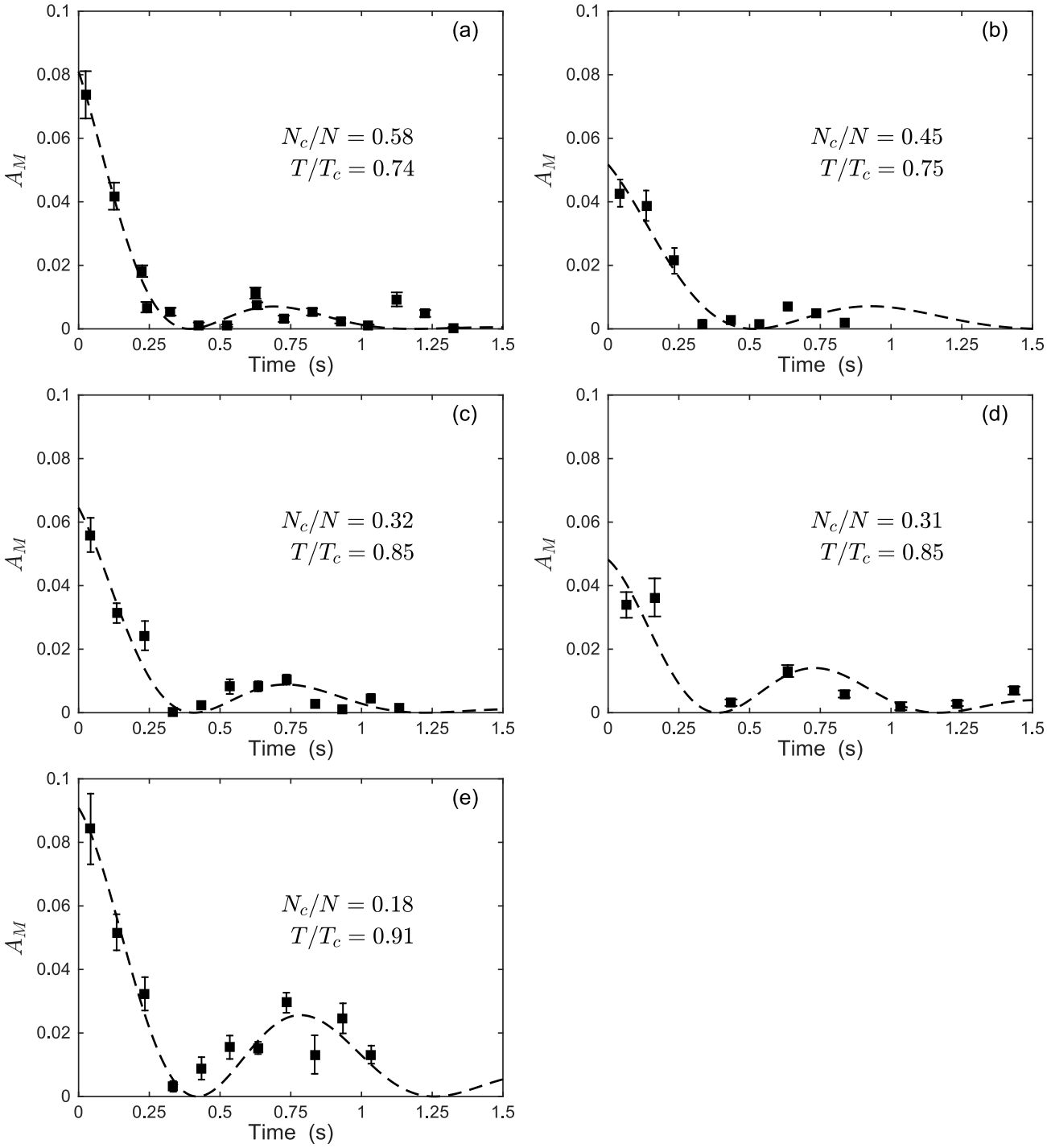

Figure 4.6: Amplitude of the monopole mode oscillation (squares) for atom numbers of (a) $N = 8.9 \times 10^5$, (b) $N = 9.7 \times 10^5$, (c) $N = 6.7 \times 10^5$, (d) $N = 5.4 \times 10^5$, and (e) $N = 7.9 \times 10^5$. Each frame is labeled with the condensate fraction (N_c/N) and temperature (T/T_c). Error bars represent the statistical uncertainty of multiple realizations of the experiment at each time point. The dashed lines are a fit of the data to Eq. (4.50), which represents the envelope function for the superposition of two sinusoids. From the fit it is found that the beat frequency is $\Delta\omega/\omega_0 \sim 0.13$ on average and the damping rate lies in the range $\Gamma_e \sim 1.5$–3.5 s^{-1}.

damping is < 0.2 s^{-1} for clouds with a full width at half maximum (FWHM) of < 125 μm. In this work, the FWHM of the cloud below the critical temperature satisfies this criterion; thus, we neglect anharmonic corrections to the trap geometry as the observed damping rate is approximately an order of magnitude larger.

4.5 Collisional dynamics

We now investigate the damping observed in the experimental data through numerical simulations within the semi-classical ZNG formalism. The coupled-modes analysis ignores collisions and exchange of particles between the two components, as well as nonlinear mean-field effects. However, below the critical temperature, these interactions between the condensate and noncondensate can shift the frequencies of collective modes and cause damping.

In Sec. 3.1.3.1, the time $\tau_{\rm coll}$ was given which was the characteristic relaxation time due to binary collisions between atoms in the cloud. There are now two collision rates, τ_{22} and τ_{12}. The former timescale is the Bose-enhanced relaxation time for the thermal cloud, and the latter is the relaxation rate of the condensate and thermal cloud to a state of diffusive equilibrium. These rates typically peak on the wings of the thermal cloud where the overlap between the components is at its greatest (see Appendix A for a discussion of equilibrium collision rates.)

There are also additional processes which arise through the mean-field couplings: Landau damping (see Refs. [147, 148, 149, 150, 151, 152, 153, 154] for further discussion) and Beliaev damping [155]. Landau damping describes a process where a collective mode decays due to its interaction with a thermal excitation, and it is expected to dominate at higher temperatures approaching the critical temperature. In the semi-classical picture, this is manifested through a thermal excitation catching the wave of the collective mode, much as surfer would, taking energy from the wave in the process. On the other hand, Beliaev damping is a process where a collective mode decays into two lower energy excitations, which is suppressed for the lowest energy collective modes of a trapped gas due to the discretization of energy levels. Thus, the Beliaev process is absent for the monopole mode, and is therefore excluded from our analysis in this chapter. Landau damping dominates the

decay of the monopole mode when the collisional processes are excluded. In the remainder of this section, we discuss the results of numerical simulation of the ZNG equations in the context of the coupled-modes analysis and experimental data already presented.

4.5.1 Simulation of the experiment

To model the experiment, we simulate a gas of $N = 8 \times 10^5$ ^{87}Rb atoms in a spherically symmetric harmonic trap with $\omega_0 = 2\pi \times 9$ Hz. Using the algorithm outlined in Ref. [139], we generate equilibrium initial states of the condensate and noncondensate for temperatures ranging from 0.1–0.9 T_c [3] . We then directly simulate the excitation of the monopole mode as in the experiment by sinusoidally modulating the frequency of the trapping potential at $\omega_D = 2\omega_0$ for four periods. We find that our results are essentially unchanged for drive frequencies of $(1+\sqrt{5}/2)\omega_0$ or $\sqrt{5}\omega_0$. We use trap frequency modulation amplitudes of $\epsilon = 0.02$, 0.03, or 0.04, and then allow the system to evolve freely for $t = 2$ s. We find that this range of ϵ excites the monopole mode of the condensate with an amplitude comparable to that observed in the experiment (i.e. 10–15% peak increase in the TF radius of the condensate from equilibrium). We note that these values are somewhat less than the quoted experimental value of $\epsilon \approx 0.1$, and speculate that this discrepancy is a result of multiple collective modes being excited in the experiment due to the difficulty of driving the trap perfectly spherically. This is in contrast to the simulations where only the monopole mode is excited, and therefore less energy is required to be added to the system to achieve the same level of excitation of the condensate.

We record the mean-square radius of the condensate as a function of time, along with snapshots of the individual density profiles. Although the experimental data sets have total atom numbers that range between about 6×10^5 and 1×10^6, we find simulations for 8×10^5 atoms represent the features of interest, namely the collapse and revival behavior and damping rate. In order to compare directly with the experimental data, we generate 2D column densities from the

[3] As $T \to T_c$ the numerical method for calculating the equilibrium state of the gas becomes unstable, and 0.9 T_c is an empirical upper bound.

simulation results, and determine the TF radii using the same bimodal fitting routine described in Sec. 4.4. Equation (4.47) is used to calculate the amplitude of the condensate monopole mode, and Eq. (4.48) is fit to single periods of the oscillation corresponding to a window of approximately 53 ms. The results of this analysis are overlaid with the experimental data in Fig. 4.7 for the three different values of ϵ. The timescale of the first collapse and revival observed in the simulation results show good agreement with the experiment.

4.5.2 Extraction of damping rates

The prediction of the coupled-modes analysis and results of the ZNG simulations show good agreement with the collapse and revival behavior observed in the experimental data (see Figs. 4.6 and 4.7). In addition, the damping observed in the results of the ZNG simulations agrees well with experimental observations. Therefore, due to the limited and noisy experimental data available, we use the results of the ZNG simulations instead of experimental data to get an estimate of the damping rates for the in-phase and out-of-phase eigenmodes predicted by the coupled-modes analysis.

We fit the simulated evolution of the condensate mean-square radius, $\left\langle R_c^2 \right\rangle = \int d\mathbf{r}\ r^2 n_c(\mathbf{r})$, by the sum of two sine waves with decaying amplitudes

$$\begin{aligned} g_c(t) &= A_1 \sin(2\pi\nu_1 t + \phi_1) e^{-\Gamma_1 t} \\ &\quad + A_2 \sin(2\pi\nu_2 t + \phi_2) e^{-\Gamma_2 t} + C_c, \end{aligned} \tag{4.51}$$

where A_i, ν_i, ϕ_i, and Γ_i are the amplitudes, frequencies, phases, and damping rates, respectively, of the two eigenmodes, and C_c is a constant offset. In the left column of Fig. 4.8, typical results of this fitting procedure for simulation results with a trap frequency modulation amplitude of $\epsilon = 0.03$. In the right column of Fig. 4.8, the oscillation of the total density is shown for reference. Time $t = 0$ is defined as the point at which the modulation of the trap frequency ceases. We choose to fit to the mean-square radius of the condensate as its time evolution is most sensitive to the presence of both eigenmodes across the temperature range investigated. The mean-square radius of the total

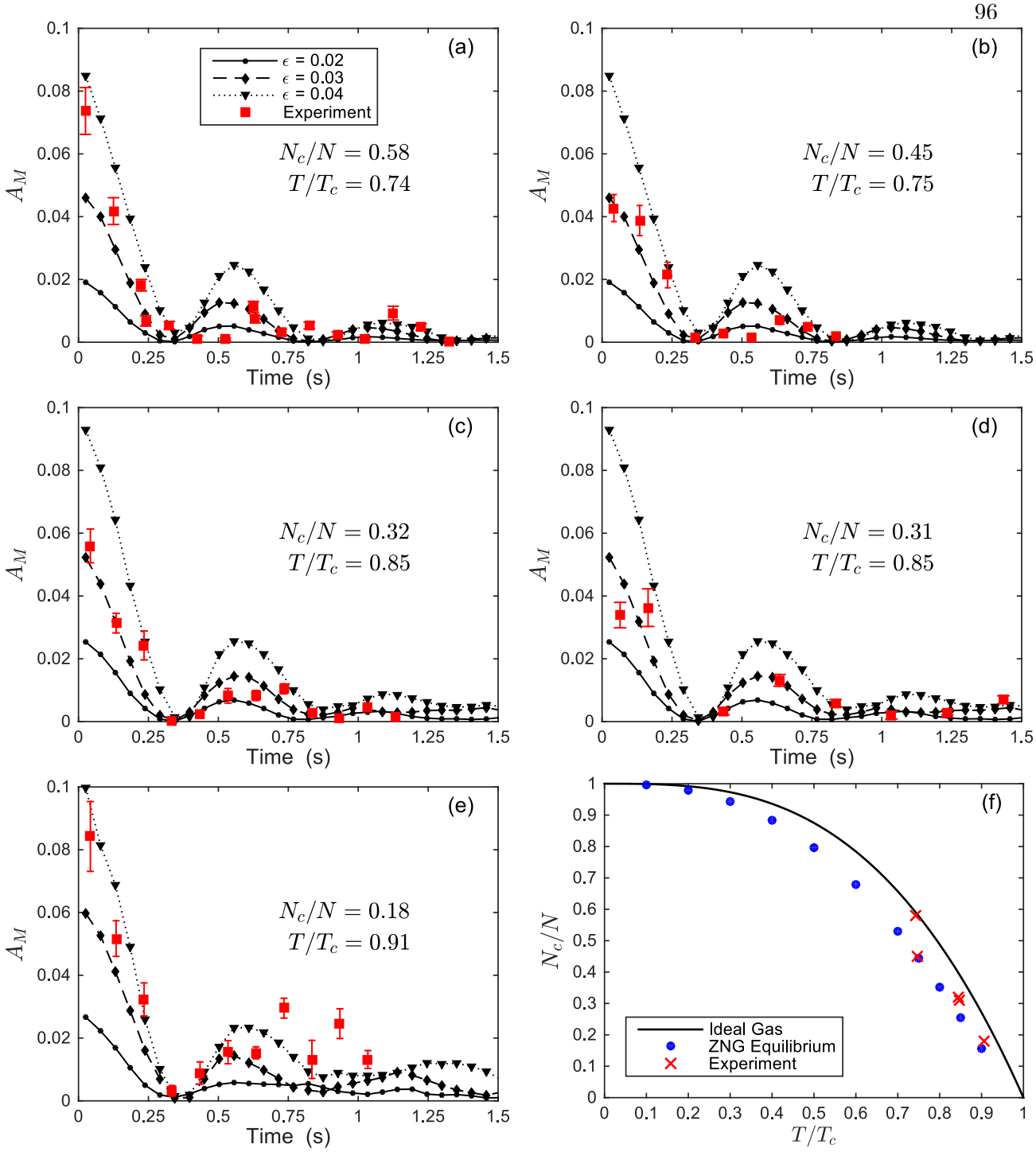

Figure 4.7: Amplitude of the monopole mode oscillation for experimental atom numbers of (a) $N = 8.9 \times 10^5$, (b) $N = 9.7 \times 10^5$, (c) $N = 6.7 \times 10^5$, (d) $N = 5.4 \times 10^5$, and (e) $N = 7.9 \times 10^5$. Each frame is labeled with the condensate fraction (N_c/N) and temperature (T/T_c), and the legend denotes the different modulation amplitudes used in the ZNG simulations. Error bars on the experimental data represent the statistical uncertainty of multiple realizations of the experiment at each time point. (f) Condensed fraction vs temperature for the ideal Bose gas, $N_c/N = 1-(T/T_c)^3$ (solid line), the equilibrium state of the ZNG simulations (blue points), and the experimental data (red crosses). All simulations are performed with $N = 8 \times 10^5$ atoms.

density becomes dominated by the noncondensate at higher temperatures, and any signature of a second eigenmode is lost. Similar behavior is observed in the evolution of the noncondensate mean-square radius.

The mode frequencies extracted from this fitting procedure show excellent agreement with the results of the coupled-modes analysis across the temperature range simulated as shown in Fig. 4.9, and add weight to the identification of the beating in the total density oscillation shown in Fig. 4.8 as arising due to the in-phase and out-of-phase modes. Simulation results at temperatures of $T = 0.1\ T_c$ and $0.2\ T_c$ are fit with a single decaying sinusoid due to the absence of a second mode. This also agrees with the prediction of the coupled-modes analysis, where only a single mode responds to a trap frequency perturbation for $T \leq 0.2\ T_c$ (see Fig. 4.5). A notable feature in Fig. 4.8 is a downward shift in the carrier frequency of $\langle R_c^2 \rangle$ with increasing temperature, an effect also observed in Ref. [112] for the monopole mode. As the temperature of the system increases the out-of-phase mode begins to get excited in conjunction with the in-phase mode, and the carrier frequency shifts to a lower, out-of-phase frequency because it represents a weighted average of the two independent mode frequencies.

It is instructive to put these results in a larger context. In the absence of driving the thermal cloud, Ref. [133] observed that the condensate breathing mode oscillation frequency is roughly constant as a function of temperature. This is due in part to both strong coupling and resultant *level repulsion* from the thermal cloud resonance at $2\omega_0$ forcing the condensate frequency upwards, which is balanced by the downward shift one obtains from the cumulative effect of coupling to all other modes in the problem. This is in contrast to the upward shift of the condensate oscillation frequency obtained from single mode fits in Refs. [21, 125, 130] for the $m = 0$ quadrupole mode above $0.7\ T_c$. The observed $m = 0$ quadrupole shift was from the zero temperature result $1.8\omega_r$, where ω_r is the radial frequency in a TOP trap, upwards towards thermal cloud resonances at $2\omega_r$. In the language of eigenmodes this was instead a shift towards the in-phase mode at $2\omega_r$ (see Ref. [29]).

The damping rate of each mode determined from the fitting procedure is shown in Fig. 4.10

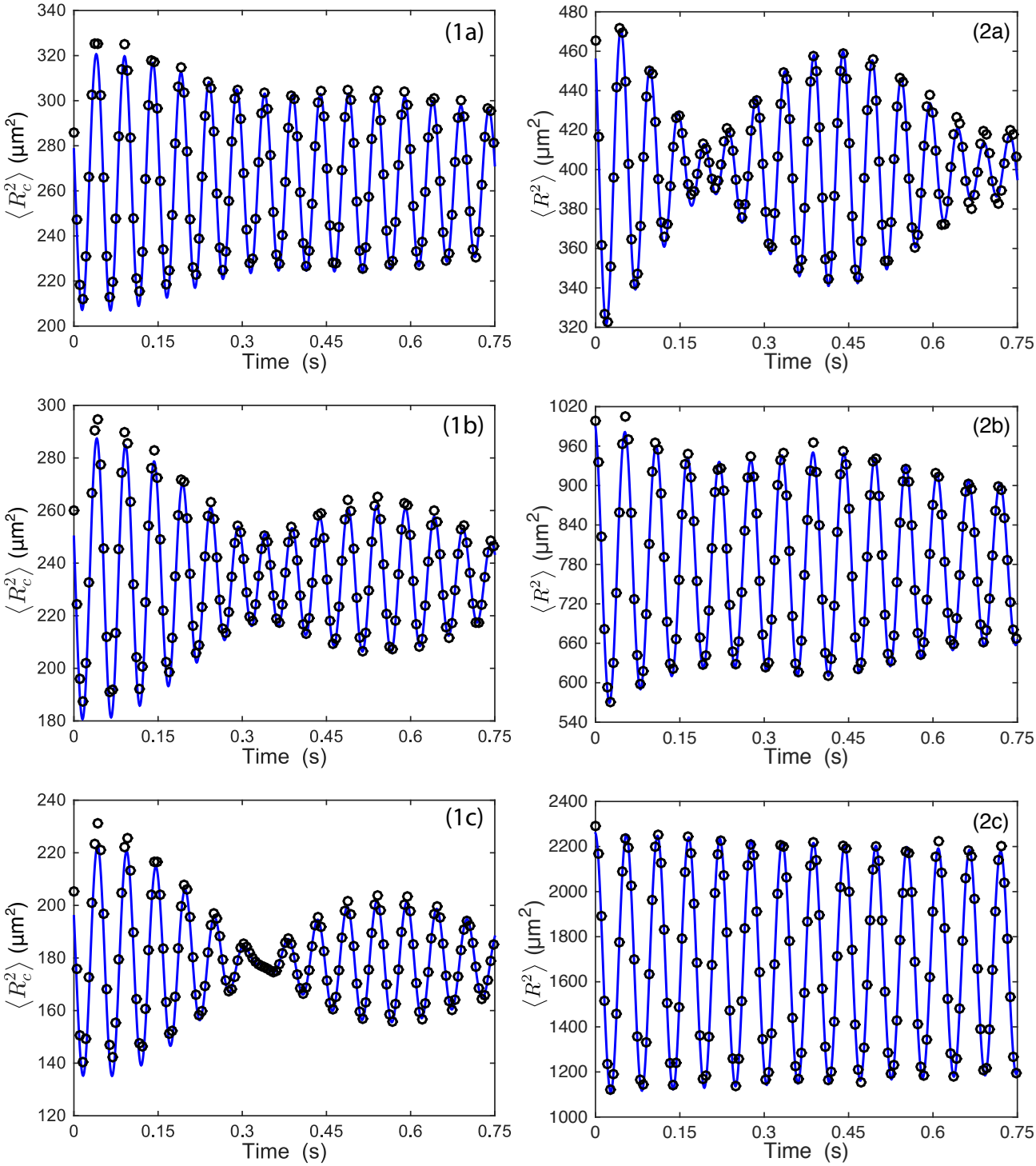

Figure 4.8: Simulated mean-square radius of the condensate (1a-1c) and total (2a-2c) densities for a trap frequency modulation amplitude of $\epsilon = 0.03$ at (a) $T = 0.4\ T_c$, (b) $0.6\ T_c$, and (c) $0.8\ T_c$ (black circles) and resulting fit of Eq. (4.51) (blue line). The density of simulated points has been reduced for clarity.

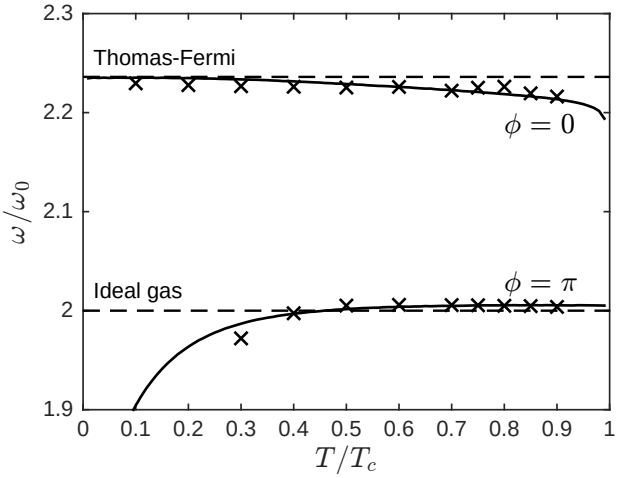

Figure 4.9: The coupled-mode results (solid line) from Fig. 4.4 overlaid with results of the ZNG simulations (crosses). Crosses are the result of fitting Eq. (4.51) to the condensate density.

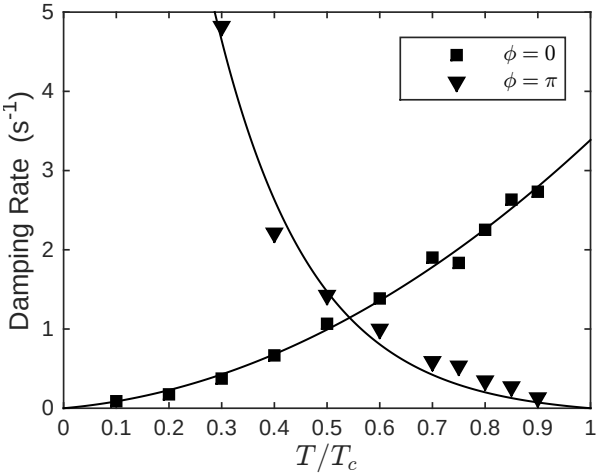

Figure 4.10: Damping rate of the in-phase (squares) and out-of-phase (triangles) mode as a result of fitting Eq. (4.51) to the simulated evolution of $\langle R_c^2 \rangle$ at each temperature for a trap frequency modulation amplitude of $\epsilon = 0.03$. The solid lines are guides to the eye. Representative fits are shown in Fig. 4.8.

as a function of temperature. In the temperature range of the experiment, there is a mismatch of the damping rates between the two eigenmodes. This mismatch, along with the beating between the two modes, captures the behavior seen experimentally of strong collapse and subsequent revival of the condensate oscillation. At lower temperatures, the in-phase mode dominates and the out-of-phase mode is strongly damped, and the inverse is true at higher temperatures. Thus, the in-phase

mode appears to be dominated by the condensate while the out-of-phase mode consists primarily of the noncondensate.

Based on the results of the coupled-modes analysis, one may suspect that the particular drive frequency used to excite the system has a large effect on the nature of the response due to the presence of two resonant excitation frequencies. However, results from ZNG simulations showed little dependence on the drive frequency, which can be attributed to the presence of damping. Damping in the system effectively broadens the resonances such that both modes are appreciably excited when the system is driven in the range $2\omega_0$ to $\sqrt{5}\omega_0$. Thus, the main characteristics of the condensate collapse-revival behavior are relatively insensitive to the particular drive frequency.

4.6 Conclusion

In conclusion, the experimentally observed non-exponential collapse and subsequent revival of the monopole mode was analyzed via a coupled-modes analysis and through simulations of the ZNG equations. The coupled-modes analysis identified two eigenmodes of the system corresponding to in-phase and out-of-phase oscillations of the condensate and noncondensate. These modes appear to be collisionless analogs to the first and second sound modes as previously discussed in Ref. [29]. Simultaneous excitation of these two modes results in the observed collapse and partial revival of the condensate monopole mode, which has a timescale compatible with the mismatch in the eigenfrequencies. Damping of the oscillations was also observed experimentally, and simulations within the ZNG formalism resulted in good agreement with the data.

These results hinge on a proper account of the dynamics of the thermal cloud including coupling with the condensed portion of the cloud. Consequently, there are many parallels between the model presented in this chapter and the two-fluid theory of liquid helium, and indeed the Landau two-fluid equations can be derived from the ZNG equations in the non-dissipative limit [139]. A discussion of sound modes in a BEC is sensible only in the hydrodynamic limit where an atom undergoes many collisions over a trap period, and only when the trap is extremely elongated and approximately uniform over a considerable length. This has been investigated experimentally in

Ref. [156], and modeled using a one-dimensional version of the ZNG equations in Ref. [157]. To my knowledge, the ZNG equations have not been simulated in the hydrodynamic regime in a trapped 3D geometry mainly due to computational limitations. It would therefore be interesting to study the transition of the in-phase and out-of-phase modes from the collisionless to the hydrodynamical regimes taking advantage of the simplifications described in Appendix A due to the spherical symmetry for an isotropic trap and sketching the transition into two-fluid behavior.

This chapter concludes the discussion of weakly-interacting Bose gases. The remaining chapters deal with regime where scattering lengths are many times the van der Waals length and presumably enhanced through a Feshbach resonance where nonperturbative effects beyond the two-atom level become important. The formalism established in this and the previous chapter however serves as a basis for their extension in Chapter 7 to include higher order correlation dynamics as would be appropriate when interactions are strong and the gas becomes highly-correlated.

Chapter 5

Efimov Physics and the Three-Body Elastic Scattering Phase Shift

This is the first chapter in a series of three revolving around the physics of strongly-interacting Bose gases. Chapters 5–6 are devoted to the nonperturbative vacuum three-body physics that arises in this regime. Chapter 7 focuses on how few-body physics beyond the level of two atoms can be systemically incorporated into the many-body problem.

Generally, for weakly-interacting Bose gases, the important role of three-body physics is to reduce the lifetime of the gas through recombination of three atoms into deeplya bound molecule and free atom, releasing enough kinetic energy to both be ejected from the trap. The rate equation that determines the time evolution of the atom loss rate scales with the density as

$$\dot{n} = -L_3 n^3, \tag{5.1}$$

where L_3 is the loss rate coefficient, which is proportional to the recombination rate $K_3 = L_3/3$ that can be extracted from transition rates in the three-body problem. The factor of 3 reflects the ejection of both the dimer and the free atom from the trap after recombination, and K_3 scales as a_0^4 for three identical ultracold bosons [158, 159][1] . For ^{87}Rb, $L_3 = 4 \times 10^{-30}$ cm^6 s^{-1}, which multiplied by typical densities of 10^{14} cm^{-3} yields a loss rate on the order of 10^{16} cm^{-3} s^{-1}, which can be significant [160], however for a pure condensate this rate is reduced by a factor of 6 [161] which was experimentally confirmed in an experiment with Bose-condensed ^{85}Rb [162]. As a Feshbach resonance is approached from the side of negative scattering length, a remarkable phenomenon occurs at roughly $|a_0| \sim 10 r_{\mathrm{vdW}}$: the formation of a ladder of three-body bound

[1] Note that Ref [158] is off by a factor of 6.

states (Efimov trimers) starts, and each formation is characterized by a resonant enhancement in the three-body recombination rate, as first observed in Ref. [34]. Exactly on resonance ($|a_0| = \infty$), an infinite number of Efimov trimers form, accumulating at zero energy from below [31, 32, 33]. Currently, there is an ongoing effort in the community to understand how these nonperturbative states impact collective behavior of the strongly-interacting Bose gas. The next three chapters therefore revolve around understanding the impact of Efimov physics on the scattering observables and the thermodynamics of the strongly-interacting Bose gas.

Before proceeding further, it is useful to solidify the terminology used in the discussion of strongly-interacting Bose gases in this thesis. In what follows, the scattering length is treated as a free parameter used to explore the range of possible phenomenon around the unitarity limit which is really a bound on the value of partial cross-sections, and it is assumed that the enhancement is due to resonance effects for instance from a Feshbach resonance. The **unitarity limit**, discussed in Sec. 2.2.3, is the limit in which the two-body partial wave cross sections are maximal, which occurs as the phase shift passes through an odd multiple of $\pi/2$ as a bound state is formed near threshold. There is also the **unitary regime**, which for ultracold gases occurs when the scattering length exceeds the inter particle spacing, ($na_0^3 \gg 1$), which also exceeds the van der Waals length and the effective range of the interaction as is the case for a broad Feshbach resonance. To describe a unitary gas considering only two-body physics, there remains only a single remaining finite length scale $n^{-1/3}$, and therefore the experimental results are considered **universal** and independent of the experimental particulars and of the atomic species. In this thesis, the criterion for a gas to be **strongly-interacting** is that the scattering length exceed the van der Waals length $a_0 \gg r_{\mathrm{vdW}}$, which is coincidentally the point at which Efimov physics becomes important. It is not appropriate to apply the solution of three-body problem in vacuum to the unitary Bose gas, and this point is discussed further in Chapter 7.

This chapter is focused on the three-body problem for identical Bosons in vacuum where each atom is restricted to a single internal level–the multi-level case relevant to spinor condensates is reserved for Chapter 6. To begin with, it is necessary to outline a convenient coordinate system for

parametrizing the motion of three atoms, which is done in Sec. 5.1. I then outline the adiabatic hyperspherical approach for three identical bosons, the three-body Schrödinger equation in this representation, and analytic solutions of the three-body problem using the Fermi pseudopotential (Eq. 2.40) and boundary conditions from Sec. 2.2.5. Solving this in the unitarity limit yields the infinite spectrum of three-body bound Efimov states studied in Sec. 5.3. The adiabatic hyperspherical representation also has the advantage that it naturally discretizes the three-body continuum, and allows a huge simplification in the ultracold limit similar to the partial wave analysis from Sec. 2.2.3. In Sec. 5.4, I discuss the three-body continuum, the emergence of Efimov physics in the scattering observables, and some of the difficulties associated with calculating the three-body elastic phase shift, which is a work in progress as of the writing of this thesis.

5.1 Parametrizing the Motion of Three Atoms

There is in general no unique parametrization of the three-body problem. In the lab frame, each atom is specified by an position vector $\mathbf{r_i}$, and therefore the problem is nine-dimensional. In this thesis, I only consider the three-body problem for pairwise interactions. The three-body Hamiltonian written in this coordinate system is therefore

$$H = \sum_{i}^{3} \frac{p_i^2}{2m} + \sum_{i<j} U(\mathbf{r_i} - \mathbf{r_j}). \tag{5.2}$$

In the COM frame, the problem is reduced to six dimensions, and can be parametrized a variety of ways. Here I begin with Jacobi coordinates which are two vectors connecting a pair of atoms and the third atom with the COM of the pair. From the Jacobi coordinates, the hyperspherical coordinates can be defined as a generalization of spherical coordinates to higher dimension.

5.1.1 Jacobi Coordinates

In the COM frame, it is possible to define two **Jacobi vectors** $\vec{\rho}_1^{(k)}, \vec{\rho}_2^{(k)}$ shown in Fig. 5.1. The superscript (k) indicates the k^{th} atom as the 'odd-man-out'. The parametrization of the system in terms of Jacobi vectors is therefore not unique as there are three possible choices for the odd-

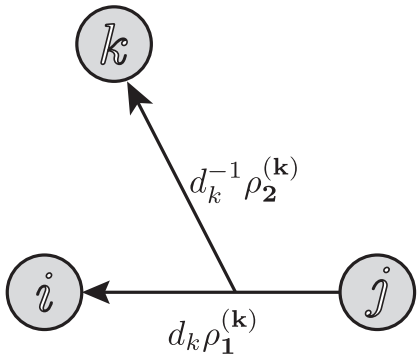

Figure 5.1: Schematic of the mass-scaled Jacobi vectors written in the odd-man-out notation.

man-out. The Jacobi vectors can each be parametrized by a magnitude and two spherical angles: $\vec{\rho}_i = (|\rho_i|, \theta_i, \phi_i)$. The Jacobi vectors are defined in terms of the lab frame coordinates as follows

$$\rho_1^{(k)} = d_k^{-1}\left(\mathbf{r}_i - \mathbf{r}_j\right), \tag{5.3}$$

$$\rho_2^{(k)} = d_k\left(\mathbf{r_k} - \frac{m_i\mathbf{r}_i + m_j\mathbf{r_j}}{m_i + m_j}\right), \tag{5.4}$$

$$d_k^2 = \frac{m_k}{\mu_{3B}}\left(1 - \frac{m_l}{M}\right), \tag{5.5}$$

$$\mu_{3B}^2 = \frac{m_1 m_2 m_3}{M}, \tag{5.6}$$

$$M = \sum_i m_i. \tag{5.7}$$

The mass-scaling factor d_k ensures that the six-dimensional volume element has the same functional form in each set:

$$dV = d^3\rho_1^{(k)} d^3\rho_2^{(k)}. \tag{5.8}$$

Each set of Jacobi coordinates is related by the so-called kinematic rotations:

$$\rho_1^{(j)} = -\rho_1^{(i)}\cos(\gamma_k) + \rho_2^{(i)}\sin(\gamma_k), \tag{5.9}$$

$$\rho_2^{(j)} = -\rho_1^{(i)}\sin(\gamma_k) - \rho_2^{(i)}\cos(\gamma_k), \tag{5.10}$$

$$\gamma_k = \epsilon_{ijk}\tan\left(\frac{m_k}{\mu_{3B}}\right)^{-1} \quad \text{(This is } \epsilon_{ijk}\pi/3 \text{ for identical masses.)} \tag{5.11}$$

The conjugate momentum are labeled $\mathbf{k_1}^{(k)}$, $\mathbf{k_2}^{(k)}$.

An advantage of the mass-scalings is that the kinetic energy operator has the same form for all permutations, which is simply the sum of the kinetic energies for the two Jacobi vectors

$$H_{rel} = -\frac{1}{2\mu_{3B}} \sum_i \nabla^2_{\rho_i} + \sum_{i<j} U(\mathbf{r_i} - \mathbf{r_j}), \tag{5.12}$$

which is the Hamiltonian for the relative motion of identical mass particles.

The Jacobi coordinates suffer from two main difficulties. First, when the system is composed of identical particles, it becomes laborious to perform many kinematic rotations. Often, the wave function is written using the **Faddeev decomposition** [163]

$$\Psi_{3B} = \sum_l \Psi^{(k)}_{3B}(\rho^{(k)}_1, \rho^{(k)}_2), \tag{5.13}$$

where each function $\Psi^{(k)}_{3B}$ is a Fadeev wave function. The flexibility of the Faddeev wave function allows description of various three-body structures in terms of few two-body angular momentum in each component. These wave functions satisfy the Faddeev equations [164]

$$(T-E)\Psi^{(1)}_{3B} + U^{(1)}\left(\Psi^{(1)}_{3B} + \Psi^{(2)}_{3B} + \Psi^{(3)}_{3B}\right) = 0, \tag{5.14}$$

$$(T-E)\Psi^{(2)}_{3B} + U^{(2)}\left(\Psi^{(1)}_{3B} + \Psi^{(2)}_{3B} + \Psi^{(3)}_{3B}\right) = 0, \tag{5.15}$$

$$(T-E)\Psi^{(3)}_{3B} + U^{(3)}\left(\Psi^{(1)}_{3B} + \Psi^{(2)}_{3B} + \Psi^{(3)}_{3B}\right) = 0, \tag{5.16}$$

where E is the total three-body energy, T is the kinetic energy operator, and $U^{(k)} = U(\mathbf{r_i} - \mathbf{r_j})$ is the pairwise interaction between particles i and j. The second difficulty that the Jacobi coordinates suffer from is a lack of a discretization of the three-body continuum: there is a continuum of energies that can be shared between the Jacobi pairs. For two bodies, this is achieved through the decomposition of the continuum into partial waves. This was first remedied by Delves [165, 166] by swapping the magnitude of the Jacobi vectors for the **hyperradius** $R^2 = \rho_1^2 + \rho_2^2$ and a **hyperrangle** $\rho_1 = R\sin\omega$, $\rho_2 = R\cos\omega$. It is also convenient to define the **hypermomentum** $K^2 = k_1^2 + k_2^2$. The Faddeev wave function can be written in Delves coordinates as $\Psi^{(k)}_{3B}(R, \omega, \theta_1, \phi_1, \theta_2, \phi_2)$, and can be decomposed into a discrete sum of spherical harmonics for the spherical angles of the Jacobi vectors and a discrete sum of hyperspherical harmonics for the hyperangle. Delves showed

that the in the hyperspherical representation of the three-body continuum the scattering S-matrix is symmetric and unitary and can be represented by a countable set of channels rather than a continuum [165, 166]. In the following section, I outline the related Smith and Witten democratic hyperspherical coordinates [167].

5.1.2 Hyperspherical Coordinates

In this section, the Smith and Witten democratic hyperspherical coordinates are presented [167, 168], which are the coordinates used in the numerical results presented later in this chapter. In the COM frame, the molecular plane of the three atoms defines a body-fixed frame whose orientation in the space-fixed COM frame is specified by the three Euler angles $(\alpha\beta\gamma)$ as is typical for describing the motion of a rigid body [169]. The orientation of the three atoms within the molecular plane is described by the hyperradius and two hyperspherical 'kinematic' angles θ and ϕ, which capture the spatial extent and relative motion of the three atoms, respectively. The problem can then be reduced entirely to the body-fixed frame where all atoms are treated on equal footing (democratically) rather than requiring kinematic rotations or the Faddeev decomposition.

Let's first make a connection with the mass-scaled Jacobi coordinates:

$$
\begin{aligned}
(\rho_1)_x &= R\cos(\theta/2-\pi/4)\sin(\phi/2+\pi/6),\\
(\rho_1)_y &= R\sin(\theta/2-\pi/4)\cos(\phi/2+\pi/6),\\
(\rho_1)_z &= 0,\\
(\rho_2)_x &= R\cos(\theta/2-\pi/4)\cos(\phi/2+\pi/6),\\
(\rho_2)_y &= R\sin(\theta/2-\pi/4)\sin(\phi/2+\pi/6),\\
(\rho_2)_z &= 0.
\end{aligned}
\tag{5.17}
$$

The domain of the hyperrangles is restricted to $\theta \in [0, \pi/2]$ and $\phi \in [0, 2\pi/3]$ to ensure that the wave-function is single valued for three indistinguishable particles. The z-axis is defined by the direction of $\rho_1 \times \rho_2$, which is perpendicular to the plane containing the three atoms. The x-axis is

the direction of the smallest moment of inertia. Under this construction, identical particle symmetry is easily imposed [168].

The wave function is rescaled $\Psi_{3B} = R^{5/2}\psi$ to simplify the kinetic energy operator in the Schrödinger equation

$$\left[-\frac{1}{2\mu_{3B}}\frac{\partial^2}{\partial R^2} + \frac{\Lambda^2}{2\mu_{3B}R^2} + U(R,\theta,\phi)\right]\psi = E\psi, \tag{5.18}$$

where $\mu_{3B} = m/\sqrt{3}$ is the three-body reduced mass for identical masses. Λ is the *grand* angular momentum operator

$$\begin{aligned}
\frac{\Lambda^2}{2\mu_{3B}R^2} &= T_\theta + T_\phi + T_r \\
T_\theta &= -\frac{2}{\mu_{3B}R^2\sin 2\theta}\frac{\partial}{\partial\theta}\sin 2\theta\frac{\partial}{\partial\theta}, \\
T_\phi &= \frac{1}{\mu_{3B}R^2\sin^2\theta}\left(i\frac{\partial}{\partial\phi} - \cos\theta\frac{J_z}{2}\right)^2, \\
T_r &= \frac{J_x^2}{\mu_{3B}R^2(1-\sin\theta)} + \frac{J_y^2}{\mu_{3B}R^2(1+\sin\theta)} + \frac{J_z^2}{2\mu R^2}.
\end{aligned} \tag{5.19}$$

The operators (J_x, J_y, J_z) are the body-frame components of the total angular momentum $\mathbf{J}$. The volume element is

$$dV = 2dR\sin 2\theta d\theta d\phi d\alpha \sin\beta d\beta d\gamma. \tag{5.20}$$

5.1.2.1 Adiabatic Hyperspherical Wave Function

A common assumption made is that the hyperradius is a *slow* variable relative to the variation of the hyperrangles $\Omega = \{\theta, \phi, \alpha, \beta, \gamma\}$ in the wave function. This leads to the formally exact expansion of the wave function $\psi(R,\Omega)$ in terms of the complete, orthonormal set of angular **channel wave functions** Φ_ν and **radial wave functions** F_ν,

$$\psi(R,\Omega) = \sum_\nu F_\nu(R)\Phi_\nu(R;\Omega). \tag{5.21}$$

The channel functions satisfy the fixed-R, hyperangular partial differential equation

$$\left[\frac{\Lambda^2 + 15/4}{2\mu_{3B}R^2} + U(R,\theta,\phi)\right]\Phi_\nu(R;\Omega) = u_\nu(R)\Phi_\nu(R;\Omega), \tag{5.22}$$

where the eigenvalue $u_\nu(R)$ depends parametrically on R and is referred to as the **adiabatic three-body potential**. Typically, the channel function is expanded on the Wigner D functions of the Euler angles, which are the basis functions for the rotation group [88], as

$$\Phi_\nu^{JM\Pi}(R;\Omega) = \sum_K \Phi_{K\nu}(R;\theta,\phi) D^J_{KM}(\alpha,\beta,\gamma). \tag{5.23}$$

The quantum numbers K and M denote the projections of $\mathbf{J}$ onto the body-fixed and space-fixed z-axes, respectively, and Π denotes the parity quantum number ($+$ or $-$). For three free particles, the solutions of Eq. 5.22 are the hyperspherical harmonics [170, 171]

$$\Lambda^2 Y_{\lambda\mu}(\Omega) = \lambda(\lambda+4) Y_{\lambda\mu}(\Omega), \tag{5.24}$$

where λ is the hyperangular momentum quantum number, and μ labels the set of degenerate states. In this thesis, only the s-wave interactions with the total symmetry state $J^\Pi = 0^+$ are considered. For free particles, $\nu = \lambda$, and the adiabatic three-body potential $u_\lambda(R)$ therefore has the form of a centrifugal potential

$$u_\lambda(R) = \frac{\lambda(\lambda+4)+15/4}{2\mu_{3B}R^2}, \tag{5.25}$$

which can be rewritten in the form of the an effective angular momentum $l_{eff}(l_{eff}+1) = \lambda(\lambda+4)+15/4$ in which case $l_{eff} = 3/2+\lambda$.

For the general interacting problem, the adiabatic three-body potential is often written in terms of the parameter $s(R)$ as

$$u_\nu(R) = \frac{s(R)^2 - 1/4}{2\mu_{3B}R^2}, \tag{5.26}$$

with the identification $\nu = s-2$. There are often other symbols used, and their meaning is made clear by comparison with the form of the hyperangular eigenvalue, either Eq. 5.25 or 5.26.

Inserting the adiabatic decomposition into the full Schrödinger equation and integrating out the hyperangular eigenfunctions yields a set of coupled ordinary differential equations, in the hyperradius R, as

$$\left[-\frac{1}{2\mu_{3B}}\frac{d^2}{dR^2} + u_\nu(R)\right] F_\nu(R) - \frac{1}{2\mu_{3B}}\sum_{\nu'}\left[2P_{\nu\nu'}(R)\frac{d}{dR} + Q_{\nu\nu'}(R)\right] F_{\nu'}(R) = EF_\nu(R). \tag{5.27}$$

The coupling elements $P_{\nu\nu'}(R)$ and $Q_{\nu\nu'}(R)$ involve partial derivatives of the channel functions as follows:

$$P_{\nu\nu'}(R) = \left\langle \Phi_\nu(R;\Omega) \left| \frac{\partial}{\partial R} \right| \Phi_{\nu'}(R;\Omega) \right\rangle$$
$$Q_{\nu\nu'}(R) = \left\langle \Phi_\nu(R;\Omega) \left| \frac{\partial^2}{\partial R^2} \right| \Phi_{\nu'}(R;\Omega) \right\rangle. \tag{5.28}$$

The P's consequently have no diagonal contribution. For a system of identical bosons with scattering length a_0, they have a particularly simple form in terms of $\varepsilon = s(R)^2$ [172, 173]:

$$P_{mn} = \frac{\sqrt{\varepsilon'_m \varepsilon'_n}}{\varepsilon_m - \varepsilon_n},$$
$$Q_{mn} - \delta_{mn}\left[-\frac{1}{4}\left(\frac{\varepsilon''_n}{\varepsilon'_n}\right)^2 + \frac{1}{6}\frac{\varepsilon'''_n}{\varepsilon'_n}\right] + (1-\delta_{mn})\left[\frac{2\varepsilon'_n\sqrt{\varepsilon'_n\varepsilon'_m}}{(\varepsilon_m-\varepsilon_n)^2} - \frac{\varepsilon''_n}{(\varepsilon_m-\varepsilon_n)}\sqrt{\frac{\varepsilon'_m}{\varepsilon'_n}}\right]. \tag{5.29}$$

In the **adiabatic limit**, the system is completely uncoupled as a function of the hyperradius and the off-diagonal P's and Q's are set to zero. This is the starting point for the analysis of the following section, which deals with analytic solutions to the hyperspherical Hamiltonian for zero-range, pairwise pseudopotential interactions. For the remainder of this and the following chapter, I consider only equal mass atoms.

5.2 Analytic Solution of the Three-Body Problem in the Zero-Range Model

In general, analytic solutions of the three-body problem are scarce, however, in the zero-range model discussed in Sec. 2.2.5, the problem can be solved with the Fermi pseudopotential by enforcing the Bethe-Peierls boundary condition at the origin. For two bodies, this boundary condition needs to be only applied once in the limit of zero separation, however, for three bodies, the boundary condition must be applied three times–once for each pairwise interaction.

$$\lim_{\rho_1^{(k)}\to 0} \Phi_\nu(R;\Omega) = \left(1 - \frac{a_0}{d_k \rho_1^{(k)}}\right) C_\nu^{(k)}, \tag{5.30}$$

where $C_\nu^{(k)}$ is a constant determined by the Bethe-Peierls boundary condition and the overall normalization of the hyperangular channel function, $|\langle\Phi_\nu|\Phi_\nu\rangle|^2 = 1$. The hyperrangular differential

equation, Eq. 5.22, can be rewritten as a Lippman-Schwinger equation and the channel function solution can be phrased implicitly through integral equation

$$\Phi_\nu(R;\Omega) = -2\mu_{3B}R^2 \int d\Omega' G^\nu(\Omega,\Omega') \sum_k^3 V_{pseudo}(d_k {\rho_{\mathbf{1}}}^{(k)}) \Phi_\nu(R;\Omega') \tag{5.31}$$

where G^ν is the hyperangular Green's function given in Ref. [172]. This integral can be evaluated directly due to the delta-functions in the pairwise potentials, and the result is a matrix equation that can be solved for the vector of coefficients $\mathbf{C}_\nu = (C_\nu^{(1)}, C_\nu^{(2)}, C_\nu^{(3)})$

$$C_\nu^{(k)} = \sum_{k'} M_\nu^{k',k} C_\nu^{(k')}, \tag{5.32}$$

where the matrix M is given by [172]

$$M_{k',k} = \begin{cases} \frac{3^{1/4}}{\sqrt{2}} \frac{a_0}{R} s \cot(s\pi/2) & k = k', \\ -\frac{2\sqrt{2}}{3^{1/4}} \frac{a_0}{R} \frac{\sin(s\pi/6)}{\sin(s\pi/2)}. & k \neq k'. \end{cases} \tag{5.33}$$

We would expect an infinite number of solutions $s(R)$ at each hyperradius, which may be obtained by solving for the roots of the **transcendental equation** $\det(M_\nu - 1) = 0$. Insertion of these roots into Eq. 5.32 yields the the solution for $\mathbf{C}_\nu$, from which the channel functions can be constructed. Often however, only the $s(R)$ are of immediate interest as they allow the adiabatic three-body potentials to be constructed from which the bound state spectrum can be studied.

When considering three identical bosons ($C_\nu^{(1)} = C_\nu^{(2)} = C_\nu^{(3)} = C_\nu$), the M matrix has only a single element. The transcendental equation generated in this case is

$$\frac{R}{a_0} = \frac{3^{1/4}}{\sqrt{2}} \frac{s\cos(s\pi/2) - (8/\sqrt{3})\sin(s\pi/6)}{\sin(s\pi/2)}, \tag{5.34}$$

which is the transcendental equation for real roots. Making the substitution $s(R) \to is(R)$ gives the transcendental equation for imaginary values

$$\frac{R}{a_0} = \frac{3^{1/4}}{\sqrt{2}} \frac{s\cosh(s\pi/2) - (8/\sqrt{3})\sinh(s\pi/6)}{\sinh(s\pi/2)}. \tag{5.35}$$

In the following section, the solutions, $s(R)$, of these equations are discussed as a function of the hyperradius, highlighting the important physics.

5.3 The Spectrum of Three-Body Bound States

The roots s of the transcendental equations for fixed R can be labeled beginning with any imaginary roots in the zeroth place and then counting the real roots of increasing value $\{is_0, s_1, ...\}$. As R is increased, the transcendental equations must be iteratively solved. This generates an array $s_i(R)$ from which an array for the three-body adiabatic three-body potential $u_{\nu_i}(R)$ given by Eq. 5.26 can be constructed. The set $\{u_{\nu_0}(R), u_{\nu_1}(R)...\}$ comprises the network of hyperradial potential curves extending from the region of validity of the zero-range interaction $R \gg r_0$ to beyond the asymptotic region $R \gg a_0$. It is convenient to refine this further into regimes which contain universal and non-universal physics for which the 'range' $r_{\rm vdW}$ is the appropriate demarcator [174]:

- **Non-universal Region:** ($R \lesssim |r_{\rm vdW}|$) sensitive to the details of the interatomic interaction beyond the scattering length.
- **Universal Region:** ($|r_{\rm vdW}| \gg R$) depends only on the scattering length.

In this section, I discuss only the adiabatic three-body potentials in the non-universal and universal regions in the resonant limit $R/|a_0| \to 0$, and obtain the bound state spectrum. Away from resonance, when the scattering length is finite, it is useful to distinguish additional regions in the universal region [174]:

(1) **Scale-Invariant Region:** ($|r_{\rm vdW}| \gg R \gg |a_0|$).

(2) **Transition Region:** ($R \sim |a_0|$).

(3) **Asymptotic Region:** ($|a_0| \gg R$).

I make this distinction in the following section (Sec. 5.4), which is focused on the three-body continuum.

Non-Universal Region: Although the zero-range model does not extend into the non-universal region, the effects of propagation through this region can be summarized by the logarithmic derivative Γ that arises from matching the wave function at the boundary ($R \sim R_0$) of the

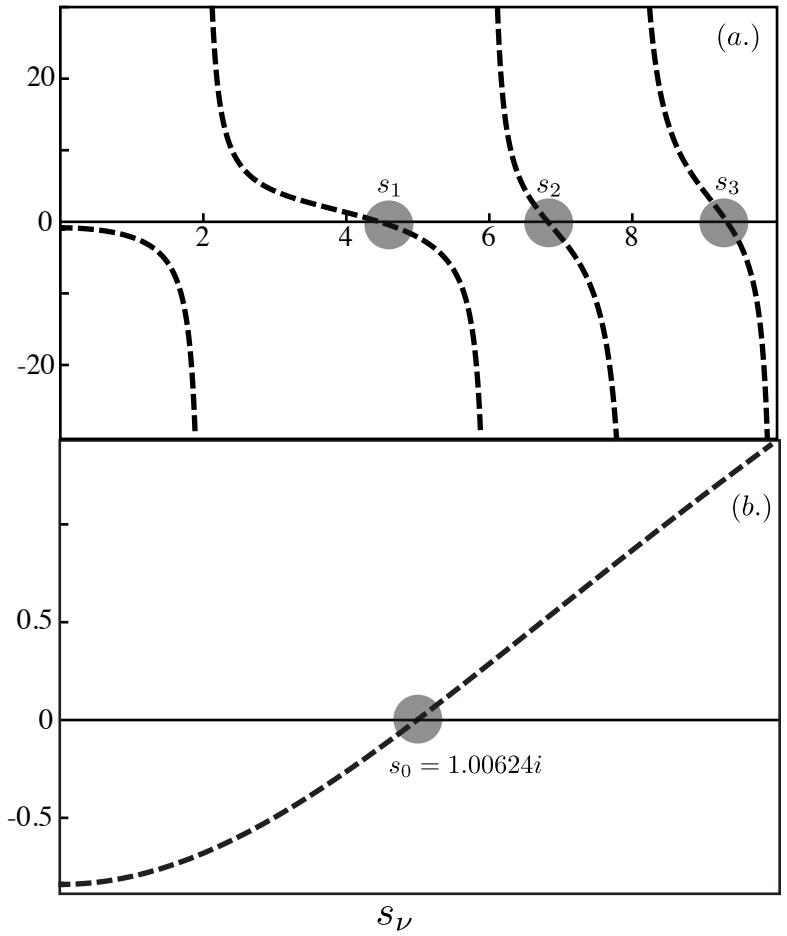

Figure 5.2: A plot of the transcendental equations (Eqs. 5.34–5.35) as a function of real (a.) and imaginary (b.) s in the resonant limit $R/|a_0| \to 0$. The s_i are the roots labeled in increasing order, where s_0 is the root associated with the Efimov potential Eq. 5.37.

universal and non-universal regions

$$\left.\frac{\Phi'_\nu(R;\Omega)}{\Phi_\nu(R;\Omega)}\right|_{R=R_0^-} = \Lambda, \tag{5.36}$$

where the prime indicates a derivative w.r.t. the hyperradius and the subscript '-' indicates that this is the logarithmic derivative of the unknown wave function for the non-universal region. As we will see shortly, Λ plays an important role in setting the spectrum of three-body bound states and also appear in the scattering observables.

Universal Region: When the hyperradius is less than the scattering length, each of the three atoms are within the two-body scattering cross section of the others, and the physics is

truly three-body. It is perhaps no surprise then that this region hosts nonperturbative physics. In Fig. 5.2, the transcendental equations are plotted over imaginary and real values of s in the resonant limit $R/a_0 \to 0$. There is a single imaginary root $is_0 \approx 1.00624i$ independent of R in this limiting case, which when inserted into the adiabatic three-body potential (Eq. 5.26) produces an *attractive* potential

$$u_{\nu_0}(R) = \frac{-s_0^2 - 1/4}{2\mu_{3B}R^2}. \tag{5.37}$$

It is well known that an attractive $1/R^2$ potential supports and *infinite* number of bound states which accumulate at zero energy. It is however not physical to imagine the critical limit $R = 0$ which extends beyond the range of validity of the zero-range model. Generally, there is some cutoff distance $R_0 \sim r_{\rm vdW}$ beyond which the interaction becomes strongly repulsive, which can be seen for instance by performing calculations with a Lennard-Jones potential or other models of finite range. The three-body bound states that form are referred to as **Efimov states**, and their properties were first discussed by V. Efimov (see Refs. [31, 32, 33]). There are also an infinite number of real roots $\{s_1, s_2, ...\}$, ($s_1 \approx 4.46529$) which correspond to repulsive adiabatic three-body potentials, and the first few are shown in Fig. 5.2a.

In the resonant limit, there is not an asymptotic region in the sense characterized above. The spectrum of Efimov states can be obtained by matching the non-universal wave function in the lowest channel with a Bessel function with short-range phase shift Δ [31]

$$F_{\nu_0}(R) \propto \sin(|s_0| \ln(KR) + \Delta). \tag{5.38}$$

At the boundary of the two regions, equating the log-derivatives gives

$$\Lambda = \frac{|s_0|}{R_0} \cot\left(|s_0| \log(KR) + \Delta\right), \tag{5.39}$$

and evaluating when the phase shift passes through $\pi/2$ gives the trimer spectrum at unitarity

$$E^{(N)} = -\frac{1}{2m_0 R_0^2} \exp\frac{2}{|s_0|} \arctan\left[\frac{\Lambda R_0}{|s_0|} - \Delta\right] e^{-2\pi N/|s_0|}. \tag{5.40}$$

Successive levels are separated by a geometric scaling $E^{(N)}/E^{(N+1)} = \exp(2\pi/|s_0|)$.

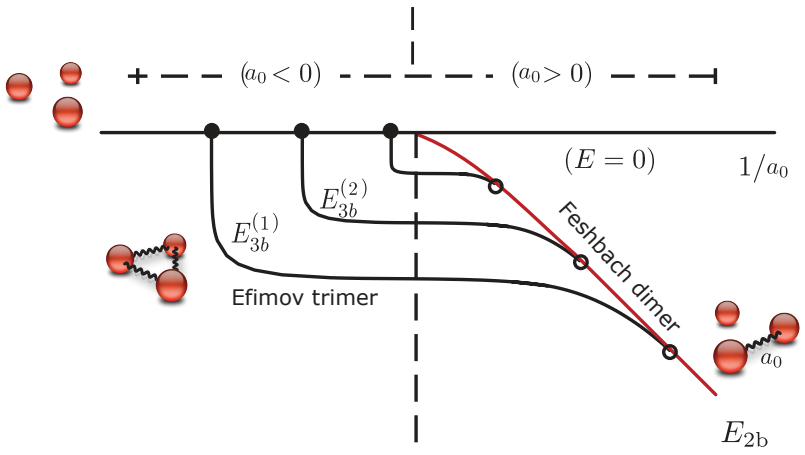

Figure 5.3: The canonical plot of the spectrum of three-body bound states (Efimov trimers) near a Feshbach resonance. At resonance, there is a condensation of an infinite number of Efimov states at threshold which is not shown.

The cumulative effect of Λ and Δ in Eq. 5.40 is to set the spectrum of Efimov states. Often this spectrum is reformulated

$$E^{(N)} = -\left[e^{-2\pi/|s_0|}\right]^N \frac{\kappa_*^2}{m}, \tag{5.41}$$

in terms of the **three-body parameter** κ_*, which is the wave number associated with the energy of the first Efimov state $E^{(0)}$ that appears as the Feshbach resonance is approached from negative scattering lengths. The scattering length a_{3B}^- at which the first Efimov state is formed is also often referred to as a three-body parameter. Recently, it was observed experimentally and confirmed theoretically that for ultracold alkali species, both κ_* and a_{3B}^- have a universal value when rescaled by the van der Waals scattering length, which seem to lie near $\kappa_* \approx 0.226/r_{\rm vdW}$ and $a_{3B}^- \approx -9.73 r_{\rm vdW}$ [175, 176, 177, 178, 179, 180, 181, 182, 183, 184, 185, 186, 187, 188, 189, 190, 191, 192, 193, 194, 195, 196, 197, 198, 199, 200]. This is due to a semiclassical suppression at short distances of the wave function as it traverses the sharp cliff created by deep two-body potentials supporting a large number of bound states.

In the next section, I move from the bound state spectrum to address the three-body continuum, focusing on the threshold behavior of the elastic three-body phase shift.

5.4 The Three-Body Continuum

The asymptotic region has a comparatively clearer meaning for the two-body problem compared to the three-body problem. Two atoms are asymptotically separated in the limit that the distance between their nuclei approaches infinity. For three atoms, there are four limits: the limit in which all three atoms are infinitely separated, and the three limits in which one of the atoms is infinitely separated from the remaining pair. This underscores a general feature which is that the two-body continuum is embedded in the three. In the resonance limit $R/a_0 \to \infty$, this does not pose a problem because each atom is within the scattering cross section of every other atom over the entire hyperradial range, and therefore the physics is truly three-body all the way out to infinity. When the scattering length is finite, from general length scale considerations, the physics of the transition region must be that of on-shell and off-shell two-body scattering events. In the hyperspherical picture, it is difficult to connect this diagrammatic view of the hyperradial regions with the adiabatic three-body potentials themselves, and this is the main obstacle against calculating observables for three-body elastic scattering, beginning at the level of the three-body elastic phase shift as we shall see in this section. First, through a WKB model in Sec. 5.4.1, we will see how Efimov physics functionally enters into the threshold behavior of the three-body elastic phase shift. The final two sections (Sec. 5.4.2–5.4.3) are concerned with connecting the diagrammatic interpretation with the adiabatic three-body potentials and separating the two-body continuum contributions to the phase shift from the three, respectively.

Let's begin by resuming our discussion of the regions began in the previous section, but now for a finite scattering length. In the **scale-invariant region** ($|r_{\mathrm{vdW}}| \gg R \gg |a_0|$), the roots behave as in the universal region in the previous section, namely they take on the resonant values. This region is invariant of the length scale set by the scattering length. As the hyperradius approaches $R \sim |a_0|$, the scattering length reenters the problem as the asymptotic region is approached.

Transition Region: Beyond the scale-invariant region, the adiabatic three-body potentials begin a changeover to their asymptotic forms. For $a_0 < 0$, the Efimov potential transitions into a

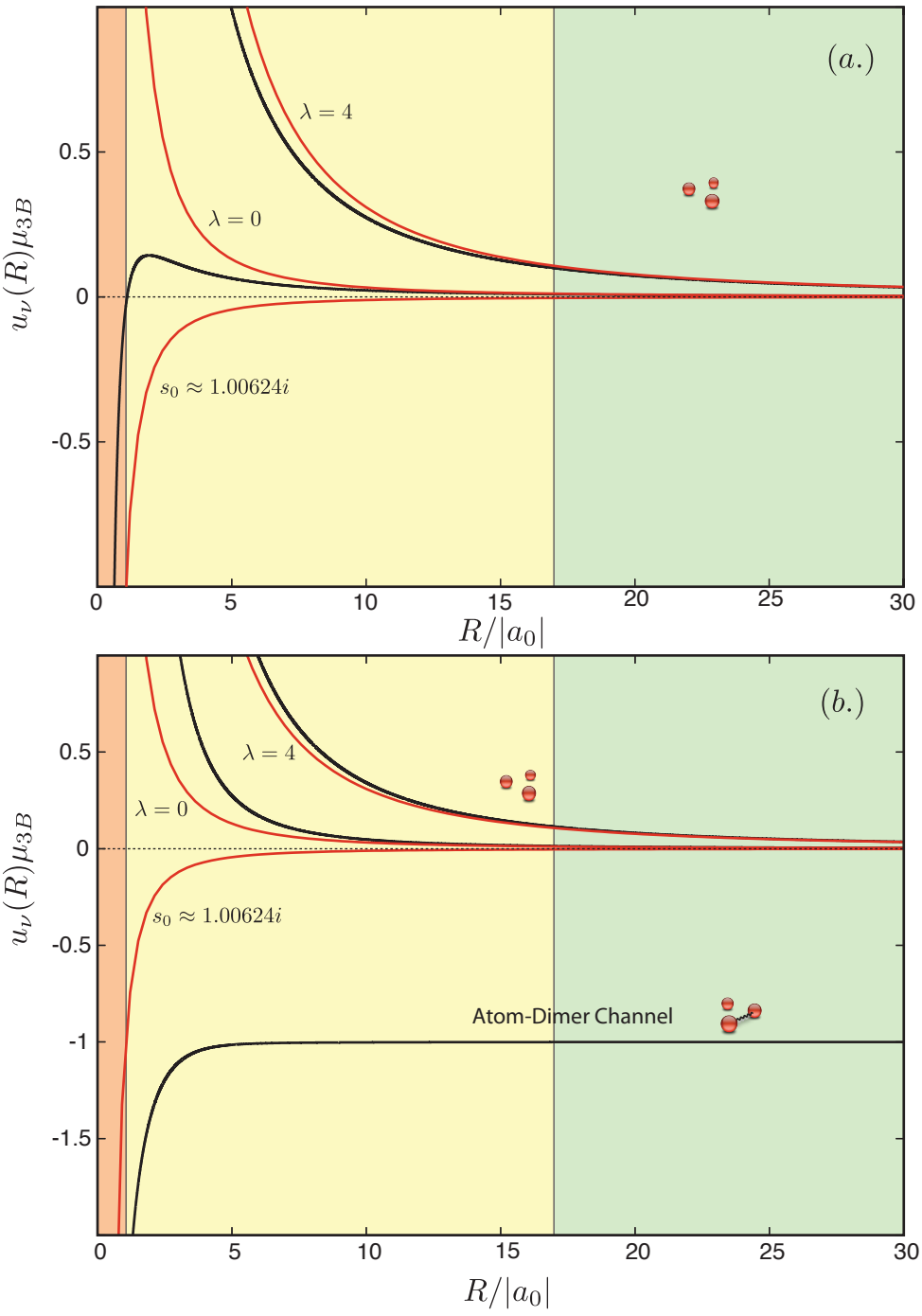

Figure 5.4: The adiabatic three-body potentials for $a_0 < 0$ (a.) and $a > 0$ (b.). The orange shaded region is the scale-invariant region, the yellow shaded region is the transition region, and the green shaded region is the asymptotic region. The black curves are a result of solving the transcendental equations (Eqs. 5.34–5.35) and the red curves are the three-body potentials corresponding to the indicated values.

repulsive centrifugal barrier, characterized by a hump whose height depends on a_0, which appears near the boundary between the transition and scale-invariant regions as shown in Fig. 5.4a. For incoming energies below this barrier, the wave function must tunnel to reach the universal region and the well of the Efimov potential. Scattering in this channel should therefore display a shape resonance when each new Efimov trimer is formed. The higher adiabatic three-body potentials corresponding to real roots transition from repulsive universal potentials to repulsive centrifugal barriers. For $a_0 > 0$, the Efimov potential transitions into the shallow s-wave Feshbach atom-dimer potential with bound-state energy $-1/ma_0^2$ shown in Fig. 5.4b. The Efimov effect therefore manifests itself in the scattering of three free atoms through transition to the atom-dimer channel and vice versa. This is the process of three-body recombination mentioned in the introduction of this chapter and of the time-reversed process three-body dissociation.

In the transition region the roots $s(R)$ and adiabatic three-body potentials are not constant. Rather, to characterize the potentials in this region, the roots can be expanded in powers of the small parameter a_0/R about their asymptotic values $\lambda + 2$

$$s_n(R) = (\lambda + 2) + \sum_{i=1} \left(\frac{a_0}{R}\right)^i \beta_\lambda^{(i)}. \tag{5.42}$$

The coefficients $\beta^{(i)}$ of this power series can be calculated by insertion of $s_n(R)$ into the transcendental equation (Eq. 5.34) and equating each power of a_0/R. When inserted into the adiabatic three-body potential (Eq. 5.26) the result is the asymptotic expansion of the adiabatic potential:

$$u_{\nu_n}(R) = \frac{\lambda(\lambda+4)+15/4}{2\mu_{3B}R^2} + \sum_{i=1}^{\infty} \frac{\alpha_\lambda^{(i+2)}}{2\mu_{3B}R^2} \left(\frac{a_0}{R}\right)^i. \tag{5.43}$$

The corrections therefore come in the form of **long-range power law tails** beginning at cubic order. I'll list here the coefficients associated with increasing order tails for $\lambda = 0$, and it is

illustrative to do this for distinct scattering lengths a_i between the pairs

$$\left[\frac{1}{R^3}\right]_{\lambda=0} \longrightarrow \frac{8}{d\pi\mu_{3B}}\sum_i \frac{a_i}{R^3}, \tag{5.44}$$

$$\left[\frac{1}{R^4}\right]_{\lambda=0} \longrightarrow \frac{24}{d^2\pi^2\mu_{3B}}\sum_i \frac{a_i^2}{R^4} + \frac{16(9+2\sqrt{3}\pi)}{9d^2\pi^2\mu_{3B}}\sum_{i\neq j}\frac{a_i a_j}{R^4}, \tag{5.45}$$

$$\begin{aligned}\left[\frac{1}{R^5}\right]_{\lambda=0} \longrightarrow & -\frac{32(\pi^2-6)}{3d^3\pi^3\mu_{3B}}\sum_i \frac{a_i^3}{R^5} + \frac{32(27+12\sqrt{3}\pi-2\pi^2)}{27d^3\pi^3\mu_{3B}}\sum_{i\neq j}\frac{a_i a_j^2}{R^5} \\ & + \frac{64(3\sqrt{3}+4\pi)}{9d^3\pi^2\mu_{3B}}\frac{a_1a_2a_3}{R^5},\end{aligned} \tag{5.46}$$

$$\begin{aligned}\left[\frac{1}{R^6}\right]_{\lambda=0} \longrightarrow & -\frac{160(2\pi^2-3)}{3d^4\pi^4\mu_{3B}}\sum_i \frac{a_i^4}{R^6} - \frac{64(-243-162\sqrt{3}\pi+297\pi^2+22\sqrt{3}\pi^3)}{243d^4\pi^4\mu_{3B}}\sum_{i\neq j}\frac{a_i a_j^3}{R^6} \\ & + \frac{64(81+54\sqrt{3}\pi-72\pi^2+2\sqrt{3}\pi^3)}{81d^4\pi^4\mu_{3B}}\sum_{i\neq j}\frac{a_i^2 a_j^2}{R^6} \\ & + \frac{128(81\sqrt{3}+135\pi+32\sqrt{3}\pi^2)}{243d^4\pi^3\mu_{3B}}\sum_{i\neq j\neq k}\frac{a_i a_j a_k^2}{R^6},\end{aligned} \tag{5.47}$$

where $d = d_k$ for equal mass atoms.

These coefficients have an interesting structure. Beginning with the cubic potential, we see that the coefficient has a two-body scaling, which is to say that it is a sum of the pair interaction strengths. Therefore, this term must represent *purely* two-body physics, which is to say physics where only two of the atoms interact while the third is unaffected, embedded in the transition region. Alternatively, this coefficient can be derived easily through first order stationary perturbation theory

$$\langle\Phi_\lambda^0(R;\Omega)|\sum_{i>j} v(r_{ij})|\Phi_\lambda^0\rangle \sim \frac{\sum_i a_i}{R^3}, \tag{5.48}$$

where $\Phi_\lambda^0(R;\Omega)$ are the free hyperangular solutions (hyperspherical harmonics). This long-range tail is therefore the hyperangular mean of the pairwise interactions at a fixed hyperradius. In Sec. 5.4.2, we will see how this term serves to 'spoil' calculations of the three-body phase shift.

The coefficients of the quartic potential arise from second order perturbation theory. The first term quadratic in each of the scattering lengths is purely two-body, however the second term

involves a product of two pairs of scattering lengths. This term represents the interaction of multiple pairs of atoms. In general, higher order tails contain all permutations of the pair scattering lengths to a given order.

It is tempting to interpret these terms diagrammatically in analogy with Feynman diagrams for the Born series in the time domain mentioned in Sec. 2.2.2 (see Fig. 2.1). It must be remembered however that these results are for fixed R. To connect with a diagrammatic approach for calculating an observable, the full expectation value over the entire adiabatic wave function $\psi(R,\Omega) = \sum_\nu F(R)\Phi_\nu(R;\Omega)$ must be taken so that all variables are integrated over. In Sec. 5.4.2, I connect this approach to some relatively old results from Amado and Rubin [201] for the threshold behavior of the three-body T-matrix.

Asymptotic Region: The long-range tails decay faster than the centrifugal barrier, and beyond a certain point these corrections become numerically insignificant, and the potential is purely centrifugal to a good approximation. The solution of the transcendental equation in this region gives only real values for s, and in the limit $a_0/R \to 0$, $\{s_1 = 2, s_2 = 6, s_3 = 8, ...\}$. This is the set of roots for three identical bosons, which does not include the root $s = 4$ for the 0^+ symmetry. In the asymptotic region, the adiabatic three-body potentials therefore correspond to repulsive centrifugal barriers, and the wave functions are phase-shifted spherical Bessel functions with angular momentum $l_{eff} = 3/2 + \lambda$ multiplied by hyperspherical harmonics

$$F_{\nu_i}(R)\Phi_{\nu_i}(R;\Omega) = \frac{e^{i\delta_{\lambda,\mu}}\sin(KR - l_{eff}\pi/2 + \delta_{\lambda,\mu})}{KR}Y_{\lambda,\mu}(\Omega), \tag{5.49}$$

where $\delta_{\lambda,\mu}$ is the three-body elastic scattering phase shift for the channel (λ,μ). This phase shift is part of the larger unitary multichannel three-body scattering S-matrix $S_{\lambda,\mu,\lambda',\mu'}$ whose off-diagonal elements describe transitions between channels. When $a_0 > 0$, the asymptotic region also contains the shallow Feshbach dimer channel (see Fig. 5.4b). The asymptotic form of the atom-dimer potential is

$$\frac{l(l+1)}{2\mu_{2B}R^2} + E_{2B}, \tag{5.50}$$

where l is the *relative* angular momentum of the dimer with respect to the other atom. In the

asymptotic limits discussed in the beginning of this section, the limit where all three atoms become well separated are dominated by the continuum channels whereas the limit where a single atom is separated from a pair are dominated by the atom-dimer channels [202].

In the following section, I formulate a WKB model which captures the functional dependence of the threshold elastic phase shift on Efimov physics. Sections 5.4.2–5.4.3 are devoted to understanding the contributions of the long-range power law tails to the elastic phase shift.

5.4.1 Signature of Efimov Physics in the Elastic Three-Body Phase Shift

The **WKB model** is a semi-classical approach to solving the Schrödinger equation, relying on the relative smallness of $\hbar$ (see Ref. [203] for an overview). The approximate form for the wave function in the WKB model is

$$F_{WKB}(R) = \frac{1}{\sqrt{K(R)}} \exp\left(\pm i S(R)\right), \tag{5.51}$$

written in terms of the action integral

$$S = \int_{R_i}^{R} K(R')dR'. \tag{5.52}$$

where the local classical momentum $K(R) = 2\mu_{3B}\sqrt{E - u_\nu(R)}$ defines a local de Broglie wavelength

$$\lambda(R) = \frac{2\pi}{K(R)}. \tag{5.53}$$

The usefulness of the WKB wave function can be gauged by the smallness of the local value of the *quantality* function

$$Q(R) = \left(\frac{3}{4}\frac{(K')^2}{K^4} - \frac{K''}{3K^3}\right) \tag{5.54}$$

compared to unity. Where is this violated? An obvious point is the classical turning point R_t where $u_\nu(R_t) = E$, $K(R_t)$ vanishes, and $Q(R_t)$ diverges making $F_{WKB}(R_t)$ singular. Even in regions where the WKB method cannot be expected to give numerically accurate results, it can often provide at least the general functional form of the wave function. It is in this latter sense that

I employ the WKB model in this section to obtain general results for the scaling of the three-body elastic phase shift including contributions from Efimov physics.

Under favorable conditions, the WKB approximation may be accurate away from R_t on one or both sides of the turning point. On the classically allowed side

$$F_{WKB}(R) = \frac{1}{\sqrt{K(R)}} \cos\left(\left|\int_{R_t}^{R} K(R')dR'\right| - \frac{\phi}{2}\right), \tag{5.55}$$

where ϕ is the phase difference (loss) between the incoming and outgoing waves due to reflection at the barrier. The wave function is matched at the turning point according to the **connection formula**

$$\frac{N}{\sqrt{|K(R)|}} \exp\left(-\left|\int_{R}^{R_t} K(R')dR'\right|\right) = \frac{2}{\sqrt{|K(R)|}} \cos\left(\left|\int_{R_t}^{R} K(R')dR'\right| - \frac{\phi}{2}\right). \tag{5.56}$$

If the potential is approximately linear at the turning point then the amplitude N and phase ϕ are given by

$$N = 1, \quad \phi = \frac{\pi}{2}. \tag{5.57}$$

This is the general result of the semiclassical or short-wave limit and is the basis of conventional WKB applications involving a classical turning point.

An important case is when the potential is the centrifugal barrier

$$u_\nu(R) = \frac{1}{2\mu_{3B}} \frac{l_{eff}(l_{eff}+1)}{R^2}. \tag{5.58}$$

The Schödinger equation can be solved exactly in this case

$$F(R) = \frac{\cos\left(KR - \frac{l_{eff}\pi}{2}\right)}{KR}, \tag{5.59}$$

where $K = \sqrt{2\mu_{3B}E}$. The asymptotic form of the WKB wave function is

$$F_{WKB}(R) = \frac{\cos\left(KR - \sqrt{l_{eff}(l_{eff}+1)}\frac{\pi}{2} - \frac{\phi}{2}\right)}{KR}. \tag{5.60}$$

Using the phase and normalization from Eq. 5.57 gives $\phi = \pi/2$ disagreeing with the exact result. This discrepancy can be repaired using the *Langer correction* where the cenrifugal potential in the

WKB approximation is 'corrected' by the mapping

$$l_{eff|}(l_{eff}+1) \to \left(l_{eff}+\frac{1}{2}\right)^2, \tag{5.61}$$

$$u_{WKB}(R) = u(R) + \frac{1}{2\mu_{3B}}\frac{\frac{1}{4}}{R^2}, \tag{5.62}$$

$$u_{langer}(R) = \frac{1}{2\mu_{3B}}\frac{\frac{1}{4}}{R^2}. \tag{5.63}$$

The Langer correction is essential to obtain the correct low-energy dependence of the wave function.

We can now extract the functional form of the elastic phase shift for the lowest hyperspherical channel. In this thesis, I do this only for $a_0 < 0$, where the ladder of Efimov states appear as a series of shape resonances. The adiabatic three-body potential in this section is simplified to provide analytic results: the Efimov potential in the universal region is flanked at smaller hyperadii by a barrier in the non-universal region, and a hump where the wave function must tunnel under to reach the asymptotic region. This problem is very similar to that analyzed by M. V. Berry in Ref. [204], where the WKB wave function was constructed for the case of three turning points.

The first pathway is to tunnel from the classical turning point $R \sim 1/K$ and reflect off of the hump at the edge of the scale-invariant region which is at a distance $R \sim |a_0|$ where the potential begins changing form. This pathway contributes a tunneling phase to the total phase shift

$$\tan(\delta_I) \approx \exp\left(-2\int_{|a_0|}^{1/K}\sqrt{E-\frac{l_{eff}(l_{eff}+1)-1/4}{R^2}}dR\right) = (K|a_0|)^{2l_{eff}+1} \tag{5.64}$$

In the threshold limit, the collision energy contribution provides comes in as higher order corrections and is therefore discarded in this simple calculation. The second pathway is to tunnel from the classical turning point into the well of the scale-invariant region and back off the potential hump on the way out (see Fig. 5.4a). This process acquires the phase

$$\tan(\delta_{II}) \approx (K|a_0|)^{2l_{eff}+1}\tan\left(\int_{|a_0|}^{R_0}\sqrt{\frac{s_0^2}{R^2}}dR\right) = (K|a_0|)^{2l_{eff}+1}\tan\left(s_0\ln\left(\frac{|a_0|}{R_0}\right)+\Delta\right). \tag{5.65}$$

The final term is the unknown phase shift due to the non-universal region. The poles of this function correspond to three-body resonances associated with Efimov trimer formation.

In the threshold limit, the total phase shift corresponds to a sum of these two contributions, and the first term ($l_{eff} = 3/2$) of the three-body effective range expansion is

$$-\frac{\tan(\delta_I + \delta_{II})}{K^4} \xrightarrow[K\to 0]{} \left(A + C\tan\left(s_0 \ln\left(\frac{|a_0|}{R_0}\right) + \Delta\right)\right) a_0^4 = A_{3B} \tag{5.66}$$

where A and C are proportionality constants. A_{3B} is the three-body **elastic scattering volume** having units of length^4, due to the three additional degrees of freedom compared to the two-body problem, and was first derived by Efimov in Ref. [32]. Near the formation of an Efimov trimer, A_{3B} diverges.

This is the leading order threshold contribution of Efimov physics to the three-body elastic phase shift. The K^4 dependence reflects the fact that this is a short range contribution, which can be checked by inputting l_{eff} in Eq. 2.31 from Chapter 2, which is the Wigner threshold law for short-range potentials. In a numerical calculation of the three-body elastic phase shift for a finite range potential, there are however contributions to the phase shift that arise at lower orders of K. It is well-known in the scattering community that long-range power law potentials can modify the usual threshold laws. In the next section, we discuss how the power law tails in the transition region contribute lower orders of K to the elastic phase shift. These contributions however do not contain the effects of three-body resonance physics from the inner well, which is described in Eq. 5.66 and therefore this section and the following can be viewed as complimentary.

5.4.2 Long-Range Contributions to the Elastic Three-Body Phase Shift

There is some old evidence that the threshold behavior of the three-body phase shift does not begin at order $O(K^4)$, coming from a paper of Amado and Rubin [201], who showed that

$$S_{3B}(K) - 1|_{\text{Connected}} \approx AK^2 + BK^3 + CK^4\ln(K) + K^4 D + O(K^5) + \cdots \tag{5.67}$$

for proportionality constants A, B, C, D where $S_{3B}(K)$ is the elastic three-body S-matrix[2] . The Efimov contributions derived in the previous section enter as nonperturbative contributions to the

[2] The coefficients A and B are unknown. C was calculated analytically in Ref. [205]. The nonperturbative portion of D was calculated in Ref. [206].

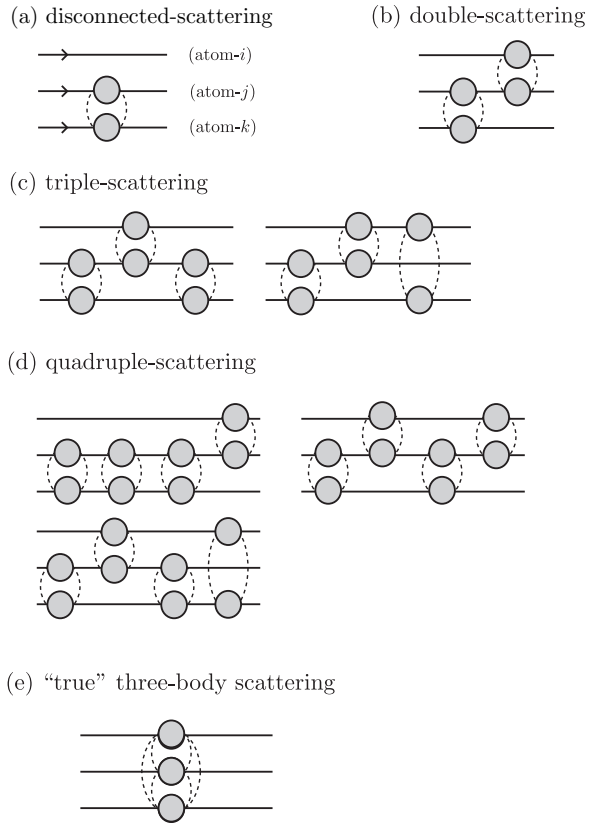

Figure 5.5: Diagrammatic representation of the three-body scattering processes which may occur with pairwise interactions. The grey circles represent a pairwise interaction summarized by the two-body T-matrix. I have excluded the permutations of each scattering diagram.

$D = D_{pert} + D_{nonpert}$ coefficient [174], where the dependence on the three-body parameter κ_* is hidden in the nonperturbative portion.

Equation 5.67 is the result of extracting the energy dependence at each order of the equivalent of the Born series[3] for three-body elastic scattering, including only the 'connected' contributions, which is to say all contributions that did not arise from disconnected scattering of a pair of atoms while the third is noninteracting, so-called **spectator scattering**. Each power in this expansion results from a certain order in the Born series and has a diagrammatic interpretation in the sense of Feynman diagrams (see Fig. 2.1). The first term is the so-called *double-scattering* contribution, the second is *triple-scattering*, etc... which are summarized in Fig. 5.5. The double scattering

[3] For three-body the corresponding series is the Faddeev series [163].

contribution results from an on-shell or off-shell binary collision followed by a binary collision between a distinct pair. There is a well-known re-scattering singularity when both collisions in double-scattering process happen on shell, and this causes difficulties when looking at, for instance, the scattering amplitude in the space of final momentum [72, 73]. Generally, any scattering event which occurs entirely on the shell of a subset of the total number of atoms appears as a singular contribution in the scattering amplitude for the total system[4] . This diagrammatic calculation in the momentum basis for the threshold behavior of the elastic three-body S-matrix has however not been connected with an approach which discretizes the continuum, such as the hyperspherical adiabatic representation. It is hoped that this connection can introduce power numerical techniques into the challenging three-body elastic scattering problem.

In the adiabatic hyperspherical representation, the transition region spans the length scale where one would expect the on-shell and off-shell binary collisions in Fig. 5.5 to occur. In what follows, I will sketch out some partial results connecting the results of Amado and Rubin with the phase shift due to the long-range power law tails in the transition region.

Scattering from long-range potentials can modify the usual Wigner threshold laws. The expansion in Eq. 5.43 contains a leading order cubic tail, and the threshold behavior for this potential is *linear* in K, which can be seen, for instance, using the WKB analysis from Ref. [207]. Let's detail the threshold behavior of each of the long-range tails separately, to show how the a tail of power $i+2$ modifies the threshold laws for general λ

$$\delta_\lambda^{(i+2)} \sim \begin{cases} K^i + \cdots, & \text{if } i < 2\lambda + 4, \\ K^{2\lambda+4} \ln K + \cdots, & \text{if } i = 2\lambda + 4, \\ K^{2\lambda+4} + \cdots & \text{if } i > 2\lambda + 4. \end{cases} \tag{5.68}$$

where the dependence on μ has been suppressed in the phase shift for notational clarity, and the subscript of the phase shift indicates the order of the corresponding long-range potential. Power law tails of order $i = 2\lambda + 4$ are therefore at the critical value between short-range and long-range,

[4] This is due to the presence of momentum-restricting delta functions describing the process.

and the logarithm generally complicates the effective range expansion and threshold laws [207]. At order K^4, the phase shift for the full problem therefore contains both long-range and short-range contributions, and there is an analogous separation of the K^4 coefficients in terms of power-law tail and short range Efimov physics complementing the perturbative and nonperturbative separation of the D coefficient in Eq. 5.67.

The coefficient of the leading order threshold behavior for a long-range potential depends only on the form of the potential and was derived by Landau in Ref. [208] for dispersion forces related to the scattering of slow particles. For the K^i ($i \neq 2\lambda + 4$) term this is

$$\delta_\lambda^{(i+2)} \approx -\frac{\sqrt{\pi}\alpha_\lambda^{(i+2)} a_0^i}{4} \frac{\Gamma(\frac{i+1}{2})\Gamma(\lambda + \frac{3}{2} - \frac{i-1}{2})}{\Gamma(\frac{i+2}{2})\Gamma(\lambda + \frac{3}{2} + \frac{i+3}{2})}. \tag{5.69}$$

Therefore, for $\lambda = 0$, the leading order expansions of the phase-shift from each power-law tail in Eq. 5.43 up to the critical value are

$$\delta_{\lambda=0}^{(3)} = \alpha_0^{(3)} \frac{15}{4} K + \cdots, \quad \delta_0^{(4)} \sim \alpha_0^{(4)} \frac{\pi}{48} K^2 + \cdots, \quad \delta_0^{(5)} \sim \alpha_0^{(5)} \frac{16}{315} K^3 + \cdots. \tag{5.70}$$

In the Born approximation, the total phase shift due to long-range power law tail in Eq. 5.43 is equivalent to a sum of these threshold results. For $\lambda = 0$, this gives

$$\delta_{\lambda=0} \quad = \quad A'K + B'K^2 + C'K^3 + D'K^4 \ln(K) + E'K^4 + \cdots, \tag{5.71}$$

which is consistent with the energy dependence of the phase-shift in Eq. (5.67), predicted by Amado and Rubin [201]. It should be noted that beyond leading order contributions to the threshold laws are also contained in the coefficients $B', C', D', ...$ and therefore the dependence is not quite as simple as what Eq. 5.70 suggests.

The coefficient A' corresponding to the cubic tail is however the only term that is left 'uncontaminated' by the threshold behavior of the higher ordered tails. This tail has a purely two-body scaling, which was addressed in Sec. 5.4. We can therefore identify it directly with disconnected spectator scattering by matching with Eq. 5.67. It is however erroneous to extend this analogy

between the higher order power law tails and Amado and Rubin's double, triplet, etc.. scattering contributions shown diagrammatically in Fig. 5.5. This is due to terms with purely two-body scaling inside of the coefficients listed in Eq. 5.45–5.47. These are the terms which would survive in the spectator problem where only one of the pairs interact. To match with results for the coefficients in Eq. 5.67, the disconnected scattering contributions must therefore be entirely removed. In the next section we will see that this is also necessary to obtain numerically converged elastic three-body phase shifts, and efforts to remove these disconnected contributions are discussed.

5.4.3 Removing Disconnected Two-Body Physics from the Elastic Three-Body Phase Shift

In Sec. 5.4.1, I investigated the signature of Efimov physics to the three-body elastic phase shift, which arise as $O(K^4)$ log-periodic contributions at threshold. In Sec. 5.4.2, contributions from long-range power law tails in the transition region to the elastic phase shift were considered where it was observed that the usual Wigner threshold laws require modification with contributions beginning at order $K, K^2, K^3, K^4 \ln K$ in addition to terms of order K^4 and higher. The resultant energy dependence was compared to the results of Amado and Rubin's diagrammatic calculation of the connected contributions. To quantitatively match adiabatic hyperspherical representation calculations to these results, a method for removing the disconnected contributions must be formulated. In this section, I discuss a factorization method due to R. G. Newton [209] and present some numerical evidence. I finish this section by pinpointing how this removal is also required to obtain phase shifts that are converged with higher values of λ.

Let's start by defining the scattering objects for the disconnected scattering problem, where only one pair of atoms is interacting. We first define the three-particle disconnected S-matrix as

$$S_i = 1 - 2\pi i \delta(E - E_K) T_i, \tag{5.72}$$

which is appropriate for the spectator scattering of particles j and k while i is noninteracting. T_i

is the disconnected three-body T-matrix, satisfying the Lippmann-Schwinger equation

$$T_i = V_i - V_i G_0^{3B}(z) T_i, \tag{5.73}$$

where G_0^{3B} is the Green's operator for the three-particle non-interacting Hamiltonian (see Eq. 2.22), and V_i is the pairwise interaction between atoms j and k.

Let's see how the disconnected T-matrix arises in the Lippmann Schwinger equation[5] for the three-body T-matrix of the full problem. The three-body S-matrix can be written in terms of the T-matrix

$$S_{3B} = 1 - 2\pi i \delta_E T_{3B}, \tag{5.74}$$

where $\delta_E = \delta(E - E_K)$ ensures the collision happens on the three-particle energy shell, and

$$T_{3B} = \sum_i T_i + \sum_{i \neq j} T_i G_0^{3B} T_j + \cdots . \tag{5.75}$$

Therefore, the entire disconnected contribution is isolated in the first term.

In Refs. [72, 73], the S-matrix was decomposed as a sum $S_{3B} = [1 - 2\pi i \delta_E \sum_i T_i] + \tilde{S}$, which isolates the disconnected portion from the remainder $\tilde{S}$. In this factorization, a generalized expression was derived for the scattering cross section for two beams impinging on a fixed target, highlighting the physical meaning of the disconnected and rescattering contributions. In this section, however, I pursue another factorization

$$S_{3B} = S_1 S_2 S_3 S_{(C)}, \tag{5.76}$$

which produces the **connected operator** $S_{(C)}$. This decomposition is adopted here because it has been proven that $S_{(C)}$ is *compact* [209]. This means that it enjoys the same important properties as the two-particle S-matrix: A discrete spectrum of **eigenphases** $\exp(2i\delta_n)$ associated with a complete set of eigenvectors. Eigenvectors of the multichannel scattering problem are generally linear combinations of the scattering wave functions of multiple channels. Additionally, the eigenphases are the eigenvalues of the unitary S-matrix and therefore lie on the unit circle. Furthermore, the

[5] Technically these are the Faddeev equations [163].

eigenphase sum, $\sum_n \delta_n^{(C)}(E) = \Delta_{\rm ep}^{(C)}(E)$, should change by π whenever a three-body bound state is formed, as well as giving a Briet-Wigner form for the resonance away from the background value $\Delta_{\rm ep}^{(C)}(0)$ [210], satisfying the three-body Levinson's theorem [211]

$$N_{3B} = \frac{1}{\pi}(\Delta_{\rm ep}^{(C)})(0) - \Delta_{\rm ep}^{(C)}(\infty)), \tag{5.77}$$

where N_{3B} is the total number of supported three-body bound states. The properties of the eigenphase sum also do not depend on the order in which the S matrix is factorized in Eq. 5.76, which can be seen from properties of the determinant, $\Delta_{ep}^{(C)} = \log\left[\det(S_3 S_2 S_1 S_{3B})\right]/2i$.

First, I follow Ref. [209] to derive and interpret the explicit form of $S_{(C)}$ that results from the factorization in Eq. 5.76. Then, I demonstrate the numerical convergence of $S_{(C)}$ in the adiabatic hyperspherical representation. Finally, I investigate whether the threshold behavior of the connected S-matrix is quadratic to leading order in K, bolstering the identification of the cubic tail with disconnected physics made in the previous section.

The derivation that Eq. 5.76 removes the disconnected contributions proceeds by requiring that $S_{(C)}$ have the following form

$$S_{(C)} = 1 - 2\pi i \delta_E T_{(C)}. \tag{5.78}$$

Substituting this expression into Eq. 5.76 yields

$$1 - 2\pi i \delta_E T = S_1 S_2 S_3 - 2\pi i S_1 S_2 S_3 \delta_E T_{(C)}. \tag{5.79}$$

Both sides can be expanded to

$$\begin{aligned} &1 - (2\pi i)\delta_E \left[\sum_i T_i + \sum_{i\neq j} T_i G_0^{3B} T_j + \cdots\right] \\ &= \left[1 - 2\pi i \delta_E \sum_i T_i + (2\pi i)^2 \delta_E \sum_{i<j} T_i \delta_E T_j - (2\pi i)^3 \delta_E \prod_i T_i \delta_E T_i \delta_E T_i\right] - 2\pi i S_1 S_2 S_3 \delta_E T_{(C)}, \end{aligned} \tag{5.80}$$

and the spectator piece subtracted. After sorting out[6] all of pieces, we get

$$T_{(C)} = S_3^\dagger S_2^\dagger S_1^\dagger (T^D_{(C)} + \cdots), \tag{5.81}$$

$$T^D_{(C)} = \sum_{i<j} \left(T_i G_0^- T_j + T_j G_0^+ T_i \right). \tag{5.82}$$

Therefore, $T_{(C)}$ contains double scattering events at leading order. However, the factorization has done more than just subtract off the spectator collisions, scrambling the original expression $T^D = \sum_{i \neq j} T_i G_0^{3B} T_j$ for the double-scattering T-operator in the process. It is therefore not correct to compare $T^D_{(C)}$ to the double scattering results of Amado and Rubin.

Newton's factorization therefore removes the disconnected scattering contributions at the cost of producing the altered connected $S_{(C)}$. With this in mind, we check the threshold behavior of the eigenphase shifts and whether or not removing the disconnected contributions leads to a convergent calculation of $S_{(C)}$ in the adiabatic hyperspherical basis.

In the previous section, I surmized that the $1/R^3$ contribution to the long-range power law tail in the transition region was purely two-body in nature and was responsible for the $O(K)$ threshold dependence of the elastic phase shift (see Eq. 5.70.) The connected eigenphases therefore should be quadratic to leading order, and it is possible to prove this threshold result in the adiabatic limit[7] where the channel couplings can be ignored. To do this, I will deal instead with the connected eigenphase sums that should also be quadratic to leading order and are also a natural candidate for assessing the converge of a calculation of $S_{(C)}$ with increasing channel number. It is possible to

[6] The relation $\delta_E = -2\pi i (G^+ - G^-)$ and the $+$ or $-$ indicates the limit from above or below of $G_0^{3B}(z + i0)$ is useful.

[7] In fact, the zero-range analysis shows that the P and Q couplings among three-body continuum states are asymptotically proportional to $1/R^2$ and $1/R^3$, respectively, while they are $1/R^{5/2}$ and $1/R^{7/2}$ between bound channels and continuum channels (see, for instance, Ref. [212].)

derive a simple relation between the sums beginning with the decomposition in Eq. 5.76

$$\det(S_{3B}) = \det\left(S_1 S_2 S_3 S_{(C)}\right), \tag{5.83}$$

$$\det(S_{3B}) = \det(S_1)\det(S_2)\det(S_3)\det(S_{(C)}), \tag{5.84}$$

$$\exp\left(2i\Delta_{\rm ep}\right) = \exp\left(2i\sum_i^3 \Delta_{\rm ep}^i\right)\exp\left(\Delta_{ep}^{(C)}\right), \tag{5.85}$$

$$\log\left[\exp\left(2i\Delta_{\rm ep}\right)\right] = \log\left[\exp\left(2i\sum_i^3 \Delta_{\rm ep}^i\right)\exp\left(\Delta_{ep}^{(C)}\right)\right], \tag{5.86}$$

$$\Delta_{\rm ep} = \sum_i^3 \Delta_{\rm ep}^i + \Delta_{ep}^{(C)}, \tag{5.87}$$

where $\Delta_{\rm ep}$ is the eigenphase sum for S_{3B}, $\Delta_{\rm ep}^i$ is the eigenphase sum for S_i, and I have utilized some standard properties of the determinant. In the adiabatic limit, the eigenphase sums are just the sum of the phase shifts in each channel ($\Delta = \sum_\lambda \delta_\lambda$) which were discussed in the previous section, Sec. 5.4.2.

Let's work out the cancelation of $O(K)$-dependence of the connected eigenphase sum first when the potential in Eq. 5.43 is truncated to include only the cubic tail and imagined to extend from $R \in [0, \infty)$

$$u_\nu(R) = \frac{\lambda(\lambda+4)+15/4}{2\mu_{3B}R^2} + \frac{\alpha_\lambda^{(3)}}{2\mu_{3B}R^2}\left(\frac{a_0}{R}\right), \tag{5.88}$$

with coefficients α_λ given in Table 5.1. From Eq. (5.69) the analytic expression for the phase shift

Table 5.1: Coefficients α_λ for the $1/R^3$ term in Eq. (5.88) and corresponding phase-shifts as given in Eq. (5.89). We denote the coefficients for the three-body system where only one of the pairs interact by $\tilde{\alpha}_\lambda$ while for three-body systems where all pairs interact we denote them by α_λ. The subscript in $\lambda_{(n)}$ indicates the corresponding degeneracy for a given value of λ.

	S-matrix: S_k		S-matrix: S_{3B}	
$\lambda_{(n)}$	$\tilde{\alpha}_\lambda^{(3)}$	$\tilde{\delta}_\lambda^{(3)}$	$\alpha_\lambda^{(3)}$	$\delta_\lambda^{(3)}$
$0_{(1)}$	$\frac{16}{d\pi}$	$-\frac{32Ka_0}{15d\pi}$	$\frac{48}{d\pi}$	$-\frac{32Ka_0}{5d\pi}$
$2_{(2)}$	$\frac{64}{d\pi}$,0	$-\frac{128Ka_0}{63d\pi}$,0	$\frac{96}{d\pi}$,$\frac{96}{d\pi}$	$-\frac{64Ka_0}{21d\pi}$,$-\frac{64Ka_0}{21d\pi}$
$4_{(3)}$	$\frac{144}{d\pi}$,0,0	$-\frac{288Ka_0}{143d\pi}$,0,0	$\frac{144}{d\pi}$,$\frac{144}{d\pi}$,$\frac{144}{d\pi}$	$-\frac{288Ka_0}{143d\pi}$,$-\frac{288Ka_0}{143d\pi}$,$-\frac{288Ka_0}{143d\pi}$
$6_{(3)}$	$\frac{256}{d\pi}$,0,0	$-\frac{512Ka_0}{255d\pi}$,0,0	$\frac{192}{d\pi}$,$\frac{192}{d\pi}$,$\frac{384}{d\pi}$	$-\frac{128Ka_0}{85d\pi}$,$-\frac{128Ka_0}{85d\pi}$,$-\frac{256Ka_0}{85d\pi}$
$8_{(3)}$	$\frac{400}{d\pi}$,0,0	$-\frac{800Ka_0}{399d\pi}$,0,0	$\frac{240}{d\pi}$,$\frac{480}{d\pi}$,$\frac{480}{d\pi}$	$-\frac{160Ka_0}{133d\pi}$,$-\frac{320Ka_0}{133d\pi}$,$-\frac{320Ka_0}{133d\pi}$

for this potential for a given λ is

$$\delta_\lambda^{(3)} = -\frac{\alpha_\lambda^{(3)}}{(\lambda+5/2)(\lambda+3/2)}(Ka_0) + O(K^2). \tag{5.89}$$

Table 5.1 lists the phase-shifts for the disconnected problem where only one of the pairs interact with identical scattering lengths ($\tilde{\delta}_\lambda$), and the phase shifts where all pairs interact (δ_λ). Inserting values from Table 5.1, it is easy to check that

$$\Delta_{\rm ep}^{(C)} = \sum_{\lambda_n}\left(\delta_{\lambda_n} - 3\tilde{\delta}_{\lambda_n}\right) = O(K^2), \tag{5.90}$$

and therefore the threshold behavior of the eigenphases are *shifted* beyond $O(K)$ when disconnected scattering is factored from S_{3B}.

Going beyond the adiabatic limit and model potential (Eq. 5.88), this shift of threshold dependence to quadratic order can be verified numerically (see Ref. [168] for a description of the code) using Lennard-Jones interactions, including all couplings between channels. The results of this calculation are shown in Fig. 5.6. In Fig. 5.6(a), the results for a system with three different *negative scattering lengths*[8] ($a_1 \approx -10r_{\rm vdW}$, $a_2 \approx -15r_{\rm vdW}$, and $a_3 \approx -20r_{\rm vdW}$) are shown. The solid red curve is the eigenphase sum from S_{3B} and the green-dashed curves are the eigenphase sums for S_1, S_2, S_3. It is apparent that $\Delta_{\rm ep}$, $\Delta_{\rm ep}^1$, $\Delta_{\rm ep}^2$, and $\Delta_{\rm ep}^3$ are all linear in K near threshold, which was expected from the analysis of the transition region in Sec. 5.4.2. The blue dotted curve is the connected eigenphase sum $\Delta_{\rm ep}^{(C)}$, which confirms the shift to quadratic order at threshold.

In Fig. 5.6(b), the results for a system with three different *positive scattering lengths*[9] ($a_1 \approx +10r_{\rm vdW}$, $a_2 \approx +15r_{\rm vdW}$ and $a_3 \approx +20r_{\rm vdW}$). The eigenphase sum is defined excluding the eigenphases associated with the bound channels in this case. Again, the connected eigenphase sum $\Delta_{\rm ep}^{(C)}$ is shifted to quadratic order at threshold.

To finish this section, I discuss the convergence of the phase shift for the long-range power law tail (Eq. 5.69) in the limit of increasing λ. For the cubic tail, the coefficient to the $1/R^3$ term of the potential, α_λ, is proportional to λ^2, and therefore the phase-shift (Eq. (5.89)) converges in the

[8] In the absence of any two-body bound states.
[9] In the presence of two-body bound states.

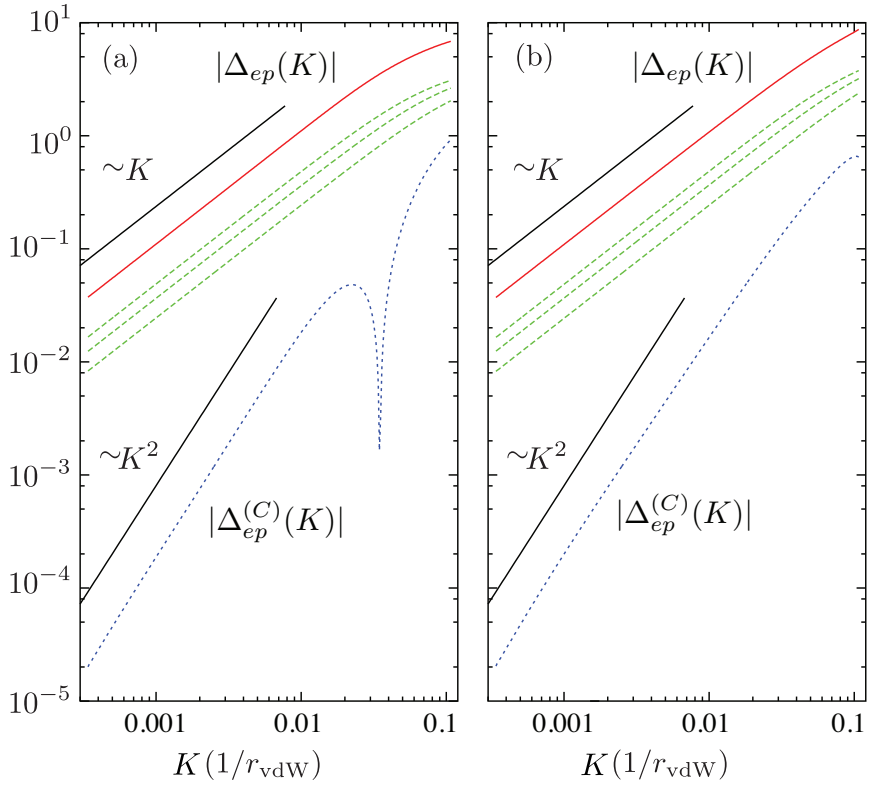

Figure 5.6: (a) Eigenphase sum for a system with three different negative scattering lengths ($a_1 \approx -10r_{\rm vdW}$, $a_2 \approx -15r_{\rm vdW}$ and $a_3 \approx -20r_{\rm vdW}$). The solid red curve is the eigenphase sum from S_{3B}, and the green-dashed curves are the eigenphase sums for S_1, S_2, S_3. The blue dotted curve is $\Delta_{\rm ep}^{(C)}$, which scales as K^2 at threshold. (b) Same as (a) but for a system with three different positive scattering lengths ($a_1 \approx +10r_{\rm vdW}$, $a_2 \approx +15r_{\rm vdW}$ and $a_3 \approx +20r_{\rm vdW}$).

limit of large λ to a constant. Therefore, the contribution of the cubic potential to the eigenphase sum *diverges* as one includes more channels. Curiously, the phase-shifts due to the higher order tails do converge. For the quartic tail

$$\delta_\lambda^{(4)} = -\frac{\alpha_\lambda^{(4)}\pi/8}{(\lambda+3)(\lambda+2)(\lambda+1)}(Ka_0)^2., \tag{5.91}$$

where $\alpha_\lambda^{(4)} \xrightarrow[\lambda\gg 1]{} O\left(\lambda^2\right)$ and the denominator scales as λ^3, and the ratio converges when $\lambda \gg 1$.

The connected S-matrix, $S_{(C)}$ is therefore convergent in the adiabatic hyperspherical representation. In the language of adiabatic three-body potentials, the divergence of the eigenphase sum in the full calculation of S_{3B} is due solely to the $1/R^3$ tail, which can be associated entirely with disconnected scattering. Disconnected scattering also contributes to the higher order long-

range tails (see Eq. 5.44) although these contributions do not lead to divergent phase shifts in this simplified picture, and this 'contamination' spoils the connection with the diagrammatic approach. Unfortunately, $S_{(C)}$ is altered and the results obtained in this section cannot be matched with Amado and Rubin's low-energy expansion in Eq. 5.67.

It remains an open question how to properly decompose the three-body S-matrix into connected and disconnected components in a representation that discretizes the continuum without spoiling double, triple, and higher order scattering contributions. Formally, the decomposition $S_{3B} = [1 + 2\pi\delta_E \sum_i T_i] + \tilde{S}$ mentioned at the beginning of this section in fact does this separation without spoiling the higher order contributions

$$\tilde{S} = 2\pi i \delta_E \left[T - \sum_i T_i \right] = 2\pi i \delta_E \left[T^D + \cdots \right]. \tag{5.92}$$

The remainder $\tilde{S}$ is therefore exactly the physical connected T-matrix containing only contributions from double-scattering upwards. Calculating the matrix elements of $\tilde{S}$ in the adiabatic hyperspherical representation[10] is therefore a promising avenue towards matching with Amado and Rubin's low-energy expansion in Eq. 5.67.

5.5 Conclusion

This chapter is the first of three devoted to the physics of strongly-interacing Bose gases. After introducing some standard coordinate space parametrizations of the three-body problem, I discussed the adiabatic hyperspherical representation, which treated the hyperradius as an adiabatic coordinate. Importantly, this representation discretizes the continuum, retaining the utility of the partial wave expansion discussed in Ch. 2, and introduces adiabatic three-body potentials which play the role of effective three-body potentials. In the unitarity limit, an infinite number of Efimov trimers form. Through a WKB model, I discussed the signature of Efimov physics in the threshold behavior of the elastic phase shift. When the scattering length is finite, this short range contribution is complemented by long-range contributions from the long-range power law tails in the transition

[10] The matrix elements of S_i should be in principle possible to calculate analytically from two-body results.

region. These long-range contributions modify the usual Wigner threshold laws for the phase shift, and I attempted to match them against well-known results from Amado and Rubin [201] obtained from a diagrammatic approach. Unfortunately, the effects of the two-body continuum embedded in the three serve to spoil this comparison as well as producing divergent three-body elastic phase shifts. To remove these disconnected scattering contributions, a decomposition due to R. G. Newton [209] was discussed, which was analytically and numerically confirmed to produce a convergent calculation of the connected three-body S-matrix. This matrix is however altered, and an alternative, promising factorization of the S-matrix into connected and disconnected components was proposed, which remains the subject of future work.

Chapter 6

Efimov Physics with Degenerate Internal Levels

This chapter contains results from Refs. [36, 37, 62].

In the previous chapter, I addressed the three-body Efimov physics that becomes important when interactions between atoms in a Bose gas become strong. When the individual atoms have access to multiple degenerate internal levels, the Bose-condensed gas is referred to as a **spinor** BEC. In this chapter, I will demonstrate how the three-body bound state spectrum of Efimov states is modified with the introduction of degenerate internal levels and discuss the signature of Efimov physics in the three-body elastic phase shift. The long-range power law tail modification of the Wigner threshold laws discussion which bookended the previous chapter will however not be extended in this thesis to spinor systems. The results of this chapter and Chapter 5, serve as the few-body foundation of the final chapter, Chapter 7, which combines these results with a many-body formalism for describing the strongly-interacting Bose gas. I begin with some brief context and overview of the spinor BEC.

In spinor condensates the atomic spin degrees-of-freedom are energetically accessible leading to a unique scenario in which *both* superfluity and magnetism can exist [64]. The first spinor condensates were made with ^{87}Rb in a double magnetic trap [213, 214] and with ^{23}Na in an optical trap [215]. There has been a subsequent explosion of experimental [215, 216, 217, 218, 219, 220, 221, 222, 223, 224, 225, 226], and theoretical [227, 228, 229, 230, 231, 232, 233, 234, 235, 236, 237] studies in the area. Studying the interplay between superfluidity and magnetism has proven to be

a rich area for probing the many-body dynamics of the static and nonequilibrium behavior of these systems leading to novel phenomena such as spin textures, spin domains, and complex spin mixing dynamics [64].

Many of the interesting phenomena in spinor condensates hinge on extreme sensitivity to the relative strengths of two-body interactions between the internal states; those interactions are typically weak for alkali atoms (with the exception of ^{85}Rb [238, 239], and possibly also ^{133}Cs and ^{7}Li) and as a consequence the spinor physics with strong interactions has largely remained unexplored. Although the usual Feshbach resonance technique for tuning the interactions [30] cannot immediately be applied to spinor condensates, several proposals for achieving such control exist [240, 241, 242, 243, 244, 245, 246], which enable possible ways to study strongly correlated spinor condensates. Evidently, as the interactions become resonant, three-body contributions need to be considered. In the strongly correlated regime, i.e., when the s-wave two-body scattering lengths associated with the hyperfine spin states exceed the typical range of interatomic interactions (the van der Waals length, $r_{\rm vdW}$), Efimov physics becomes important [32, 174, 247], and several new aspects have to be considered. For instance, the existence of an infinity of weakly bound Efimov trimers strongly affects the scattering observables at ultracold energies and can potentially impact the spin dynamics in spinor condensates.

One of the major differences between the usual "spinless" Efimov physics and the effect for spinor systems is the presence of multiple length scales in the problem. In spinor condensates the atomic energy levels are $(2f+1)$-fold degenerate (f is the atomic hyperfine angular momentum and $m_f = -f...f$ its azimuthal component), and there exist $f+1$ rotationally-invariant s-wave scattering lengths [64]. In the context of nuclear physics, where isospin symmetry plays an important role, the work of Bulgac and Efimov [35] demonstrated a much richer structure for Efimov physics when the isospin degree of freedom was considered.

This chapter begins with a summary of the multichannel generalization of the adiabatic hyperspherical representation presented in Chapter 5 appropriate for the three-body problem with multiple internal levels. I then begin with a simple toy model for the three-body problem with

two degenerate internal levels to illustrate how the spectrum of Efimov state shifts as the mixing between three-body internal states is adjusted. Then, the Efimov physics for spin-1, -2 and -3 systems are analyzed by first determining the complex topology of the three-body hyperspherical potentials and by enumerating the possible families of Efimov states present in each case. Special attention is given to the spin-2 ^{85}Rb condensate due to the naturally large values for the atomic scattering lengths found in Ref. [238, 239]. Finally, I derive the 3-body scattering length using the WKB model from Sec. 5.4.1 for an individual case to demonstrate the general procedure when spin degrees of freedom have been introduced. This provides the fundamental building blocks for studying the effect of three-body physics on the ground state magnetic ordering of spinor condensates in Chapter 7.

6.1 Adiabatic hyperspherical representation for spinor systems

Our study of few-body physics in spinor condensates begins from the multichannel generalization of the zero-range Fermi pseudopotential for s-wave interactions. In Refs. [248, 172, 249, 250, 251], a suitable generalization was proposed to be

$$\hat{v}(r) = \frac{4\pi\hat{A}}{m}\delta^3(\vec{r})\frac{\partial}{\partial r}r, \tag{6.1}$$

where $\hat{A}$ is a **scattering length operator** which incorporates all the important multichannel structure of the two-body interactions [248]. For spinor condensates we assume the scattering length operator in Eq. (6.1) can be defined for each pair of atoms as

$$\hat{A} = \sum_{F_{2\mathrm{b}}M_{F_{2\mathrm{b}}}} |F_{2\mathrm{b}}M_{F_{2\mathrm{b}}}\rangle a_{F_{2\mathrm{b}}}\langle F_{2\mathrm{b}}M_{F_{2\mathrm{b}}}|, \tag{6.2}$$

where

$$|F_{2\mathrm{b}}M_{F_{2\mathrm{b}}}\rangle \equiv |(f_1f_2)F_{2\mathrm{b}}M_{F_{2\mathrm{b}}}\rangle = \sum_{m_{f_1}m_{f_2}} \langle f_1 m_{f_1} f_2 m_{f_2}|F_{2\mathrm{b}}M_{F_{2\mathrm{b}}}\rangle |f_1 m_{f_1}\rangle |f_2 m_{f_2}\rangle. \tag{6.3}$$

is the two-body spin functions of total angular momentum $|f_1 - f_2| \leq F_{2\mathrm{b}} \leq f_1 + f_2$ and projection $M_{F_{2\mathrm{b}}} = m_{f_1} + m_{f_2}$, expressed in terms of the Clebsch-Gordan coefficients. Therefore, the two-body interaction in Eq. (6.1) is diagonal in the spin basis $\{|\sigma\rangle\} = \{|F_{2\mathrm{b}} M_{F_{2\mathrm{b}}}\rangle\}$. We note that, due to bosonic symmetry only the symmetric spin states ($F_{2\mathrm{b}}$ even) are allowed to interact with rotationally-invariant scattering lengths $a_{F_{2\mathrm{b}}} \equiv \{a_0, a_2, ..., a_{2f}\}$[1] . These scattering lengths set important length scales in the system. Many-body properties of the system such as the miscibility of spin components are sensitive to the relative strength and sign of the scattering lengths [64]. Their strength also signifies the appearance of universal three-body physics in the scattering observables as we will see in Chapter 7.

The three-body problem is solved using a multichannel generalization of the adiabatic hyperspherical method via a Green's function approach developed in Ref. [248, 172, 249]. The three-body wave-function can be generalized for the multichannel problem as

$$\psi(R, \Omega) = \sum_{\nu} F_\nu(R) \sum_{\Sigma} \Phi_\nu^\Sigma(R; \Omega) |\Sigma\rangle \tag{6.4}$$

where $\{|\Sigma\rangle\} = \{|m_{f_1}, m_{f_2}, m_{f_3}\rangle\}$ are the three-body spin functions, formed by the combination of all possible product states, chosen to simplify the formulation. The adiabatic channel functions are eigenstates of the fixed-R hyperangular Schrödinger equation

$$\sum_{\Sigma'} \Big[\frac{\hat{\Lambda}^2(\Omega) + 15/4}{2\mu_{3B} R^2} \delta_{\Sigma\Sigma'} + \langle \Sigma' | \hat{V}(R, \Omega) | \Sigma \rangle + E_\Sigma \delta_{\Sigma\Sigma'} \Big] \Phi_\nu^\Sigma(R; \Omega) = u_\nu(R) \Phi_\nu^\Sigma(R; \Omega), \tag{6.5}$$

with corresponding eigenvalues given by the adiabatic potentials $u(R)$ which determine the hyperradial motion and describe (in conjunction with the nonadiabatic couplings) the possible bound states and scattering properties of the system. $\hat{V}$ is the sum of all possible pairwise interactions in spin space [Eq. (6.1)], given by

$$\hat{V}_{pseudo} = \frac{4\pi}{m} \sum_{i<j} |f_k m_{f_k}\rangle \left[\hat{A}^{(k)} \delta^3(d\vec{\rho}_1^{(k)}) \frac{\partial}{\partial \rho_1^{(k)}} \rho_1^{(k)} \right] \langle f_k m_{f_k}|. \tag{6.6}$$

[1] Note the unavoidable abuse of the notation 'a_0'. The meaning should be clear contextually.

In the present study the three-body energy levels, E_Σ, which is the sum of the energies of the three atoms, are degenerate and set to zero.

Equation (6.5) is solved using a hyperangular Green's function and the corresponding Lippmann-Schwinger equation [248] for each component of the channel function,

$$\Phi_\Sigma(R;\Omega) = -2\mu_{3B}R^2 \sum_{\Sigma',k} \int \mathrm{d}\Omega' G_{\Sigma\Sigma}(\Omega,\Omega') \times v^{(k)}_{\Sigma\Sigma'}(R,\Omega')\Phi_{\Sigma'}(R;\Omega'), \tag{6.7}$$

where

$$v^{(k)}_{\Sigma\Sigma'}(R,\Omega) = \langle\Sigma|V(r_{ij})|\Sigma'\rangle. \tag{6.8}$$

Evaluating the integral over $v^{(k)}_{\Sigma\Sigma'}$, considering only states of total orbital angular momentum $L = 0$, and solving the Lippmann-Schwinger equation reduces to determining values of s for which the determinant of the matrix

$$\hat{Q} = \left[\frac{3^{1/4}}{2^{1/2}R}\left(M^{(1)} + M^{(2)}P_- + M^{(3)}P_+\right) - 1\right] \tag{6.9}$$

vanishes [250, 251, 248]. In the equation above the matrix element for the M matrices are given by

$$M^{(i)}_{\Sigma\Sigma'} = \begin{cases} A^{(i)}_{\Sigma\Sigma'} s\cot(s\pi/2), & i = 1, \\ -A^{(i)}_{\Sigma\Sigma'}\frac{4\sin(s\pi/6)}{\sqrt{3}\sin(s\pi/2)}, & i = 2,3, \end{cases} \tag{6.10}$$

where $A^{(i)}_{\Sigma\Sigma'}$ is the matrix element for the two-body scattering matrix written in the three-body spin basis,

$$\begin{aligned} A^{(i)}_{\Sigma\Sigma'} &= \langle\Sigma|\hat{A}^{(i)}|\Sigma'\rangle \\ &= \sum_{F_{2\mathrm{b}},M_{F_{2\mathrm{b}}}} a_{F_{2\mathrm{b}}}\langle m_{f_j}m_{f_k}|F_{2\mathrm{b}}M_{F_{2\mathrm{b}}}\rangle \\ &\quad\times\langle F_{2\mathrm{b}}M_{F_{2\mathrm{b}}}|m'_{f_j}m'_{f_k}\rangle\delta_{m_{f_i}m'_{f_i}} \end{aligned} \tag{6.11}$$

with the ith particle as spectator to the interaction. The P_+ and P_- matrices represent cyclic and

anti-cyclic permutations of the the three-body spin basis

$$\begin{aligned}(P_+)_{\Sigma\Sigma'} &= \langle\Sigma|P_{123}|\Sigma'\rangle \\ &= \langle m_{f_1}, m_{f_2}, m_{f_3}|P_{123}|m'_{f_1}, m'_{f_2}, m'_{f_3}\rangle \\ &= \delta_{m_{f_1},m'_{f_2}}\delta_{m_{f_2},m'_{f_3}}\delta_{m_{f_3},m'_{f_1}} \qquad (6.12)\\ (P_-)_{\Sigma\Sigma'} &= \langle\Sigma|P_{132}|\Sigma'\rangle \\ &= \langle m_{f_1}, m_{f_2}, m_{f_3}|P_{132}|m'_{f_1}, m'_{f_2}, m'_{f_3}\rangle \\ &= \delta_{m_{f_1},m'_{f_3}}\delta_{m_{f_2},m'_{f_1}}\delta_{m_{f_3},m'_{f_2}}. \qquad (6.13)\end{aligned}$$

The spin basis $\{|\Sigma\rangle\}$ was chosen to to give simple expressions for the components of $\hat{Q}$ which were written in the odd-man-out notation. In this form, however, $\hat{Q}$ does not account for any symmetry property in the system. This is fixed by the unitary transformation $\hat{S}\hat{Q}\hat{S}^T$ with

$$(S)_{\Sigma\Sigma'} = \langle\Sigma|\left(\sum_{F_{2\mathrm{b}}}|F_{3\mathrm{b}}M_{F_{3\mathrm{b}}}(F_{2\mathrm{b}})\rangle\langle F_{3\mathrm{b}}M_{F_{3\mathrm{b}}}(F_{2\mathrm{b}})|\right)|\Sigma'\rangle, \qquad (6.14)$$

where the three-body spin functions of total angular momentum $|F_{2\mathrm{b}} - f| \leq F_{3\mathrm{b}} \leq |F_{2\mathrm{b}} + f|$ and projection $M_{F_{3\mathrm{b}}} = M_{F_{2\mathrm{b}}} + m_f$ are given by

$$\begin{aligned}&|F_{3\mathrm{b}}M_{F_{3\mathrm{b}}}(F_{2\mathrm{b}})\rangle \equiv |(f_1f_2f_3)F_{3\mathrm{b}}M_{F_{3\mathrm{b}}}(F_{2\mathrm{b}})\rangle = \\ &\sum_{M_{F_{2\mathrm{b}}}m_{f_3}}\langle F_{2\mathrm{b}}M_{F_{2\mathrm{b}}}f_3m_{f_3}|F_{3\mathrm{b}}M_{F_{3\mathrm{b}}}\rangle|F_{2\mathrm{b}}M_{F_{2\mathrm{b}}}\rangle|f_3m_{f_3}\rangle. \qquad (6.15)\end{aligned}$$

Therefore, evaluating the $\det[\hat{S}\hat{Q}\hat{S}^T]$=0 results in a transcendental equation whose roots $s(R)$ determine the channel functions $\Phi(R;\Omega)$ and the three-body potentials $u(R)$ with well defined hyperfine angular momentum ($F_{3\mathrm{b}}$ and $M_{F_{3\mathrm{b}}}$) and permutation symmetry. In the spinless problem discussed in Chapter 5, the solution for three identical bosons in the resonant limit $R/a_0 \to 0$ gives the lone imaginary root $s_0 \approx 1.00624i$, which produces the attractive three-body potential. This potential supports an infinite number of bound trimers. In the spinor case elaborated above, the degeneracy of the hyperfine spin-manifold yields fundamentally different three-body physics as demonstrated through a toy model in the following section.

6.2 Toy Model: Efimov States with Two Internal States

Before jumping into the three-body problem on the hyperfine spin manifold, we will first explores the parameter space of the matrix $\hat{A}$ through a toy model where there are only two degenerate internal levels labeled $|1\rangle$ and $|2\rangle$. The toy model will then be generalized and a connection with the hyperfine spinor three-body problem and the appearance of novel Efimov roots made before the full solutions are discussed. In our two-level toy model, $\hat{A}$ is a real-valued symmetric 3×3 matrix with eigenvalues a_α, a_β, and a_γ. The full parameter space of $\hat{A}$ is large, but by considering a simple case the structure becomes more apparent. Consider the scenario where $A_{1,3} = A_{2,3} = 0$ with eigenvalues

$$a_{\alpha/\beta} = \left(\frac{A_{1,1} + A_{2,2}}{2}\right) \pm \left[A_{1,2}^2 + \left(\frac{A_{1,1} - A_{2,2}}{2}\right)^2\right]^{1/2} \quad \text{and} \quad a_\gamma = A_{3,3}, \tag{6.16}$$

and eigenvectors

$$|\sigma_\alpha\rangle = \cos\theta|11\rangle + \sin\theta|12\rangle_S, \quad |\sigma_\beta\rangle = \sin\theta|11\rangle - \cos\theta|12\rangle_S, \quad \text{and} \quad |\sigma_\gamma\rangle = |22\rangle, \tag{6.17}$$

parameterized by the **mixing angle**

$$\tan\theta = \frac{2A_{1,2}}{\left[(A_{1,1} - A_{2,2}) + \left[4A_{1,2}^2 + (A_{1,1} - A_{2,2})^2\right]^{1/2}\right]}. \tag{6.18}$$

By construction, variation of the angle $\theta \in [0, \pi/2]$ ensures that the scattering lengths a_α, a_β, and a_γ remain constant while the eigenvectors $|\sigma_\alpha\rangle$ and $|\sigma_\beta\rangle$ describe admixtures of the basis states $|11\rangle$ and $|12\rangle_S$.

Let's discuss the results for the first two roots s_0 and s_0, shown in Fig. 6.1 for the hyperradial region $a_\alpha \ll R \ll a_\beta$. When $\theta = 0$, there are two imaginary roots $s_0 = s_1 \approx 0.41370i$, associated with the three-body internal states $|221\rangle$, $|122\rangle$ (plus all other permutations). The root $0.41370i$ is the result for two identical bosons and one dissimilar atom from the single-level problem[2] . When $\theta = \pi/2$, there is only one imaginary root $s_0 \approx 1.00624i$ associated with the three-body configuration $|111\rangle$, which is the single-level root for three identical bosons discussed previously. In

[2] This root can be obtained by setting $C_1 = C_2 \neq C_3$ in the matrix equation (Eq. 5.32).

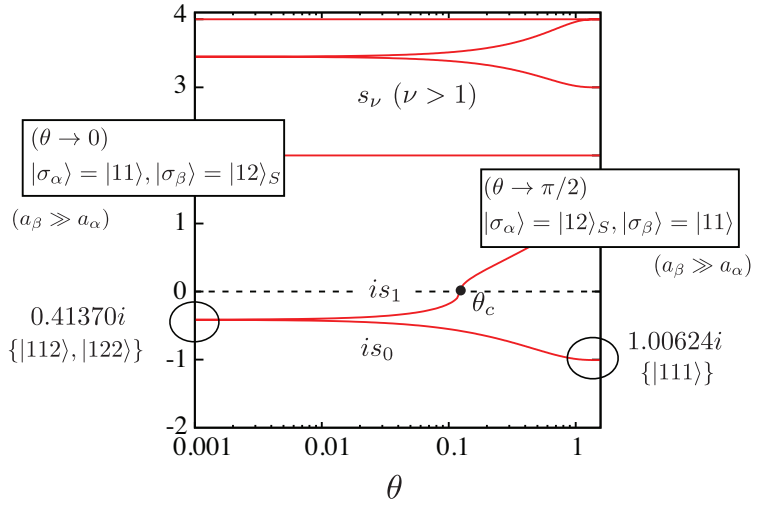

Figure 6.1: The first few roots s_ν obtained for the toy model in the hyperradial region $a_\alpha \ll R \ll a_\beta$. The roots are plotted versus the mixing angle θ.

between these limiting results, the Efimov states are in a *superposition* of internal levels described by the mixing angle (see Fig. 6.2). It is in this **mixing region** that the roots s_0 and s_1 depart from their single-level results and take on **novel roots** for the problem of equal mass bosons which are a mix of the limiting case results from the single-level problem.

The toy model is a result of a unitary transformation, $\hat{A} \to \hat{U}^\dagger \hat{A} \hat{U}$. Equivalently, it is a result of a transformation (rotation) of the basis $\{|11\rangle, |12\rangle_S, |22\rangle\} \to \{|\sigma_\alpha\rangle, |\sigma_\beta\rangle, |22\rangle\}$. What is then the class of unitary transformations which produce novel families of Efimov states? Importantly, the eigenvector of $\hat{A}$ attached to the resonant channel must mix two-body product states under the transformation, which cannot arise from a unitary transformation on the one-body level. Clearly this restricts the set of unitary transformations that produce novel Efimov states, although I don't go into this further here.

There is a simple connection between these results and those from for spin-1, 2, and 3 presented in the following two sections. When the internal levels are composed of the hyperfine spin multiplet there is the additional requirement that the two-body eigenstates be simultaneous eigenstates of both the symmetrization operator and spin operator $\hat{F}^2$. The unitary matrix that diagonalizes the matrix $\hat{F}^2$ carries the product basis $|m_{f_1}\rangle \otimes |m_{f_2}\rangle$ into the $|F_{2\mathrm{B}}, m_{F2\mathrm{b}}\rangle$ basis, and

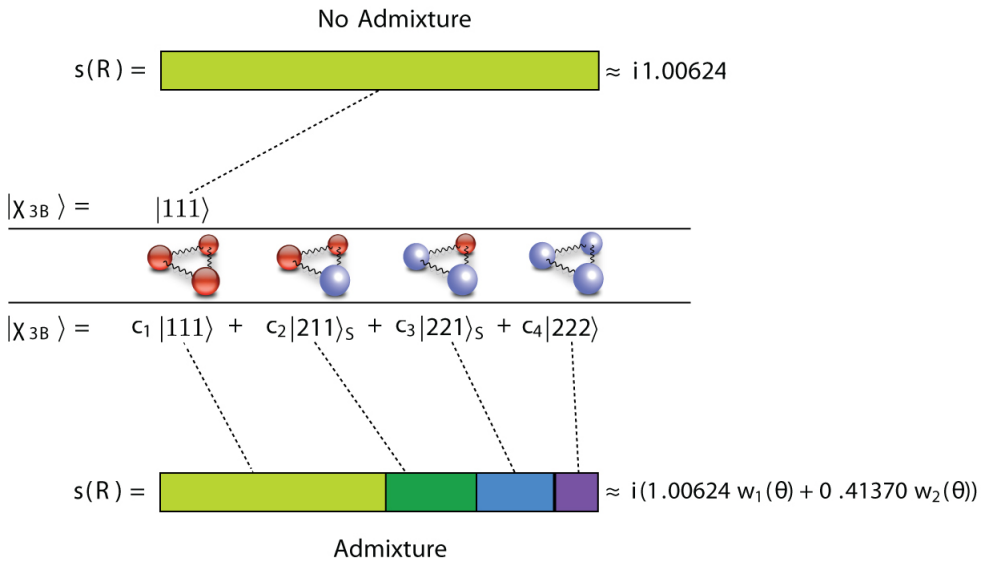

Figure 6.2: The roots $s_\nu(R)$ reflect that the internal state $|\chi_{3B}\rangle$ of the Efimov trimer is in a superposition of internal levels. When there is no admixture, the roots are identical to the single-level problem. When there is nonzero admixture ($c_i \neq 0$), the roots are a weighted average ($w_1(\theta) + w_2(\theta) = 1$) of the single-level roots associated with the individual internal states comprising the superposition. Here, this behavior is shown schematically for the lowest root is_0 which tracks between $i1.00624$ and $i0.41370$ depending on the mixing angle (see the lowest curve of Fig. 6.1).

the elements of this matrix are Clebsch-Gordan coefficients, which is also equivalent to a unitary transformation of the matrix $\hat{A}$. In the toy model, the admixture was set by the mixing angle θ and treated as a free parameter for the purpose of exploring the behavior of the model. In the spinor case, this admixture is set by the values of the Clebsch-Gordan coefficients. As in the toy model, this admixture produces roots s_ν which are associated with three-body spin configurations that can be composed of a linear combination of product state spin functions and are capable of producing novel families of Efimov states.

6.3 Spin-1 systems

This section analyzes the spin-1 three-body problem, focusing on the structure of the three-body potentials and the families of Efimov states. In order to explore the roots of $\det[\hat{S}\hat{Q}\hat{S}^T]$=0 and the physics resulting from them, we assume the relevant scattering lengths for the problem,

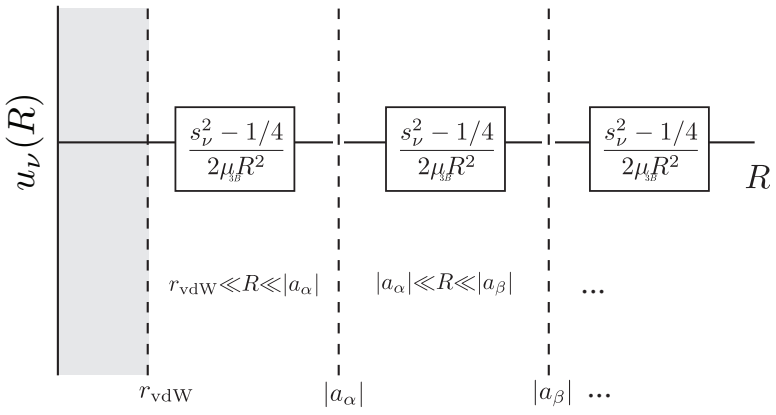

Figure 6.3: Schematic representation of the relevant regions in R of the three-body potentials $u(R)$. The shaded area, $R < r_{\rm vdW}$, represents the region where the three-body potentials are expected to be non-universal. For all other regions, the potentials are universally given by the form in Eq. (**??**) with $s(R) \equiv s$.

$a_{F_{2b}} \equiv \{a_0, a_2, ..., a_{2f}\}$, to differ greatly in magnitude from each other. By doing so, the values for s with a range, say, $|a_\alpha| \ll R \ll |a_\beta|$ is constant and the corresponding values can be easily listed and emphasize the attractive (s imaginary) or repulsive (s real) $1/R^2$ interaction that characterizes the Efimov physics. When this condition of well-separated scattering length magnitudes is not satisfied, one must in general return to the exact solutions of the above transcendental equation. In the regimes considered here, there will exist typically various regions in which a detailed analysis must be performed (see Fig. 6.3). Here this analysis is carried out for every possible case.

Symmetry considerations that allow us to disregard some three-body spin states are less evident than in the two-body case and we begin by analysing the three-body spin functions for $f = 1$ atoms for each value of F_{3b} separately. Here we will consider only states with $M_{F_{3b}} = 0$ but the same considerations also applies for $M_{F_{3b}} \neq 0$.

For $F_{3b} = 0$ one can, by inspection, determine that the corresponding spin function

$$|00(1)\rangle = \frac{|1{-}1\rangle|1\rangle}{\sqrt{3}} - \frac{|10\rangle|0\rangle}{\sqrt{3}} + \frac{|11\rangle|{-}1\rangle}{\sqrt{3}}, \tag{6.19}$$

is antisymmetric under permutations of any two spins. Similar to the two-body case, a three-body antisymmetric spin state requires an antisymmetric spacial wave function in order to form a symmetric total wave function. Since in our model only s-wave interactions are allowed, antisymmetric

three-body states are noninteracting, and we neglect them from our analysis and calculations.

For $F_{3b} = 1$, the analysis is more complicated. Now, there exist three spin states with $F_{3b} = 1$, each one corresponding to the allowed values for F_{2b}. They are given by,

$$|10(0)\rangle = |00\rangle|0\rangle, \tag{6.20}$$

$$|10(1)\rangle = -\frac{|1{-}1\rangle|1\rangle}{\sqrt{2}} + \frac{|11\rangle|{-}1\rangle}{\sqrt{2}}, \tag{6.21}$$

$$|10(2)\rangle = \frac{|2{-}1\rangle|1\rangle}{\sqrt{10/3}} - \frac{|20\rangle|0\rangle}{\sqrt{5/2}} + \frac{|21\rangle|{-}1\rangle}{\sqrt{10/3}}. \tag{6.22}$$

Besides the fact that permutations of spins 1 and 2 are symmetric (F_{2b}=even) or antisymmetric (F_{2b}=odd), no clear symmetry property can be derived by inspection. The three spin functions for $F_{3b} = 1$ can be symmetryzed to form a pair of mixed symmetry states (one symmetric and other antisymmetric with respect to permutations of spins 1 and 2) and a fully symmetric spin state [88], given by

$$|10(0,2)\rangle = \tfrac{2}{3}|10(2)\rangle + \tfrac{\sqrt{5}}{3}|10(0)\rangle. \tag{6.23}$$

Although in our calculations it is crucial include all these states, we determined that collision processes involving three atoms in mixed symmetry states are suppressed at low energies due to stronger centrifugal barriers in the three-body potentials. Therefore, in this case, the $F_{3b} = 1$ totally symmetric state is dominant. For $F_{3b} = 2$ states, the corresponding spin functions

$$|20(1)\rangle = \frac{|1{-}1\rangle|1\rangle}{\sqrt{6}} + \frac{|10\rangle|0\rangle}{\sqrt{3/2}} + \frac{|11\rangle|{-}1\rangle}{\sqrt{6}}, \tag{6.24}$$

$$|20(2)\rangle = -\frac{|2{-}1\rangle|1\rangle}{\sqrt{2}} + \frac{|21\rangle|{-}1\rangle}{\sqrt{2}}, \tag{6.25}$$

form a pair of mixed symmetry states. Similar to $F_{3b} = 1$, we determined that for $F_{3b} = 2$, collision processes involving three atoms in such states are also suppressed at low energies due to stronger centrifugal barriers in the three-body potentials. Consequently, they are neglected for the analysis of collisions between three atoms. For $F_{3b} = 3$, there exists only one spin function

$$|30(2)\rangle = \frac{|2{-}1\rangle|1\rangle}{\sqrt{5}} + \frac{|20\rangle|0\rangle}{\sqrt{5/3}} + \frac{|21\rangle|{-}1\rangle}{\sqrt{5}}, \tag{6.26}$$

that forms a totally symmetric spin state and, therefore, it is included in our analysis.

Let's now derive the transcendental equations that determine s_ν, and consequently the three-body potentials $u_\nu(R)$. For $F_{3\mathrm{b}} = 1$, the spin functions are fully symmetric, as discussed above, and the values for s are determined by solving the transcendental equation,

$$\begin{aligned}&\frac{3^{\frac{1}{4}}(a_0+a_2)s\cot(\frac{\pi}{2}s)}{2^{\frac{1}{2}}R} - \frac{3^{\frac{1}{2}}(a_0a_2)s^2\cot(\frac{\pi}{2}s)^2}{2R^2}\\ &- \frac{2^{\frac{3}{2}}(2a_0+a_2)\sin(\frac{\pi}{6}s)}{3^{\frac{5}{4}}\sin(\frac{\pi}{2}s)R} + \frac{2\ a_0a_2s\cot(\frac{\pi}{2}s)\sin(\frac{\pi}{6}s)}{\sin(\frac{\pi}{2}s)R^2}\\ &+ \frac{16\ a_0a_2\sin(\frac{\pi}{6}s)^2}{3^{\frac{1}{2}}\sin(\frac{\pi}{2}s)^2R^2} = 1. \end{aligned} \tag{6.27}$$

(Imaginary roots can be obtained by mapping $s \to is$.) The above transcendental equation depends on both two-body scattering lengths, a_0 and a_2. For $F_{3\mathrm{b}} = 2$ and 3 the spin states are symmetric and mixed-symmetry states [36], respectively, and the interaction strength s is obtained, respectively, through,

$$\frac{3^{1/4}a_2s\cot(\frac{\pi}{2}s)}{2^{1/2}R} + \frac{2\ 2^{1/2}a_2s\sin(\frac{\pi}{6}s)}{3^{1/4}\sin(\frac{\pi}{2}s)R} = 1, \tag{6.28}$$

and

$$\frac{3^{1/4}a_2s\cot(\frac{\pi}{2}s)}{2^{1/2}R} + \frac{4\ 2^{1/2}a_2s\sin(\frac{\pi}{6}s)}{3^{1/4}\sin(\frac{\pi}{2}s)R} = 1. \tag{6.29}$$

Note that for $F_{3\mathrm{b}} = 2$ and 3 the transcendental equations depend only on a_2. Table 6.1 lists the solutions of Eqs. (6.27)–(6.29) for the regions in R in which the value of s is constant —in Table 6.2 we use $R \ll |a_{\{\mathrm{n}_1,\mathrm{n}_2,\ldots\}}|$ ($|a_{\{\mathrm{n}_1,\mathrm{n}_2,\ldots\}}| \ll R$) as a shorthand for the condition that R must be much less (greater) than all elements in the set $\{|a_{\mathrm{n}_1}|, |a_{\mathrm{n}_2}|, \ldots\}$. Note that we also list the relevant scattering lengths for each value of $F_{3\mathrm{b}}$. For the cases where an imaginary root exists, i.e., when Efimov states are allowed, we list both the imaginary root and the lowest real root. For cases in which an imaginary root does not exist, we list only the lowest real root. Interestly, note that when R is much smaller than all relevant scattering lengths, $R \ll |a_{\{0,2\}}|$, the imaginary root, $s_0 \approx 1.0062i$, is the same than the usual three identical boson problem. For the regions $|a_0| \ll R \ll |a_2|$ and $|a_2| \ll R \ll |a_0|$, i.e., when the a_0 and a_2 are not effectively resonant, respectively, the possible

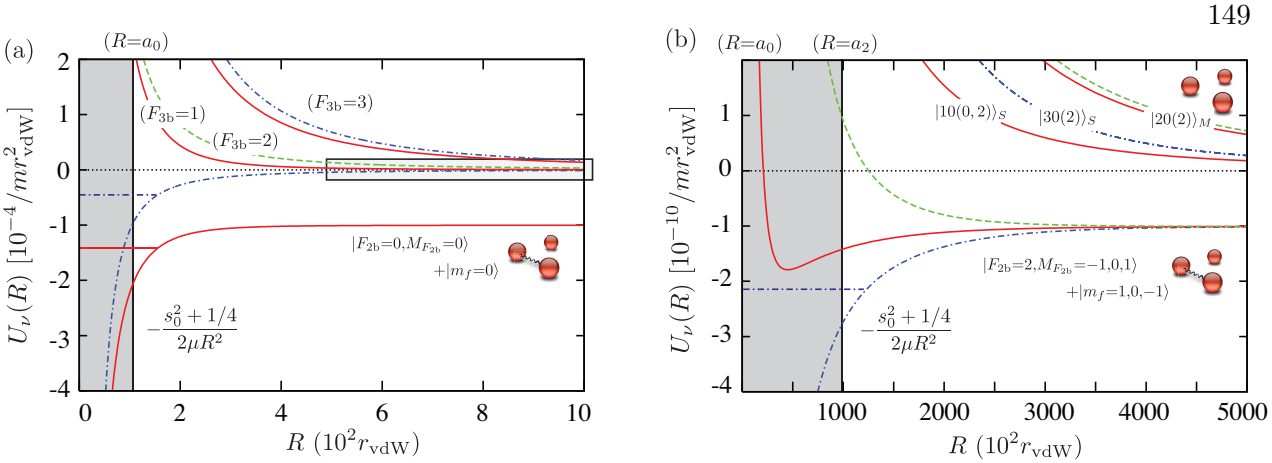

Figure 6.4: $F_{3b} = 1$ (red solid line), 2 (green dashed line), and 3 (blue dash-dotted line) hyperspherical adiabatic potentials for $f = 1$ atoms with $a_0 = 10^2 r_{vdW}$ and $a_2 = 10^5 r_{vdW}$. (a) For $R \leq \{a_0, a_2\}$ (shaded region) two attractive potentials exist (both with $s_0 \approx 1.0062i$), allowing for two families of Efimov states, and for $R > a_0$, one of these potentials turns into an atom-dimer channel $|F_{2b} = 0, M_{F_{2b}} = 0\rangle|f = 1, m_f = 0\rangle$. (b) For $a_0 \leq R \leq a_2$ (shaded region), only one family of Efimov states exists ($s_0 \approx 1.0062i$), and for $R \gg a_2$ three (asymptotically degenerate) potentials describe atom-dimer channels, $|F_{2b} = 2, M_{F_{2b}} = -1, 0, 1\rangle|f = 1, m_f = 1, 0, -1\rangle$.

roots can be different than the ones obtained for the usual bosonic problem. These new roots result from the fact that the spin functions (Eq. (6.15))are superpositions of single particle product states as discussed in the toy model problem, Sec. 6.2 (see Fig. 6.2.)

Figure 6.4 shows the three-body potentials for $f = 1$ as a result of solving Eq. (6.5) for the allowed values of F_{3b}. The scattering lengths chosen illustrate only one of a pair of possibilities for the relative strengths of the scattering lengths. The hyperradius is written in terms of the typical range of interatomic interactions, r_{vdW}. The totally symmetric $F_{3b} = 1, 3$ states are associated with a pair of attractive potentials for $R \ll \{a_0, a_2\}$. This pair is associated with $s_0 \approx 1.0062i$, and allow for the coexistence of two families of Efimov states (represented in Fig. 6.4 by the horizontal solid and dash-dotted lines.) As the hyperradius exceeds a_0, the $F_{3b} = 1$ attractive potential becomes an atom-dimer channel for collisions between the dimer $|F_{2b} = 0, M_{F_{2b}} = 0\rangle$ with energy $-1/ma_0^2$ and a free atom in the $|m_f = 0\rangle$ state. In the intermediate region $a_0 \ll R \ll a_2$, only the Efimov potential in the $F_{3b} = 3$ state remains and is associated with $s_0 \approx 1.0062i$. For $a_2 \ll R$, the $F_{3b} = 3$ Efimov potential joins repulsive barriers from $F_{3b} = 1, 2$ in an atom-dimer channel

Table 6.1: Values of s_ν relevant for f=1 and 2 spinor condensates covering all possible regions of R and for different magnitudes of the relevant scattering lengths. (The $f = 1, 2$ values are from Ref. [36]) We list the lowest few values of s_ν for each $F_{3\mathrm{b}}$ and their multiplicity (superscript) if greater than one. Below, we use $R \ll |a_{\{\mathrm{n}_1,\mathrm{n}_2,\ldots\}}|$ ($|a_{\{\mathrm{n}_1,\mathrm{n}_2,\ldots\}}| \ll R$) as a shorthand for the condition that R must be much less (greater) than all elements in the set $\{|a_{\mathrm{n}_1}|, |a_{\mathrm{n}_2}|, \ldots\}$.

$(f = 1)$ Relevant $a_{F_{2\mathrm{b}}}$	$F_{3\mathrm{b}} = 1$ $\{a_0, a_2\}$	$F_{3\mathrm{b}} = 2$ $\{a_2\}$	$F_{3\mathrm{b}} = 3$ $\{a_2\}$
$R \ll \lvert a_{\{0,2\}}\rvert$	$1.0062i, 2.1662$	2.1662	$1.0062i, 4.4653$
$\lvert a_0\rvert \ll R \ll \lvert a_2\rvert$	0.7429	2.1662	$1.0062i, 4.4653$
$\lvert a_2\rvert \ll R \ll \lvert a_0\rvert$	0.4097	4	2
$R \gg \lvert a_{\{0,2\}}\rvert$	2	4	2

$(f = 2)$ Relevant $a_{F_{2\mathrm{b}}}$	$F_{3\mathrm{b}} = 0$ $\{a_2\}$	$F_{3\mathrm{b}} = 1$ $\{a_2\}$	$F_{3\mathrm{b}} = 2$ $\{a_0, a_2, a_4\}$	$F_{3\mathrm{b}} = 3$ $\{a_2, a_4\}$
$R \ll \lvert a_{\{0,2,4\}}\rvert$	$1.0062i, 4.4653$	2.1662	$1.0062i, 2.1662^{(2)}$	$1.0062i, 2.1662$
$\lvert a_0\rvert \ll R \ll \lvert a_{\{2,4\}}\rvert$	$1.0062i, 4.4653$	2.1662	0.49050	$1.0062i, 2.1662$
$\lvert a_2\rvert \ll R \ll \lvert a_{\{0,4\}}\rvert$	2	4	$0.7473i, 2.1662$	1.1044
$\lvert a_4\rvert \ll R \ll \lvert a_{\{0,2\}}\rvert$	$1.0062i, 4.4653$	2.1662	$0.3788i, 2.1662$	$0.5528i, 3.5151$
$\lvert a_{\{0,2\}}\rvert \ll R \ll \lvert a_4\rvert$	2	4	0.97895	1.1044
$\lvert a_{\{0,4\}}\rvert \ll R \ll \lvert a_2\rvert$	$1.0062i, 4.4653$	2.1662	1.3173	$0.5528i, 3.5151$
$\lvert a_{\{2,4\}}\rvert \ll R \ll \lvert a_0\rvert$	2	4	0.68609	2
$R \gg \lvert a_{\{0,2,4\}}\rvert$	2	4	2	2

$(f = 2)$ Relevant	$F_{3\mathrm{b}} = 4$ $\{a_2, a_4\}$	$F_{3\mathrm{b}} = 5$ $\{a_4\}$	$F_{3\mathrm{b}} = 6$ $\{a_4\}$
$R \ll \lvert a_{\{0,2,4\}}\rvert$	$1.0062i, 2.1662$	2.1662	$1.0062i, 4.4653$
$\lvert a_0\rvert \ll R \ll \lvert a_{\{2,4\}}\rvert$	$1.0062i, 2.1662$	2.1662	$1.0062i, 4.4653$
$\lvert a_2\rvert \ll R \ll \lvert a_{\{0,4\}}\rvert$	0.66080	2.1662	$1.0062i, 4.4653$
$\lvert a_4\rvert \ll R \ll \lvert a_{\{0,2\}}\rvert$	0.52186	4	2
$\lvert a_{\{0,2\}}\rvert \ll R \ll \lvert a_4\rvert$	0.66080	2.1662	$1.0062i, 4.4653$
$\lvert a_{\{0,4\}}\rvert \ll R \ll \lvert a_2\rvert$	0.52186	4	2
$\lvert a_{\{2,4\}}\rvert \ll R \ll \lvert a_0\rvert$	2	4	2
$R \gg \lvert a_{\{0,2,4\}}\rvert$	2	4	2

Table 6.2: Values of s_ν relevant for $f = 3$ spinor condensates covering all possible regions of R and for different magnitudes of the relevant scattering lengths. (The $f = 3$ values are from Ref. [37].) We list the lowest few values of s_ν for each $F_{3\mathrm{b}}$ and their multiplicity (superscript) if greater than one. Below, we use $R \ll |a_{\{\mathrm{n}_1,\mathrm{n}_2,\ldots\}}|$ ($|a_{\{\mathrm{n}_1,\mathrm{n}_2,\ldots\}}| \ll R$) as a shorthand for the condition that R must be much less (greater) than all elements in the set $\{|a_{\mathrm{n}_1}|, |a_{\mathrm{n}_2}|, \ldots\}$.

$(f = 3)$ Relevant $a_{F_{2\mathrm{b}}}$	$F_{3\mathrm{b}} = 1$ $\{a_2, a_4\}$	$F_{3\mathrm{b}} = 2$ $\{a_2, a_4\}$	$F_{3\mathrm{b}} = 3$ $\{a_0, a_2, a_4, a_6\}$	$F_{3\mathrm{b}} = 4$ $\{a_2, a_4, a_6\}$	$F_{3\mathrm{b}} = 5$ $\{a_2, a_4, a_6\}$
$R \ll \lvert a_{\{0,2,4,6\}}\rvert$	$1.0062i, 2.1662$	$2.1662^{(2)}$	$1.0062i^{(2)}, 2.1662^{(2)}$	$1.0062i, 2.1662^{(2)}$	$1.0062i, 2.1662^{(2)}$
$\lvert a_0\rvert \ll R \ll \lvert a_{\{2,4,6\}}\rvert$	$1.0062i, 2.1662$	$2.1662^{(2)}$	$1.0062i, 0.3420$	$1.0062i, 2.1662^{(2)}$	$1.0062i, 2.1662^{(2)}$
$\lvert a_2\rvert \ll R \ll \lvert a_{\{0,4,6\}}\rvert$	0.6608	2.1662	$1.0062i, 0.5469$	0.8754	0.2588
$\lvert a_4\rvert \ll R \ll \lvert a_{\{0,2,6\}}\rvert$	0.5219	2.1662	$1.0062i, 1.1901$	$0.9352i, 2.1662$	$0.6678i, 2.1662$
$\lvert a_6\rvert \ll R \ll \lvert a_{\{0,2,4\}}\rvert$	$1.0062i, 2.1662$	$2.1662^{(2)}$	$1.0062i, 0.4112i$	$0.4309i, 2.1662$	$0.3351i$
$\lvert a_{\{0,2\}}\rvert \ll R \ll \lvert a_{\{4,6\}}\rvert$	0.6608	2.1662	$0.6521i, 1.0098$	0.8754	0.2588
$\lvert a_{\{0,4\}}\rvert \ll R \ll \lvert a_{\{2,6\}}\rvert$	0.5219	2.1662	$0.6080i, 1.6045$	$0.9352i, 2.1662$	$0.6678i, 2.1662$
$\lvert a_{\{0,6\}}\rvert \ll R \ll \lvert a_{\{2,4\}}\rvert$	$1.0062i, 2.1662$	2.1662	$0.9666i, 1.1343$	$0.4309i, 2.1662$	$0.3351i, 2.1662$
$\lvert a_{\{2,4\}}\rvert \ll R \ll \lvert a_{\{0,6\}}\rvert$	2	$4^{(2)}$	$0.5858i, 1.7691$	1.0111	0.9552
$\lvert a_{\{2,6\}}\rvert \ll R \ll \lvert a_{\{0,4\}}\rvert$	0.6608	2.1662	$0.9100i, 1.1558$	1.6693	1.2189
$\lvert a_{\{4,6\}}\rvert \ll R \ll \lvert a_{\{0,2\}}\rvert$	0.5219	2.1662	$0.4289i, 1.2015$	$0.0803i, 3.3774$	0.8199
$\lvert a_{\{0,2,4\}}\rvert \ll R \ll \lvert a_6\rvert$	2	4	0.9984	1.0111	0.9552
$\lvert a_{\{0,2,6\}}\rvert \ll R \ll \lvert a_4\rvert$	0.6608	2.1662	$0.6415i, 2$	1.6693	1.2189
$\lvert a_{\{0,4,6\}}\rvert \ll R \ll \lvert a_2\rvert$	0.5219	2.1662	0.6392	$0.0803i, 3.3774$	0.8199
$\lvert a_{\{2,4,6\}}\rvert \ll R \ll \lvert a_0\rvert$	2	4	0.7819	2	2
$R \gg \lvert a_{\{0,2,4,6\}}\rvert$	2	$4^{(2)}$	$2^{(2)}$	2	2

$(f = 3)$ Relevant $a_{F_{2\mathrm{b}}}$	$F_{3\mathrm{b}} = 6$ $\{a_4, a_6\}$	$F_{3\mathrm{b}} = 7$ $\{a_4, a_6\}$	$F_{3\mathrm{b}} = 8$ $\{a_6\}$	$F_{3\mathrm{b}} = 9$ $\{a_6\}$
$R \ll \lvert a_{\{0,2,4,6\}}\rvert$	$1.0062i, 2.1662$	$1.0062i, 2.1662$	2.1162	$1.0062i, 4.4653$
$\lvert a_0\rvert \ll R \ll \lvert a_{\{2,4,6\}}\rvert$	$1.0062i, 2.1662$	$1.0062i, 2.1662$	2.1162	$1.0062i, 4.4653$
$\lvert a_2\rvert \ll R \ll \lvert a_{\{0,4,6\}}\rvert$	$1.0062i, 2.1662$	$1.0062i, 2.1662$	2.1162	$1.0062i, 4.4653$
$\lvert a_4\rvert \ll R \ll \lvert a_{\{0,2,6\}}\rvert$	1.1329	0.6372	2.1162	$1.0062i, 4.4653$
$\lvert a_6\rvert \ll R \ll \lvert a_{\{0,2,4\}}\rvert$	$0.5842i, 3.5329$	0.5491	4	2
$\lvert a_{\{0,2\}}\rvert \ll R \ll \lvert a_{\{4,6\}}\rvert$	$1.0062i, 2.1662$	$1.0062i, 2.1662$	2.1162	$1.0062i, 4.4653$
$\lvert a_{\{0,4\}}\rvert \ll R \ll \lvert a_{\{2,6\}}\rvert$	1.1329	0.6372	2.1162	$1.0062i, 4.4653$
$\lvert a_{\{0,6\}}\rvert \ll R \ll \lvert a_{\{2,4\}}\rvert$	$0.5842i, 3.5329$	0.5491	4	2
$\lvert a_{\{2,4\}}\rvert \ll R \ll \lvert a_{\{0,6\}}\rvert$	1.1329	0.6372	2.1162	$1.0062i, 4.4653$
$\lvert a_{\{2,6\}}\rvert \ll R \ll \lvert a_{\{0,4\}}\rvert$	$0.5842i, 3.5329$	0.5491	4	2
$\lvert a_{\{4,6\}}\rvert \ll R \ll \lvert a_{\{0,2\}}\rvert$	2	2	4	2
$\lvert a_{\{0,2,4\}}\rvert \ll R \ll \lvert a_6\rvert$	1.1329	$.6372$	2.1162	$1.0062i, 4.4653$
$\lvert a_{\{0,2,6\}}\rvert \ll R \ll \lvert a_4\rvert$	$0.5842i, 3.5329$	0.5491	4	2
$\lvert a_{\{0,4,6\}}\rvert \ll R \ll \lvert a_2\rvert$	2	2	4	2
$\lvert a_{\{2,4,6\}}\rvert \ll R \ll \lvert a_0\rvert$	2	2	4	2
$R \gg \lvert a_{\{0,2,4,6\}}\rvert$	2	2	4	2

$|F_{2b} = 2, m_f = -1, 0, 1\rangle|m_f = -1, 0, 1\rangle$, which introduces the interesting possibility of studying atom-dimer spin mixtures [36].

As a final note, if a small (but finite) magnetic field is applied, the Efimov states in $F_{3b} = 1$ and 3 can interact creating an overlapping series of states. The physics we study in this chapter is that of zero applied magnetic field, which implies that the hyperfine angular momentum is conserved. We make no claim about the mechanism by which the scattering lengths are controlled; rather we explore the parameter space of all permutations of the relative strengths of the scattering lengths. In the case of a small applied magnetic field, Efimov states associated with different three-body hyperfine angular momentum states can be coupled, thus creating an overlapping series. Such controllability can produce **ultra-long-lived states** [252] whose presence can affect the spin dynamics of the condensate depending on the short-range physics. In the following section, the case of higher spin is analyzed where many families of Efimov states with additional novel roots appear, along with the presence of overlapping series of Efimov states in the *absence* of an applied field.

6.4 Spin-2 and -3 Systems

In this section, the three-body potentials and Efimov states for $f = 2$ and 3 spinor condensates are detailed. For spin-2 there are three rotationally invariant scattering lengths $\{a_0, a_2, a_4\}$ and $F_{3b} = 0...6$. The three-body spin states [Eq. (6.15)] for $F_{3b} = 0$, 2, 3, 4, and 6 are symmetric while for $F_{3b} = 1$ and 5 they are of mixed-symmetry. Shown in Table 6.1 are the relevant roots s_ν and relevant scattering lengths for each F_{3b} state. Similar to the $f = 1$ case, for $f = 2$ the roots for the regions in which R is smaller than all relevant scattering lengths correspond to the roots for the usual identical bosons problem. All other regions display new roots. For instance, within the region $|a_4| \ll R \ll |a_{\{0,2\}}|$ imaginary roots $s_0 \approx 0.3788i$ ($F_{3b} = 2$) and $s_0 \approx 0.5528i$ ($F_{3b} = 3$) can be found. These values are novel in the context of the three-body problem with identical masses.

Although typically the scattering lengths for most alkali species are small (comparable to r_{vdW}), one notable exception is ^{85}Rb with $f = 2$. For that system $a_0 \approx -8.97 r_{vdW}$, $a_2 \approx -6.91 r_{vdW}$,

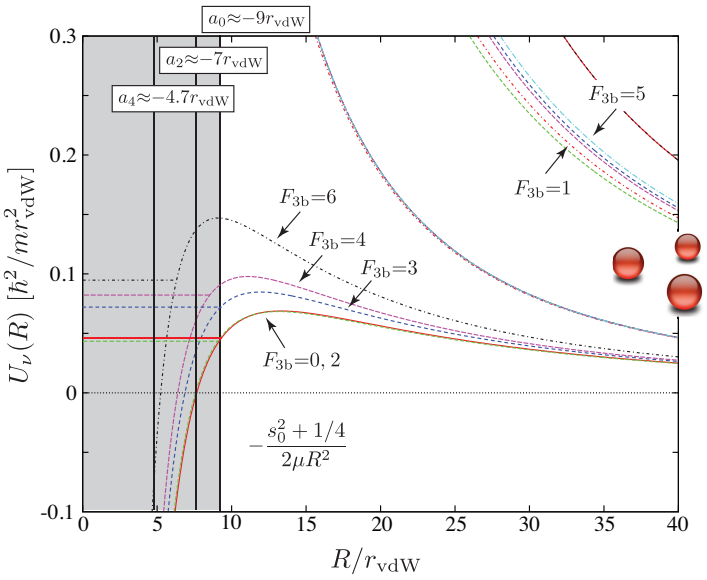

Figure 6.5: $F_{3b} = 0$ (red solid lines), 1 (red dot-dashed lines), 2 (green dashed lines), 3 (blue dashed lines), 4 (purple dashed lines), 5 (cyan dot-dashed lines) and 6 (black dot-dashed lines) hyperspherical adiabatic potentials for $f = 2$ ^{85}Rb atoms with $a_0 \approx -8.97r_{\rm vdW}$, $a_2 \approx -6.91r_{\rm vdW}$, and $a_4 \approx -4.73r_{\rm vdW}$. Note that the potentials for the mixed-symmetry states, $F_{3b} = 1$ and 5, do not display an Efimov potential.

and $a_4 \approx -4.73r_{\rm vdW}$ [238, 239]. Recent experimental and theoretical advances with alkali atoms have determined that the value of the scattering length at which the first Efimov state appears is approximately $-10r_{\rm vdW}$ [175, 176, 177, 178, 179, 180, 181, 182, 183, 184, 185, 186, 187, 188, 189, 190, 191, 192, 193, 194, 195, 196, 197, 198, 199, 200]. Therefore, for $f = 2$ ^{85}Rb spinor condensates, it is not unreasonable to expect that the Efimov physics can strongly impact the spin dynamics and many-body physics. In Fig. 6.5, the hyperspherical adiabatic three-body potentials for spin-2 ^{85}Rb are shown. As one can see, the potentials for $F_{3b} = 0$, 2, 3, 4 and 6 states support an attractive Efimov potentials for distances smaller than and comparable to the relevant scattering lengths, but forming a repulsive barrier as the hyperradius exceeds those distances. The potentials for the mixed-symmetry states, $F_{3b} = 1$ and 5, are completely repulsive and support no Efimov states

Finally, for three identical spin-3 atoms there are four rotationally invariant scattering lengths $\{a_0, a_2, a_4, a_6\}$ and $F_{3b} = 0, ..., 9$. For spin-3, the $F_{3b} = 0$ spin state is fully anti-symmetric, while $F_{3b} = 2$ and 8 states are mixed-symmetry states and all others being fully symmetric states.

Candidates for interesting Efimov physics (i.e., some of the relevant scattering lengths are large) are ^{85}Rb, ^{133}Cs and ^{7}Li. In Table 6.2, the spin-3 values of s_ν for all values of $F_{3\mathrm{b}}$ and all hyperradial ranges are presented in addition to the spin-2 and spin-1 results from Ref. [36]. Where the spin-2 analysis produced only a few novel imaginary values of s_ν, there are many more families Efimov states for spin-3. Of particular note is the appearance of overlapping Efimov series for $F_{3\mathrm{b}} = 3$ when $R \ll |a_{\{0,2,4,6\}}|$ and $|a_{\{6\}} \ll R \ll |a_{\{0,2,4\}}|$. Even at zero applied field these overlapping states have the potential of being ultra-long lived [252] depending on the short-range physics. Analysis of these overlapping states is beyond the scope of the present work. The final section concludes with an analysis of the signature of spinor Efimov physics in the three-body elastic phase shift.

6.5 Signatures of Spinor Efimov Physics in the Elastic Three-Body Phase Shift

In this section, I extend the WKB model from Sec. 5.4.1 to the spinor three-body problem to derive the functional dependence of the elastic three-body phase shift for a given value of total hyperfine spin on Efimov physics. This is done here for only one example as the procedure can be easily generalized (see Ref. [36] for tabulated expressions.) The main new feature is the presence of scattering lengths associated with two-body collisions in a total hyperfine state. There are then many possible reflections as the potential changes at hyperadii comparable to the magnitude of the relevant scattering lengths. For spin-1 atoms with $F_{3B} = 1$, $a_0 < 0$, $a_2 < 0$, and $|a_0| \gg |a_2|$ there are three hyperradial regions as shown in Fig. 6.6 and therefore three possible pathways. Pathway one reflects after tunneling from the classical turning point to $R \sim |a_0|$

$$\tan(\delta_I) \approx K|a_0|^{2l+1}. \tag{6.30}$$

The second pathway tunnels to the region $R \sim |a_2|$ and reflects before entering the inner well

$$\begin{aligned}\tan(\delta_{II}) &\approx \left(-2\left\{\int_{|a_2|}^{|a_0|}\sqrt{\frac{s_1^2}{R^2}}dR + \int_{|a_0|}^{1/K}\sqrt{\frac{l_{eff}(l_{eff}+1)}{R^2}+\frac{1/4}{R^2}}dR\right\}\right), \\ &\approx \left(\frac{a_2}{a_0}\right)^{2s_1}(K|a_0|^{2l_{eff}+1}).\end{aligned} \tag{6.31}$$

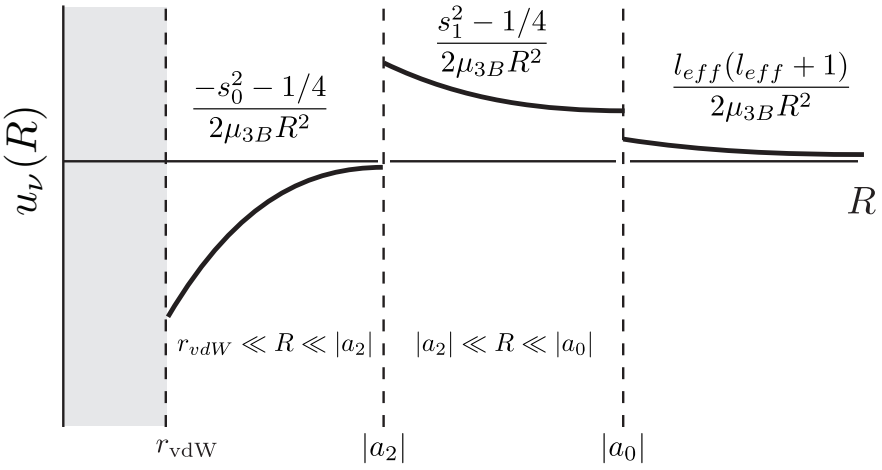

Figure 6.6: Schematic of the three-body potential for spin-1 with total three-body hyperfine spin $F_{3B} = 1$ and hyperfine scattering lengths $|a_0| \gg |a_2|$. The relevant roots are $s_0 \approx i10062$ and $s_1 \approx 0.4097$ from Table 6.1.

And the third pathway tunnels all of the way to the inner well and is reflected at $R_0 \sim r_{\rm vdW}$

$$\tan(\delta_{III}) \approx \left(\frac{a_2}{a_0}\right)^{2s_1} (K|a_0|^{2l_{eff}+1}) \tan\left(s_0 \ln\left(\frac{|a_2|}{R_0}\right) + \Delta\right). \tag{6.32}$$

The threshold behavior of the contribution of Efimov physics to the elastic three-body phase shift for $l_{eff} = 3/2$ is therefore

$$-\frac{\tan(\delta_I + \delta_{II} + \delta_{III})}{k^4} \xrightarrow[K\to 0]{} \gamma a_0^4 + \left(\alpha + \beta \tan\left[s_0 \ln\left(\frac{|a_2|}{R_0}\right) + \Delta\right]\right)\left(\frac{|a_2|}{|a_0|}\right)^{2s_1} a_0^4 = A_{3B}^{(1)} \tag{6.33}$$

where the subscript denotes the three-body scattering length for $F_{3B} = 1$, and α, β, and γ are undetermined proportionality constants. When compared to the single-level result (Eq. 5.66), there is now additional dependence on the ratio of hyperfine scattering lengths. This ratio arises from the part of the calculation which accounted for the tunneling between $R \sim |a_0|$ and $R \sim |a_2|$, and in the limiting case $|a_0| \gg |a_2|$ is responsible for the attenuation of the flux that reaches the inner well.

6.6 Conclusion

When individual atoms have access to degenerate internal levels, the spectrum of Efimov states is modified from the single-level results of Chapter 5. The strongly-interacting spinor Bose

gas is a regime which has yet to be experimentally accessed, and so the results from this chapter for the Efimov physics in this many-body system are of a speculative nature. There are however many exciting features on the few-body level absent from the single-level problem including possibly long-lived Efimov states and novel geometric scalings. In Chapter 7, I detail how the existence of Efimov states can impact both the superfluid phase of the condensate and also the ground state magnetic structure.

There are still many unknown aspects of the relatively unstudied spinor three-body problem including the Efimov physics for heterogenous mixtures, the Efimov spectrum in the infinite spin limit [3] , and the solution for finite-range potentials where care must be taken when enforcing a particular symmetrization through boundary conditions of the wave function. These interesting avenues await future investigation.

[3] This is a classical limit in the sense that the angular momentum can be thought of as a continuous variable.

Chapter 7

One, Two, Three, Many: Few Body Physics in Strongly Interacting Bose Gases

This chapter contains results published in Refs. [36, 37]. I review some known results from T. Köhler and K. Burnett in Refs. [52, 53] in some detail to attempt to make this chapter as self-contained as possible.

This is the final chapter in a series of three focused on strongly-interacting Bose gases. In Chapters 5–6, I discussed the three-body problem for ultracold bosons, the bound state spectrum of Efimov states for single and multiple internal levels, and the signature of Efimov physics in the continuum along with the general problem of understanding the three-body elastic phase shift. In this chapter, I generalize the many-body theory developed in Chapter 4 to include few-body physics beyond the two-atom level. This is done systematically in this chapter through introduction of the method of cumulants. Along the way, the GPE from Chapter 4 is rederived, and many of the tacit assumptions of the derivation in Sec. 4.1 become exposed in this more general framework. This chapter finishes with a discussion of the emergence of Efimov physics in the superfluid and magnetic ordering of a strongly-interacting Bose gas. Before jumping in, however, it is instructive to provide some general context from the field of strongly-interacting systems, which is provided in the remainder of this introduction. Sec. 7.1 adds to the length scale discussion fro the beginning of Chapter 5 to include the length scale of the inter particle separation $n^{-1/3}$.

Nobel-prize winning physicist P. W. Anderson famously quipped: "More is different" [253] in attack of the reductionist line of thinking that the only scientists studying anything fundamental are

those working on fundamental laws. Strongly-correlated[1] systems are a sharp rebuke to this reductionist philosophy, including such important examples as quark-gluon plasmas, high-temperature and organic superconductors, and clouds of strongly-interacting ultracold atoms [254]. A common theme of these systems is that they cannot be understood by extrapolating the behavior of one or two non-interacting particles to understand the bulk properties of the system. To understand these materials and their potential applications, the interactions between particles must be taken into account through novel approaches. However, successful efforts in this area are frustratingly scarce.

For ultracold strongly-interacting Bose gases in the unitary regime, where individual atoms are interacting as strongly as possible and are therefore highly correlated, even the physics of three atoms is different: When two atoms wont bind, an infinite number of Efimov trimers appear in the gas, as discussed in Chapters 5–6. This regime is fraught by the disastrous scaling of the three-body inelastic loss rate, discussed in the beginning of Chapter 5, growing as the scattering length raised to the fourth power. The strongly-interacting Bose gas should be considered therefore as a quasi-stable system which will eventually decay over the characteristic time scale for three-body recombination. Nevertheless, recent results from JILA using ^{85}Rb [59] indicate that through a quench of the interaction strength to the unitary limit, this timescale is exceeded by the relaxation rate to local thermodynamic equilibrium, and so the thermodynamics of the unitary Bose gas are currently of considerable interest.

This chapter aims at the question of how knowing the correlations of three atoms can act as a platform to improve our understanding of ultracold strongly-interacting many-body systems, and so we begin in the neighborhood of a Feshbach resonance where the scattering length is many times r_{vdW} but still smaller than the interaparticle spacing $n^{-1/3}$, so that much of the machinery of mean-field theory from Chapter 4 can be retained and extended. These length scale matters are addressed in the following section.

[1] In this chapter, the 'strongly-correlated' is used interchangeably with 'strongly-interacting.'

7.1 Time and Length Scales in Strongly-Interacting Bose Gases

Referring to a many-body system as strongly-interacting or strongly-correlated requires qualification. This distinction is characterized by three length scales: the scattering length a_0, the range of the potential given by the van der Waals length $r_{\rm vdW}$, and the inter particle spacing $n^{-1/3}$. I discuss appropriate theories for different relevant magnitudes of these length scales.

The limit $a_0 \ll n^{-1/3}$ is the regime where the theories of Chapter 3–4 are appropriate as the dynamics of the mean-field are temporally separated from the duration of a single collision. Here, interactions between atoms can be well approximated by scattering results in vacuum. Additionally, atoms are spaced at distances which are larger than the range of the potential $r_{\rm vdW} \ll n^{-1/3}$ and so short range correlations are unimportant.

In the limit $a_0 \gg r_{\rm vdW}$, Efimov trimers begin to form past $|a_0| \approx 10 r_{\rm vdW}$, introducing universal physics into the problem. In this thesis, this limit signals the regime of strongly-interacting Bose gases as discussed earlier in Chapter 5. In the unitary limit $n a_0^3 \gg 1$, the basis of the mean-field theories of Chapter 2 breaks down as the free flight time of individual atoms is not temporally separated from the duration of a collision. It is no longer appropriate to consider the collisions in the condensate as taking place in vacuum, and medium effects must be incorporated somehow; this has been qualitatively accounted for on the few-body level by introducing an artificial harmonic trap with oscillator length proportional to the inter particle spacing (see Refs [255, 256, 257, 258]). There are (at least) three viewpoints on how to address the unitary Bose gas:

(1) Feign ignorance and proceed with the weakly-interacting theory of Chapter 2 by tuning the scattering length to arbitrarily large values. This theory diverges with increasing scattering length.

(2) Formulate a beyond mean-field theory of the gas.

(3) Utilize a two-channel many-body model that includes the closed-channel bound state physics responsible for the energy dependence of the scattering observables and large scattering

length near resonance. Such a theory has been formulated for bosons and fermions near a Feshbach resonance, referred to as the theory of **resonance superfluidity** (see for instance Refs. [54, 55, 56]) and a two-channel mean-field-like set of equations established based on the smallness of the effective range, r_0 and the background scattering length, a_{bg} compared to the inter particle spacing $n^{-1/3}$. This theory was highly successful over a decade ago studying the unitary Fermi gas and transitions smoothly through the resonance.

In the outlook portion of the conclusion of this thesis, I discuss a blueprint of the third viewpoint appropriate for the unitary Bose gas. This theory is attractive as it is both divergenceless, mean-field like, and directly marries multichannel scattering calculations including bound state physics with many-body theories of strongly-interacting gases.

It is however important to first discuss strongly interacting Bose gases when na_0^3 is still less than unity and sketch the impact of universal three-body physics on the thermodynamics of the many-body state. In this regime, interactions are strong but still separated in time. This regime is the subject of this chapter, and I refer to it simply as the strongly-interacting Bose gas, reserving the classification of unitary Bose gas for the case where the diluteness parameter exceeds unity. This regime allows the retention of mean-field concepts from Chapter 2, but now the theory must be augmented to include the effects of three-body physics. Furthermore, an additional length scale, l_{3B}, associated with the size of the Efimov trimer and additional timescales associated with the lifetime of the trimer and the timescale for inelastic loss from three-body recombination must enter the theory. These relevant length scales are summarized in Fig. 7.1. I discuss how the extension of the mean-field theory from Chapter 4 can be extended to include three-body physics in the following section.

The final limit, $r_0 \approx n^{-1/3}$, is appropriate to fluid states like liquid Helium. For these systems, the intricate details of the interactions at short distances where the effects of electronic cloud repulsion are relevant, and zero-range models are not appropriate. In this regime, hydrodynamical theories can be formulated based on bulk flow of a fluid consistent with the symmetries and

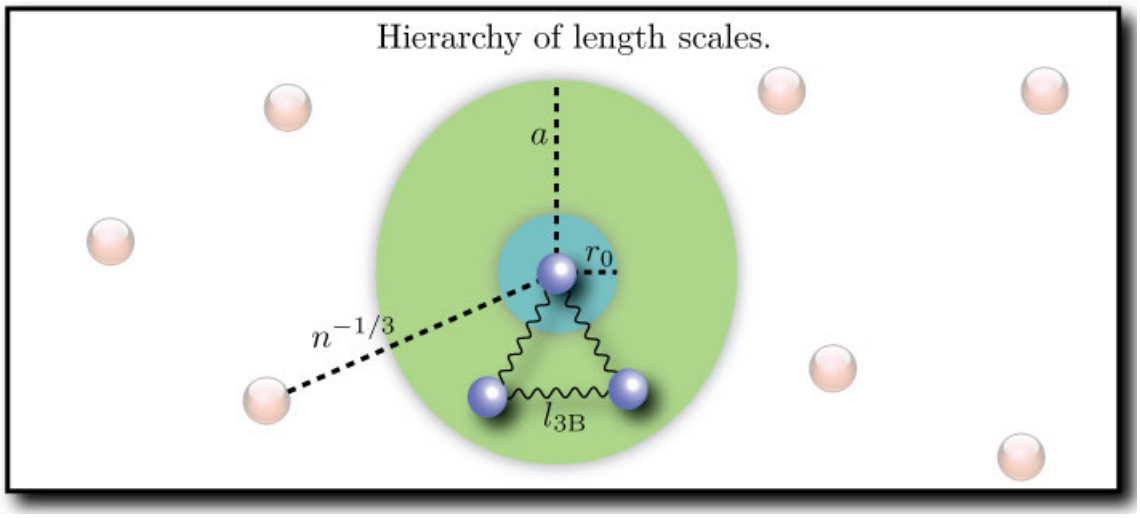

Figure 7.1: Relevant length scales in the strongly-interacting Bose gas (not drawn to scale.) The blue atoms are part of an Efimov trimer with characteristic length scale l_{3B}. The effective range r_0 is less than the scattering length, which is less than the interparticle spacing, $r_0 \ll a_0 \ll n^{-1/3}$, and the inter particle spacing is indicated between a blue atom and a red atom of the background gas.

conservation laws of the system (see the early seminal theoretical works [25, 26, 28] and a recent historical perspective [118]).

7.2 The Cumulant Expansion Method

In this section, I generalize the theory of the weakly interacting Bose gases, by outlining a complete set of coupled equations for the dynamics correlations to all orders, which is based on the Bogoliubov-Born-Green-Yvon-Kirkwood (BBGYK) hierarchy and cumulant expansion method (see Fig. 7.2 for the chain of dependence) [51, 259, 97]. I then discuss the structure and various limits of these equations in Sec. 7.2.1. These equations must be truncated to formulated a theory which is closed, and I discuss self-consistent solutions from first order truncation in Sec. 7.3, rederiving the GPE and its extension including quartic nonlinearities with coupling strength depending on three-body scattering quantities, tracing the work of T. Köhler in Refs. [52, 53]. This three-body GPE forms the basis for the third section, Sec. 7.4, focused on the emergence of three-body physics in the superfluid and magnetic ground state phases of the strongly-interacting Bose gas.

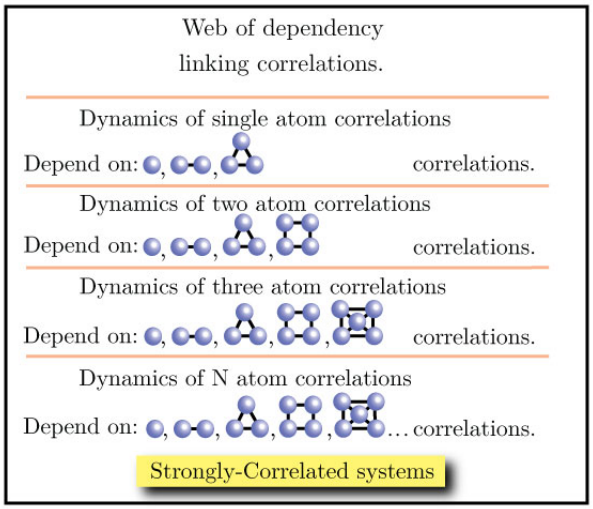

Figure 7.2: The cumulant expansion generates equations of motion for n-atom correlations that depend explicitly on the dynamics of order less than $n + 2$. This forms a hierarchy of explicit and implicit dependence.

All of the information contained in the many-body wave function can be gleaned in principle from the dynamics of correlations taken to all orders. This is equivalent to reconstructing a general probability distribution through its associated cumulants that to lowest order are the mean, variance, and skewness shape parameters. In statistics, often only the lowest order cumulants suffice to model weakly correlated data, and this is also true in weakly interacting Bose gases where state-of-the-art theories, including those discussed in Chapters 3–4, track only the dynamics of one and two particle correlations. One possible approach using the master equation (see Ref. [260]) coarse grains the system and constructs a distribution function composed of a set of master variables. If master variables beyond quadratic order are included, the Marcinkiewicz theorem, or M-theorem states that the positive-definitness of the probability distribution function is violated [261]. The method of cumulants does not suffer from these difficulties.

It is natural to start with a definition of cumulants in terms of expectation values in the context of quantum mechanical operators. Given a set of operators $\{B_1, ..., B_N\}$, expectation

values can be factored in terms of cumulants as follows

$$\begin{aligned}
\langle B_1 \rangle &= \langle B_1 \rangle_c \\
\langle B_1 B_2 \rangle &= \langle B_1 B_2 \rangle_c + \langle B_1 \rangle_c \langle B_2 \rangle_c \\
\langle B_1 B_2 B_3 \rangle &= \langle B_2 B_2 B_3 \rangle_c + \langle B_1 B_2 \rangle_c \langle B_3 \rangle_c + \langle B_2 \rangle_c \langle B_1 B_3 \rangle_c \\
&\quad + \langle B_1 \rangle_c \langle B_2 B_3 \rangle_c + \langle B_1 \rangle_c \langle B_2 \rangle_c \langle B_3 \rangle_c \\
&\vdots
\end{aligned} \tag{7.1}$$

The bracket $\langle B_1 .... B_{j-1} B_j \rangle_c$ indicates a **cumulant** of j^{th} order. Eq. 7.1 is the cumulant expansion of expectation values up to third order. Alternatively, at each order cumulants can be written in terms of expectation values by inverting the cumulant expansion. The form of Eq. 7.1, however, highlights the meaning of the cumulant: the jth order cumulant contains only j-body physics whereas the expectation value of the same order contains the physics of j, j-1,...,1 atoms. For bosonic operators, which will be the only type of operators considered in this chapter, the canonical commutation relations state that

$$\langle B_i B_j^\dagger \rangle_c = \delta_{ij} + \langle B_j^\dagger B_i \rangle_c. \tag{7.2}$$

Wick's theorem, which is appropriate, for instance, when using grand-canonical equilibrium density matrix, is a special case of the above remarks where the cumulant expansion has been truncated to second order [262, 263, 89]. When the cumulant expansion is truncated at second order, Eq. 7.1 can be simplified

$$\begin{aligned}
\langle B_1 \rangle &= \langle B_1 \rangle_c \\
\langle B_1 B_2 \rangle &= \langle B_1 B_2 \rangle_c + \langle B_1 \rangle_c \langle B_2 \rangle_c \\
\langle B_1 B_2 B_3 \rangle &= \langle B_1 B_2 \rangle_c \langle B_3 \rangle_c + \langle B_2 \rangle_c \langle B_1 B_3 \rangle_c \\
&\quad + \langle B_1 \rangle_c \langle B_2 B_3 \rangle_c + \langle B_1 \rangle_c \langle B_2 \rangle_c \langle B_3 \rangle_c \\
... &= ...
\end{aligned} \tag{7.3}$$

Truncating the cumulant expansion at second order is equivalent to taking expectation values with respect to a gaussian distribution.

Provided the system is not too far away from equilibrium, cumulants of increasing order decrease unlike higher order expectation values. For the ideal Bose gas in equilibrium discussed in Sec. 2.4, cumulants beyond second order vanish and the system is well described by a gaussian density matrix. Higher order cumulants therefore provide a measure of the extent to which the system is away from the interaction-free equilibrium [51, 52, 50].

From the Heisenberg equation of motion, a linked set of equations of motion for expectation values from the many-body Hamiltonian can be constructed

$$i\frac{\partial}{\partial t}\langle B_1...B_i\rangle = \langle [B_1...B_i, H]\rangle\,. \tag{7.4}$$

Through the cumulant expansion, these equations of motion can be reformulated into an equivalent hierarchy of equations of motion for the cumulants, and the chain can be broken unambiguously at any desired order [51]. Arguments for closing the cumulant equations of motion at a given order are discussed further in Sec. 7.3, and I focus now on the reformulation of expectation value equations of motion into cumulant equations of motion up to the third order borrowing the notation and terminology of Ref. [52].

Let's start with the many-body Hamiltonian for pairwise interactions[2]

$$H = \int d\mathbf{x}\psi^\dagger(\mathbf{x})H_{1B}(\mathbf{x})\psi(\mathbf{x}) + \frac{1}{2}\int d\mathbf{x_1}\int d\mathbf{x_2}\psi^\dagger(\mathbf{x_1})\psi^\dagger(\mathbf{x_2})V(\mathbf{x_1}-\mathbf{x_2})\psi(\mathbf{x_2})\psi(\mathbf{x_1}), \tag{7.5}$$

where $V(\mathbf{x_1}-\mathbf{x_2})$ is left general purposefully and not taken be contact interaction. In Section 7.3, I will connect with the GPE from Chapter 4 where the link between two-body scattering physics and the condensate equation of motion is justified explicitly. The first, second, and third order

[2] Introduced first in Sec. 2.3.2 (Eq. 2.76).

cumulants are

$$\Psi(\mathbf{x},t) = \langle\psi(\mathbf{x})\rangle_c(t), \tag{7.6}$$

$$\Phi(\mathbf{x_1},\mathbf{x_2},t) = \langle\psi(\mathbf{x_1})\psi(\mathbf{x_2})\rangle_c(t), \tag{7.7}$$

$$\Gamma(\mathbf{x_1},\mathbf{x_2},t) = \langle\psi^\dagger(\mathbf{x_1})\psi(\mathbf{x_2})\rangle_c(t) \tag{7.8}$$

$$\Lambda(\mathbf{x_1},\mathbf{x_2},\mathbf{x_3},t) = \langle\psi^\dagger(\mathbf{x_1})\psi(\mathbf{x_2})\psi(\mathbf{x_3})\rangle_c(t) \tag{7.9}$$

$$\chi(\mathbf{x_1},\mathbf{x_2},\mathbf{x_3},t) = \langle\psi(\mathbf{x_1})\psi(\mathbf{x_2})\psi(\mathbf{x_3})\rangle_c(t) \tag{7.10}$$

where the first-order cumulant Ψ is the condensate wave function, the second order cumulant Φ is the **pairing field**, Γ with the **one-body density matrix for the cloud of excitations** out of the condensate, and Λ and χ are the **triplet** cumulants, following the language of F. Lalöe [264]. For reference, the one-body correlation function is

$$\rho^{(1)}(\mathbf{x_1},\mathbf{x_2},t) = \langle\psi^\dagger(\mathbf{x_1})\psi(\mathbf{x_1})\rangle_c(t) = \Gamma(\mathbf{x_1},\mathbf{x_2},t) + \Psi(\mathbf{x_1},t)\Psi(\mathbf{x_2},t), \tag{7.11}$$

associated with the total density of the gas $\rho^{(1)}(\mathbf{x},\mathbf{x},t)$.

The first order equation of motion for condensate wave function Ψ is

$$\begin{aligned} i\frac{\partial}{\partial t}\Psi(\mathbf{x},t) = H_{1B}(\mathbf{x})\Psi(\mathbf{x},t) &+ \int d\mathbf{y}V(\mathbf{x}-\mathbf{y})|\Psi(\mathbf{y},t)|^2\Psi(\mathbf{x},t) \\ &+ \int d\mathbf{y}V(\mathbf{x}-\mathbf{y})\Phi(\mathbf{x},\mathbf{y},t)\Psi^*(\mathbf{y},t) \\ &+ \int d\mathbf{y}V(\mathbf{x}-\mathbf{y})\left[\Gamma(\mathbf{x},\mathbf{y},t)\Psi(\mathbf{y},t) + \Gamma(\mathbf{y},\mathbf{y},t)\Psi(\mathbf{x},t)\right] \\ &+ \int d\mathbf{y}V(\mathbf{x}-\mathbf{y})\Lambda(\mathbf{y},\mathbf{y},\mathbf{x},t). \end{aligned} \tag{7.12}$$

This illustrates a general feature of all cumulant equations of motion: the nth order cumulant equation includes cumulants up to order n+2 explicitly and terms which contain in total n and n+2 operators . The structure of Eq. 7.12 and the following equations of motion for the second and third order cumulants will be discussed in Sec. 7.2.1

The second order equation of motion for the pairing field Φ is

$$\begin{aligned} i\frac{\partial}{\partial t}\Phi(\mathbf{x_1},\mathbf{x_2},t) &= H_{2B}(\mathbf{x_1},\mathbf{x_2})\Phi(\mathbf{x_1},\mathbf{x_2},t) + V(\mathbf{x_1}-\mathbf{x_2})\Psi(\mathbf{x_1},t)\Psi(\mathbf{x_2},t) \\ &+ \int d\mathbf{y} V(\mathbf{x_1}-\mathbf{y})\left[\Phi(\mathbf{x_1},\mathbf{x_2},t)\Psi(\mathbf{y},t) + \Phi(\mathbf{x_2},\mathbf{y},t)\Psi(\mathbf{x_1},t)\right] \\ &+ \int d\mathbf{y} V(\mathbf{x_1}-\mathbf{y})\left[\Gamma(\mathbf{y},\mathbf{y},t)\Phi(\mathbf{x_1},\mathbf{x_2},t) + \Gamma(\mathbf{y},\mathbf{y},t)\Phi(\mathbf{x_1},\mathbf{x_2},t)\right] \\ &+ \int d\mathbf{y} V(\mathbf{x_1}-\mathbf{y})\left[\Lambda(\mathbf{y},\mathbf{x_2},\mathbf{x_1},t)\Psi(\mathbf{y},t) + \Lambda(\mathbf{y},\mathbf{y},\mathbf{x_2},t)\Psi(\mathbf{x_1},t)\right] \\ &+ \int d\mathbf{y} V(\mathbf{x_1}-\mathbf{y})\chi(\mathbf{y},\mathbf{x_2},\mathbf{x_1},t)\Psi^*(\mathbf{y},t) \\ &+ \{\mathbf{x_1}\leftrightarrow\mathbf{x_2}\}, \end{aligned} \tag{7.13}$$

where fourth order cumulants have not been included mainly for sake of clarity, the arrow $\leftrightarrow$ denotes the exchange of coordinates in the bracket, and $H_{2B}(\mathbf{x_1},\mathbf{x_2}) = H_{1B}(\mathbf{x_1}) + H_{1B}(\mathbf{x_2}) + V(\mathbf{x_{1x_2}})$ is the two-body Hamiltonian.

The second order equation of motion for the excitation field Γ is

$$\begin{aligned} i\frac{\partial}{\partial t}\Gamma(\mathbf{x_1},\mathbf{x_2},t) &= \left[H_{1B}(\mathbf{x_1}) - H_{1B}(\mathbf{x_2})\right]\Gamma(\mathbf{x_1},\mathbf{x_2},t) \\ &+ \int d\mathbf{y} V(\mathbf{x_1}-\mathbf{y})\left[\Phi^*(\mathbf{y},\mathbf{x_2},t)\Phi(\mathbf{x_1},\mathbf{y},t) + \Phi^*(\mathbf{y},\mathbf{x_2},t)\Psi(\mathbf{x_1},t)\Psi(\mathbf{y},t)\right] \\ &+ \int d\mathbf{y} V(\mathbf{x_1}-\mathbf{y})\left[\Gamma(\mathbf{y},\mathbf{x_1},t)\Psi(\mathbf{x_1},t)\Psi^*(\mathbf{y},t) + \Gamma(\mathbf{x_1},\mathbf{x_2},t)|\Psi(\mathbf{y},t)|^2\right] \\ &+ \int d\mathbf{y} V(\mathbf{x_1}-\mathbf{y})\left[\Gamma(\mathbf{y},\mathbf{x_2},t)\Gamma(\mathbf{x_1},\mathbf{y},t) + \Gamma(\mathbf{x_1},\mathbf{x_2},t)\Gamma(\mathbf{y},\mathbf{y},t)\right] \\ &+ \int d\mathbf{y} V(\mathbf{x_1}-\mathbf{y})\left[\Lambda^*(\mathbf{x_2},\mathbf{y},\mathbf{x_1},t)^*\Psi(\mathbf{y},t) + \Lambda^*(\mathbf{x_2},\mathbf{y},\mathbf{y},t)\Psi(\mathbf{x_1},t)\right] \\ &+ \int d\mathbf{y} V(\mathbf{x_1}-\mathbf{y})\Lambda(\mathbf{x_2},\mathbf{y},\mathbf{x_1},t)\Psi^*(\mathbf{y},t) \\ &- \{\mathbf{x_1}\leftrightarrow\mathbf{x_2}\}^*, \end{aligned} \tag{7.14}$$

where again the fourth order cumulants have not been included.

The third order equations of motion for the triplet cumulants are lengthy, and for the purposes of this thesis, it is sufficient to include only terms which include up to three operator products.

The equation of motion for Λ is

$$\begin{aligned} i\frac{\partial}{\partial t}\Lambda(\mathbf{x_1},\mathbf{x_2},\mathbf{x_3},t) &= \left[H_{2B}(\mathbf{x_1},\mathbf{x_2}) - H_{1B}(\mathbf{x_3})\right]\Lambda(\mathbf{x_1},\mathbf{x_2},\mathbf{x_3},t) \\ &+ V(\mathbf{x_1}-\mathbf{x_2})\left[\Psi(\mathbf{x_2},t)\Gamma(\mathbf{x_1},\mathbf{x_3},t) + \Psi(\mathbf{x_1},t)\Gamma(\mathbf{x_2},\mathbf{x_3},t)\right], \end{aligned} \tag{7.15}$$

and the equation of motion for χ is

$$\begin{aligned} i\frac{\partial}{\partial t}\chi(\mathbf{x_1},\mathbf{x_2},\mathbf{x_3},t) &= H_{3B}\chi(\mathbf{x_1},\mathbf{x_2},\mathbf{x_3},t) \\ &+ V_{3B}\left[\Phi(\mathbf{x_1},\mathbf{x_2},t)\Psi(\mathbf{x_3},t) + \{\mathbf{x_1}\to\mathbf{x_2}\to\mathbf{x_3}\} + \{\mathbf{x_1}\to\mathbf{x_3}\to\mathbf{x_2}\}\right], \end{aligned} \tag{7.16}$$

where $H_{3B} = \sum_i H_{1B}(\mathbf{x_i}) + V_{3B}$ is the three-body Hamiltonian, and $V_{3B} = \sum_{i<j} V(\mathbf{x_i}-\mathbf{x_j})$ is the sum of all possible pairwise interactions.

7.2.1 Structure of the Cumulant Equations of Motion

The complicated structure of the cumulant equations of motions Eqs. 7.12–7.16 can be unraveled by investigating their free and vacuum limits which I discuss presently.

There are two main approaches to truncating the cumulant equations of motion. For example, choosing to truncate at first order, all cumulants of higher order could be ignored [51, 50]. This results in the GPE in the first Born approximation

$$i\frac{\partial}{\partial t}\Psi(\mathbf{x},t) = H_{1B}(\mathbf{x})\Psi(\mathbf{x},t) + \int d\mathbf{y} V(\mathbf{x}-\mathbf{y})|\Psi(\mathbf{y},t)|^2\Psi(\mathbf{x},t). \tag{7.17}$$

Truncating at second order gives the Hartree-Fock Bogoliubov equations of motion for the condensate, pairing, and excitation fields [89].

The second approach requires that for truncation at nth order, the **free equations** for the n+1 and n+2 order cumulants must solved self-consistently [52] and inserted into the nth order cumulant equation. For the jth order cumulant equation of motion, the free equation is obtained by neglecting all terms that involve products of operators higher than order n. For instance,

Eqs. 7.15–7.16 are already in their free form. When the self-consistent solutions for the n+1 and n+2 order cumulants are inserted into the nth order cumulant equation of motion, they contain the n+1 and n+2 body T-matrices from the few-body scattering problem in vacuum. Therefore, they significantly extend the validity of the first approach beyond the first Born approximation to include multiple scattering, in the sense of the Born series. This is the truncation scheme used in this chapter, specifically in Sec. 7.3 to re-derive the GPE. Importantly, this scheme explicitly links the few-body scattering problem with the cumulants of the many-body problem establishing the theme of this chapter.

The free equations are different from the cumulant equations of motion in the vacuum limit, the **vacuum equations**. What is meant by the jth order cumulant describing the physics of j-atoms becomes precise in the vacuum limit, corresponding to setting cumulants containing both daggered and undaggered operators to zero along with eliminating the condensate wave function– there is no broken phase in vacuum. The vacuum limit of the noncondensate field, for instance, can be understood from the equilibrium result for an ideal gas of bosons in a box in the grand-canonical ensemble

$$\Gamma(\mathbf{r},\mathbf{r}') \approx \frac{N}{V} e^{-\pi(\mathbf{r}-\mathbf{r}')/\lambda_{th}^2}, \tag{7.18}$$

which is a gaussian decaying with a width proportional to the thermal de Broglie wavelength, corresponding to the coherence length of a classical gas. This expression vanishes in the vacuum limit where the atom number, N, approaches zero while the volume, V, is held fixed.

The vacuum limit of Eqs. 7.12–7.16 yields two nonzero cumulant equations of motion for the pairing Φ and triplet χ fields

$$i\frac{\partial}{\partial t}\Phi(\mathbf{x_1},\mathbf{x_2},t) = H_{2B}\Phi(\mathbf{x_1},\mathbf{x_2},t), \tag{7.19}$$

$$i\frac{\partial}{\partial t}\chi(\mathbf{x_1},\mathbf{x_2},\mathbf{x_3},t) = H_{3B}\chi(\mathbf{x_1},\mathbf{x_2},\mathbf{x_3},t), \tag{7.20}$$

which are formally identical to the two and three-body Schrödinger equations. These two equations

can be solved using the **Green's function method**

$$\Phi(\mathbf{x_1}, \mathbf{x_2}, t) = iG_{2B}^{(+)}(t, t_0)\Phi(\mathbf{x_1}, \mathbf{x_2}, t_0), \tag{7.21}$$

$$\chi(\mathbf{x_1}, \mathbf{x_2}, \mathbf{x_3}, t) = iG_{3B}^{(+)}(t, t_0)\chi(\mathbf{x_1}, \mathbf{x_2}, \mathbf{x_3}, t_0), \tag{7.22}$$

where $G_{NB}^{(+)}(t, t_0)$ is the N-body retarded Green's function [265], which *propagates* the wave function from the initial time, t_0, to the present time, t, with defining equation

$$\left(i\hbar\frac{\partial}{\partial t} - H_{NB}\right) G_{NB}^{(+)}(t, t_0) = \delta(t - t_0), \tag{7.23}$$

where H_{NB} is the N-body Hamiltonian. The advantage of the Green's function method is that the additional source terms in the free equations can be handled naturally. For the pairing field, the solution to the free equation is

$$\Phi(\mathbf{x_1}, \mathbf{x_2}, t) = iG_{2B}^{(+)}(t, t_0)\Phi(\mathbf{x_1}, \mathbf{x_2}, t_0) + \int_{t_0}^{\infty} dt_1 G_{2B}^{(+)}(t, t_1)V(\mathbf{x_1} - \mathbf{x_2})\Psi(\mathbf{x_1}, t_1)\Psi(\mathbf{x_2}, t_1), \tag{7.24}$$

and an easy check using Eq. 7.23 confirms that the original free equation is satisfied. For the triplet χ field, the solution to the free equation is therefore

$$\begin{aligned}
\chi(\mathbf{x_1}, \mathbf{x_2}, \mathbf{x_3}, t) &= iG_{3B}^{(+)}(t, t_0)\chi(\mathbf{x_1}, \mathbf{x_2}, \mathbf{x_3}, t_0) \\
&+ \int_{t_0}^{\infty} dt_1 G_{3B}^{(+)}(t, t_1)V_{3B}[\Phi(\mathbf{x_1}, \mathbf{x_2}, t_1)\Psi(\mathbf{x_3}, t_1) \\
&+ \{\mathbf{x_1} \to \mathbf{x_2} \to \mathbf{x_3}\} + \{\mathbf{x_1} \to \mathbf{x_3} \to \mathbf{x_2}\}] \\
&+ \int_{t_0}^{\infty} dt_1 G_{3B}^{(+)}(t, t_1)V_{3B}\left[\Psi(\mathbf{x_1}, t_1)\Psi(\mathbf{x_2}, t_1)\Psi(\mathbf{x_3}, t_1)\right].
\end{aligned} \tag{7.25}$$

It should be emphasized that knowledge of the N-body Green's function is equivalent to knowledge of the complete set of eigenstates of the N-body problem including the bound and continuous spectrum. Therefore, obtaining for the Green's function is just as difficult as solving the N-body Schrödinger equation. The main advantage to the Green's function formalism is that it allows the self-consistent solutions of Sec. 7.3 to be neatly formulated. Alternatively, the vacuum equations can be written in a partial wave decomposition for the spherical and hyperspherical dependence truncated in the ultracold limit.

From the above arguments, it is clear that the N-body Schrödinger equation is a limiting case of the nth order cumulant equation of motion when medium effects are negligible. At short distance, the triplet and singlet potential wells are much deeper, on the order of hundreds of kelvins (see Fig. 2.3), compared to the energy scale of background medium contributions[3] $\sim ng_0$. The nth order cumulant is therefore well described by the vacuum N-body scattering physics at short-range. It is erroneous to extend this picture to long ranges where the interatomic interactions become negligible and density effects persist. This agrees with the picture of the gas when $na_0^3 \ll 1$ discussed in Sec. 7.1, namely that collision physics can be separated from the evolution of the mean-fields. From these length scale considerations come the inverse argument for relevant energy scales of the problem, namely that the high momentum portion of the momentum density is dominated by short-range vacuum scattering physics. This is the essence of Tan's relations [266, 267, 268], which relate the short-range few-body wave function to the bulk observables including the tail of the momentum distribution and the energy of the gas through a set of universal parameters, called the "**contacts**." The N-body contact measures the probability for N particles to be very close together and is extracted from the N-body vacuum scattering wave function. From the above arguments, it is clear that, for instance, the two-body contact should appear in the the pair correlation function, $g^{(2)}(\mathbf{r}, \mathbf{r}') \approx \Phi(\mathbf{r}, \mathbf{r}') + \Psi(\mathbf{r})\Psi(\mathbf{r}')$. In the zero-range model, valid when the range of the potential is much smaller than all other length scales in the system, this is indeed the case, and the pair correlation function and two-body wave function both scale as r^{-2} directly proportional to the two-body contact, C_2. These ideas also relate the triplet cumulant χ at short distances with the three-body wave function through the definition of the three-body contact, C_3 [269, 270]. As an example of how the contact enters into the large-momentum tail of the distribution, I've summarized the following result without proof

$$n(k) \to \frac{C_2}{k^4} + \frac{F(k)}{k^5} C_3, \tag{7.26}$$

where C_2 and C_3 depend on the two-body scattering length and a three-body parameter associated

[3] In Chapter 4, we estimated this for the weakly-interacting breathing mode experiment, finding $ng_0 < 0.1T_c$.

with Efimov physics [270]. Although interesting from the standpoint of the signatures of few-body physics emerging in global properties of the many-body system, the contact is not the focus of this chapter, and so I only briefly mention it here contextually.

In a medium, the density dependent terms in the cumulant equations of motion for the pairing and triplet fields become important on the order of the average interparticle spacing. Equations 7.13 and 7.16 can therefore be viewed as two and three-body Schödinger equations that include the **dressing effect** of the background gas. In the limit of a static background gas, which is appropriate for short-range processes occurring over shorter timescales than the mean-field evolution, the solution of these nonlinear Schrödinger equations yields the complete spectrum of eigenstates in the presence of a medium and also gives the general, short-time dynamics as the simple oscillatory evolution of a superposition of the dressed eigenstates. This viewpoint was implemented approximately in the past to study coherent atom-molecule oscillations by introducing an artificial harmonic trapping potential with oscillator length proportional to $n^{-1/3}$ and trapping frequency as a fit parameter [256, 257]. This model was recently applied to the unitary Bose gas on the two and three-body level to calculate the dressed eigenstates, momentum distribution, and obtain rough estimates for the lifetime of the gas [255].

On longer timescales comparable to the period of the artificial trapping potential or the timescale for mean-field evolution, these approximate methods break down. A full dynamical solution of the coupled equations of motion, Eqs. 7.12–7.16, is required, and this is obviously a very computationally demanding undertaking, beyond the scope of this thesis.

These remarks illustrate the general structure of the cumulant equations of motion and highlight the link with the few-body problem in vacuum. They are therefore a powerful tool for understanding Bose gases beyond the level of one and two-body correlations and provide a natural avenue to study signatures of the Efimov effect in the strongly-interacting Bose gas, pursued further in the following section.

7.3 Self-Consistent Solutions of the Cumulant Equations of Motion

This section is devoted to constructing equations of motion for the condensate wave function using the cumulant equations, Eqs. 7.12–7.16. Truncating the cumulant equations at first order, the GPE can be derived by solving the second and third order cumulant free equations of motion self-consistently. This provides an alternate derivation to that of Sec. 4.1, illuminating some of the tacit assumptions made earlier. Using these self-consistent solutions, powers of the condensate wave function in Eqs. 7.12–7.16 can be collected and fed back into the first order cumulant equation. In this way, terms of quartic order in the condensate wave function can be added to the GPE and the three-body GPE constructed. This equation allows three-body physics to be included into the condensate equation of motion, which is the starting point for an analysis of the impact of Efimov physics on the strongly-interacting Bose gas pursued in the following section, Sec. 7.4.

7.3.1 Truncation of the Cumulant Equations at First Order: The GPE

When the cumulant equations are truncated at first order, the relevant equations are Eq. 7.12 and the free equations for the cumulants Φ, Γ and , Λ on which the first order cumulant depends explicitly. The free equations for Φ and Γ are the first lines of Eqs. 7.13 and 7.14, and the free equation for Λ is Eq. 7.15 which has already been written in free form. The first order cumulant equation does not depend explicitly on the other triplet cumulant, χ, and so it is not part of this self-consistent solution although it will play a pivotal role in the following section, Sec. 7.3.2 as a source of higher order contributions to the GPE, containing three-body physics.

From the free equations for Γ and Λ it is clear that if both cumulants vanish initially at time $t = t_0$, they do not evolve, and their contributions can be neglected. Additionally, if the initial state of the gas is the a ideal gas ground state, the many-body wave function is a coherent state and all expectation values factor into products of the condensate wave function. Therefore, cumulants higher than first order vanish initially, which includes the pairing field. The self-consistent solution

of the pairing field is therefore a special case of Eq. 7.24

$$\Phi(\mathbf{x_1}, \mathbf{x_2}, t) = \int_{t_0}^{\infty} dt_1 G_{2B}^{(+)}(t, t_1) V(\mathbf{x_1} - \mathbf{x_2}) \Psi(\mathbf{x_1}, t_1) \Psi(\mathbf{x_2}, t_1), \tag{7.27}$$

from which it is clear that the evolution of Φ is seeded by the condensate source terms. Inserting this result into the first order cumulant equation yields the following equation for the condensate wave function

$$\begin{aligned} i\frac{\partial}{\partial t}\Psi(\mathbf{x}, t) &= H_{1B}(\mathbf{x})\Psi(\mathbf{x}, t) + \int d\mathbf{y} V \left[\Psi(\mathbf{y}, t)\Psi(\mathbf{x}, t) + \Phi(\mathbf{x}, \mathbf{y}, t)\right] \Psi^*(\mathbf{y}, t) \\ &= H_{1B}(\mathbf{x})\Psi(\mathbf{x}, t) + \int d\mathbf{y} \int_{t_0}^{\infty} dt_1 \left[V\delta(t - t_1) + V G_{2B}^{(+)}(t, t_1) V\right] \Psi(\mathbf{x}, t_1)\Psi(\mathbf{y}, t_1)\Psi^*(\mathbf{y}, t) \end{aligned} \tag{7.28}$$

where the argument of $V(\mathbf{x}-\mathbf{y})$ has been suppressed for reasons of clarity. The quantity in brackets is the definition of the retarded two-body T-matrix [75] in the time domain, $T_{2B}^{(+)}(t, t_1)$, and Eq. 7.28 can be written concisely

$$i\frac{\partial}{\partial t}\Psi(\mathbf{x}, t) = H_{1B}(\mathbf{x})\Psi(\mathbf{x}, t) + \int d\mathbf{y} \int_{t_0}^{\infty} dt_1 T_{2B}^{(+)}(t, t_1)\Psi(\mathbf{x}, t_1)\Psi(\mathbf{y}, t_1)\Psi^*(\mathbf{y}, t). \tag{7.29}$$

Comparison of this equation with Eq. 7.17 reveals the Born approximation. This equation is **non-Markovian**, meaning that it has *memory* of the past behavior of the system and is more general than the GPE. Self-consistent solutions of the cumulant equation to a given order therefore contain effects from higher order correlations through non-Markovian contributions and few-body T-matrices beyond the first Born approximation.

It is of value to briefly trace how the Markov limit of Eq. 7.29 yields the familiar form of the GPE for gases not far from the ideal gas equilibrium. The first step is to go to the interaction picture, where the fast oscillation associated with the non-interacting portion of the Hamiltonian can be separated from the oscillation due to the mean-field interaction . To do this, the cumulants are rewritten in the eigenbasis of the one-body Hamiltonian, H_{1B} with single-particle orbitals ϕ_i and energy E_i. The first order cumulant projected onto this basis is written as $\Psi_i(t)$, and in the interaction picture

$$\Psi_i(t) = \Psi_i^I(t) e^{-iE_i t}, \tag{7.30}$$

which removes the fast oscillation due to the one-body orbital energy, E_i. The temporal evolution of $\Psi_i^I(t)$ then depends on the mean-field interaction term which is weak when the gas is not far from the interaction free equilibrium. $T_{2B}^{(+)}(t,t_1)$ is however strongly peaked about $t_1 = t$ with width proportional to the duration of the collision. In the integrand of the non-Markovian contribution, all first-order cumulants can be evaluated then at time t, and the equation of motion in the interaction picture is

$$i\frac{\partial}{\partial t}\Psi_i^I(t) = e^{iE_it}\sum_{j,k,l} e^{i(E_j+E_k+E_l)t}\Psi_j^I(t)\Psi_k^I(t)(\Psi_l^I(t))^* \left[\int_{-\infty}^{t-t_0} d\tau_s\langle i,l|T_{2B}^{(+)}(t,t-\tau)|j,k\rangle_s e^{-i(E_j+E_k)\tau}\right], \tag{7.31}$$

where the 's' subscript indicates a symmetrized ket and where the quantity in brackets is a Fourier transform to the energy domain in the limit $t-t_0 \to \infty$, which can be taken without penalty due to the vanishing of the retarded T-matrix for times before t_0, yielding the familiar two-body T-matrix for vacuum scattering provided the length scale of the collision is much smaller than the oscillator length of the trap. After this transformation, Eq. 7.31 can be cast into the GPE in the orbital basis in the Schödinger picture

$$i\frac{\partial}{\partial t}\Psi_i(t) = E_i\Psi_i(t) + \sum_{j,k,l} {}_s\langle i,l|T_{2B}(E_j+E_k+i0)|j,k\rangle_s\Psi_j(t)\Psi_k(t)\Psi_l(t)^*, \tag{7.32}$$

from which the GPE of Chapter 2 can be recovered using a contact interaction in the Born approximation.

It is clear then how the Markov approximation can break down for instance with resonance scattering where the collision duration can in principle extend indefinitely exactly on resonance, rendering the GPE meaningless. The weak time dependence argument for the mean-field interaction is also not appropriate for nonequilibrium states far from the ideal gas limit. These scenarios highlight wider range of applicability of self-consistent solutions of the cumulant equations and the importance of understanding the underlying few-body scattering physics in vacuum.

7.3.2 Higher Powers of the Condensate Wave Function: The Three-Body GPE

The Markovian GPE derived in the previous section has a mean-field interaction quadratic in the condensate wave function. If instead of using the free equation for Φ, the full equation, Eq. 7.13 is considered, it is clear that a condensate equation of motion be derived that includes higher order powers of Ψ

$$i\frac{\partial}{\partial t}\Psi = H_{1B}\Psi + g_2|\Psi|^2\Psi + g_3|\Psi|^4\Psi + ... \tag{7.33}$$

The reason that the next order correction with coupling strength g_3 is quartic instead of say cubic is because the cumulant equation for Φ contains contributions which are second and fourth order operator products. The cumulant equation for Λ contains third and fifth order operator products (not shown), but this term is not multiplied by the condensate wave function in the first order cumulant equation of motion, Eq. 7.12.

The full functional form of g_3 was derived by T. Köhler in Ref. [53] using the cumulant formalism, and it is sufficient for present purposes to just sketching how three-body physics enters into this coupling constant. Let's follow one of the paths that contributes three-body physics starting with the solution of Eq. 7.13 using the Green's function formalism

$$\begin{aligned}\Phi(\mathbf{x_1},\mathbf{x_2},t) &= \int_{t_0}^{\infty} dt_1 G_{2B}^{(+)}(t,t_1)V(\mathbf{x_1}-\mathbf{x_2})\Psi(\mathbf{x_1},t_1)\Psi(\mathbf{x_2},t_1) \\ &+ \int_{t_0}^{\infty} dt_1 \int_{t_0}^{\infty} dt_2 \int d\mathbf{y}\; G_{2B}^{(+)}(t,t_1)V(\mathbf{x_1}-\mathbf{y})G_{3B}^{(+)}(t_1,t_2)V_{3B}\Phi(\mathbf{y},\mathbf{x_2},t_2)\Psi(\mathbf{x_1},t_2) + ...,\end{aligned} \tag{7.34}$$

where the first line contributes the retarded two-body T-matrix to the quadratic mean-field term in the GPE as was shown in the previous subsection. The second line contains the leading order contribution in Ψ from the self-consistent solution of the free equation for χ, Eq. 7.25. The dots on the right hand side indicate that there many additional terms in the exact expression not considered that may end up in the final result for g_3 but not included here for sake of clarity.

The remaining dependence on Φ in Eq. 7.33 is replaced by the free solution, Eq. 7.27, which yields a final expression that is quadratic and quartic in the condensate wave function. Inserting

this into the condensate equation of motion yields a non-Markovian GPE that includes the retarded three-body T-matrix in the quartic term. Just as in the previous subsection, the Markov approximation can be made assuming the two and three-body collision duration is much faster than the mean-field evolution of Ψ. The two and three-body T-matrices can be separated from the quadratic and quartic products of Ψ and act as coupling functions. The final result for g_2 and g_3 is [53]

$$\begin{aligned} g_2 &= \frac{4\pi}{m} a_0 \\ g_3 &= \frac{(2\pi\hbar)^6}{2} T_{3B}^{(5)}(E \to 0) + ..., \end{aligned} \tag{7.35}$$

where $T_{3B}^{(5)}(E \to 0)$ is the threshold result for fifth order multiple scattering diagrams and upwards, which includes the contributions from the 'true' three-body scattering in the universal region discussed in Sec. 5.4.1. The terms not listed in the dots are logarithmic terms to fourth order in the scattering length, reflecting contributions that are third and fourth order in the two-body scattering T-matrix. In the following section, the significance Efimov physics in the three-body contribution to g_3 is discussed for strongly-interacting Bose gases.

7.4 Emergence of Efimov Physics in Strongly-Interacting Bose Gases

In Sec. 5.4.1 and Sec. 6.5, the threshold behavior of the contribution of Efimov physics to the elastic scattering phase shift [$\sim \mathrm{Re}(T_{3B}^{(5)}$] was sketched using a WKB model. The imaginary part of $T_{3B}^{(5)}$ is proportional to the the three-body recombination rate, which determines the lifetime and stability of the gas. The real part of $T_{3B}^{(5)}$, is proportional to the three-body elastic scattering volume, A_{3B}, which can be positive, negative, and larger that the two-body scattering length. It sets additional length scale in the problem and can be grouped with the class of three-body length scales, including l_{3B} in Fig. 7.1 which indicated the characteristic size of trimers in the gas.

In this section, only the case where $a_0 < 0$ is considered, and Efimov physics appears in A_{3B} through a set of poles at location of trimer formation, analogous with the structure of the two-body scattering length near Feshbach resonances discussed in Sec. 5.4.1. Curiously, near one of these poles, the gas can in principle still be dilute with respect to two-body interactions but not dilute

with respect to three. A Bose gas can therefore be in the unitary regime of three-body resonance scattering physics and be considered strongly-interacting. The thermodynamics of this state and of the unitary Bose gas at a Feshbach resonance are extremely intriguing but beyond the scope of this thesis, however, I touch upon these states in the conclusion of this thesis. This section is concerned with the case where the quartic nonlinearities in the GPE are larger than the quadratic nonlinearities *near* a three-body resonance.

7.4.1 Quantum Droplets and Magnetic Ordering

The ground state structure of a weakly-interacting Bose gas can be understood by solving the GPE for the stationary wave function $\Psi(t) = \Psi \exp(-i\mu t)$ as was done in Sec. 4.1. For instance, in the Thomas Fermi limit, where the interaction energy exceeds the kinetic energy, the condensate has the parabolic form

$$|\Psi(\mathbf{r})|^2 = \frac{\mu - V_{ext}(\mathbf{r})}{g_2} \tag{7.36}$$

where V_{ext} is the harmonic trapping potential. When the quartic interaction is introduced into the GPE, the ground state shape changes

$$|\Psi(\mathbf{r})|^2 = \sqrt{\frac{2(\mu - V_{ext}(\mathbf{r}))}{g_2} + \left(\frac{g_2}{g_3}\right)^2} - \frac{g_2}{g_3}. \tag{7.37}$$

When $g_2 < 0$, the effective attraction forces the collapse of the condensate beyond a critical value $N_c a_0/a_{ho} \lesssim -0.67$ [271]. This collapse was observed in Ref. [272] where the burst of bright matter-wave solitons during the collapse inspired the 'Bosenova' label.

When an unstable condensate collapses, the density of the gas increases, and corrections to the GPE that are higher order in the density such as the beyond mean-field LHY correction [137, 136] due to quantum fluctuations, or the quartic nonlinearity dictate the dynamics of the collapse. Collapse experiments are therefore one probe of higher-order density corrections to the weakly-interacting theory of the Bose gas.

On the repulsive side of a three-body resonance, just as a new trimer has been formed, $g_3 > 0$, and it is an open question whether the effective three-body repulsion, due to enhancements to $T_{3B}^{(5)}$

from Efimov physics, can stabilize the collapsing gas, although a recent experiment Ref. [273] suggests that such terms do play a role. Work by A. Bulgac in Refs. [38, 39] suggest that in this regime, the system could become self-bound forming bosonic **droplet states**. This state of matter is one possible signature of three-body correlations and Efimov physics in the system. The radius, R_d, of such droplet states is predicted to scale with the number of atoms, N, in the droplet and the ratio g_2/g_3

$$R_d = \left(\frac{g_3}{2\pi|g_2|}N\right)^{1/3}. \tag{7.38}$$

Analysis in Refs. [274, 275, 276] concluded that the quartic nonlinearity in the GPE introduces a first-order phase transition between the condensate and droplet state.

Recent theoretical works [36, 37] postulate that g_3 can not only take the system into novel phases of superfluidity, it can also impact the magnetic ordering when spin-degrees of freedom are unfrozen. For strongly-interacting spinor Bose gases, the three-body GPE must be reformulated to account for spin degrees of freedom in the system. The position space field annihilation operator which can create or destroy an atom in a particular spin level is decomposed on the one-body spin basis, using the one-body hyperfine spin states, as $\vec{\psi}(\mathbf{r}) = (\psi_{-f}(\mathbf{r}), ..., \psi_0(\mathbf{r}), ..., \psi_f(\mathbf{r}))$, where the subscript corresponds to the magnetic sublevels. The many-body Hamiltonian for spinor gases is

$$H = \int d\mathbf{x}\psi_a^\dagger(\mathbf{x})H_{1B}(\mathbf{x})\psi_a(\mathbf{x}) + \frac{1}{2}\int d\mathbf{x_1}\int d\mathbf{x_2}\psi_a^\dagger(\mathbf{x_1})\psi_b^\dagger(\mathbf{x_2})\langle a|\langle b|\hat{V}(\mathbf{x_1}-\mathbf{x_2})|b'\rangle|a'\rangle\psi_{b'}(\mathbf{x_2})\psi_{a'}(\mathbf{x_1}), \tag{7.39}$$

where the repeated indices are to be summed per the Einstein convention. The pairwise interaction projects onto two-body total spin states, and in the zero-range model it can be rewritten in operator form

$$\hat{V}(\mathbf{r}) = \frac{4\pi}{m}\hat{A}_{2B}\delta^{(3)}(\mathbf{r}) = \frac{4\pi}{m}\delta^{(3)}(\mathbf{r})\sum_{F_{2\mathrm{b}}} a_{F_{2\mathrm{b}}}\mathrm{P}_{F_{2\mathrm{b}}}, \tag{7.40}$$

where $\mathrm{P}_{F_{2\mathrm{b}}} = \sum_{M_{F_{2\mathrm{b}}}} |F_{2\mathrm{b}}M_{F_{2\mathrm{b}}}\rangle\langle F_{2\mathrm{b}}M_{F_{2\mathrm{b}}}|$ are projection operators into a two-body total hyperfine state. In Ref. [227] it was shown that the relation,

$$\left(\vec{f}_1\cdot\vec{f}_2\right)^n = \sum_{F_{2\mathrm{b}}}\left[\frac{F_{2\mathrm{b}}\left(F_{2\mathrm{b}}+1\right)}{2} - f\left(f+1\right)\right]^n \mathrm{P}_{F_{2\mathrm{b}}} \tag{7.41}$$

allows us to rewrite $\hat{A}_{2B}$ as

$$\hat{A}_{2B} = \sum_{n=0}^{f} \alpha_{2\mathrm{b}}^{(n)} \left(\vec{f}_1 \cdot \vec{f}_2 \right)^n , \tag{7.42}$$

where the $\alpha_{2\mathrm{b}}$'s are linear combinations of the scattering lengths $\{a_0, a_2, ..., a_{2f}\}$.

The above formulation allows us to rewrite the scattering length operator $\hat{A}_{2B}$ in Eq. (7.42) for $f = 1$ atoms in terms of two parameters in complete analogy with the reformulation of the singlet and triplet potentials in Sec. 2.2.4 Eq. 2.37,

$$\hat{A}_{2B} = \alpha_{2\mathrm{b}}^{(0)} + \alpha_{2\mathrm{b}}^{(1)} \left(\vec{f}_1 \cdot \vec{f}_2 \right), \tag{7.43}$$

where

$$\alpha_{2\mathrm{b}}^{(0)} = \frac{a_0 + 2a_2}{3} \quad \text{and} \quad \alpha_{2\mathrm{b}}^{(1)} = \frac{a_2 - a_0}{3}, \tag{7.44}$$

representing a direct interaction terms and an spin-exchange term, respectively. It has been shown in Refs. [227, 228] that these two parameters do characterize important phases of the gas. For instance, depending on the sign of $\alpha_{2\mathrm{b}}^{(1)}$, the ground state of the spinor condensate is antiferromagnetic ($\alpha_{2\mathrm{b}}^{(1)} < 0$) or ferromagnetic ($\alpha_{2\mathrm{b}}^{(1)} > 0$) ordered [227, 228, 64]. For $f = 2$, the scattering length operator $\hat{A}_{2B}$ in Eq. (7.42) can be rewritten in terms of three parameters

$$\begin{aligned} \alpha_{2\mathrm{b}}^{(0)} &= -\frac{2a_0}{5} + \frac{8a_2}{7} + \frac{9a_4}{35}, \\ \alpha_{2\mathrm{b}}^{(1)} &= -\frac{a_0}{30} - \frac{2a_2}{21} + \frac{9a_4}{70}, \\ \alpha_{2\mathrm{b}}^{(2)} &= \frac{a_0}{30} - \frac{a_2}{21} + \frac{a_4}{70}. \end{aligned} \tag{7.45}$$

We note that in the literature the $\hat{A}_{2B}$ operator for $f = 2$ has been rewritten in terms of the projector P_0 allowing for a structure similar to d-wave BCS superfluids [277]. For $f = 2$, there are three categories of ground state magnetic orderings depending on the relative strengths of the scattering lengths: cyclic, polar, and ferromagnetic (see Ref. [277].) The cyclic phase arises from the additional P_0 term which describes scattering of a pair of atoms into the $F_{2\mathrm{b}} = 0$ singlet state introducing an additional order parameter describing the formation of singlet pairs in the system. For $f = 3$, the four parameters that characterize $\hat{A}_{2B}$ [Eq. (7.42)] are: $\alpha_{2\mathrm{b}}^{(0)} = 9a_0/35 - 4a_2/7 + 486a_4/385 + 4a_6/77$,

$\alpha_{2\mathrm{b}}^{(2)} = 9a_0/70 - 17a_2/63 + 81a_4/770 + 25a_6/693$, $\alpha_{2\mathrm{b}}^{(4)} = -a_0/315 + 5a_2/378 - 6a_4/385 + 23a_6/4158$, and $\alpha_{2\mathrm{b}}^{(6)} = -a_0/630 + a_2/378 - a_4/770 + a_6/4158$. $\hat{A}_{2B}$ was rewritten in Ref. [278] including P_0 and rewritten in Ref. [279] including a nematic tensor for the dipolar spinor condensate ^{52}Cr using the terminology of liquid crystals for the many ground state magnetic phases of the system at zero and nonzero fields which we do not go into further

There are, however, many ways to rewrite $\hat{A}_{2B}$ in the literature that better suggest treatments similar, for instance, to magnetism, BCS theory, and liquid crystal theory. For the three-body mean-field interactions, however, we choose to simply extend the above analysis and in an analogous form to Eq. (7.42), in light of the lack of suggestive three-body treatments from other theories to our knowledge. Therefore, we define the three-body scattering volume operator as

$$\hat{A}_{3\mathrm{b}} = \sum_{F_{3\mathrm{b}}} A_{3B}^{(F_{3\mathrm{b}})} \mathcal{P}_{F_{3\mathrm{b}}}, \tag{7.46}$$

where

$$\mathcal{P}_{F_{3\mathrm{b}}} = \sum_{M_{F_{3\mathrm{b}}} F_{2\mathrm{b}}} |F_{3\mathrm{b}} M_{F_{3\mathrm{b}}}(F_{2\mathrm{b}})\rangle\langle F_{3\mathrm{b}} M_{F_{3\mathrm{b}}}(F_{2\mathrm{b}})|. \tag{7.47}$$

In the equation above, A_{3B} is the usual three-body scattering volume (units of length^4) as defined in Refs. [31, 32, 205, 206, 39, 38] for the allowed values of $F_{3\mathrm{b}}$. Note that our usage of the term "three-body scattering volume" is the same as that in Efimov's original work in Refs. [31, 32], and it corresponds, in the adiabatic hyperspherical representation, to elastic processes involving only the lowest three-body continuum channel.

We now proceed in a similar fashion to the two-body case and rewrite $\hat{A}_{3\mathrm{b}}$ in Eq. (7.46) to emphasize spin-exchange terms. Using the usual relations for angular momentum addition and the orthogonality of the projection operators, one can obtain the following relation,

$$\left(\sum_{i<j} \vec{f}_i \cdot \vec{f}_j \right)^n = \sum_{F_{3\mathrm{b}}} \left[\frac{F_{3\mathrm{b}}(F_{3\mathrm{b}}+1)}{2} - \frac{3f(f+1)}{2} \right]^n \mathcal{P}_{F_{3\mathrm{b}}}, \tag{7.48}$$

which allows us to write the three-body scattering volume operator $\hat{A}_{3\mathrm{b}}$ as

$$\hat{A}_{3\mathrm{b}} = \sum_{n=0}^{N_{3\mathrm{b}}-1} \alpha_{3\mathrm{b}}^{(n)} \left(\sum_{i<j} \vec{f}_i \cdot \vec{f}_j \right)^n, \tag{7.49}$$

where $N_{3\mathrm{b}}$ is the number of relevant three-body scattering volumes, i.e., the three-body scattering volume for the values of $F_{3\mathrm{b}}$ whose spin functions are fully symmetric. (Anti-symmetric and mixed-symmetry states correspond to higher partial waves and are not considered in the present work.) Therefore, the three-body mean-field contributions to the spin dynamics is now determined in terms of the parameters $\alpha_{3\mathrm{b}}$, which are linear combination of the physical three-body scattering volumes for all allowed values of $F_{3\mathrm{b}}$.

For $f = 1$ atoms, only the three-body scattering volumes for $F_{3\mathrm{b}} = 1$ and 3 contribute to the interaction (see Table 6.2), allowing us to write the three-body scattering volume operator $\hat{A}_{3\mathrm{b}}$ in Eq. (7.49) in terms of only two parameters,

$$\hat{A}_{3\mathrm{b}} = \alpha_{3\mathrm{b}}^{(0)} + \alpha_{3\mathrm{b}}^{(1)} \left(\sum_{i<j} \vec{f}_i \cdot \vec{f}_j \right), \tag{7.50}$$

where

$$\alpha_{3\mathrm{b}}^{(0)} = \frac{3A_{3B}^{(1)} + 2A_{3B}^{(3)}}{5}, \quad \text{and} \quad \alpha_{3\mathrm{b}}^{(1)} = \frac{A_{3B}^{(3)} - A_{3B}^{(1)}}{5}, \tag{7.51}$$

representing a direct interaction term and an spin-exchange term, respectively. This is in close analogy to the form of the two-body scattering length operator for $f = 1$ atoms [see Eq. (7.43)]. For $f = 2$ atoms, only the states with $F_{3\mathrm{b}} = 0$, 2, 3, 4, and 6 contribute in the interaction, resulting in the following parameters for Eq. (7.49),

$$\begin{aligned}
\alpha_{3\mathrm{b}}^{(0)} &= \frac{2a_{3\mathrm{b}}^{(0)}}{35} - \frac{2a_{3\mathrm{b}}^{(2)}}{7} + \frac{3a_{3\mathrm{b}}^{(3)}}{5} + \frac{243a_{3\mathrm{b}}^{(4)}}{385} - \frac{a_{3\mathrm{b}}^{(6)}}{385}, \\
\alpha_{3\mathrm{b}}^{(1)} &= -\frac{a_{3\mathrm{b}}^{(0)}}{30} + \frac{23a_{3\mathrm{b}}^{(2)}}{126} - \frac{29a_{3\mathrm{b}}^{(3)}}{60} + \frac{513a_{3\mathrm{b}}^{(4)}}{1540} + \frac{a_{3\mathrm{b}}^{(6)}}{990}, \\
\alpha_{3\mathrm{b}}^{(2)} &= -\frac{29a_{3\mathrm{b}}^{(0)}}{1260} + \frac{13a_{3\mathrm{b}}^{(2)}}{126} - \frac{43a_{3\mathrm{b}}^{(3)}}{360} + \frac{117a_{3\mathrm{b}}^{(4)}}{3080} + \frac{a_{3\mathrm{b}}^{(6)}}{770}, \\
\alpha_{3\mathrm{b}}^{(3)} &= -\frac{a_{3\mathrm{b}}^{(0)}}{945} + \frac{a_{3\mathrm{b}}^{(2)}}{1134} + \frac{a_{3\mathrm{b}}^{(3)}}{540} - \frac{3a_{3\mathrm{b}}^{(4)}}{1540} + \frac{17a_{3\mathrm{b}}^{(6)}}{62370}, \\
\alpha_{3\mathrm{b}}^{(4)} &= \frac{a_{3\mathrm{b}}^{(0)}}{3780} - \frac{a_{3\mathrm{b}}^{(2)}}{1134} + \frac{a_{3\mathrm{b}}^{(3)}}{1080} - \frac{a_{3\mathrm{b}}^{(4)}}{3080} + \frac{a_{3\mathrm{b}}^{(6)}}{62370}.
\end{aligned} \tag{7.52}$$

For $f = 3$ atoms, the degree of complexity increases rapidly where now the states with $F_{3\mathrm{b}} = 1$, 3, 4, 5, 6, 7, and 9 contribute in the interaction (see Table 6.2) and analog expressions for $\alpha_{3\mathrm{b}}$ can be obtained.

In order to estimate the two- and three-body mean-field contributions and their relative importance, we analyze the two- and three-body coupling constants

$$g_{2\mathrm{b}}^{(i)} = \frac{4\pi}{m}\alpha_{2\mathrm{b}}^{(i)} \quad \text{and} \quad g_{3\mathrm{b}}^{(i)} = 3^{1/2}\frac{12\pi}{m}\alpha_{3\mathrm{b}}^{(i)}, \tag{7.53}$$

respectively [38]. This way, we can estimate the two- and three-body mean-field energies simply as $ng_{2\mathrm{b}}$ and $n^2 g_{3\mathrm{b}}$, respectively, with n being the atomic density. This makes clear that relative importance of three-body effects will depend on the density (the denser the gas the more important three-body contributions are.) For instance, as pointed out in Ref. [36], the $f = 1$ ferromagnetic and anti-ferromagnetic phases can be affected by three-body physics whenever the three-body mean-field energy exceeds the two-body mean-field energy, i.e.,

$$n^2|g_{3\mathrm{b}}^{(1)}| > n|g_{2\mathrm{b}}^{(1)}|, \tag{7.54}$$

and are of opposite sign. It is interesting noting that for most of the alkali species the two-body scattering lengths are typically small, implying that the two-body direct and spin-exchange mean-field energies are also small opening up ways to explore the importance of three-body effects for the system. The fact that the two-body scattering lengths are small does not necessarily imply that the three-body scattering volumes, A_{3B}, are also small. A notable case is the $f = 1$ ^{87}Rb spinor condensate where not only are the scattering lengths small, but they are also approximately the same. For this case, $a_0 \approx 1.23 r_{\mathrm{vdW}}$ and $a_2 = 1.21 r_{\mathrm{vdW}}$ [238, 239] implying an extremely small spin-exchange energy term $\alpha_{2\mathrm{b}}^{(1)} \approx -5.6 \times 10^{-3} r_{\mathrm{vdW}}$ [see Eq. (7.44)], and the three-body spin-exchange can be important. Determining the three-body contributions (the actual value of the three-body scattering volumes) for such cases is extremely challenging since it would require a full numerical calculation including realistic two- and three-body interactions.

In the strongly interacting regime, not only do the three-body interactions become important, but they also become universal [36]. The Efimov physics for the spin problem displays many features that can allow for an independent control of both two- and three-body physics opening up ways to strongly modify the spin dynamics in the condensate. From the analysis above, it is clear that

the impact of Efimov physics to the spin dynamics is made through its role in three-body elastic processes. In general, Efimov states are manifested in the three-body scattering observables through log-periodic interference and resonant effects.

For $f = 1$, an interesting case emerges when both a_0 and a_2 assume large and negative values. In the case where $|a_0| \gg |a_2|$ an analytical expression for the relevant three-body scattering volume for $F_{3\mathrm{b}} = 1$ was derived in Sec. 6.5, and the other relevant three-body scattering volume for $F_{3\mathrm{b}} = 3$ can also be derived using similar pathway arguments

$$A_{3B}^{(1)} = \left[\alpha - \beta \tan\left(s_0 \ln \frac{a_2}{a_1^-}\right)\right] \left(\frac{a_2}{a_0}\right)^{0.82} a_0^4 + \gamma a_0^4, \tag{7.55}$$

$$A_{3B}^{(3)} = \left[\alpha - \beta \tan\left(s_0 \ln \frac{a_2}{a_3^-}\right)\right] a_2^4, \tag{7.56}$$

where $s_0 \approx 1.0062$, and α, β and γ are universal constants that can be determined from numerical calculations for each value of $F_{3\mathrm{b}}$. The factor (a_2/a_0) above originates from the regions where the three-body potentials are repulsive–see Table 6.2. For negative values of a_0 and a_2, the Efimov physics is manifested in elastic processes when a Efimov state becomes bound. In the above equations, $a_{F_{3\mathrm{b}}}^-$ are the values where a $F_{3\mathrm{b}} = 1$ and 3 Efimov resonances occur. Near such values of $a_{F_{3\mathrm{b}}}^-$, the three-body scattering volume A_{3B} can be extremely large, assuming both positive and negative values, allowing for control of the spin dynamics via the spin-exchange term in Eq. (7.51). In reality, since three-body losses are present and Efimov states have a finite lifetime, A_{3B} does not strictly diverge and, in fact, is a complex quantity whose real and imaginary parts describe elastic and inelastic collisions—one can introduce loss effects in the expressions above (and below) by adding an imaginary phase term $i\eta$ in the argument of the tangent, where η is the so-called three-body inelasticity parameter [174, 247]. Nevertheless, for typical values of η [174, 247] one can still expect substantial tunability of the three-body spin-exchange dynamics.

For $f = 2$ atoms, evidently, the complexity in determining the three-body spin-dynamics increases. As we mentioned above, an interesting case is presented for $f = 2$ ^{85}Rb atoms, where all the relevant two-body scattering lengths are large and negative ($a_0 \approx -8.97 r_{\mathrm{vdW}}$, $a_2 \approx -6.91 r_{\mathrm{vdW}}$, and $a_4 \approx -4.73 r_{\mathrm{vdW}}$ [238, 239]) and close to the value in which identical bosons display an Efimov

resonance, $-10r_{\rm vdW}$ [175, 176, 177, 178, 179, 180, 181, 182, 183, 184, 185, 186, 187, 188, 189, 190, 191, 192, 193, 194, 195, 196, 197, 198, 199, 200]. This implies that Efimov resonances might enhance three-body spin-exchange. Since the magnitude of the scattering lengths in this case are comparable, it makes it difficult to obtain an accurate universal expression for the three–body scattering lengths. Nevertheless, it is instructive to analyze the results obtained by assuming $|a_0| \gg |a_2| \gg |a_4|$. In this case, the relevant three-body scattering volumes are given by

$$A_{3B}^{(0)} = \left[\alpha - \beta \tan\left(s_0 \ln \frac{a_2}{a_0^-}\right)\right] a_2^4 \tag{7.57}$$

$$A_{3B}^{(2)} = \left[\alpha - \beta \tan\left(s_0 \ln \frac{a_4}{a_2^-} + s_0' \ln \frac{a_2}{a_4}\right)\right] \left(\frac{a_2}{a_0}\right)^{1.37} a_0^4 + \gamma a_0^4 \tag{7.58}$$

$$A_{3B}^{(3)} = \left[\alpha - \beta \tan\left(s_0 \ln \frac{a_4}{a_3^-} + s_0' \ln \frac{a_2}{a_4}\right)\right] a_2^4 \tag{7.59}$$

$$A_{3B}^{(4)} = \left[\alpha - \beta \tan\left(s_0 \ln \frac{a_4}{a_4^-}\right)\right] \left(\frac{a_4}{a_2}\right)^{1.04} a_2^4 + \gamma a_2^4 \tag{7.60}$$

$$A_{3B}^{(6)} = \left[\alpha - \beta \tan\left(s_0 \ln \frac{a_4}{a_6^-}\right)\right] a_4^4 \tag{7.61}$$

where $s_0 \approx 1.0062$, $s_0' \approx 0.3788$, and $a_{F_{3\rm b}}^- < 0$ are the values of the two-body scattering lengths where a $F_{3\rm b}$ Efimov resonance occur. Note that now two distinct families of Efimov states (associated to s_0 and s_0') can affect the spin dynamics. Although we expect the values for $a_{F_{3\rm b}}^-$ to be close to -10$r_{\rm vdW}$ an analysis similar to the one for identical bosons [197, 198] is necessary to precisely determine such values.

For higher spin the three-body contribution introduces additional complexity on the manifold of possible ground state phases of the spinor condensate. The full study of the impact of three-body contributions on the many-body phases of spinor condensates remains however the subject of future investigation.

7.5 Conclusion

The cumulant expansion method generates a linked set of equations for all orders of correlation dynamics in the many-body system. For ultracold strongly-interacting Bose gases, the vacuum limit of these equations is formally identical to the one, two, three, etc... atom Schrödinger

equation. This framework is therefore a natural way to incorporate few-body physics into the many-body problem. As a demonstration, the GPE was rederived by making the Markov and first Born approximations. The generality of the framework allowed higher order terms in the diluteness parameter to be included into the GPE to produce the three-body GPE. This upgraded GPE depends on the three-body T-matrix, whose real part is proportional to the elastic three-body phase shift, which was analyzed in Chapters 3–4. When an Efimov trimer is near threshold, the real part of the three-body T-matrix can display resonant enhancement similar to the Feshbach resonance discussed in Sec. 2.2.4. This chapter closed with an analysis of how this resonant enhancement can impact the ground state superfluid and magnetic structure of the strongly-interacting Bose gas.

Although the cumulant expansion method was employed in this section to derive the GPE and higher order corrections in the diluteness parameter, neither the chain of dependence nor complete studies of the underlying dynamics of three-particle correlations have been explored in detail to date. This is largely due to the crux requirement: three-particle correlation dynamics depend on the scattering physics of three atoms, including the effect of Efimov trimers. The discussion of the elastic three-body phase shift in Chapter 5 highlighted how this necessary ingredient for constructing the three-particle T-matrix is notoriously difficult to calculate.

The cumulant expansion method provides an avenue to insert the few-body scattering solutions into the many-body problem, however, near a scattering resonance, the bound spectrum becomes crucial to the problem and must be included in the many-body problem somehow. In the conclusion chapter of this thesis, Chapter 8, I propose the union of the cumulant expansion method and resonance superfluidity method [55], which is a set of procedures for building bound state physics into the many-body problem. This union could potentially yield a mean-field-like set of equations for the unitary Bose gas, and so stands as an important future extension of the work in this thesis.

Chapter 8

Conclusion

The pace of scientific advancement is *nonlinear*, as was famously codified by Thomas Kuhn in his famous book on scientific revolutions [280]. There is **normal science** which consists of filling in the defects and gaps of existing theories, and then there is the crisis and resultant **paradigm shift** due to the violation of our expectations from normal science. Normal science is paradigm based. As a practicing theorist, the immediate avenue taken with any new problem or result is to first reflect on what *worked in the past*. And it is precisely the intermittent failure of this approach which leads to the reshaping of our understanding of the natural world.

The work presented in Chapter 3 drew from established methodology for analyzing the Boltzmann equation, which is by now a very mature subject more than a century after its first formulation. The Boltzmann equation and underlying assumptions predated Einstein's work on Brownian motion and the experimental verification of the atomistic view of nature and was extremely controversial. Demonstrating agreement between experiment and theory for the undamped breathing mode in an isotropic harmonic trap is therefore an important piece to understanding the inherent limitations on the observation of an undamped, nonequilibrium monopole mode given a realistic trapping scenario. This work reaffirms and refines the foundation of the kinetic theory of gases.

The results of an experimental and theoretical collaboration presented Chapter 4 falls under the set of collective mode experiments on finite temperature BECs initiated almost two decades ago. These are the first such results for an isotropic trapping geometry which has only recently been technologically achieved. The unexpected temperature dependence of the $m = 0$ quadrupole

mode in Ref. [21] (see Fig. 4.1), inspired theoretical analysis that explicitly included the dynamics of the thermal cloud. From the set of successful theories, we applied the coupled-modes analysis of Bijlsma and Stoof [29] and the ZNG formalism [139] to analyze the breathing mode experiment for an extremely spherical trap, drawing an analogy between the observed collapse revival of the oscillation envelope with the hydrodynamic theory of the first and second sound modes in liquid helium. This is an application of theoretical frameworks that have worked in the past combined with ideas about the transport properties of helium II originating from Landau, Tisza, and London more than a half century ago, and the results feed into the ongoing construction of *consensus* in the ultracold gas community about the range of validity of various theories of the finite temperature BEC.

The results of these chapters underscored the relatively firm foundational footing of our understanding of weakly-interacting Bose gases. In the regime of strong interactions, nonperturbative effects beyond the level of one and two atoms become important. Chapter 5 introduced the nonperturbative Efimov states that arise on the three-body level in this regime, characterized their bound state spectrum at unitarity, and presented results for the three-body elastic scattering problem; Chapter 6 discussed the Efimov physics of three-atoms with access to multiple degenerate internal levels, finding novel families of (spinor) Efimov states. The spectrum of Efimov states was probed experimentally for the first time using an ultracold gas of ^{133}Cs in Ref. [34]. This and subsequent demonstrations with a range of atomic species, provided the unexpected universality of the three-body parameter for ultracold alkali species. The predicted spectrum for spinor Efimov states remains unconfirmed.

It remains an open question how Efimov physics emerges in the thermodynamics of strongly-interacting Bose gases. In Chapter 7, one framework for understanding these effects, the method of cumulant expansion, was outlined. Within this framework, a natural connection between the few-body Schrödinger equation can be established in the vacuum limit, and medium effects serve to dress the few-body problem. This framework was used to establish the leading order contribution of elastic three-body scattering to the condensate equation of motion, which permitted a study of the

impact Efimov physics on the superfluid and magnetic phases in spinor condensates. Quantitative predictions for the role and onset of these effects however remains elusive due primarily to the difficulty of extracting scattering observables from the elastic three-body scattering problem.

Experiments in this regime are also plagued by the disastrous scaling of inelastic three-body loss processes as the scattering length approaches the resonance limit. Cutting-edge experiments representing the state-of-the-art in the field of ultracold gases have recently made progress in investigating the unitary Bose gas. Using nondegenerate clouds, experiments at the Cavendish Laboratory [57] and at the École Normale Supérieure [58] uncovered regimes where loss rates are suppressed and accessed the strongly-interacting regime. For the quantum degenerate unitary Bose gas, a remarkable experiment [59] at JILA in Boulder Colorado quenched to the center of the resonance and observed a quasistable state with universal dynamics saturating on a shorter timescale than the expected three-body loss rate. It has been proposed that the JILA measured momentum distribution contains the effect of Efimov physics [281, 282], and an interferometry experiment from the Cavendish laboratory has shown effects that cannot be explained by two-body correlations in the gas [283]. Although many questions remain open, these developments point toward a deeper understanding of strongly-correlated and strongly-interacting systems on the horizon. In the following section, I discuss briefly how the results of Chapters 5–7 might be used in conjunction with lessons learned from the unitary Fermi gas to construct a mean-field like theory to describe the unitary Bose gas.

8.1 Outlook

In the conclusion portion of each chapter of this thesis, avenues of future work have been highlighted. Perhaps none of these possibilities touch on an area producing such startling results as the unitary Bose gas, and so I devote this final outlook to discussion of a candidate theory.

In Sec. 7.1, I discussed three possible avenues towards describing the unitary Bose gas. One of these candidates stems from the resonance superfluidity model [54, 55, 56], which is a two-channel many-body model that deals with the closed channel Feshbach dimer explicitly. The addition of the

second channel is accounted for through the addition of auxiliary molecular field operator $\psi_m(\mathbf{x})$ which obeys Bose statistics. Just as was done in Sec. 2.2.5, an effective theory can be derived [55] which reproduces the energy dependence of the scattering observables at the Feshbach resonance and has been renomarlized to hide the cutoff dependence in the detuning, channel coupling, and strength of the contact interaction. Importantly, this model was very successful in studying the related unitary Fermi gas over a decade ago, which is stable due to the long lifetime of the Feshbach dimer and statistical suppression of three-body losses.

This model has yet to be applied to the recent results for the unitary Bose gas, nor has a generalization to include bound state physics of higher numbers of atoms been derived. This is partly due to the difficulty and relative importance of three-body correlation dynamics for the unitary Bose gas compared to the unitary Fermi gas where Efimov physics is suppressed by identical particle symmetry in the ultracold limit. The theory of resonance superfluidity outlines a general procedure for installing bound states of any number of atoms, including, in principle, trimers. The cumulant theory outlined in Chapter 7, which was originally extended to the level of three-body correlations in Ref. [53] to analyze higher order contributions to the GPE in the diluteness parameter, is the logical candidate for studying the coupled dynamics of one, two, and three-body correlations in the gas as discussed in Chapter 7. There is therefore a hierarchy of candidate theories for the unitary Bose gas based on the union of the cumulant expansion method and the resonance superfluidity model, which increasingly reflect the underlying few-body bound state physics:

(1) The coupled equations of one, two, and three-body correlations, excluding bound state physics as generated in Chapter 7.

(2) The coupled equations of one, two, and three-body correlations, including the Feshbach dimer as a molecular BEC. This requires the introduction of an auxiliary dimer field operator $\psi_m(\mathbf{x})$.

(3) The coupled equations of one, two, and three-body correlations, including the Feshbach dimer as a molecular BEC, and the Efimov states as a trimer BEC. Additionally, this

requires the introduction of an auxiliary trimer field operator $\psi_t(\mathbf{x})$.

These are effective theories, and must reproduce the energy dependence of the scattering observables over the experimental energy range using a set of fitting parameters. Therefore it is essential to understand the behavior of the phase shift discussed in Chapter 5. Importantly, the finite size of the Efimov trimer provides a new length scale to the third candidate theory in addition to the interparticle spacing, breaking the universal scaling of observables as powers of the inter particle spacing $n^{-1/3}$.

Bibliography

[1] Toshiya Kinoshita, Trevor Wenger, and David S Weiss. A quantum newton's cradle. Nature, 440(7086):900–903, 2006.

[2] Ludwig Boltzmann. Wissenschaftliche abhandlungen, volume 1. Cambridge University Press, 2012.

[3] KM O'hara, SL Hemmer, ME Gehm, SR Granade, and JE Thomas. Observation of a strongly interacting degenerate fermi gas of atoms. Science, 298(5601):2179–2182, 2002.

[4] CA Regal and DS Jin. Measurement of positive and negative scattering lengths in a fermi gas of atoms. Physical review letters, 90(23):230404, 2003.

[5] Thomas Bourdel, Julien Cubizolles, L Khaykovich, KMF Magalhaes, SJJMF Kokkelmans, GV Shlyapnikov, and Christophe Salomon. Measurement of the interaction energy near a feshbach resonance in a l i 6 fermi gas. Physical review letters, 91(2):020402, 2003.

[6] DM Stamper-Kurn, H-J Miesner, S Inouye, MR Andrews, and W Ketterle. Collisionless and hydrodynamic excitations of a bose-einstein condensate. Physical Review Letters, 81(3):500, 1998.

[7] M Leduc, J Leonard, F Pereira dos Santos, E Jahier, S Schwartz, and C Cohen-Tannoudji. Hydrodynamic modes in a trapped gas of metastable helium above the bose-einstein transition. Acta Physica Polonica. Series B, 33(8):2213–2224, 2002.

[8] SD Gensemer and DS Jin. Transition from collisionless to hydrodynamic behavior in an ultracold fermi gas. Physical review letters, 87(17):173201, 2001.

[9] F Toschi, P Capuzzi, S Succi, P Vignolo, and MP Tosi. Transition to hydrodynamics in colliding fermion clouds. Journal of Physics B: Atomic, Molecular and Optical Physics, 37(7):S91, 2004.

[10] F Toschi, P Vignolo, S Succi, and MP Tosi. Dynamics of trapped two-component fermi gas: Temperature dependence of the transition from collisionless to collisional regime. Physical Review A, 67(4):041605, 2003.

[11] I Shvarchuck, Ch Buggle, DS Petrov, K Dieckmann, M Zielonkowski, M Kemmann, TG Tiecke, W Von Klitzing, GV Shlyapnikov, and JTM Walraven. Bose-einstein condensation into nonequilibrium states studied by condensate focusing. Physical review letters, 89(27):270404, 2002.

[12] Ch Buggle, I Shvarchuck, W Von Klitzing, and JTM Walraven. Hydrodynamic clouds and bose-einstein condensation. In Journal de Physique IV (Proceedings), volume 116, pages 211–217. EDP sciences, 2004.

[13] I Shvarchuck, Ch Buggle, DS Petrov, M Kemmann, W von Klitzing, GV Shlyapnikov, and JTM Walraven. Hydrodynamic behavior in expanding thermal clouds of 87 rb. Physical Review A, 68(6):063603, 2003.

[14] Fabrice Gerbier, Joseph H Thywissen, Simon Richard, Mathilde Hugbart, Philippe Bouyer, and Alain Aspect. Critical temperature of a trapped, weakly interacting bose gas. Physical review letters, 92(3):030405, 2004.

[15] Markus Greiner, Cindy A Regal, and Deborah S Jin. Emergence of a molecular bose–einstein condensate from a fermi gas. Nature, 426(6966):537–540, 2003.

[16] Selim Jochim, Markus Bartenstein, Alexander Altmeyer, Gerhard Hendl, Stefan Riedl, Cheng Chin, J Hecker Denschlag, and Rudolf Grimm. Bose-einstein condensation of molecules. Science, 302(5653):2101–2103, 2003.

[17] J Cubizolles, T Bourdel, SJJMF Kokkelmans, GV Shlyapnikov, and C Salomon. Production of long-lived ultracold l i 2 molecules from a fermi gas. Physical review letters, 91(24):240401, 2003.

[18] Martin W Zwierlein, Claudiu A Stan, Christian H Schunck, Sebastian MF Raupach, Subhadeep Gupta, Zoran Hadzibabic, and Wolfgang Ketterle. Observation of bose-einstein condensation of molecules. Physical review letters, 91(25):250401, 2003.

[19] D. S. Jin, J.R. Ensher, M. R. Matthews, C. E. Wieman, and E. A. Cornell. Phys. Rev. Lett., 77:420, 1996.

[20] M. O. Mewes, M. R. Andrews, N. J. van Druten, D. M. Stamper-Kurn, D. S. Durfee, C. G. Townsend, and W. Ketterle. Phys. Rev. Lett., 77(988), 1996.

[21] D. S. Jin, M. R. Matthews, J.R. Ensher, C. E. Wieman, and E. A. Cornell. Phys. Rev. Lett., 78:764, 1997.

[22] Onofrio Maragò, Gerald Hechenblaikner, Eleanor Hodby, and Christopher Foot. Phys. Rev. Lett., 86:3938, 2001.

[23] F. Chevy, V. Bretin, P. Rosenbusch, K. W. Madison, and J. Dalibard. Phys. Rev. Lett., 88:250402, 2002.

[24] DS Lobser, AES Barentine, EA Cornell, and HJ Lewandowski. Observation of a persistent non-equilibrium state in cold atoms. Nature Physics, 11(12):1009–1012, 2015.

[25] Ladislas Tisza. Sur la supraconductibilite thermique de l'helium ii liquide et la statistique de bose-einstein. CR Acad. Sci, 207(22):1035, 1938.

[26] László Tisza. Transport phenomena in helium ii. Nature, 141:913, 1938.

[27] Fritz London. On the bose-einstein condensation. Physical Review, 54(11):947, 1938.

[28] L Landau. Theory of the superfluidity of helium ii. Physical Review, 60(4):356, 1941.

[29] MJ Bijlsma and HTC Stoof. Collisionless modes of a trapped bose gas. Physical Review A, 60(5):3973, 1999.

[30] Cheng Chin, Rudolf Grimm, Paul Julienne, and Eite Tiesinga. Feshbach resonances in ultracold gases. Reviews of Modern Physics, 82(2):1225, 2010.

[31] V Efimov. Hard-core interaction and 3-nucleon problem. SOVIET JOURNAL OF NUCLEAR PHYSICS-USSR, 10(1):62, 1970.

[32] Vitaly Efimov. Low-energy properties of 3 resonantly interacting particles. SOVIET JOURNAL OF NUCLEAR PHYSICS-USSR, 29(4):546–553, 1979.

[33] V Efimov. Energy levels of three resonantly interacting particles. Nuclear Physics A, 210(1):157–188, 1973.

[34] T Kraemer, M Mark, P Waldburger, JG Danzl, C Chin, B Engeser, AD Lange, K Pilch, A Jaakkola, H-C Nägerl, et al. Evidence for efimov quantum states in an ultracold gas of caesium atoms. Nature, 440(7082):315–318, 2006.

[35] A Bulgak and V Efimov. Spin effect on the level spectrum of three resonantly interacting particles. Yadernaya Fizika, 22(2):296–307, 1975.

[36] V. E. Colussi, Chris H. Greene, and J. P. D'Incao. Three-body physics in strongly correlated spinor condensates. Phys. Rev. Lett., 113:045302, Jul 2014.

[37] V E Colussi, Chris H Greene, and J P DIncao. Universal few-body physics in resonantly interacting spinor condensates. Journal of Physics B: Atomic, Molecular and Optical Physics, 49(6):064012, 2016.

[38] Aurel Bulgac. Dilute quantum droplets. Phys. Rev. Lett., 89:050402, Jul 2002.

[39] Paulo F. Bedaque, Aurel Bulgac, and Gautam Rupak. Quantum corrections to dilute bose liquids. Phys. Rev. A, 68:033606, Sep 2003.

[40] Holger Kadau, Matthias Schmitt, Matthias Wenzel, Clarissa Wink, Thomas Maier, Igor Ferrier-Barbut, and Tilman Pfau. Observing the rosensweig instability of a quantum ferrofluid. Nature, 530(7589):194–197, 2016.

[41] Matthias Schmitt, Matthias Wenzel, Fabian Böttcher, Igor Ferrier-Barbut, and Tilman Pfau. Self-bound droplets of a dilute magnetic quantum liquid. Nature, 539(7628):259–262, 2016.

[42] Igor Ferrier-Barbut, Holger Kadau, Matthias Schmitt, Matthias Wenzel, and Tilman Pfau. Observation of quantum droplets in a strongly dipolar bose gas. Physical Review Letters, 116(21):215301, 2016.

[43] RN Bisset and PB Blakie. Crystallization of a dilute atomic dipolar condensate. Physical Review A, 92(6):061603, 2015.

[44] L Chomaz, S Baier, D Petter, MJ Mark, F Wächtler, L Santos, and F Ferlaino. Quantum-fluctuation-driven crossover from a dilute bose-einstein condensate to a macrodroplet in a dipolar quantum fluid. Physical Review X, 6(4):041039, 2016.

[45] PB Blakie. Properties of a dipolar condensate with three-body interactions. Physical Review A, 93(3):033644, 2016.

[46] Kui-Tian Xi and Hiroki Saito. Droplet formation in a bose-einstein condensate with strong dipole-dipole interaction. Physical Review A, 93(1):011604, 2016.

[47] A Macia, J Sánchez-Baena, J Boronat, and F Mazzanti. Droplets of trapped quantum dipolar bosons. Physical Review Letters, 117(20):205301, 2016.

[48] Hiroki Saito. Path-integral monte carlo study on a droplet of a dipolar bose–einstein condensate stabilized by quantum fluctuation. Journal of the Physical Society of Japan, 85(5):053001, 2016.

[49] D Baillie, RM Wilson, RN Bisset, and PB Blakie. Self-bound dipolar droplet: a localized matter-wave in free space. arXiv preprint arXiv:1606.00824, 2016.

[50] NP Proukakis and K Burnett. Generalized mean fields for trapped atomic bose-einstein condensates. National Institute of Standards and Technology, Journal of Research, 101(4):457–469, 1996.

[51] Jens Fricke. Transport equations including many-particle correlations for an arbitrary quantum system: A general formalism. Annals of Physics, 252(2):479 – 498, 1996.

[52] Thorsten Köhler and Keith Burnett. Microscopic quantum dynamics approach to the dilute condensed bose gas. Physical Review A, 65(3):033601, 2002.

[53] Thorsten Köhler. Three-body problem in a dilute bose-einstein condensate. Physical review letters, 89(21):210404, 2002.

[54] M Holland, SJJMF Kokkelmans, ML Chiofalo, and R Walser. Resonance superfluidity in a quantum degenerate fermi gas. Physical Review Letters, 87(12):120406, 2001.

[55] SJJMF Kokkelmans, JN Milstein, ML Chiofalo, R Walser, and MJ Holland. Resonance superfluidity: Renormalization of resonance scattering theory. Physical Review A, 65(5):053617, 2002.

[56] ML Chiofalo, SJJMF Kokkelmans, JN Milstein, and MJ Holland. Signatures of resonance superfluidity in a quantum fermi gas. Physical review letters, 88(9):090402, 2002.

[57] Richard J Fletcher, Alexander L Gaunt, Nir Navon, Robert P Smith, and Zoran Hadzibabic. Stability of a unitary bose gas. Physical review letters, 111(12):125303, 2013.

[58] BS Rem, AT Grier, I Ferrier-Barbut, U Eismann, T Langen, N Navon, L Khaykovich, F Werner, DS Petrov, F Chevy, et al. Lifetime of the bose gas with resonant interactions. Physical review letters, 110(16):163202, 2013.

[59] Philip Makotyn, Catherine E Klauss, David L Goldberger, EA Cornell, and Deborah S Jin. Universal dynamics of a degenerate unitary bose gas. Nature Physics, 10(2):116–119, 2014.

[60] VE Colussi, Cameron JE Straatsma, Dana Z Anderson, and MJ Holland. Undamped nonequilibrium dynamics of a nondegenerate bose gas in a 3d isotropic trap. New Journal of Physics, 17(10):103029, 2015.

[61] CJE Straatsma, VE Colussi, MJ Davis, DS Lobser, MJ Holland, DZ Anderson, HJ Lewandowski, and EA Cornell. Collapse and revival of the monopole mode of a degenerate bose gas in an isotropic harmonic trap. Physical Review A, 94(4):043640, 2016.

[62] VE Colussi, Chris H Greene, and JP DIncao. On the appearance of families of efimov states in the spinor three-body problem. In EPJ Web of Conferences, volume 113, page 02003. EDP Sciences, 2016.

[63] Daniel Scott Lobser. Observation of a Persistent Non-Equilibrium State in an Extremely Isotropic Harmonic Potential. PhD thesis, UNIVERSITY OF COLORADO AT BOULDER, 2015.

[64] Dan M Stamper-Kurn and Masahito Ueda. Spinor bose gases: Symmetries, magnetism, and quantum dynamics. Reviews of Modern Physics, 85(3):1191, 2013.

[65] Christopher J Pethick and Henrik Smith. Bose-Einstein condensation in dilute gases. Cambridge university press, 2002.

[66] Brian Harold Bransden and Charles Jean Joachain. Physics of atoms and molecules. Pearson Education India, 2003.

[67] Alan L Migdall, John V Prodan, William D Phillips, Thomas H Bergeman, and Harold J Metcalf. First observation of magnetically trapped neutral atoms. Physical Review Letters, 54(24):2596, 1985.

[68] Wolfgang Petrich, Michael H Anderson, Jason R Ensher, and Eric A Cornell. Stable, tightly confining magnetic trap for evaporative cooling of neutral atoms. Physical Review Letters, 74(17):3352, 1995.

[69] M. H. Anderson, J.R. Ensher, M. R. Matthews, C. E. Wieman, and E. A. Cornell. Science, 269:198, 1995.

[70] A Messiah. Quantum Mechanics (2 Volumes in 1). Dover Publications, New York, 1999.

[71] Brian E Granger, Edward L Hamilton, and Chris H Greene. Quantum and semiclassical analysis of long-range rydberg molecules. Physical Review A, 64(4):042508, 2001.

[72] Vladimir S Potapov and John R Taylor. Three-particle scattering rates and singularities of the t matrix. ii. Physical Review A, 16(6):2276, 1977.

[73] Vladimir S Potapov and John R Taylor. Three-particle scattering rates and singularities of the t matrix. i. Physical Review A, 16(6):2264, 1977.

[74] A Rahman. Correlations in the motion of atoms in liquid argon. Physical Review, 136(2A):A405, 1964.

[75] John R Taylor. Scattering theory: the quantum theory of nonrelativistic collisions. Courier Corporation, 2012.

[76] B DeMarco, JL Bohn, JP Burke Jr, M Holland, and DS Jin. Measurement of p-wave threshold law using evaporatively cooled fermionic atoms. Physical review letters, 82(21):4208, 1999.

[77] M Krauss and WJ Stevens. Effective core potentials and accurate energy curves for cs2 and other alkali diatomics. The Journal of Chemical Physics, 93(6):4236–4242, 1990.

[78] C Amiot. Laser-induced fluorescence of rb2: The (1) $1\sigma+$ g (x),(2) $1\sigma+$ g,(1) 1πu (b),(1) 1πg, and (2) 1πu (c) electronic states. The Journal of Chemical Physics, 93(12):8591–8604, 1990.

[79] J. P. Burke Jr. Theoretical investigation of cold alkali atom collisions. PhD thesis, University of Colorado, 1999.

[80] Massimo Inguscio, Sandro Stringari, and C Wieman. Bose-Einstein condensation in atomic gases, volume 140. IOS Press, 1999.

[81] Claude Cohen-Tannoudji, Bernard Diu, and Frank Laloe. Quantum mechanics, volume 2. Quantum Mechanics, Volume 2, by Claude Cohen-Tannoudji, Bernard Diu, Frank Laloe, pp. 626. ISBN 0-471-16435-6. Wiley-VCH, June 1986., page 626, 1986.

[82] Herman Feshbach. A unified theory of nuclear reactions. ii. Annals of Physics, 19(2):287–313, 1962.

[83] VV Flambaum, GF Gribakin, and C Harabati. Analytical calculation of cold-atom scattering. Physical Review A, 59(3):1998, 1999.

[84] Enrico Fermi. Sopra lo spostamento per pressione delle righe elevate delle serie spettrali. Il Nuovo Cimento (1924-1942), 11(3):157–166, 1934.

[85] Hans Bethe and Rudolf Peierls. Quantum theory of the diplon. Proceedings of the Royal Society of London. Series A, Mathematical and Physical Sciences, 148(863):146–156, 1935.

[86] George B Arfken, Hans J Weber, and Frank E Harris. Mathematical methods for physicists: a comprehensive guide. Academic press, 2011.

[87] Francis J Flanigan. Complex variables: harmonic and analytic functions. Courier Corporation, 1972.

[88] Morton Hamermesh. Group theory and its application to physical problems. Courier Corporation, 1962.

[89] Jean-Paul Blaizot and Georges Ripka. Quantum theory of finite systems, volume 3. Mit Press Cambridge, 1986.

[90] Daniel V Schroeder. An introduction to thermal physics, volume 60. Addison Wesley New York, 2000.

[91] James Clerk Maxwell. The Scientific Letters and Papers of James Clerk Maxwell: 1846-1862, volume 1. CUP Archive, 1990.

[92] James Clerk Maxwell. The Scientific Papers of James Clerk Maxwell..., volume 2. J. Hermann, 1890.

[93] Ludwig Boltzmann. Weitere studien über das wärmegleichgewicht unter gasmolekülen. In Kinetische Theorie II, pages 115–225. Springer, 1970.

[94] Stephen G Brush. Kinetic theory: Irreversible processes. Elsevier, 2013.

[95] Kerson Huang. Statistical mechanics. Wiley, New York, 1963.

[96] Leo P Kadanoff and Gordon A Baym. Quantum statistical mechanics. Benjamin, 1962.

[97] NN Bogolyubov. Problems of a dynamical theory in statistical mechanics. GostInzdat, Moscow, 1946.

[98] Hermann Haken. Laser theory. Springer Science & Business Media, 2012.

[99] David Guéry-Odelin, JG Muga, MJ Ruiz-Montero, and E Trizac. Nonequilibrium solutions of the boltzmann equation under the action of an external force. Physical review letters, 112(18):180602, 2014.

[100] David Guéry-Odelin, Francesca Zambelli, Jean Dalibard, and Sandro Stringari. Collective oscillations of a classical gas confined in harmonic traps. Physical Review A, 60(6):4851, 1999.

[101] U Al Khawaja, CJ Pethick, and H Smith. Kinetic theory of collective modes in atomic clouds above the bose–einstein transition temperature. Journal of low temperature physics, 118(1-2):127–141, 2000.

[102] GM Kavoulakis, Christopher J Pethick, and H Smith. Damping of hydrodynamic modes in a trapped bose gas above the bose-einstein transition temperature. Physical Review A, 57(4):2938, 1998.

[103] Yu Kagan, EL Surkov, and GV Shlyapnikov. Evolution of a bose gas in anisotropic time-dependent traps. Physical Review A, 55(1):R18, 1997.

[104] Y Castin and R Dum. Bose-einstein condensates in time dependent traps. Physical Review Letters, 77(27):5315, 1996.

[105] Victor M Perez-Garcia, H Michinel, JI Cirac, M Lewenstein, and P Zoller. Low energy excitations of a bose-einstein condensate: A time-dependent variational analysis. Physical review letters, 77(27):5320, 1996.

[106] KG Singh and DS Rokhsar. Collective excitations of a confined bose condensate. Physical review letters, 77(9):1667, 1996.

[107] David Guéry-Odelin. Mean-field effects in a trapped gas. Physical Review A, 66(3):033613, 2002.

[108] P Pedri, D Guéry-Odelin, and S Stringari. Dynamics of a classical gas including dissipative and mean-field effects. Physical Review A, 68(4):043608, 2003.

[109] Ch Buggle, P Pedri, W von Klitzing, and JTM Walraven. Shape oscillations in nondegenerate bose gases: Transition from the collisionless to the hydrodynamic regime. Physical Review A, 72(4):043610, 2005.

[110] David Guéry-Odelin. Spinning up and down a boltzmann gas. Physical Review A, 62(3):033607, 2000.

[111] LD Landau. Em lifshitz fluid mechanics. Course of Theoretical Physics, 6, 1959.

[112] B Jackson and E Zaremba. Modeling bose-einstein condensed gases at finite temperatures with n-body simulations. Physical Review A, 66(3):033606, 2002.

[113] Andrew Christopher James Wade, D Baillie, and PB Blakie. Direct simulation monte carlo method for cold-atom dynamics: Classical boltzmann equation in the quantum collision regime. Physical Review A, 84(2):023612, 2011.

[114] R Hockney and J Eastwood. Computer simulations using particles mcgraw-hill. New York, 1981.

[115] Jesus-Maria Sanz-Serna and Mari-Paz Calvo. Numerical Hamiltonian problems, volume 7 of Applied Mathematics and Mathematical Computation. Chapman & Hall, London, 1994.

[116] Haruo Yoshida. Recent progress in the theory and application of symplectic integrators. In Qualitative and Quantitative Behaviour of Planetary Systems, pages 27–43. Springer, 1993.

[117] William H Press, Saul A Teukolsky, William T Vetterling, and Brian P Flannery. Numerical recipes in FORTRAN: the art of scientific computing, volume 2. Cambridge university press New York, 1992.

[118] Russell J Donnelly. The two-fluid theory and second sound in liquid helium. Phys. Today, 62(10):34–39, 2009.

[119] K. B. Davis, M. O. Mewes, M. R. Andrews, N. J. van Druten, D. S. Durfee, D. M. Stamper-Kurn, and W. Ketterle. Phys. Rev. Lett., 75:3969, 1995.

[120] M. Edwards, P. A. Ruprecht, K. Burnett, R. J. Dodd, and C. W. Clark. Phys. Rev. Lett., 77:1671, 1996.

[121] S. Stringari. Phys. Rev. Lett., 77:2360, 1996.

[122] U. Al Khawaja and H. T. C. Stoof. Phys. Rev. A, 62:053602, 2000.

[123] E. Zaremba, A. Griffin, and T. Nikuni. Phys. Rev. A, 57:4695, 1998.

[124] V. Shenoy and T.-L. Ho. Phys. Rev. Lett., 80:3895, 1998.

[125] B. Jackson and E. Zaremba. Phys. Rev. Lett., 88:180402, 2002.

[126] B. Jackson and E. Zaremba. Laser Phys., 12:93, 2002.

[127] B. Jackson and E. Zaremba. Laser Phys., 13:1004, 2003.

[128] S. A. Morgan. J. Phys. B.: At. Mol. Opt. Phys., 33:3847, 2000.

[129] M. Rusch, S. A. Morgan, D. A. W. Hutchinson, and K. Burnett. Phys. Rev. Lett., 85:4844, 2000.

[130] S. A. Morgan, M. Rusch, D. A. W. Hutchinson, and K. Burnett. Phys. Rev. Lett., 91:250403, 2003.

[131] S. A. Morgan. Phys. Rev. A, 69:023609, 2004.

[132] S. A. Morgan. Phys. Rev. A, 72:043609, 2005.

[133] A. J. Geddes, S. A. Morgan, and D. A. W. Hutchinson. Prs. R. Soc. A, 461:3647, 2005.

[134] Eugene Zaremba, Tetsuro Nikuni, and Allan Griffin. Dynamics of trapped bose gases at finite temperatures. Journal of Low Temperature Physics, 116(3-4):277–345, 1999.

[135] Claude Cohen-Tannoudji and David Guéry-Odelin. Advances in atomic physics. World Scientific, Singapore, 32:36, 2011.

[136] Tsin D Lee, Kerson Huang, and Chen N Yang. Eigenvalues and eigenfunctions of a bose system of hard spheres and its low-temperature properties. Physical Review, 106(6):1135, 1957.

[137] TD Lee and CN Yang. Many-body problem in quantum mechanics and quantum statistical mechanics. Physical Review, 105(3):1119, 1957.

[138] MR Andrews, DM Kurn, H-J Miesner, DS Durfee, CG Townsend, S Inouye, and W Ketterle. Propagation of sound in a bose-einstein condensate. Physical review letters, 79(4):553, 1997.

[139] Allan Griffin, Tetsuro Nikuni, and Eugene Zaremba. Bose-condensed gases at finite temperatures. Cambridge University Press, 2009.

[140] B. Jackson and E. Zaremba. Phys. Rev. Lett., 87:100404, 2001.

[141] B. Jackson, N. P. Proukakis, and C. F. Barenghi. Phys. Rev. A, 75:051601R, 2007.

[142] B. Jackson, N. P. Proukakis, C. F. Barenghi, and E. Zaremba. Phys. Rev. A, 79:053615, 2009.

[143] A. J. Allen, E. Zaremba, C. F. Barenghi, and N. P. Proukakis. Phys. Rev. A, 87:013630, 2013.

[144] A. J. Allen, N. G. Parker, N. P. Proukakis, and C. F. Barenghi. J. Phys. Conf. Ser., 544:012023, 2014.

[145] K. L. Lee and N. P. Proukakis. arXiv:1607.06939 [cond-mat.quant-gas].

[146] W. Ketterle, D. S. Durfee, and D. M. Stamper-Kurn. Making, probing and understanding Bose-Einstein condensates. In M. Inguscio, S. Stringari, and C. E. Wieman, editors, Bose-Einstein Condensation in Atomic Gases, Proceedings of the International School of Physics "Enrico Fermi", pages 67–176, 1999.

[147] P. C. Hohenberg and P. C. Martin. Ann. Phys., 34:291, 1965.

[148] P. Szépfalusy and I. Kondor. Ann. Phys., 82:1, 1974.

[149] W. V. Liu. Phys. Rev. Lett., 79:4056, 1997.

[150] L. P. Pitaevskii and S. Stringari. Phys. Lett., 235:398, 1997.

[151] P. O. Fedichev, G. V. Shlyapnikov, and J. T. M. Walraven. Phys. Rev. Lett., 80:2269, 1998.

[152] M. Guilleumas and L. P. Pitaevskii. Phys. Rev. A, 61:013602, 1999.

[153] K. Das and T. Bergeman. Phys. Rev. A, 64:013613, 2001.

[154] B. Jackson and E. Zaremba. New J. Phys., 5:88, 2003.

[155] S. T. Beliaev. Zh. Eksp. Teor. Fiz., 34:433, 1958.

[156] R Meppelink, SB Koller, and P van Der Straten. Sound propagation in a bose-einstein condensate at finite temperatures. Physical Review A, 80(4):043605, 2009.

[157] Emiko Arahata and Tetsuro Nikuni. Propagation of first and second sound in a highly elongated trapped bose-condensed gas at finite temperatures. Physical Review A, 87(3):033610, 2013.

[158] BD Esry, Chris H Greene, and James P Burke Jr. Recombination of three atoms in the ultracold limit. Physical review letters, 83(9):1751, 1999.

[159] Esben Nielsen and JH Macek. Low-energy recombination of identical bosons by three-body collisions. Physical review letters, 83(8):1566, 1999.

[160] AJ Moerdijk, HMJM Boesten, and BJ Verhaar. Decay of trapped ultracold alkali atoms by recombination. Physical Review A, 53(2):916, 1996.

[161] Yu Kagan, BV Svistunov, and GV Shlyapnikov. Effect of bose condensation on inelastic processes in gases. JETP Lett, 42(4), 1985.

[162] EA Burt, RW Ghrist, CJ Myatt, MJ Holland, EA Cornell, and CE Wieman. Coherence, correlations, and collisions: What one learns about bose-einstein condensates from their decay. Physical Review Letters, 79(3):337, 1997.

[163] LD Faddeev. Scattering theory for a three-particle system. Zhur. Eksptl'. i Teoret. Fiz., 39, 1960.

[164] DV Fedorov and AS Jensen. Efimov effect in coordinate space faddeev equations. Physical review letters, 71(25):4103, 1993.

[165] LM Delves. Tertiary and general-order collisions. Nuclear Physics, 9(3):391–399, 1958.

[166] LM Delves. Tertiary and general-order collisions (ii). Nuclear Physics, 20:275–308, 1960.

[167] Jeremy G Frey and Brian J Howard. The calculation of the ground state energy of weakly bound van der waals trimers using the method of hyperspherical harmonics i. the bornoppenheimer and adiabatic approximations. Chemical physics, 99(3):415–426, 1985.

[168] H Suno, BD Esry, Chris H Greene, and James P Burke Jr. Three-body recombination of cold helium atoms. Physical Review A, 65(4):042725, 2002.

[169] Herbert Goldstein. Classical mechanics. Pearson Education India, 1965.

[170] Yu F Smirnov and KV Shitikova. Physics of elementary particles and atomic nuclei. Fiz. Elem. Chastits. At. Yadra, 8:847, 1977.

[171] John S Avery. Hyperspherical harmonics: applications in quantum theory, volume 5. Springer Science & Business Media, 2012.

[172] Seth T Rittenhouse, Nirav P Mehta, and Chris H Greene. Greens functions and the adiabatic hyperspherical method. Physical Review A, 82(2):022706, 2010.

[173] Esben Nielsen, Dmitri Vladimir Fedorov, AS Jensen, and E Garrido. The three-body problem with short-range interactions. Physics Reports, 347(5):373–459, 2001.

[174] Eric Braaten and H-W Hammer. Universality in few-body systems with large scattering length. Physics Reports, 428(5):259–390, 2006.

[175] F Ferlaino, A Zenesini, M Berninger, B Huang, H-C Nägerl, and R Grimm. Efimov resonances in ultracold quantum gases. Few-Body Systems, 51(2-4):113–133, 2011.

[176] M Berninger, A Zenesini, B Huang, W Harm, H-C Nägerl, F Ferlaino, R Grimm, PS Julienne, and JM Hutson. Universality of the three-body parameter for efimov states in ultracold cesium. Physical review letters, 107(12):120401, 2011.

[177] Matteo Zaccanti, Benjamin Deissler, Chiara DErrico, Marco Fattori, Mattia Jona-Lasinio, Stefan Müller, Giacomo Roati, Massimo Inguscio, and Giovanni Modugno. Observation of an efimov spectrum in an atomic system. Nature Physics, 5(8):586–591, 2009.

[178] G Barontini, C Weber, F Rabatti, J Catani, G Thalhammer, M Inguscio, and F Minardi. Observation of heteronuclear atomic efimov resonances. Physical review letters, 103(4):043201, 2009.

[179] Sanjukta Roy, Manuele Landini, Andreas Trenkwalder, Giulia Semeghini, Giacomo Spagnolli, Andrea Simoni, Marco Fattori, Massimo Inguscio, and Giovanni Modugno. Test of the universality of the three-body efimov parameter at narrow feshbach resonances. Physical review letters, 111(5):053202, 2013.

[180] Scott E Pollack, Daniel Dries, and Randall G Hulet. Universality in three-and four-body bound states of ultracold atoms. Science, 326(5960):1683–1685, 2009.

[181] P Dyke, SE Pollack, and RG Hulet. Finite-range corrections near a feshbach resonance and their role in the efimov effect. Physical Review A, 88(2):023625, 2013.

[182] Noam Gross, Zav Shotan, Servaas Kokkelmans, and Lev Khaykovich. Observation of universality in ultracold li 7 three-body recombination. Physical review letters, 103(16):163202, 2009.

[183] Noam Gross, Zav Shotan, Servaas Kokkelmans, and Lev Khaykovich. Nuclear-spin-independent short-range three-body physics in ultracold atoms. Physical review letters, 105(10):103203, 2010.

[184] Olga Machtey, David A Kessler, and Lev Khaykovich. Universal dimer in a collisionally opaque medium: Experimental observables and efimov resonances. Physical review letters, 108(13):130403, 2012.

[185] Timo Bastian Ottenstein, T Lompe, M Kohnen, AN Wenz, and S Jochim. Collisional stability of a three-component degenerate fermi gas. Physical review letters, 101(20):203202, 2008.

[186] T Lompe, TB Ottenstein, F Serwane, K Viering, AN Wenz, G Zürn, and S Jochim. Atom-dimer scattering in a three-component fermi gas. Physical review letters, 105(10):103201, 2010.

[187] JH Huckans, JR Williams, EL Hazlett, RW Stites, and KM OHara. Three-body recombination in a three-state fermi gas with widely tunable interactions. Physical review letters, 102(16):165302, 2009.

[188] JR Williams, EL Hazlett, JH Huckans, RW Stites, Y Zhang, and KM OHara. Evidence for an excited-state efimov trimer in a three-component fermi gas. Physical review letters, 103(13):130404, 2009.

[189] Shuta Nakajima, Munekazu Horikoshi, Takashi Mukaiyama, Pascal Naidon, and Masahito Ueda. Nonuniversal efimov atom-dimer resonances in a three-component mixture of li 6. Physical review letters, 105(2):023201, 2010.

[190] RJ Wild, P Makotyn, JM Pino, EA Cornell, and DS Jin. Measurements of tans contact in an atomic bose-einstein condensate. Physical review letters, 108(14):145305, 2012.

[191] Ruth S Bloom, Ming-Guang Hu, Tyler D Cumby, and Deborah S Jin. Tests of universal three-body physics in an ultracold bose-fermi mixture. Physical review letters, 111(10):105301, 2013.

[192] Cheng Chin. Universal scaling of efimov resonance positions in cold atom systems. arXiv preprint arXiv:1111.1484, 2011.

[193] Pascal Naidon, Emiko Hiyama, and Masahito Ueda. Universality and the three-body parameter of 4 he trimers. Physical Review A, 86(1):012502, 2012.

[194] Pascal Naidon, Shimpei Endo, and Masahito Ueda. Physical origin of the universal three-body parameter in atomic efimov physics. Physical Review A, 90(2):022106, 2014.

[195] Pascal Naidon, Shimpei Endo, and Masahito Ueda. Microscopic origin and universality classes of the efimov three-body parameter. Physical review letters, 112(10):105301, 2014.

[196] Yusuke Horinouchi and Masahito Ueda. Onset of a limit cycle and universal three-body parameter in efimov physics. Physical review letters, 114(2):025301, 2015.

[197] Jia Wang, JP DIncao, BD Esry, and Chris H Greene. Origin of the three-body parameter universality in efimov physics. Physical review letters, 108(26):263001, 2012.

[198] Yujun Wang, Jia Wang, JP DIncao, and Chris H Greene. Universal three-body parameter in heteronuclear atomic systems. Physical review letters, 109(24):243201, 2012.

[199] Richard Schmidt, Steffen Patrick Rath, and Wilhelm Zwerger. Efimov physics beyond universality. The European Physical Journal B, 85(11):1–6, 2012.

[200] Peder Klokmose Sørensen, DV Fedorov, AS Jensen, and Nikolaj Thomas Zinner. Efimov physics and the three-body parameter within a two-channel framework. Physical Review A, 86(5):052516, 2012.

[201] RD Amado and Morton H Rubin. Low-energy expansion for elastic three-body scattering. Physical Review Letters, 25(3):194, 1970.

[202] Roger G Newton. The asymptotic form of three-particle wavefunctions and the cross sections. Annals of Physics, 74(2):324–351, 1972.

[203] Harald Friedrich and H Friedrich. Theoretical atomic physics, volume 3. Springer, 2006.

[204] MV Berry. Semi-classical scattering phase shifts in the presence of metastable states. Proceedings of the Physical Society, 88(2):285, 1966.

[205] Eric Braaten and Agustin Nieto. Quantum corrections to the energy density of a homogeneous bose gas. The European Physical Journal B-Condensed Matter and Complex Systems, 11(1):143–159, 1999.

[206] Eric Braaten, H-W Hammer, and Thomas Mehen. Dilute bose-einstein condensate with large scattering length. Physical review letters, 88(4):040401, 2002.

[207] HR Sadeghpour, JL Bohn, MJ Cavagnero, BD Esry, II Fabrikant, JH Macek, and ARP Rau. Collisions near threshold in atomic and molecular physics. Journal of Physics B: Atomic, Molecular and Optical Physics, 33(5):R93, 2000.

[208] Lev Davidovich Landau, Evgenii Mikhailovich Lifshitz, JB Sykes, John Stewart Bell, and ME Rose. Quantum mechanics, non-relativistic theory. Physics Today, 11:56, 1958.

[209] Roger G Newton. The three-particle s matrix. Journal of Mathematical Physics, 15(3):338–343, 1974.

[210] AU Hazi. Behavior of the eigenphase sum near a resonance. Physical Review A, 19(2):920, 1979.

[211] Jon Alan Wright. Generalization of levinson's theorem to three-body systems. Physical Review, 139(1B):B137, 1965.

[212] JP DIncao and BD Esry. Manifestations of the efimov effect for three identical bosons. Physical Review A, 72(3):032710, 2005.

[213] DS Hall, MR Matthews, JR Ensher, CE Wieman, and EA Cornell. Dynamics of component separation in a binary mixture of bose-einstein condensates. Physical Review Letters, 81(8):1539, 1998.

[214] DS Hall, MR Matthews, CE Wieman, and EA Cornell. Measurements of relative phase in two-component bose-einstein condensates. Physical Review Letters, 81(8):1543, 1998.

[215] J Stenger, S Inouye, DM Stamper-Kurn, H-J Miesner, AP Chikkatur, and W Ketterle. Spin domains in ground-state bose–einstein condensates. Nature, 396(6709):345–348, 1998.

[216] DM Stamper-Kurn, H-J Miesner, AP Chikkatur, S Inouye, J Stenger, and W Ketterle. Quantum tunneling across spin domains in a bose-einstein condensate. Physical review letters, 83(4):661, 1999.

[217] A Görlitz, TL Gustavson, AE Leanhardt, R Löw, AP Chikkatur, S Gupta, S Inouye, DE Pritchard, and W Ketterle. Sodium bose-einstein condensates in the f= 2 state in a large-volume optical trap. Physical review letters, 90(9):090401, 2003.

[218] AE Leanhardt, Y Shin, David Kielpinski, DE Pritchard, and W Ketterle. Coreless vortex formation in a spinor bose-einstein condensate. Physical review letters, 90(14):140403, 2003.

[219] M-S Chang, CD Hamley, MD Barrett, JA Sauer, KM Fortier, W Zhang, L You, and MS Chapman. Observation of spinor dynamics in optically trapped rb 87 bose-einstein condensates. Physical review letters, 92(14):140403, 2004.

[220] J Kronjäger, C Becker, M Brinkmann, R Walser, Patrick Navez, K Bongs, and K Sengstock. Evolution of a spinor condensate: Coherent dynamics, dephasing, and revivals. Physical Review A, 72(6):063619, 2005.

[221] Artur Widera, Fabrice Gerbier, Simon Fölling, Tatjana Gericke, Olaf Mandel, and Immanuel Bloch. Coherent collisional spin dynamics in optical lattices. Physical review letters, 95(19):190405, 2005.

[222] LE Sadler, JM Higbie, SR Leslie, M Vengalattore, and DM Stamper-Kurn. Spontaneous symmetry breaking in a quenched ferromagnetic spinor bose–einstein condensate. Nature, 443(7109):312–315, 2006.

[223] RW Cherng, Vladimir Gritsev, DM Stamper-Kurn, and Eugene Demler. Dynamical instability of the x y spiral state of ferromagnetic condensates. Physical review letters, 100(18):180404, 2008.

[224] SR Leslie, J Guzman, M Vengalattore, Jay D Sau, Marvin L Cohen, and DM Stamper-Kurn. Amplification of fluctuations in a spinor bose-einstein condensate. Physical Review A, 79(4):043631, 2009.

[225] M Vengalattore, J Guzman, SR Leslie, F Serwane, and DM Stamper-Kurn. Periodic spin textures in a degenerate f= 1 rb 87 spinor bose gas. Physical Review A, 81(5):053612, 2010.

[226] J Guzman, G-B Jo, Andre N Wenz, Kater W Murch, Claire K Thomas, and Dan Moss Stamper-Kurn. Long-time-scale dynamics of spin textures in a degenerate f= 1 87 rb spinor bose gas. Physical Review A, 84(6):063625, 2011.

[227] Tin-Lun Ho. Spinor bose condensates in optical traps. Physical review letters, 81(4):742, 1998.

[228] Tetsuo Ohmi and Kazushige Machida. Bose-einstein condensation with internal degrees of freedom in alkali atom gases. Journal of the Physical Society of Japan, 67(6):1822–1825, 1998.

[229] CK Law, Han Pu, and NP Bigelow. Quantum spins mixing in spinor bose-einstein condensates. Physical review letters, 81(24):5257, 1998.

[230] H Pu, CK Law, S Raghavan, JH Eberly, and NP Bigelow. Spin-mixing dynamics of a spinor bose-einstein condensate. Physical Review A, 60(2):1463, 1999.

[231] S Yi, ÖE Müstecaplıoğlu, and L You. Dynamics of quantum phases in a spinor condensate. Physical Review A, 68(1):013613, 2003.

[232] Jun'ichi Ieda, Takahiko Miyakawa, and Miki Wadati. Exact analysis of soliton dynamics in spinor bose-einstein condensates. Physical review letters, 93(19):194102, 2004.

[233] Ryan Barnett, Ari Turner, and Eugene Demler. Classifying novel phases of spinor atoms. Physical review letters, 97(18):180412, 2006.

[234] Jay D Sau, SR Leslie, DM Stamper-Kurn, and Marvin L Cohen. Theory of domain formation in inhomogeneous ferromagnetic dipolar condensates within the truncated wigner approximation. Physical Review A, 80(2):023622, 2009.

[235] Yuki Kawaguchi, Michikazu Kobayashi, Muneto Nitta, and Masahito Ueda. Topological excitations in spinor bose-einstein condensates. Progress of Theoretical Physics Supplement, 186:455–462, 2010.

[236] Yuki Kawaguchi and Masahito Ueda. Symmetry classification of spinor bose-einstein condensates. Physical Review A, 84(5):053616, 2011.

[237] Yuki Kawaguchi and Masahito Ueda. spinor bose–einstein condensates. Physics Reports, 520(5):253–381, 2012.

[238] Nille N Klausen, John L Bohn, and Chris H Greene. Nature of spinor bose-einstein condensates in rubidium. Physical Review A, 64(5):053602, 2001.

[239] EGM Van Kempen, SJJMF Kokkelmans, DJ Heinzen, and BJ Verhaar. Interisotope determination of ultracold rubidium interactions from three high-precision experiments. Physical review letters, 88(9):093201, 2002.

[240] Fabrice Gerbier, Artur Widera, Simon Fölling, Olaf Mandel, and Immanuel Bloch. Resonant control of spin dynamics in ultracold quantum gases by microwave dressing. Physical Review A, 73(4):041602, 2006.

[241] Peng Zhang, Pascal Naidon, and Masahito Ueda. Independent control of scattering lengths in multicomponent quantum gases. Physical review letters, 103(13):133202, 2009.

[242] CD Hamley, EM Bookjans, G Behin-Aein, P Ahmadi, and MS Chapman. Photoassociation spectroscopy of a spin-1 bose-einstein condensate. Physical Review A, 79(2):023401, 2009.

[243] AM Kaufman, RP Anderson, Thomas M Hanna, E Tiesinga, PS Julienne, and DS Hall. Radio-frequency dressing of multiple feshbach resonances. Physical Review A, 80(5):050701, 2009.

[244] TV Tscherbul, T Calarco, I Lesanovsky, RV Krems, A Dalgarno, and J Schmiedmayer. rf-field-induced feshbach resonances. Physical Review A, 81(5):050701, 2010.

[245] Thomas M Hanna, Eite Tiesinga, and Paul S Julienne. Creation and manipulation of feshbach resonances with radiofrequency radiation. New Journal of Physics, 12(8):083031, 2010.

[246] DJ Papoular, GV Shlyapnikov, and J Dalibard. Microwave-induced fano-feshbach resonances. Physical Review A, 81(4):041603, 2010.

[247] Yujun Wang, Jose P DIncao, Brett D Esry, and CC Lin. Ultracold few-body systems. Advances in Atomic, Molecular, and Optical Physics, 62:1, 2013.

[248] Nirav P Mehta, Seth T Rittenhouse, JP DIncao, and Chris H Greene. Efimov states embedded in the three-body continuum. Physical Review A, 78(2):020701, 2008.

[249] Seth T. Rittenhouse. Control and Dynamics of Few-Body Systems at Ultracold Temperatures. PhD thesis, UNIVERSITY OF COLORADO AT BOULDER, 2009.

[250] OI Kartavtsev and JH Macek. Low-energy three-body recombination near a feshbach resonance. Few-Body Systems, 31(2-4):249–254, 2002.

[251] JH Macek. Multichannel zero-range potentials in the hyperspherical theory of three-body dynamics. Few-Body Systems, 31(2-4):241–248, 2002.

[252] Qiaoling Wang and Chris H Greene. Parameter-dependent multichannel rydberg spectra. Physical Review A, 44(3):1874, 1991.

[253] Philip W Anderson et al. More is different. Science, 177(4047):393–396, 1972.

[254] Jorge Quintanilla and Chris Hooley. The strong-correlations puzzle. Physics World, 22(06):32, 2009.

[255] A. G. Sykes, J. P. Corson, J. P. D'Incao, A. P. Koller, C. H. Greene, A. M. Rey, K. R. A. Hazzard, and J. L. Bohn. Quenching to unitarity: Quantum dynamics in a three-dimensional bose gas. Phys. Rev. A, 89:021601, Feb 2014.

[256] Bogdan Borca, D Blume, and Chris H Greene. A two-atom picture of coherent atom–molecule quantum beats. New Journal of Physics, 5(1):111, 2003.

[257] Krzysztof Góral, Thorsten Köhler, Simon A Gardiner, Eite Tiesinga, and Paul S Julienne. Adiabatic association of ultracold molecules via magnetic-field tunable interactions. Journal of Physics B: Atomic, Molecular and Optical Physics, 37(17):3457, 2004.

[258] Thomas Busch, Berthold-Georg Englert, Kazimierz Rzażewski, and Martin Wilkens. Two cold atoms in a harmonic trap. Foundations of Physics, 28(4):549–559, 1998.

[259] Aleksandr Ilich Akhiezer and Sergei Vladimirovich Peletminskii. Methods of Statistical Physics: International Series in Natural Philosophy, volume 104. Elsevier, 2013.

[260] R Walser, J Williams, J Cooper, and M Holland. Quantum kinetic theory for a condensed bosonic gas. Physical Review A, 59(5):3878, 1999.

[261] Mark R. Hermann and J. A. Fleck. Split-operator spectral method for solving the time-dependent schrödinger equation in spherical coordinates. Phys. Rev. A, 38:6000–6012, Dec 1988.

[262] Alexander L Fetter and John Dirk Walecka. Quantum theory of many-particle systems. Courier Corporation, 2003.

[263] Gian-Carlo Wick. The evaluation of the collision matrix. Physical review, 80(2):268, 1950.

[264] Franck Laloë. Dilute degenerate gases. In Bose-Einstein condensation. Cambridge University Press, 1995.

[265] Roger G Newton. Scattering theory of waves and particles. Springer Science & Business Media, 2013.

[266] Shina Tan. Energetics of a strongly correlated fermi gas. Annals of Physics, 323(12):2952–2970, 2008.

[267] Shina Tan. Generalized virial theorem and pressure relation for a strongly correlated fermi gas. Annals of Physics, 323(12):2987–2990, 2008.

[268] Shina Tan. Large momentum part of a strongly correlated fermi gas. Annals of Physics, 323(12):2971–2986, 2008.

[269] Felix Werner and Yvan Castin. Exact relations for quantum-mechanical few-body and many-body problems with short-range interactions in two and three dimensions. arXiv preprint arXiv:1001.0774, 2010.

[270] Eric Braaten, Daekyoung Kang, and Lucas Platter. Universal relations for identical bosons from three-body physics. Phys. Rev. Lett., 106:153005, Apr 2011.

[271] Alexander L Fetter. Ground state and excited states of a confined condensed bose gas. Physical Review A, 53(6):4245, 1996.

[272] Simon L Cornish, Sarah T Thompson, and Carl E Wieman. Formation of bright matter-wave solitons during the collapse of attractive bose-einstein condensates. Physical review letters, 96(17):170401, 2006.

[273] Patrick J Everitt, Mahasen A Sooriyabandara, Gordon D McDonald, Kyle S Hardman, Ciaron Quinlivan, Manju Perumbil, Paul Wigley, John E Debs, John D Close, Carlos CN Kuhn, et al. Observation of breathers in an attractive bose gas. arXiv preprint arXiv:1509.06844, 2015.

[274] P. B. Blakie. Properties of a dipolar condensate with three-body interactions. Phys. Rev. A, 93:033644, Mar 2016.

[275] A Gammal, T Frederico, Lauro Tomio, and Ph Chomaz. Atomic bose-einstein condensation with three-body interactions and collective excitations. Journal of Physics B: Atomic, Molecular and Optical Physics, 33(19):4053, 2000.

[276] Nail Akhmediev, Mukunda P Das, and AV Vagov. Bose-einstein condensation of atoms with attractive interaction. International Journal of Modern Physics B, 13(05n06):625–631, 1999.

[277] CV Ciobanu, S-K Yip, and Tin-Lun Ho. Phase diagrams of f= 2 spinor bose-einstein condensates. Physical Review A, 61(3):033607, 2000.

[278] Jean-Sébastien Bernier, K Sengupta, and Yong Baek Kim. Mott phases and superfluid-insulator transition of dipolar spin-three bosons in an optical lattice: Implications for cr 52 atoms. Physical Review B, 76(1):014502, 2007.

[279] Roberto B Diener and Tin-Lun Ho. Cr 52 spinor condensate: A biaxial or uniaxial spin nematic. Physical review letters, 96(19):190405, 2006.

[280] Thomas S Kuhn. The structure of scientific revolutions. University of Chicago press, 2012.

[281] D Hudson Smith, Eric Braaten, Daekyoung Kang, and Lucas Platter. Two-body and three-body contacts for identical bosons near unitarity. Physical review letters, 112(11):110402, 2014.

[282] Marcus Barth and Johannes Hofmann. Efimov correlations in strongly interacting bose gases. Physical Review A, 92(6):062716, 2015.

[283] Richard J Fletcher, Raphael Lopes, Jay Man, Nir Navon, Robert P Smith, Martin W Zwierlein, and Zoran Hadzibabic. Two and three-body contacts in the unitary bose gas. arXiv preprint arXiv:1608.04377, 2016.

[284] P. A. Ruprecht, M. J. Holland, K. Burnett, and M. Edwards. Phys. Rev. A, 51:4704, 1995.

[285] G. A. Bird. Molecular Gas Dynamics and the Direct Simulation of Gas Flows. Clarendon, Oxford, 2nd edition, 1994.

[286] C. K. Birdsall and A. B. Langdon. Plasma Physics via Computer Simulation. Taylor and Francis, Boca Raton, Florida, 2004.

[287] D. J. Larson, D. W. Hewett, and A. B. Langdon. Comput. Phys. Commun., 90:260, 1995.

[288] J. P. Verboncoeur. J. Comput. Phys., 174:421, 2001.

[289] C. Cornet and D. T. K. Kwok. J. Comput. Phys., 225:808, 2007.

[290] G Kügerl and F Schürrer. P klm expansion of the scattering kernel of the nonlinear boltzmann equation and its convergence rate. Physical Review A, 39(3):1429, 1989.

[291] Weston M Stacey. Nuclear reactor physics. John Wiley & Sons, 2007.

[292] Esther Marley Conwell. High field transport in semiconductors. Number 9. Academic Press, 1967.

[293] Johannes Märkle. Hybrid systems at finite temperatures. PhD thesis, Universität Tübingen, 2014.

[294] Brian Jackson and Eugene Zaremba. Dynamical simulations of trapped bose gases at finite temperatures. arXiv preprint arXiv:cond-mat/0106652, 2008.

Appendix A

Numerical Simulation of Finite Temperature Bose Gases

The ZNG equations describe the evolution of a degenerate Bose gas in a six-dimensional phase space $(\mathbf{r}, \mathbf{p})$, which is a computationally demanding problem. However, making use of symmetries to reduce the number of degrees of freedom needed to describe the system can lead to significant numerical advantages. Here, we make use of the spherical symmetry of the trap which reduces the dimensionality of the problem from six to three, leaving a radial displacement r, a momentum magnitude p, and an angular variable, $\cos\theta$, describing the orientation of the vector $\mathbf{p}$ with respect to $\mathbf{r}$. The main algorithm for numerically solving the ZNG equations is discussed in detail in Refs. [112, 139], and in this Appendix we describe the additional details needed to apply this algorithm to solve the GGPE and QBE in a spherically symmetric geometry.

With spherical symmetry the condensate wavefunction depends only on r, and a 1D GGPE can be used to describe its evolution. Furthermore, rewriting the GGPE in terms of the variable $\phi(r) = r\Phi(r)$ eliminates the first derivative term in the Laplacian, allowing for application of simple Dirichlet boundary conditions where $\phi(r) \to 0$ as $r \to 0, \infty$. We employ the Crank-Nicolson method [284] to solve the GGPE in this form.

As in Ref. [112], a tracer particle method is used to evolve the noncondensate distribution function in phase space such that a Monte Carlo sampling method can be employed to simulate the effects of collisions. We use 2×10^5 tracer particles for all simulations presented in Chapter 3. At each time step the tracer particle positions and momenta are updated based on Newton's equations of motion. Following the method outlined by Bird [285], we take advantage of the spherical symmetry

by only storing the radial coordinate of each tracer particle. However, the complete motion of each particle in 3D space must be tracked such that three momentum components are stored for each particle. At the beginning of each time step we utilize the rotational symmetry of the problem and arbitrarily align the position vector of each particle with the x axis. The action of the y and z directed momentum components is to then push the particle off this axis. It is straightforward to calculate the new radial position of the particle; however, the off-axis motion causes a rotation of the particle trajectory and the momentum components must be rotated accordingly. The new particle position on the x axis is

$$x = r_i + \frac{p_x}{m}\Delta t, \tag{A.1}$$

where r_i is the initial radial position of the particle, p_x its momentum along the x axis, and Δt is the length of the current time step. The action of p_y and p_z moves the particle off axis by a distance

$$d = \sqrt{\left(\frac{p_y}{m}\Delta t\right)^2 + \left(\frac{p_z}{m}\Delta t\right)^2}, \tag{A.2}$$

such that the new radial position r_f of the particle is

$$r_f = \sqrt{x^2 + d^2}. \tag{A.3}$$

The sine and cosine of the rotation angle are then given by

$$\sin\varphi = d/r_f, \tag{A.4}$$

$$\cos\varphi = x/r_f, \tag{A.5}$$

and an azimuthal angle is chosen at random such that $\phi \in [0, 2\pi]$. Finally, the new momentum components are calculated,

$$p_{x,f} = p_x\cos\varphi + \sqrt{p_y^2 + p_z^2}\sin\varphi, \tag{A.6}$$

$$p_{y,f} = p_{c,f}\sin\phi, \tag{A.7}$$

$$p_{z,f} = p_{c,f}\cos\phi, \tag{A.8}$$

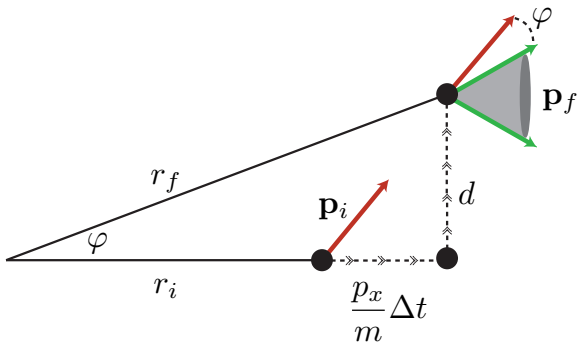

Figure A.1: The particle is rotated from its initial trajectory along r_i by an angle φ due to the off axis components of $\mathbf{p}_i$. After the particle position is updated to r_f the momentum components are rotated and realigned with the position vector. Due to spherical symmetry the azimuthal angle is not unique and is chosen randomly. This is represented by the area of revolution of $\mathbf{p}_f$ about the final position vector r_f.

where $p_{c,f} = -p_x \sin\varphi + \sqrt{p_y^2 + p_z^2}\cos\varphi$. Figure A.1 provides a graphical representation of the particle movement algorithm. Note that although three momentum components are stored for each particle in addition to the position, the algorithm is effectively three-dimensional since the azimuthal angle is randomized at each time step.

After the tracer particles are moved they are binned in phase space to get an estimate of the local noncondensate density and collision rates. The particles are first binned in radial shells using a constant volume binning scheme. Given the size of the simulation domain, l_r, and the total number of bins, N_b, the position of each bin edge is given by

$$r_{b,i} = l_r \left(\frac{i}{N_b}\right)^{1/3}, \tag{A.9}$$

where $i \in [0, N_b]$ is an integer representing the bin index. The simulations performed here use $l_r = 60a_{ho}$ and $N_b = 8\times10^4$. This scheme results in wider bins near the origin, and progressively narrower bins as r increases, which we find reproduces the equilibrium collision rates more accurately than a scheme with equal width bins in r. Once the particles are binned in space a 2D scheme is implemented for binning the particles in momentum space based on p and $\cos\theta$, where p is the magnitude of the particle momentum. The momentum space bins are equally spaced, and we use

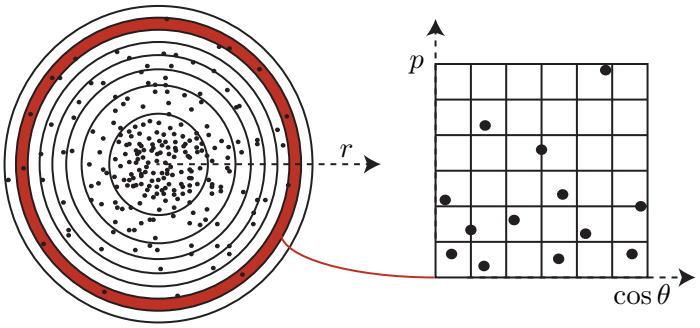

Figure A.2: Cartoon depiction of the phase space binning process. Particles (black points) are binned in position space using constant volume shells with the radial width of each bin decreasing with r. Within each spatial bin the particles are further binned in momentum space using a 2D grid of equal area bins based on the magnitude of their momentum p and trajectory $\cos\theta = \hat{\mathbf{p}} \cdot \hat{\mathbf{r}}$.

20 bins in p and 10 bins in $\cos\theta$ for the simulations performed here. Figure A.2 provides a graphical representation of the binning procedure.

After binning, the tracer particles are used to reconstruct the noncondensate density and phase space distribution function on the discrete numerical grid defined for evolution of the condensate. The density term is required for updating the condensate wave function as well as the momentum of the tracer particles, whereas the phase-space distribution function is necessary for computing the collision rates. Typically, a cloud-in-cell method [286] is employed to reconstruct a discrete function (e.g., density) from the tracer particle distribution by linearly weighting each particle to the nearest grid points defined by the binning process (i.e., the edges of each bin). Following this weighting step, the reconstructed function can be interpolated from the binning grid to another numerical grid if necessary. However, in spherical coordinates a linear weighting scheme results in errors, particularly near the grid boundaries [287]. Therefore, we employ a volume weighting scheme where the particles are weighted to grid points in proportion to the volume of space between the particle and a given grid point [288, 289]. We find this technique improves the accuracy of function reconstruction from the tracer particle distribution, thus allowing fewer tracer particles to be used, which results in improved computation speed. Although not explored in this

thesis, this technique can be extended to cylindrical geometries, which might provide a modest speed-up compared to simulations which assume no symmetries.

Binning with respect to r, p, and $\cos\theta$ suggests an alternate solution method where the distribution function is expanded in the basis of Legendre polynomials, and the QBE can be decomposed into a set of coupled differential equations for each partial wave [290]. These equations can be solved without recourse to Monte Carlo integration as is commonly done in 1D for semiconductor and nuclear reactor transport theories (for example see Refs. [291, 292]). This point is however not taken further here, although it would be an intriguing method the avoids the use of tracer particles to simulate the anomalous density.

The algorithm utilized in Sec. 3.4 utilizes the Monte Carlo procedure of the ZNG approach without the C_{12} terms and the condensate, and is therefore similar to the Direct Simulation Monte-Carlo (DSMC) due to Bird [285].

A.1 Benchmarks

In this section, benchmarks of the spherical ZNG code used in this thesis against ZNG codes from previous works are presented, including: the 3D cylindrical code used in Ref. [139, 112], and the adaptive 3D Cartesian code from Ref. [293]. Our code is limited in the benchmarks that can be made due to the spherical symmetry (i.e. no dipole/Kohn mode etc...) Our benchmarks consist of demonstrating that the code is stable in equilibrium and re-equilibrates properly after a quench of the thermal cloud to a lower temperature. Although not discussed, the first sanity check we performed was to ensure that individual collision events left the total energy invariant.

A.1.1 Equilibrium

Achieving a stable equilibrium populations in a ZNG simulation is a nontrivial affair. Despite the appearance of stable thermal and condensate population in Fig. A.3, both clouds are exchanging atoms and energy continually. The stability of the populations is ensured through detailed balance of the exchange collisions, i.e. that the C_{12}^{in} process is equal to it's time-reversed partner of the C_{12}^{out}

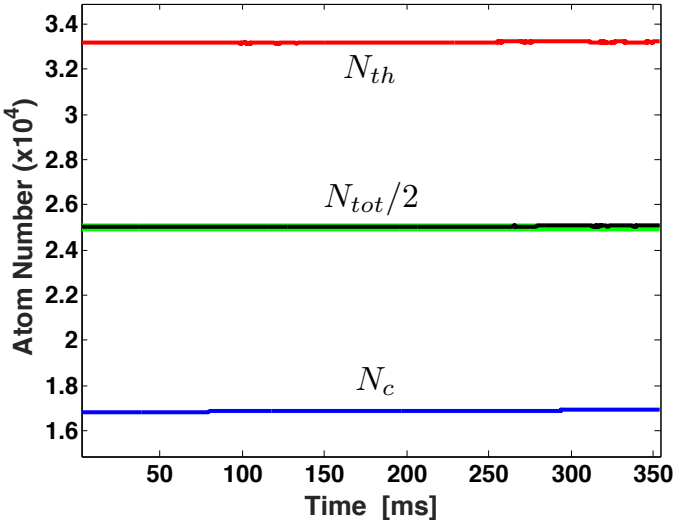

Figure A.3: Results from simulation of our spherical ZNG code for the equilibrium thermal and condensate populations with 5×10^4 total atoms in a 9 Hz trap at 12 nK. The total atom number stays within the fluctuation bounds (green region.)

process[1] . In Fig. A.4, an analytic calculation using the equilibrium Bose distributiont to calculate the spatial dependence of the C_{22} and C_{12} collision rates is compared to the rates extracted from numerical simulation of the equilibrium state.

In this simulation, fixed total atom number is not an enforced constraint on the system. In general it will have small fluctuations around the starting value due to the different ways in which the condensate and thermal atom number are updated in the simulation. In Fig. A.3, the total atom number fluctuates about its initial value showing no longterm drift outside of the fluctuation bound denoted by the green region.

As a final remark, that the populations in Fig. A.3 do not change over time should be contrasted with the ZNG code in Ref. [293][2] whose initial populations adjust by as much as a few percent. This initial adjustment is a result of the simulation finding a new numerical equilibrium as a result of discretization effects in the problem. Our spherical ZNG code appears to capture the actual equilibrium state with minimum discretization effects given the comparative fineness of the grid.

[1] The terminology 'in' and 'out' is in reference to Fig. 4.3.
[2] See Fig. 2.16 in this reference.

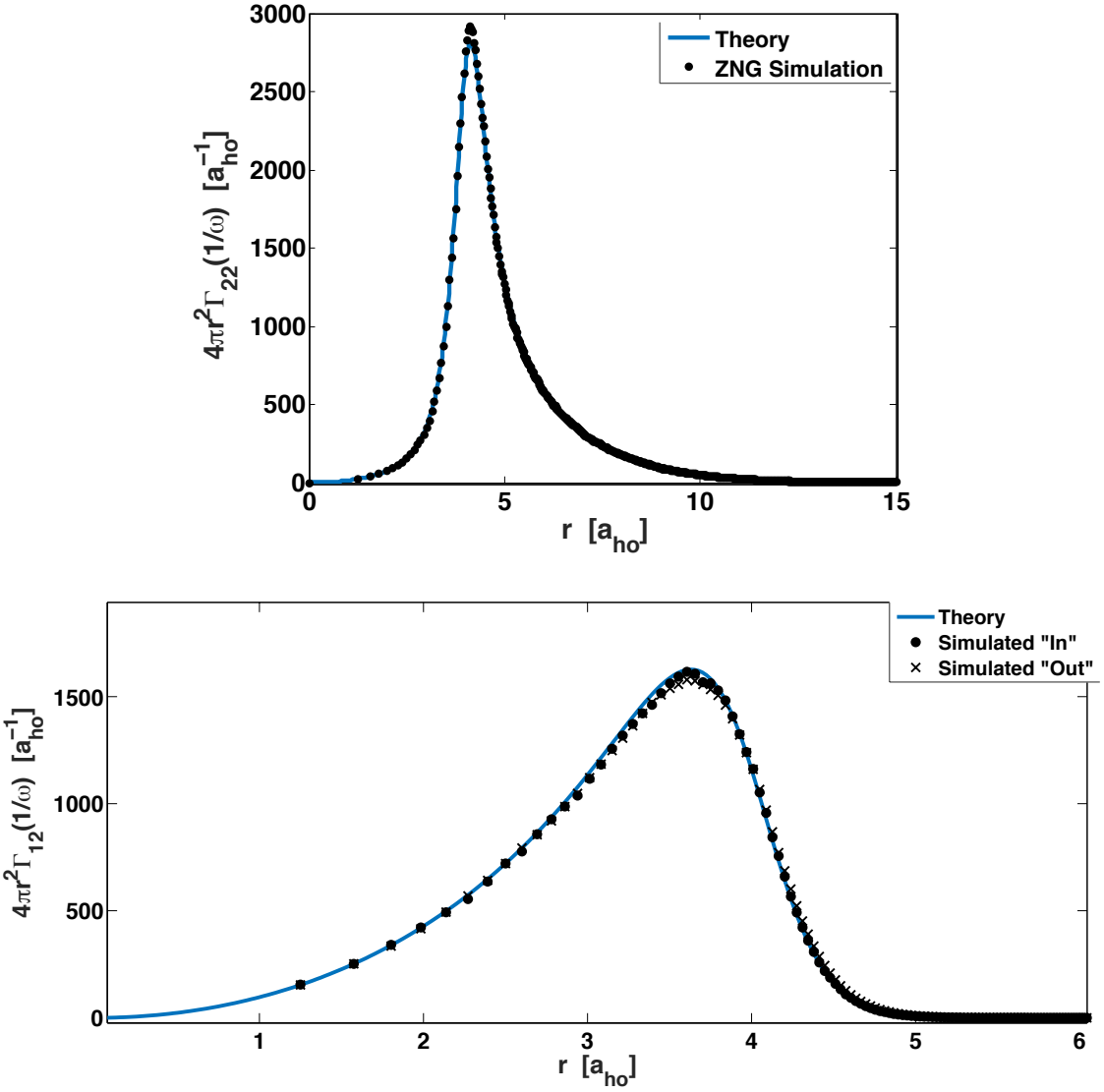

Figure A.4: The collision rates per unit length as a function of position in an 187 Hz trap with 5×10^4 total atoms at 200 nK. In both plots, the data points are a result of Monte Carlo sampling of the collision processes, and the solid curves are a result of an analytic calculation using the Bose distribution. Excellent agreement of the analytic and numerical rates is essential to running a stable simulation.

A.1.2 Rethermalization after a quench

Achieving a stable equilibrium is an important test of detailed balance in the system. Additionally, our spherical code must be benchmarked in a dynamical, out-of-equilibrium situation before being applied to the study of collective oscillations. In the ZNG literature [139, 294], a

quench of the thermal cloud temperature in an isotropic trap was investigated, and the results of this simulation serve as an excellent benchmark of our code. Taking an equilibrium distribution, the quench is accomplished by adjusting the momentum distribution of the thermal atoms to a temperature which is half of the equilibrium temperature. The lower velocities of the thermal atoms result in a collapse of the thermal cloud which contracts towards the center of the cloud and the entire system undergoes oscillations which are then damped as the system rethermalizes. These oscillations are visible in the populations shown in the upper panel of Fig. A.5 where the two timescales in the problem are apparent: a shorter timescale for the balancing of populations $\approx$10 ms and a longer timescale for the damping of the oscillations $\approx$30 ms.

In Fig. A.5, the result of three simulations are shown: a simulation using 3D cylindrical binning geometry (reproduced from Ref. [294]), a simulation using a 3D adaptive Cartesian binning geometry (reproduced from Ref. [293]), and a simulation of our spherical ZNG code. This comparison raises two important points. The first of which is that these simulations all begin with different starting populations and end up displaced by roughly the same amount. This is a result of discretization effects in the simulations where the numerical equilibrium state is different from the actual equilibrium state. This difference is minimized in codes with finer spatial meshes which are adapted to the symmetry of the problem, and whose equilibrium populations do not drift after being initialized. The discretization effects are most pronounced in the 3D cylindrical and 3D adaptive Cartesian and minimized in our spherical code. The second important point is the drift of the total atom number shown in Fig. A.5 (lower panel). As mentioned in the previous subsection, fixed total atom number is not a constraint on the system and undergoes $\sqrt{N_{tot}}$ fluctuations as a result of the noise from the Monte Carlo sampling. A long term drift of the total atom number outside of these bounds indicates usually poor reconstruction of the distribution function and can arise from a suboptimal choice in the binning geometry of the problem. The 3D cylindrical code violates these bounds, however the 3D adaptive Cartesian and spherical ZNG codes do not.

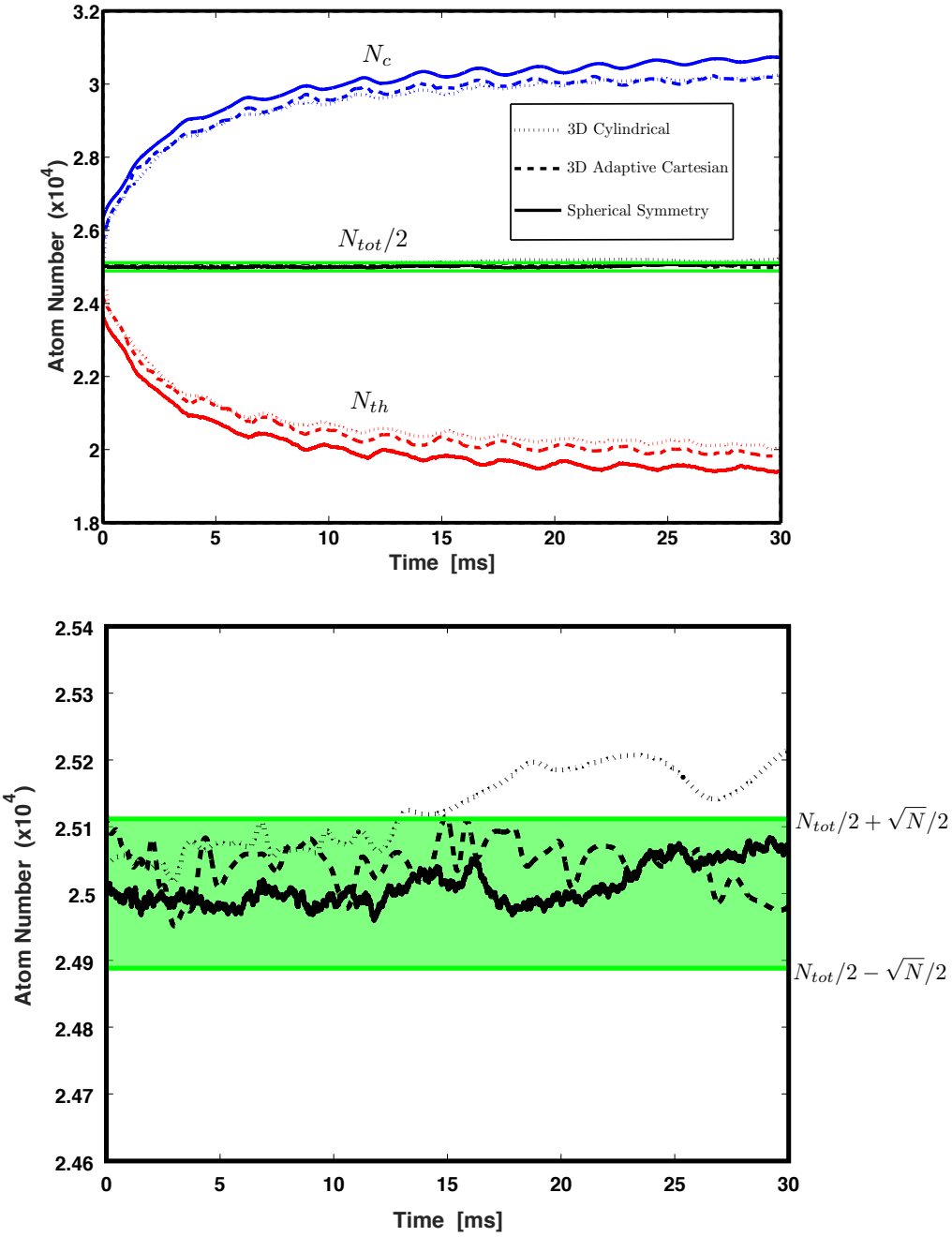

Figure A.5: (a.) The results of a quench of the thermal cloud in a 187 Hz trap with 5×10^4 total atoms and an initial temperature of 200 nK. The three sets of data points are from a 3D cylindrical ZNG code reproduced from Ref. [294], a 3D adaptive Cartesian code reproduced from Ref. [293], and our spherical ZNG code. (b.) The drift of the total atom numbers for the three simulations. The green area is the fluctuation bound.